IEEE
GEOSCIENCE
AND REMOTE SENSING
MAGAZINE

SEPTEMBER 2020 VOLUME 8 NUMBER 3

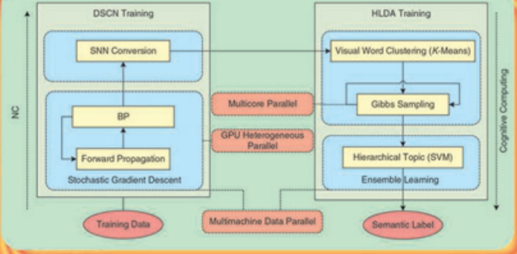

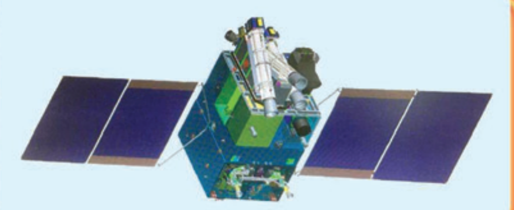

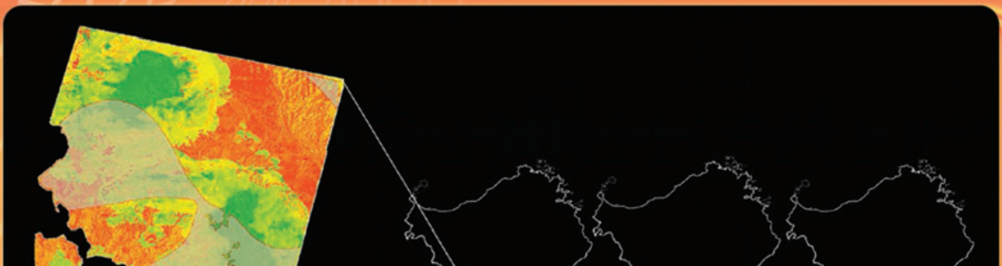

The Range of Remote Sensing

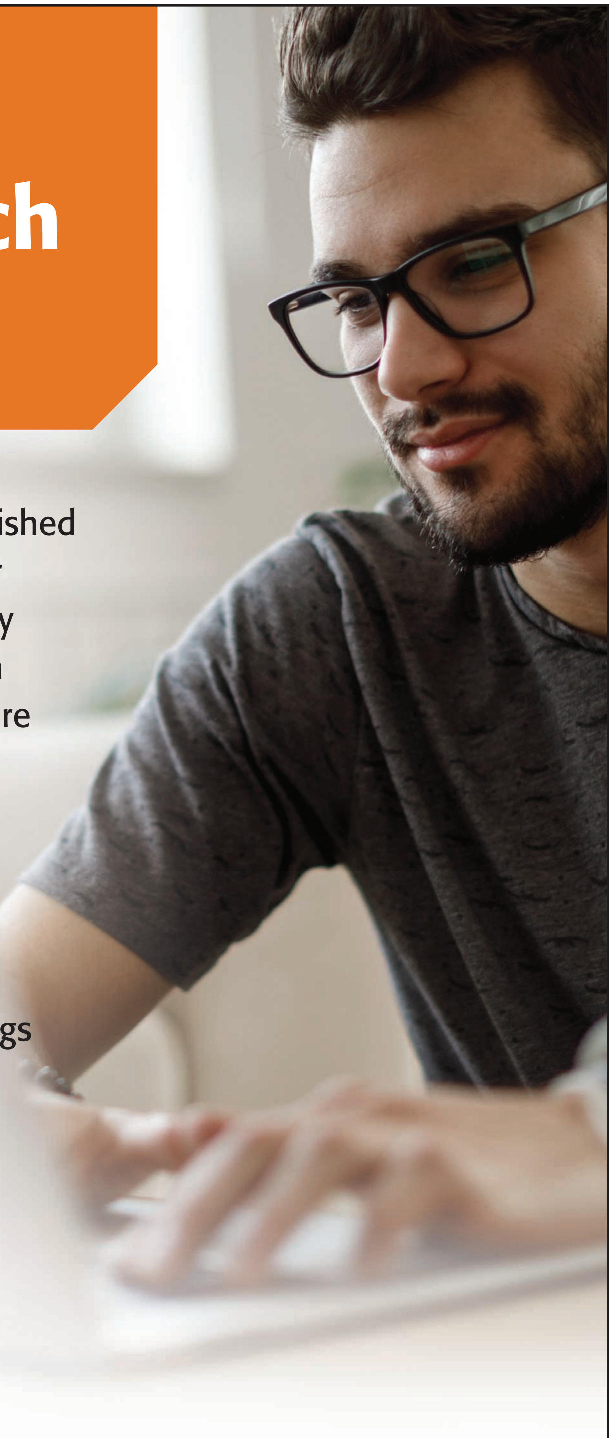

SEPTEMBER 2020
VOLUME 8, NUMBER 3
WWW.GRSS-IEEE.ORG

IEEE GEOSCIENCE AND REMOTE SENSING MAGAZINE

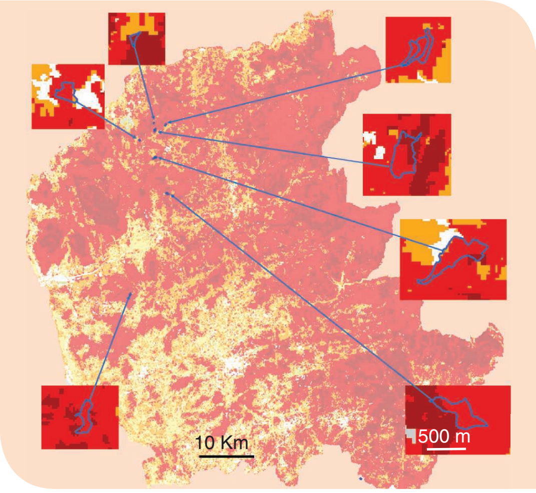

PG. 37

ON THE COVER:
This issue covers nearly the full range of interests in remote sensing, with articles on the satellite platform and instrumentation, calibration infrastructure, product generation, and the algorithms used for these products.

BACKGROUND IMAGE LICENSED BY INGRAM PUBLISHING

SCOPE

IEEE Geoscience and Remote Sensing Magazine (*GRSM*) will inform readers of activities in the IEEE Geoscience and Remote Sensing Society, its technical committees, and chapters. *GRSM* will also inform and educate readers via technical papers, provide information on international remote sensing activities and new satellite missions, publish contributions on education activities, industrial and university profiles, conference news, book reviews, and a calendar of important events.

FEATURES

Digital Object Identifier 10.1109/MGRS.2020.3010432

COLUMNS & DEPARTMENTS

MISSION STATEMENT

The IEEE Geoscience and Remote Sensing Society of the IEEE seeks to advance science and technology in geoscience, remote sensing and related fields using conferences, education, and other resources.

IEEE GEOSCIENCE AND REMOTE SENSING MAGAZINE

EDITORIAL BOARD

Dr. James L. Garrison
Editor-in-Chief
School of Aeronautics and Astronautics
Purdue University
West Lafayette, Indiana 47907
USA
Email: jlg@ieee.org

Dr. Farid Melgani
University of Trento, Italy
Email: farid.melgani@unitn.it

Dr. Linda Hayden
Center of Excellence in Remote Sensing Education and Research
Elizabeth City State University, USA
Email: haydenl@mindspring.com

Dr. Irena Hajnsek
ETH Zürich and DLR
Switzerland
Email: Irena.Hajnsek@dlr.de

Dr. Michael Inggs
University of Cape Town
South Africa
Email: mikings@gmail.com

Dr. John Kerekes
Cochair, Conference Advisory Committee
Rochester Institute of Technology, USA
Email: kerekes@cis.rit.edu

Dr. David M. Le Vine
NASA Goddard Space Flight Center, USA
Email: David.M.LeVine@nasa.gov

Dr. Gail Skofronick Jackson
NASA Goddard Space Flight Center, USA
Email: Gail.S.Jackson@nasa.gov

Dr. Marwan Younis
DLR, Germany
Email: marwan.younis@dlr.de

GRS OFFICERS

President
Dr. Paolo Gamba
University of Pavia, Italy

Executive Vice President
Dr. David B. Kunkee
The Aerospace Corporation, USA

Vice President of Publications
Dr. William Emery
University of Colorado, USA

Vice President of Information Resources
Dr. Mariko Sofie Burgin
Jet Propulsion Laboratory (JPL), USA

Vice President of Professional Activities
Dr. Lorenzo Bruzzone
University of Trento, Italy

Vice President of Meetings and Symposia
Dr. Saibun Tjuatja
The University of Texas at Arlington

Vice President of Technical Activities
Dr. Irena Hajnsek
German Aerospace Center, Germany

Secretary
Dr. Thomas J. Jackson
USDA-ARS Hydrology and Remote Sensing Lab, USA

Chief Financial Officer
Dr. John Kerekes
Rochester Institute of Technology, USA

IEEE PERIODICALS MAGAZINES DEPARTMENT

Managing Editor
Mark Gallaher

Senior Managing Editor
Geraldine Krolin-Taylor

Senior Art Director
Janet Dudar

Associate Art Director
Gail A. Schnitzer

Production Coordinator
Theresa L. Smith

Director, Business Development–Media & Advertising
Mark David
+1 732 465 6473
m.david@ieee.org
Fax: +1 732 981 1855

Advertising Production Manager
Felicia Spagnoli

Production Director
Peter M. Tuohy

Editorial Services Director
Kevin Lisankie

Staff Director, Publishing Operations
Dawn M. Melley

IEEE Geoscience and Remote Sensing Magazine (ISSN 2168-6831) is published quarterly by The Institute of Electrical and Electronics Engineers, Inc., IEEE Headquarters: 3 Park Ave., 17th Floor, New York, NY 10016-5997, +1 212 419 7900. Responsibility for the contents rests upon the authors and not upon the IEEE, the Society, or its members. IEEE Service Center (for orders, subscriptions, address changes): 445 Hoes Lane, Piscataway, NJ 08854, +1 732 981 0060. Individual copies: IEEE members US$20.00 (first copy only), nonmembers US$110.00 per copy. Subscription rates: included in Society fee for each member of the IEEE Geoscience and Remote Sensing Society. Nonmember subscription prices available on request. Copyright and Reprint Permissions: Abstracting is permitted with credit to the source. Libraries are permitted to photocopy beyond the limits of U.S. Copyright Law for private use of patrons: 1) those post-1977 articles that carry a code at the bottom of the first page, provided the per-copy fee indicated in the code is paid through the Copyright Clearance Center, 222 Rosewood Drive, Danvers, MA 01923 USA; 2) pre-1978 articles without fee. For all other copying, reprint, or republication information, write to: Copyrights and Permission Department, IEEE Publishing Services, 445 Hoes Lane, Piscataway, NJ 08854 USA. Copyright © 2020 by the Institute of Electrical and Electronics Engineers, Inc. All rights reserved. Application to Mail at Periodicals Postage Prices is pending at New York, New York, and at additional mailing offices. Canadian GST #125634188. Canada Post Corporation (Canadian distribution) publications mail agreement number 40013885. Return undeliverable Canadian addresses to PO Box 122, Niagara Falls, ON L2E 6S8 Canada. Printed in USA.

IEEE prohibits discrimination, harassment, and bullying. For more information, visit http://www.ieee.org/web/aboutus/whatis/policies/p9-26.html.

SUSTAINABLE FORESTRY INITIATIVE Certified Chain of Custody
Promoting Sustainable Forestry
www.sfiprogram.org
SFI-01681

Digital Object Identifier 10.1109/MGRS.2020.3010433

BY JAMES L. GARRISON

Welcome to the September Issue

Welcome to the September 2020 issue of *IEEE Geoscience and Remote Sensing Magazine* (*GRSM*)! I start off with some very good news. Clarivate Analytics has released the 2019 *Journal Citation Reports*, Science Edition. The impact factor of *GRSM* has again increased substantially, to 13, placing us first in both the Remote Sensing and the Imaging Science and Photographic Technology categories. The magazine's impact factor also ranks third in the Geochemistry and Geophysics category.

Following on the heels of our extensive two-part special issue on interferometric synthetic aperture radar (SAR), the features in this issue have a much broader scope, covering nearly the full range of interests in remote sensing. We start with the satellite platform and the instruments that produce raw observations, and we then move on to the infrastructure needed for calibrating and validating these measurements. We next review important examples demonstrating the types of valuable products that can be generated from these measurements and conclude with a tutorial focused on the algorithms involved in generating such products.

Our first feature describes *ZiYuan3-0* (*ZY3-03*), the third satellite in China's civilian stereo surveying and mapping satellite series. It is designed to provide high-resolution stereo images, multispectral images, and auxiliary data over Chinese territory and will be fundamental for establishing a geospatial framework and updating national geographic information. *ZY3* products are applicable to many different fields, including land resource management, forestry protection, agriculture monitoring, and natural disaster reduction.

The article reviews many of the satellite system's design considerations, including the precise time synchronization attitude and orbit determination required to meet demands of the mapping mission. It also describes the three principal instruments—panchromatic camera, multispectral camera, and laser altimeter—and introduces the data products, which should be widely distributed in the near future. *ZY3-03* was successfully launched on 25 July 2020. At the time of this writing, it is undergoing on-orbit testing.

Moving from spaceborne instruments back down to Earth, our second feature reviews the Tibetan Plateau Integrated MultiScale Moisture and Temperature Observatory (TP-IMSO), a large network of ground-based instrumentation to deepen our understanding of how multiple satellite products can support studies on climate and land surface process models, the water cycle, and the soil–atmosphere interface. The TP-IMSO collects atmospheric, soil, and vegetation variables using a wireless network and an advanced data management system with an open data policy.

Field data at different scales matching those of satellite pixels are of profound significance in validation and algorithm improvement for satellite remote sensing products. It has been difficult to obtain such comprehensive field observation data on the Tibetan Plateau because of spatiotemporal variation and complex topography. Conventional meteorological stations are also scare in the western Tibetan Plateau. The TP-IMSO, therefore, provides an important capability in that region.

Data products provided by remote sensing are only of value if they can be used to provide some societal benefit. Our third feature addresses an important example of such a benefit, with a review of utilizing remote sensing in the Prevention and Recovery of Forest Fires Emergency in the Mediterranean Area (PREFER) project. PREFER, supported by the Seventh Framework Programme (FP7) of the European Union, developed products to reduce the damage caused by forest fires by improving preparedness for and prevention of new fires as well as post-fire recovery and reconstruction. These products utilize optical data, high-resolution SAR, and digital elevation maps and

Digital Object Identifier 10.1109/MGRS.2020.3010434
Date of current version: 21 September 2020

also account for human intervention (93% of fires are caused by human activities).

Our fourth feature is a tutorial on algorithms for target classification and recognition in high-resolution images. The authors use parallel processing to improve the efficiency of Cross-model Neural Cognitive Computing algorithms without loss of recognition precision. Three pseudocode examples are provided for the algorithms along with demonstrations based on the visual images of ships taken from Google Earth and X-band SAR images of military vehicles obtained from a public database.

We have two very interesting "Software and Data Sets" columns in this issue. The first describes the Signals of Opportunity Coherent Bistatic Scattering Simulator (SCoBi). Signals of opportunity (SoOp) is an exciting new technique that has the potential to offer cost-effective global remote sensing for land applications.

SCoBi is a fully polarimetric simulator for coherent SoOp scattering from bare or vegetated terrains, in which soil is modeled as a single- or multilayered dielectric medium. It takes into account important antenna characteristics and enables interferometric analysis by providing the complex field quantities. The SCoBi simulator framework is released under the GNU General Public License. A user's manual, developer's manual, and set of tutorial videos are provided to optimize the time and effort spent by Earth science researchers on bistatic forward modeling.

The second "Software and Data Sets" column article introduces So2Sat LCZ42, a benchmark data set for global local-climate-zone (LCZ) classification. Access to labeled reference data is a challenge in any supervised machine learning endeavors, especially for an automated analysis of remote sensing images on a global scale. So2Sat LCZ42 was created to meet this need in urban research. The data set consists of LCZ labels for approximately half a million *Sentinel-1* and *Sentinel-2* image patches in 42 urban agglomerations (plus 10 additional smaller areas) around the world, produced by a group of domain experts following a carefully designed workflow and evaluation process. A human evaluation procedure with independent voting by 10 experts showed an average class confidence of 85%. Open access to this high-quality data set is provided to the research community.

Our first of two "Technical Committees" columns presents the results of a member survey conducted at the start of the year to assess how familiar members are with the activities of their technical committees (TCs), get opinions on missing topics, and solicit suggestions for improvements. These suggestions will be used to improve operation of the seven IEEE Geoscience and Remote Sensing Society (GRSS) TCs.

The GRSS Standards for Earth Observations TC is the subject of the second "Technical Committees" column. This TC was created in 2017 to address the need for technical standards to support the processing, management, analysis, and quality assessment of remote sensing data. At the present time, five standards are in development.

The "Education" column in this issue honors IEEE Fellow, Prof. Sebastiano Bruno Serpico, full professor of telecommunications at the Polytechnic School of the University of Genoa, who was recently presented with the prestigious GRSS Education Award. Congratulations to Prof. Serpico!

The University of New South Wales Canberra Student Chapter is the subject of our "Chapters" column in this issue. Established in 2018, it is the first IEEE GRSS Student Chapter in Australia and has already accumulated an impressive record of seminars and conference presentations.

Concluding this issue, the "Women in GRSS" column discusses the challenges the organizers encountered in adapting activities for a virtual conference at IGARSS 2020. (Please see the "President's Message" for more details on how our flagship conference and general Society operations have been readjusted in response to the COVID-19 global pandemic.) In short, the IDEA committee has done an excellent job in transitioning the planned content to the online format.

We continue to seek submissions in all areas of geoscience and remote sensing but wish to remind potential authors that *GRSM* is not a forum for first presentation of original research. Tutorial and feature articles intended to inform and educate readers in the broad remote sensing community are welcome. Manuscripts presenting new research, however, should be directed to one of the three GRSS journals.

To provide potential authors with more timely feedback, *GRSM* will implement a two-stage review process, starting in January 2021. A short white paper (five pages or fewer) should be submitted first, for review by associate editors or members of the editorial board. Following a positive review of the white paper, authors may be invited to submit a full manuscript, which will then undergo a complete peer review.

Contributions to our regular columns—"Chapters," "Space Agencies," "Women in GRSS," "Education," "Software and Data Sets," and "Conference Reports"—are also welcome. White papers, columns, and invited manuscripts should be submitted through ScholarOne Manuscripts at http://mc.manuscriptcentral.com/grsm. Proposals for special issues should be sent to me directly at jlg@ieee.org.

Please stay safe!

GRS

BY PAOLO GAMBA

Facing Challenges, Creating Opportunities

Traditionally, the September "President's Message" is dedicated to highlighting the International Geoscience and Remote Sensing Symposium (IGARSS), normally held in July. However, this year, as of this writing, we are still waiting to attend the first-ever virtual IGARSS, to be held from 26 September to 2 October 2020 (see https://www.igarss2020.org). This is one of the challenges we are facing due to the COVID-19 pandemic that has changed our lifestyle so much and is going to have an impact on the way we, as IEEE Geoscience and Remote Sensing Society (GRSS) members, interact and work together for quite a while.

The virtual IGARSS 2020 is going to be a different event from our traditional IGARSS—but not all that different with regard to opportunities to interact and connect. We are forced to replace the in-person connection and meetings with virtual meetings and electronic connections. However, the content will be the same, and the attitude of our membership toward sharing and discussing interesting scientific and technical results is and always will be the same. We are members of this Society because we believe that there is an advantage in working together to achieve greater scientific and technical goals and we understand that only by sharing and working together can we achieve them. As a matter of fact, IGARSS will provide the same opportunities, via presentations and live discussions, from which we benefit during traditional in-person conferences (https://s3.amazonaws.com/video.igarss2020.org/IGARSS2020_in_a_nutshell.mp4).

Of course, since there may be issues with some electronic connections, we have put into place a lot of "redundancy" in the form of prerecorded presentations as well as additional people available to manage the sessions. We will have both session chairs and session managers, with different yet complementary tasks, to help sessions run smoothly and be useful to every attendee. Equally important to the many members who are involved in our seven technical communities (TCs; see http://www.grss-ieee.org/community/technical-committees/), there will be opportunities to interact even without the traditional TC and Chapters dinner.

The same is true for our Chapter chairs, who have traditionally met in person each year, beginning with IGARSS 2015 in Beijing, to discuss their activities as well as share best practices and good ideas for projects and ChapNet initiatives. Instead of the traditional in-person meeting, this year there have been and will continue to be webinars and online meetings that provide the same opportunities to interact and connect. Please stay tuned and look for the multiple emails (and social media posts!) you have received or will be receiving from IGARSS about the Technology, Industry, and Education (TIE) Forum events. All TIE events, including the links to webinar videos already offered as well as registration links for future ones, are available on the IGARSS 2020 website at https://igarss2020.org/TIEEvents.asp.

I encourage you to take a look and share the links and other resources with your local and technical communities because these stable sources of information will be useful to anyone who would like to better understand our Society's TIE and Chapter activities and how to participate in them. There are many advantages to being a GRSS member, but an invaluable one for many of us is the opportunity to become part of one of our technical or geographical communities. This is something you may wish to consider starting in your own country or topic of interest!

Another challenge we have had to face due to COVID-19 is the implementation of some of the educational activities planned in connection with (or as a complement to) IGARSS. This is the case for the GRSS Summer School (GR4S), typically held just before IGARSS (https://hilo.hawaii.edu/depts/geography/igarss-2020/). However, during the past two years the GRSS has begun organizing similar events in other parts of the world, including experiential training activities for students

---

Digital Object Identifier 10.1109/MGRS.2020.3015418
Date of current version: 21 September 2020

and (young) professionals. To meet this objective, I have appointed an ad hoc committee, the GR4S Team, to coordinate activities among existing schools and foster new ones. The GR4S Team, led by Jun Li for the first months of this year and by Andrea Marinoni starting in April, has faced the challenge of organizing these events in an unprecedented situation. In spite of this, they were very successful, and two GR4Ss have already been organized and delivered virtually in July (in Hawaii and in P.R. China). One more GR4S is planned for September in Norway, and there are contacts with CONAE, the Argentinian Space Agency, for their Spring School in December, typically cosponsored by the GRSS. These virtual educational events have been attended by thousands of students and allowed the GRSS to reach a large number of young people interested in studying remote sensing topics and doing research in an area of interest to the GRSS. This is a great way to expand the reach of our community and engage new people, inviting them to become part of our membership.

Another challenge that has been successfully tackled during the first six months of 2020 is an update to the status of our *IEEE Journal of Selected Topics in Applied Earth Observations and Remote Sensing* (*J-STARS*; http://www.grss-ieee.org/publication-category/jstars/). *J-STARS* became an open access journal in January 2020 and has a very competitive and subsidized article processing charge (APC) of US$1,250. This APC will stay the same in 2021, allowing GRSS members to publish their papers at a reasonable cost in a fully open access journal with a recently released impact factor for 2019 of 3.827, a nearly 13% increase since 2018. As a matter of fact, moving *J-STARS* to open access has increased the number of submissions (more than 950 in 2020 to date, with a forecast total of 1,600 submissions by the end of 2020), demonstrating the interest by our membership in this opportunity. We are glad that the GRSS Administrative Committee's decision in March 2019 to move *J-STARS* to open access has met the needs of our membership. We would further like to thank both current Editor-in-Chief Jenny Du and incoming Editor-in-Chief Jun Li (starting in January 2021) for their work. Currently, there are more than 30 open calls for *J-STARS* special sections on very important topics, ranging from machine learning-based remote sensing to big data processing to superresolution of remotely sensed images. Please check the website at http://www.grss-ieee.org/jstars-special-issues/ to find out if there is a topic of interest to you. Remember, however, that submissions to *J-STARS* beyond these designated special topics are also welcome because *J-STARS* accepts papers in all areas of interest to GRSS members.

All in all, 2020 has been, and will likely remain, a challenging year. However, the Society has coped very well and adapted to the multiple challenges we have faced. We have had to cancel some events that were carefully planned to increase our regional presence (in Latin America and in India); however, these activities have been rescheduled for 2021 or 2022. Nevertheless, some of the larger goals have been achieved, and the GRSS has successfully met some of the principal challenges before us. I believe that the implementation of IGARSS 2020 is one of these situations, and I look forward to meeting you virtually during the conference all of us are awaiting at the end of September!

Kind regards, and stay safe!

GRS

Announcing Revamped Technology, Industry, and Education Activities for 2020

The TIE (technology, industry, and education) activities that are part of the annual IGARSS conference are being conducted in a new format this year. These activities will be presented as a series of free webinars distributed during the summer and autumn of 2020. We are in the process of finalizing the activities, but they will include educational seminars, code workshops, panels, and a virtual mixer! These activities are being brought to you by a number of GRSS groups including Young Professionals, IDEA, Educational Activities, and the industry outreach team. Watch your inbox, the IGARSS 2020 TIE page on igarss2020.org, and the GRSS social media channels for more information. We look forward to seeing you virtually this year! No conference registration needed!

Digital Object Identifier 10.1109/MGRS.2020.3019161

The China *ZY3-03* Mission

Surveying and mapping technology for high-resolution remote sensing satellites

©SHUTTERSTOCKPHOTO.COM/CONCORDIA DISCORS

XINMING TANG, XIAOMING GAO, HAIYI CAO, FAN MO, ZHENMING WANG, WENXIA XU, GUANGBIN ZHU, QINGXING YUE, FEN HU, HONG ZHU, AND JING LU

Digital Object Identifier 10.1109/MGRS.2019.2929770
Date of current version: 20 March 2020

The *ZiYuan3* (*ZY3*) is a civilian stereo surveying and mapping satellite from China operating under the framework of the Earth resources satellite series, and its objective is to fulfill 1:50,000 mapping and update larger-scale fundamental geographic information products. This article introduces the *ZY3-03* satellite's mission and payload specifications as well as its data utilization and distribution policy. In the future, the *ZY3-03* will realize the demands of China's national economic and social development and play an important role in the fields of Earth observation and environmental protection.

HISTORY

In the past 30 years, China has developed several satellite series, such as the meteorological series *Fengyun* ("Wind and Cloud"); ocean series *Haiyang* ("Ocean"); Earth resources series *Ziyuan* (ZY) ("Resource"); high-resolution Earth observation series *Gaofen* (*GF*) ("High Resolution"); environment- and disaster-monitoring small satellite constellation ("Environment and Disaster"); and experimental series *Shijian* ("Experiment") for new technological exploration [1]. China's national Earth Observation System contributes not only to rapid economic and social development but also to the international Earth Observation System.

With the rapid development of China's resource series satellites, an Earth observation system with medium and high resolution, wide coverage, and multitemporal capabilities has been established [2]. The derived data products from in-orbit satellites, including the *ZY02C*, *ZY3-01*, *ZY3-02*, *GF1-A*, *GF1-B*, *GF1-C*, *GF1-D*, *GF2*, and *GF6*, have been applied comprehensively and are mainly used in the fields of land and forestry monitoring, agriculture management, environmental protection, surveying, and mapping, among others.

The *ZY3* is China's civilian stereo surveying and mapping satellite series operating under the framework of the Earth resources series and is included in the medium- and long-term development plan for China's Civil Space Infrastructure (2015–2025). Compared with other similar satellites, such as the *SPOT 5* [3] and *ALOS-1* [4] series, the *ZY3* has better geolocation accuracy without ground control points (GCPs) of up to 10 m.

The *ZY3* has been used for 1:50,000 stereo mapping or even larger-scale national fundamental geographic product updates. The surveying and mapping technology of high-resolution remote sensing satellites is fundamental for the establishment of China's geospatial framework and informationized mapping system, and it has become an indispensable part of updating national geographic information.

DEMANDS

FUNDAMENTAL SURVEYING AND MAPPING

Topographic maps at the 1:50,000 scale were first developed in China in the 1970s. Since then, frequent revisions have been required due to rapid changes in land utilization. Increasing numbers of high-resolution remote sensing satellites have been used for 1:50,000-scale surveying and mapping in China. The objective of the *ZY3* series is to provide data for fulfilling 1:50,000 mapping and updating 1:25,000 or even larger-scale topographic maps.

GEOGRAPHICAL SITUATION MONITORING

Geographical situation monitoring is an important aspect of the geographic information field. High-resolution remote sensing images can provide data support and are helpful for quantitative monitoring and statistical analysis. By accelerating the development of surveying and mapping satellite application systems, satellite data can provide strong support for geographical situation monitoring.

GEOSPATIAL INFORMATION INDUSTRY

With the development of geographic information system (GIS) software technology, the application of technical exploration is no longer a problem for GIS, and data resources have become the key factor in the success of geographic application systems. The lack of fundamental geographic data is currently a bottleneck that limits the development of the geospatial information industry in China, and data products still cannot fulfill the demands of the data industry. Although there have been great achievements in the geographic data production industry, data availability, quality, and updates still do not meet the requirements of applications. High-resolution mapping satellite data will become an important supplement for these applications.

EMERGENCY SURVEYING AND MAPPING SUPPORT

Natural disasters occur frequently in China; therefore, we need to obtain the latest geographic data and information in disaster areas to support emergency services. For public emergencies (such as natural disasters and accidents), public health, and social security, surveying and mapping satellites can provide geographic information products and establish a database for emergency services.

GLOBAL GEOSPATIAL INFORMATION ACQUISITION AND SERVICES

In the mainstream of economic globalization, the Belt and Road Initiative (B&R), which covers more than 60 countries and regions around the world, has been proposed as part of China's national development strategy. With their continuous and direct observation capability, remote sensing satellite technologies can provide strong support for the B&R initiative and promote economic structures and international cooperation.

ZY3 SERIES OVERVIEW

The *ZY3* series comprises the first civilian stereo surveying and mapping satellites in China. The first satellite in the series, the *ZY3-01*, was successfully launched on 9 January 2012 and includes three high-resolution panchromatic cameras and one multispectral camera. The panchromatic camera is assembled in time-delay-integration charge-coupled-device (TDI CCD) mode. The front-view and back-view cameras both have a 3.5-m spatial resolution and 51-km ground swath, whereas the nadir-view and multispectral cameras can provide spatial resolutions of 2.1 and 5.8 m, respectively, each with a ground swath of 51 km.

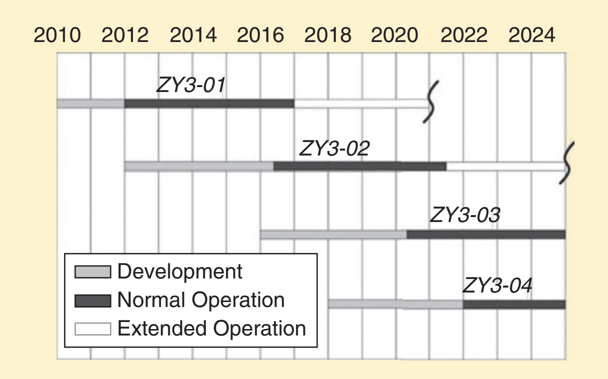

FIGURE 1. The *ZY3* satellite series development plan.

The *ZY3-02* is the second satellite in the *ZY3* series. It was successfully launched on 30 May 2016. Compared with the *ZY3-01*, some technical improvements were made in the *ZY3-02*. First, without altering the optical camera lens, the resolution of the front-view and back-view cameras was improved from 3.5 to 2.7 m by replacing the 7-µm TDI CCD. Second, the multispectral camera installation was redesigned to better realize the fusion effects of the panchromatic and multispectral images. Third, the software system onboard was updated, greatly improving the convenience and efficiency of the satellite ground control system. Fourth, in addition to the optical payloads, the *ZY3-02* is equipped with an experimental laser altimeter, used to improve the vertical accuracy.

To maintain the service continuity of the *ZY3* series, the *ZY3-03* satellite will be ready for launch in the middle of 2020. The in-orbit duration of the *ZY3-03* will be extended to eight years, compared with five years for the *ZY3-02*, and the system performance will be improved with the inclusion of a laser altimeter for stereo surveying and mapping, significantly enhancing the vertical accuracy. Furthermore, the *ZY3-04* is expected to be launched two years after the *ZY3-03*. The *ZY3* series development plan is shown in Figure 1.

Real-time data from the *ZY3* series are mostly received by three fixed ground stations located in Miyun, Kashi, and Sanya, China, and one mobile ground station located in southwestern China. In addition to real-time satellite data, other data are stored in the solid-state memory of the satellite and, later, downlinked to the ground stations. The *ZY3* series receiving system is shown in Figure 2.

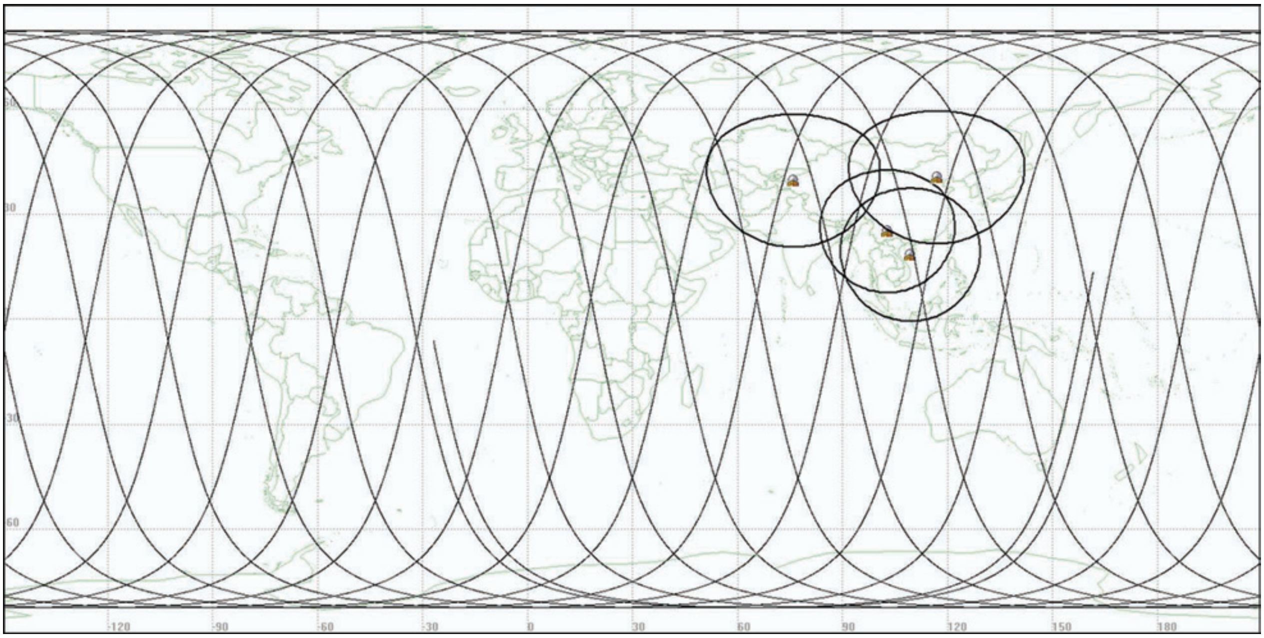

FIGURE 2. The *ZY3* satellite series receiving system.

The *ZY3-03* is designed to provide high-resolution stereo images, multispectral images, and auxiliary data over China's territory in a long-term, stable, and efficient manner. The dual-satellite operation mode will be enabled after the launch of the *ZY3-03*, reducing the revisit cycle time to fewer than three days, compared with five days for one operational satellite. In addition, the global coverage time will be reduced significantly.

THE *ZY3-03* PLATFORM

The *ZY3-03* is a three-axis-stabilized Earth observation satellite that is being manufactured by the China Academy of Space Technology (Figure 3). The platform, although based on upgraded avionics, retains the architecture of the *ZY3-01* and *ZY3-02*.

The satellite consists of payloads and service systems. The payloads mainly include a three-line-array camera, a multispectral camera, a laser altimeter, a digital-transmission subsystem, digital antennas, and an image-recording subsystem. The service systems comprise the power supply, control, propulsion, and data and thermal management subsystems, which provide support services, such as installation, power, control, and temperature maintenance for the payloads.

The *ZY3-03* runs in a sun-synchronous orbit at an altitude of approximately 505 km and is capable of producing seamless imagery covering Earth's surface from latitudes of 84° south to 84° north. The spacecraft designed for the *ZY3-03* mission is a three-axis-stabilized satellite directly placed into Earth orbit by the launcher. The platform provides high pointing accuracy (approximately 0.1° on each axis), and the weight of the spacecraft is approximately 2,650 kg.

The main characteristics of the *ZY3-03* spacecraft are shown in Table 1. It uses a mature *ZY3* satellite platform with a stable structure. To fulfill the demands of the mapping mission, the *ZY3-03* service system fully inherits the fine state of the *ZY3* series platform, which is designed with improvements in precise attitude determination (PAD), precise orbit determination, and time synchronization. The main technical specifications of the service system are shown in Table 2.

PRECISE ATTITUDE DETERMINATION

To enhance attitude accuracy and stability, star sensors and gyroscopes are always equipped with state-of-the-art satellites. Star sensors are used to determine the absolute inertial attitude without drift at low frequencies to reach the highest accuracy possible, and gyroscopes are used to measure the angular velocity at high frequencies.

The PAD system (PADS) is designed to fulfill 1:50,000-scale surveying and mapping requirements. The attitude determination accuracy of the *ZY3-03* is 1 arc-second, surpassing other satellites with similar specifications. The *ZY3-03* is equipped with three star trackers and four groups of gyroscopes to acquire the attitude data. The raw data of the star trackers and gyroscopes are processed onboard with an extend Kalman filter to realize real-time attitude determination, followed by a forward–backward Kalman filter for high-precision attitude postprocessing. To ensure that the time is consistent and uniform in the satellite, time synchronization of all subsystems is controlled by the timing system.

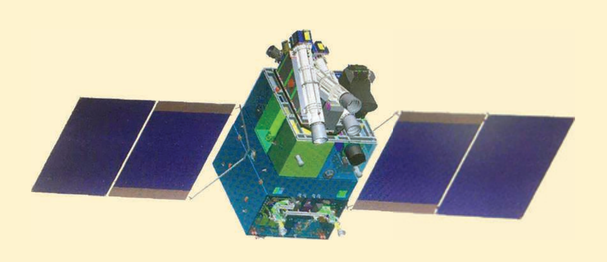

FIGURE 3. An artist's interpretation of the *ZY3-03*.

TABLE 1. THE *ZY3-03* SPACECRAFT CHARACTERISTICS.

FEATURES	SPECIFICATIONS
Orbit	Sun-synchronous at 505 km 59-day repeat cycle
Mean local solar time	10:30 a.m.
Orbital period	97 min
Attitude stabilization	Three-axis stabilized
Weight	2,650 kg
Mission duration	Eight years
Swath width	51 km

TABLE 2. THE *ZY3-03* SERVICE SYSTEM CHARACTERISTICS.

FEATURES	SPECIFICATIONS
Attitude control system	Pointing accuracy: ≤0.02° (three-axis, 3 σ) Stability: ≤5 × 10^{-4}°/s (three-axis, 3 σ) Drift angle correction: 0.02° (3 σ, calculated based on nadir-view camera)
Time-synchronization accuracy	≤50 μs
Time reference system	Universal time coordinated, Beijing
Satellite laser ranging	Corner reflector equipped on platform
Remote observe and control	Method: USB Mode: plain code transmission
Star tracker	Inertial attitude determination accuracy: ≤5″ (*xy*-plane, 3σ) Sampling frequency: 4 Hz
Gyroscope	Drift error: 0.02°/h Sampling frequency: 4 Hz
GPS signal receiver	Type: dual band Location accuracy: 10 m (real time, 1 σ)

The PADS performance of the *ZY3-01* and *ZY3-02* satisfies the design specifications and operation requirements [5]; therefore, the PADS will be applied to the *ZY3-03* with inherent high-accuracy attitude determination and fine control capabilities. The *ZY3-03* attitude determination simulations on three axes (roll, pitch, and yaw) in orbit coordination are shown in Figure 4.

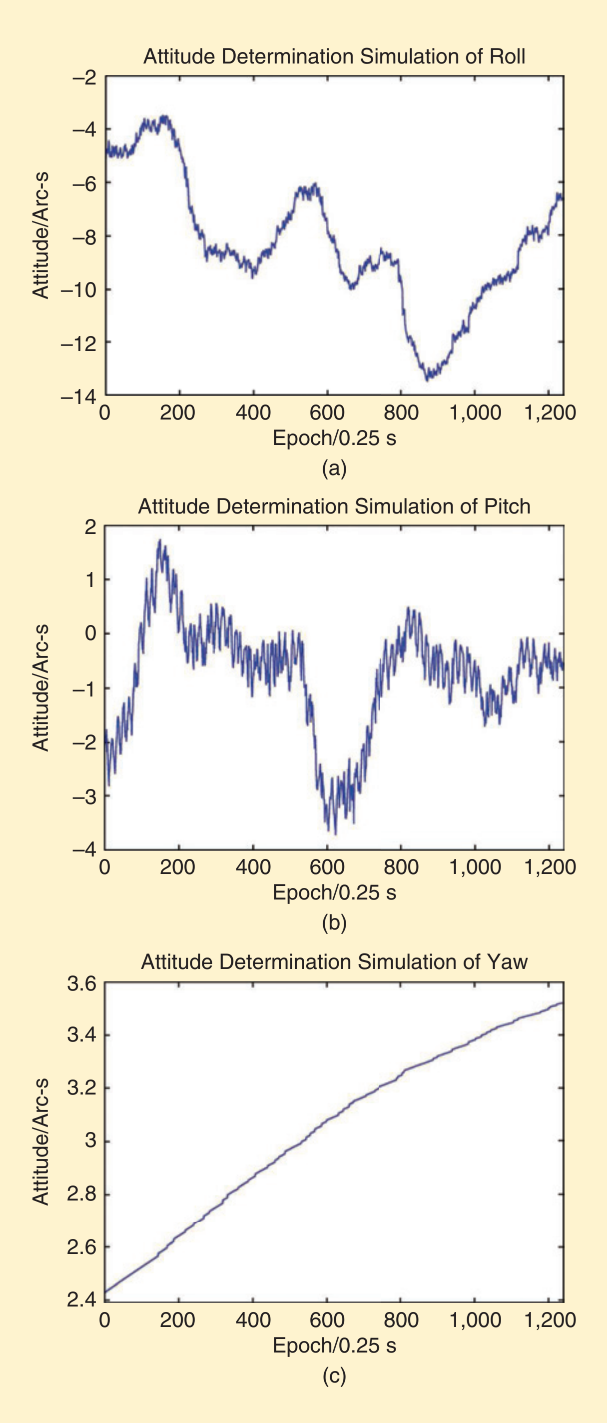

FIGURE 4. *ZY3-03* attitude determination simulations for (a) roll, (b) pitch, and (c) yaw.

PRECISE ORBIT DETERMINATION

The satellite's orbit position is an exterior orientation element for space photogrammetry, and it directly affects the surveying and mapping precision. The *ZY3-03* will be equipped with both dual-frequency GPS receivers and a laser reflector array (LRA) to improve the satellite's precise orbit-determination capability.

GPS signals are obtained and the signal carrier phase and pseudo-range are measured to form the original information for the dual-frequency GPS receivers. The GPS information is stored in the data storage unit of the satellite and is sent down to the ground receiving station via the digital transmission subsystem. The ground application system processes and classifies the raw data to complete the satellite's precise orbit determination. Meanwhile, the LRA uses satellite laser range technology to verify the orbit measurement results derived from the GPS receiver.

Due to the performance of the precise orbit determination, with an accuracy of 5 to 7 cm for the three axes of the *ZY3-01* and *ZY3-02* [6], the dual-frequency GPS receivers and LRA will be applied on the *ZY3-03* to guarantee high-precision orbit determination. The *ZY3-03* orbit determination simulations are shown in Figure 5.

TIME SYNCHRONIZATION

To ensure accuracy of the geolocation imagery, all of the satellite subsystems need to work within the same time reference, and the time synchronization accuracy must be better than 50 μs. The time synchronization system is designed such that all satellite subsystems work with the unified timing resource [7].

The dual-frequency GPS system is used as the reference clock source for the *ZY3-03* time synchronization system. Utilizing the entire second characteristic of the GPS signal, the normal working receiver will generate a second pulse signal per second with a precision of 1 μs. The signal is processed, amplified, and sent to the other subsystems of the satellite. These subsystems then adjust their own time system with the received second pulse signal as the reference to realize the overall time synchronization within the satellite. While the GPS receiver transmits the second pulse signal, the receiver also broadcasts the time data corresponding to the second pulse signal through the bus. Each subsystem obtains the specific time information corresponding to the received second pulse signal through the bus in time. The matching of the second pulse signal and the time data through internal data processing enables complete and effective time synchronization of the satellite. The time synchronization accuracies of the *ZY3-01* and *ZY3-02* are both better than 20 μs, and the *ZY3-03* time synchronization accuracy is also expected to reach this level, fulfilling the satellite design requirements.

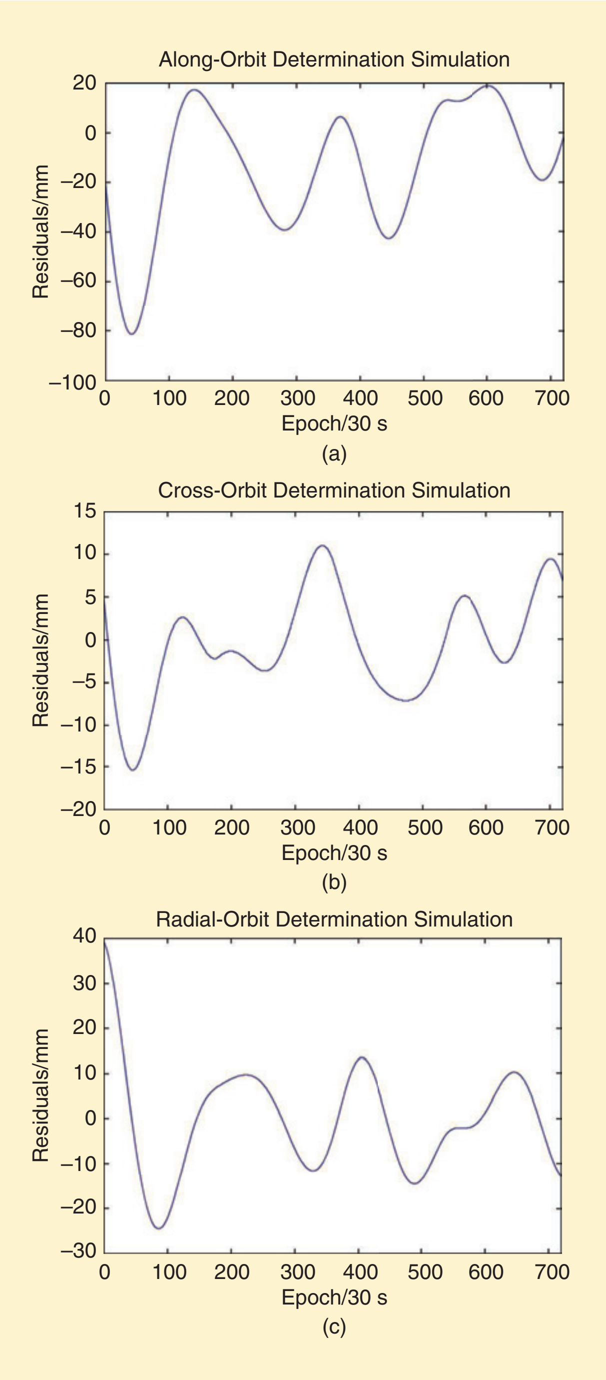

FIGURE 5. The *ZY3-03* orbit determination simulations for (a) along orbit, (b) cross orbit, and (c) radial orbit.

TABLE 3. THE *ZY3-03* SENSOR SPECIFICATIONS.

FEATURES	SPECIFICATIONS
Camera and ground sample distance (GSD)	Panchromatic (nadir view): 2.1 m Panchromatic (forward/backward view): 2.7 m Multispectral: 5.8 m
Swath width	Panchromatic (nadir/forward/backward): 51 km Multispectral: 51 km
Data-acquisition capacity	Panchromatic: 2,000,000 km^2/day Multispectral: 2,000,000 km^2/day

TABLE 4. THE CHARACTERISTICS OF THE *ZY3-03* THREE-LINE-ARRAY CAMERA.

FEATURES	SPECIFICATIONS
Number of cameras	Three (nadir, forward, and backward views)
Wavelength	0.5–0.8 μm
GSD	2.1 m (nadir view) 2.7 m (forward and backward views)
Focal length	1,700 mm
Modulation transfer function	>0.2
Swath width	51 km (nadir plane image)
Pixel size	7 μm
Field angle	6°
Bit number	10 b

SATELLITE OPERATING MODE

The *ZY3-03* provides three operating modes: real-time transmission, record and playback, and transfer while recording.

- *Real-time-transmission mode*: Within the receiving range of the ground station, the satellite downlinks to the ground receiving station the real-time, nadir-view panchromatic image; forward- and backward-view panchromatic images; multispectral image; star charts; gyroscope; and GPS receiver data as well as other data.
- *Record-and-playback mode*: The satellite records the real-time, nadir-view panchromatic image; forward- and backward-view panchromatic images; multispectral image; GPS receiver data; star charts; and gyroscope data as well as other data to the solid-state memory when outside the receiving range of the ground receiving station and downlinks the recorded data when the satellite is within the receiving range.
- *Transfer-while-recording mode*: Within the receiving range of the ground station, the satellite downlinks to the ground receiving station the real-time, nadir-view panchromatic image; forward- and backward-view panchromatic images; multispectral image; star charts; gyroscope; and GPS receiver data as well as other data. Meanwhile, all data are recorded to the solid-state memory of the satellite. When within the receiving range of China's ground station, the satellite downlinks the recorded data.

THE *ZY3-03* PAYLOAD

The payload of the *ZY3-03* includes the three-line-array panchromatic camera, multispectral camera, laser

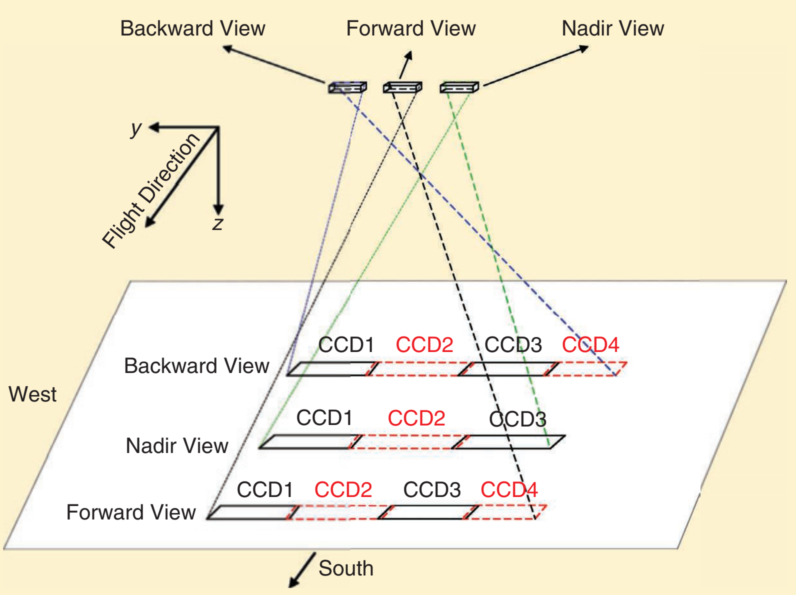

FIGURE 6. The relationship between the panchromatic camera focal and data output of the *ZY3-03*.

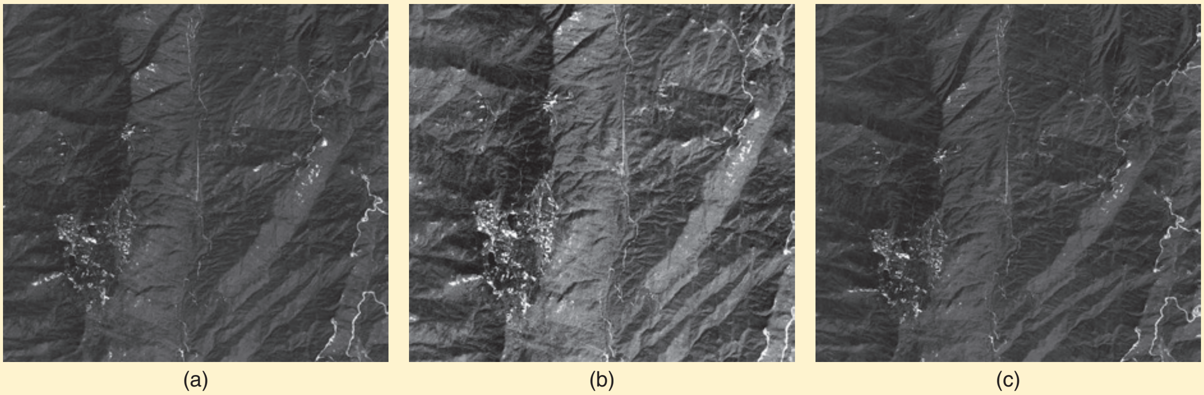
(a) (b) (c)

FIGURE 7. The *ZY3-03* simulated panchromatic images for the (a) forward, (b) nadir, and (c) backward images.

altimeter, digital transmission subsystem, digital antennas, and image data-recording subsystem. The *ZY3-03* sensor specifications are shown in Table 3.

THREE-LINE-ARRAY CAMERA

The three-line-array camera of the *ZY3-03* consists of three high-resolution panchromatic cameras that capture the nadir, front, and back views. The spatial resolutions of the front- and back-view cameras are both 2.7 m, with ground swaths of 51 km, whereas the nadir-view camera provides a spatial resolution of 2.1 m and a ground swath of 51 km. The *ZY3-03* is an optical satellite assembled with a linear-array CCD in push-broom imaging mode [8]. The pixel size of the nadir camera is 7 µm. The nadir camera is stitched by three pieces of the TDI CCD sensors, which have 8,192 pixels. The front- and back-view cameras are

TABLE 5. THE CHARACTERISTICS OF THE *ZY3-03* MULTISPECTRAL CAMERA.

FEATURES	SPECIFICATIONS
Number of bands	Four
Wavelength	Blue: 450–520 nm Green: 520–590 nm Red: 630–690 nm Infrared: 770–890 nm
GSD	5.8 m
Focal length	1,750 mm
Modulation transfer function	>0.25
Swath width	51 km
Pixel size	20 µm
Bit number	10 b

stitched by four pieces of the TDI CCD sensors, with 4,096 pixels.

The three-line-array camera consists of three panchromatic cameras to obtain along-track data simultaneously at three different perspectives. To achieve high elevation accuracy, the forward and backward cameras are inclined at ±22° from the nadir camera, which corresponds to a base-to-height ratio of 0.89 at an altitude of 505 km. The characteristics of the *ZY3-03* three-line-array camera are shown in Table 4. The relationship between the *ZY3-03* panchromatic camera focal and data output is shown in Figure 6, and the *ZY3-03* simulated panchromatic images for the three-line-array camera are shown in Figure 7.

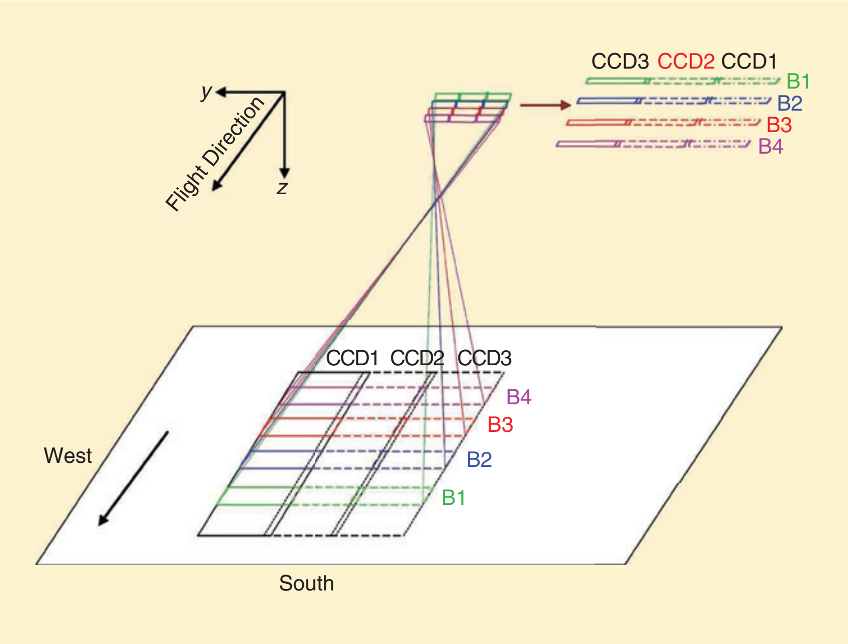

FIGURE 8. The relationship between the multispectral camera focal and data output of the *ZY3-03*.

MULTISPECTRAL CAMERA

The multispectral camera is an off-axis optical system with the advantages of uncovering without color aberration, a high-modulation transfer function, and a large viewing field. The multispectral camera has blue, green, red, and infrared spectral bands and provides a multispectral image with a spatial resolution of 5.8 m and a 51-km ground swath. The characteristics of the *ZY3-03* multispectral camera are shown in Table 5.

The multispectral camera is assembled from the three TDI CCD sensors, which have 3,072 pixels. The relationship between the *ZY3-03* multispectral camera focal and data output is shown in Figure 8, and the *ZY3-03* simulated multispectral image with 5.8-m resolution is shown in Figure 9.

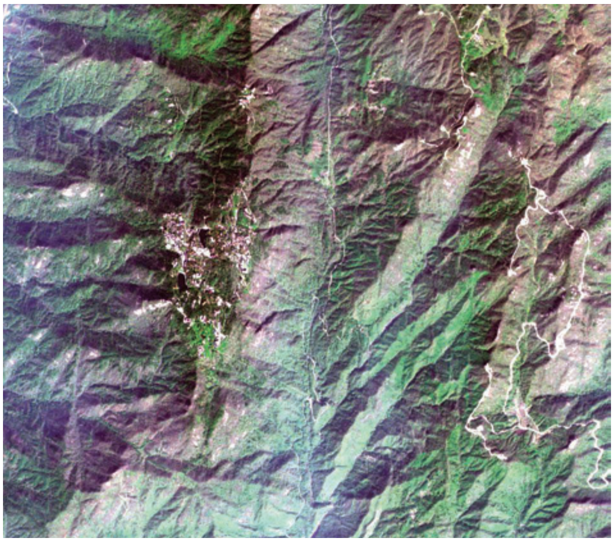

FIGURE 9. A *ZY3-03* simulated multispectral image.

LASER ALTIMETER

The *ZY3-03* is equipped with a laser altimeter, which is used to improve vertical accuracy for stereo surveying and mapping. The characteristics of the *ZY3-03* laser altimeter are shown in Table 6.

OTHER CONTENTS

The *ZY3-03* digital transmission subsystem is composed of data processing and a ground digital-transmission channel. The subsystem is configured with two X-band data-transmission channels at 450 Mb/s. The panchromatic camera image is designed with two optional compression ratios of 2:1 and 4:1, whereas the multispectral camera image is designed with a 3:1 compression ratio or lossless compression. The data-recording subsystem is configured with two pieces of solid storage of 500 Gb, which is used to record images and other raw data. The digital antenna subsystem includes two mechanical point beam antennas and servo controllers to enable data transmission from the satellite to the ground station.

DATA PRODUCTS AND POLICY

DATA PRODUCTS

All *ZY3-03* products are classified into three types: image, digital terrain, and thematic. The image products include sensor-corrected, geocoded ellipsoid-corrected, enhanced geocoded ellipsoid-corrected, and geocoded terrain-corrected products and the digital orthophoto map. The digital-terrain products include digital surface modeling, digital elevation modeling, and the digital line graph. The thematic products include the reflectivity product, normalized-difference vegetation index, leaf-area index, aspect, and slope, among others. A series of accessorial files is attached with the *ZY3-03* products to support further data processing [9]. The *ZY3-03* data products are shown in Table 7.

With the successful launch of the *ZY3-01* and *ZY3-02*, China's comprehensive civil satellite surveying and mapping technical framework was established, and the space information can be accessed by users worldwide. The image planimetric accuracy of the *ZY3* series is better than 10 m, and the vertical accuracy is better than 6 m. With a small number of GCPs, the planimetric accuracy and vertical accuracy can reach 3–4 m and 2–3 m, respectively. The images from the *ZY3* satellites have been mainly used for 1:50,000-scale basic geographic information product, map revision, and national geographical condition surveillance. China's government divisions also actively apply *ZY3* products in relevant fields, such as land resource investigation, forestry protection, agriculture monitoring, and natural disaster reduction.

TABLE 6. THE CHARACTERISTICS OF THE *ZY3-03* LASER ALTIMETER.

FEATURES	SPECIFICATIONS
Footprint size	70 m
Wavelength	1,064 nm
Repeated frequency	≥2 Hz
Pulse width	≤8 ns
Number of transmissions	1×10^8
Effect distance	500 ± 20 km
Ranging precision	1 m

DATA DISTRIBUTION

A cloud service platform was constructed for the *ZY3* and other satellite series data distributions and services. It is operated by the Land Satellite Remote Sensing Application Center (LASAC), Ministry of Natural Resources of the People's Republic of China. Network distribution nodes of the *ZY3* cloud service platform were established in all provinces of China. International network nodes were also successfully deployed in Britain, Austria, Thailand, Laos, Norway, Mongolia, Ghana, and Uganda, thereby greatly promoting the global distribution and application of *ZY3* products.

ZY3-03 data will be integrated into the cloud service platform in the future. LASAC emphasizes actively carrying out multilevel and multiform cooperation in satellite mapping technologies and data sharing in China and worldwide. If you are interested in *ZY3* data, you can log onto the website for information (http://www.sasclouds.com/). LASAC is dedicated to promoting *ZY3* data utilization and global distribution and applications. LASAC plans in the future to publish the *ZY3* Research Announcement to conduct data utilization analysis, scientific research, calibration, and validation (http://www.lasac.cn/).

CONCLUSIONS

The *ZY3-03* mission requirements, platform, payloads, data products, and policy were discussed in this article. The *ZY3-03* satellite will acquire many Earth observation images and meet the national requirement of 1:50,000-scale topographic maps. The mission will ensure the continuity of the *ZY3* series data and product services. The combination of advanced and conventional technologies will improve the mission parameters of the *ZY3-03* so that it

TABLE 7. THE *ZY3-03* PRODUCTS.

PRODUCT TYPE	NAME	PLANE/STEREOSCOPIC	APPLICATIONS
Image	Sensor corrected	Plane/stereoscopic	Stereoscopic observation and surveying
	Geocoded ellipsoid-corrected	Plane/stereoscopic	Spatial information interpretation
	Enhanced geocoded ellipsoid-corrected	Plane/stereoscopic	High-accuracy positioning
	Geocoded terrain-corrected	Plane	High-accuracy positioning and change detection
	Digital orthophoto map	Plane	Digital mapping
Digital terrain	Digital surface model	Plane/stereoscopic	Slope and aspect analyses, among others
	Digital elevation model	Plane/stereoscopic	Intervisibility analyses, among others
	Digital line graph	Plane	Route planning, among others
Thematic	Reflectivity product	Plane	Thematic application
	Normalized-difference vegetation index	Plane	Thematic application
	Leaf-area index	Plane	Thematic application
	Aspect and slope	Plane	Thematic application
	Etc.	Plane	Thematic application

achieves high performance, low cost, and high reliability and meets the requirements of cartography, regional observation, disaster monitoring, and resource exploration, among other applications. In the near future, *ZY3-03* data will be available widely via LASAC.

ACKNOWLEDGMENTS

This study was supported by the National Key R&D Programme of China (2016YFB0501005) and the National Basic Surveying and Mapping Science and Technology Plan (2018KJ0204/2018KJ0304).

AUTHOR INFORMATION

Xinming Tang (tangxinming99@qq.com) received his M.Sc. degree in land administration in 1998 and his Ph.D. degree in geo-information science and computer application in 2004, both from the University of Twente, Enschede, The Netherlands. He is currently the academic deputy director of the Land Satellite Remote Sensing Application Center, Ministry of Natural Resources of the People's Republic of China, Beijing. His research interests focus on spatial information science and technology, including remote sensing, geographic information systems, and their integration. He has been president of Commission I Working Group IV of the International Society for Photogrammetry and Remote Sensing.

Xiaoming Gao (13691074823@163.com) received her M.Sc. and Ph.D. degrees in geographic information systems from Wuhan University, China, in 2005 and 2017, respectively. She is currently the director of the Satellite Planning and Development Department of the Land Satellite Remote Sensing Application Center, Ministry of Natural Resources of the People's Republic of China, Beijing. Her research interests focus on spatial information science and technology, including remote sensing satellite plan and parameters design.

Haiyi Cao (haiyicao66@163.com) received her M.E. degree from the China Academy of Space Technology (CAST) in 1990. She is a researcher of the China Academy of Space Technology (CAST) and China Aerospace Science and Technology Corporation (CASC) and has been engaged in system design of remote sensing satellites. She was chief engineer for the development and verification of several satellites and is currently the chief engineer for the *ZY3* series and other satellites. In addition, she serves as a member of the standing committee of CAST Science and Technology and is an academic pioneer of CASC. During her time as chief engineer, the *ZY3* series has ranked at the forefront of the international community. She has obtained many awards at and above the national ministerial level and has enjoyed a special government subsidy.

Fan Mo (surveymofan@163.com) is with the Land Satellite Remote Sensing Application Center, Ministry of Natural Resources of the People's Republic of China.

Zhenming Wang (87190435@qq.com) is with the Land Satellite Remote Sensing Application Center, Ministry of Natural Resources of the People's Republic of China.

Wenxia Xu (xuwenxia@spacechina.com) is with the Chinese Academy of Space Technology, Beijing.

Guangbin Zhu (sasmac_zgb@163.com) is with the Land Satellite Remote Sensing Application Center, Ministry of Natural Resources of the People's Republic of China.

Qingxing Yue (qingxingyue06@sina.com) is with the Land Satellite Remote Sensing Application Center, Ministry of Natural Resources of the People's Republic of China.

Fen Hu (154948273@qq.com) is with the Land Satellite Remote Sensing Application Center, Ministry of Natural Resources of the People's Republic of China.

Hong Zhu (zhuhong19890408@163.com) is with the Land Satellite Remote Sensing Application Center, Ministry of Natural Resources of the People's Republic of China.

Jing Lu (573330453@qq.com) is with the Land Satellite Remote Sensing Application Center, Ministry of Natural Resources of the People's Republic of China.

REFERENCES

[1] G. Xingfa and T. Xudong, "Overview of China Earth Observation Satellite Programs [Space Agencies]," *IEEE Geosci. Remote Sens. Mag.*, vol. 3, no. 3, pp. 113–129, 2015. doi: 10.1109/MGRS.2015.2467172.

[2] Chinese Resources Satellite Application Center, "ZY-3 satellite introduction." Accessed on: 2019. [Online]. Available: http://www.cresda.com/.

[3] L. Deren, Z. Guo, J. Wanshou, and Y. Xiuxiao, "SPOT-5 HRS satellite imagery block adjustment without GCPS or with single GCP," *Geo. Spat. Inf. Sci.*, vol. 31, no. 5, pp. 377–381, 2006.

[4] A. Rosenqvist, M. Shimada, N. Ito, and M. Watanabe, "ALOS PALSAR: A pathfinder mission for global-scale monitoring of the environment," *IEEE Trans. Geosci. Remote Sens.*, vol. 45, no. 11, pp. 3307–3316, 2007. doi: 10.1109/TGRS.2007.901027.

[5] T. Xinming, X. Junfeng, X. Wang, and W. Jiang, "High-precision attitude post-processing and initial verification for the ZY-3 satellite," *Remote Sens.*, vol. 7, no. 1, pp. 111–134, 2014. doi: 10.3390/rs70100111.

[6] Z. Chunmei and T. Xinming, "Precise orbit determination for the ZY-3 satellite mission using GPS receiver," *J. Astronautics*, vol. 34, no. 9, pp. 1202–1206, 2013.

[7] T. Xinming, H. Fen, W. Mi, P. Jun, J. Shuying, and L. Gang, "Inner FoV stitching of spaceborne TDI CCD images based on sensor geometry and projection plane in object space," *Remote Sens.*, vol. 6, no. 7, pp. 6386–6406, 2014. doi: 10.3390/rs6076386.

[8] C. Haiyi, L. Xigang, L. Shaohui, and Z. Xinwei, "ZY-3 satellite remote sensing technology," *Spacecraft Recovery Remote Sens.*, vol. 33, no. 3, pp. 7–15, 2012.

[9] T. Xinming et al., "Triple linear-array imaging geometry model of Ziyuan-3 surveying satellite and its validation," *Acta Geodaetica et Cartographica Sinica*, vol. 41, no. 2, pp. 191–198, 2012.

GRS

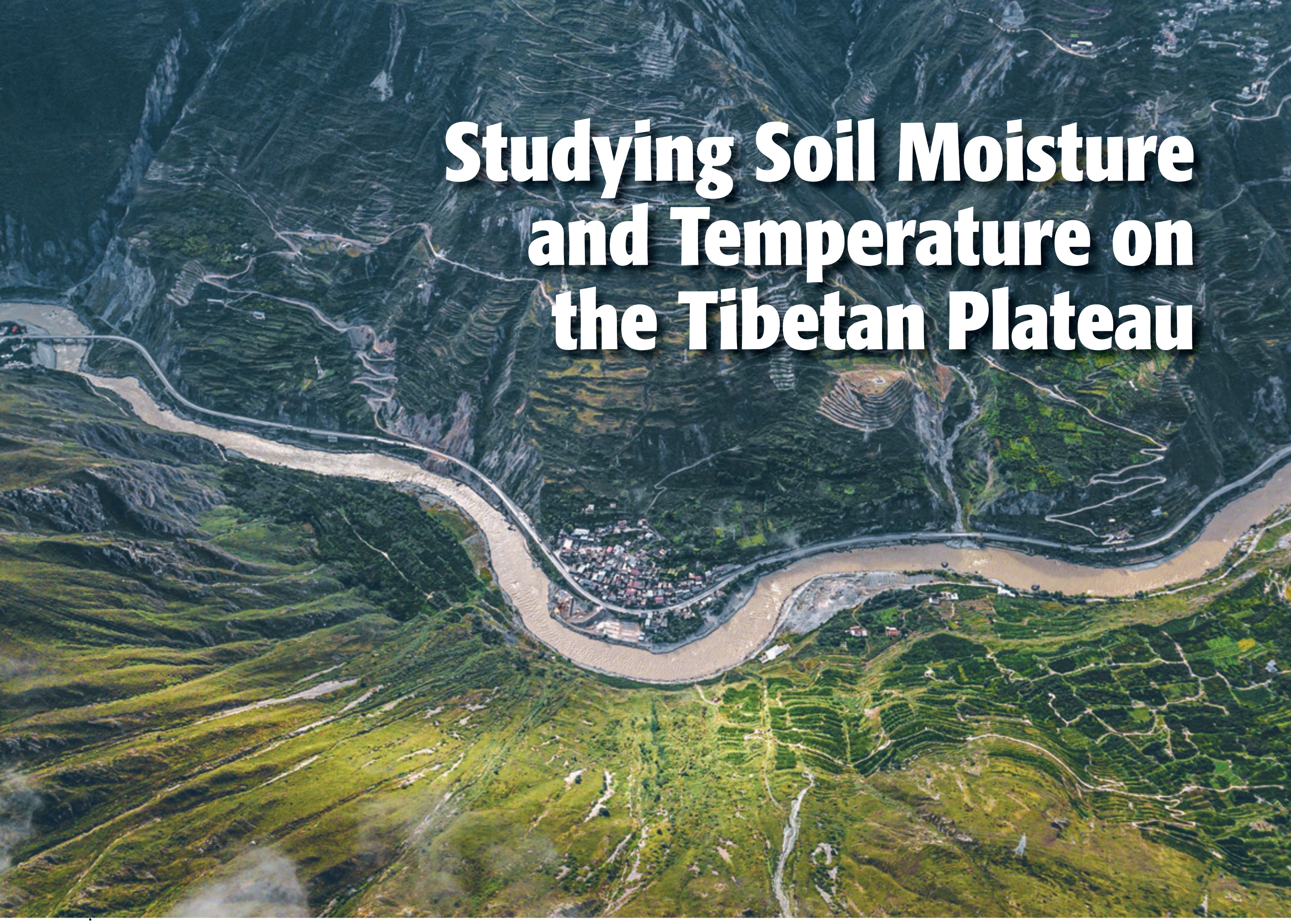

Studying Soil Moisture and Temperature on the Tibetan Plateau

©SHUTTERSTOCK.COM/D.KVASNETSKYY

Initial results of an integrated, multiscale observatory

**LIXIN DONG, SHIHAO TANG,
MICHAEL H. COSH, PING ZHAO, PINTING LU,
KANSHE ZHOU, SHUAI HAN, MIN MIN, NA XU,
LIN CHEN, AND FU WANG**

Scarce in situ data in the western and central Tibetan Plateau (TP) hinder scientific research on physical process representation in climate models. Satellite remote sensing and climate models are effective data sources in complex topography and harsh environments, but they have not been effectively validated or improved for lack of multiscale observations matching their pixel or grid scales. Therefore, it is necessary to develop an integrated, multiscale observatory. With the support of the Third Tibetan Plateau Atmospheric Scientific Experiment (TIPEX-III), a satellite pixel-oriented TP Integrated MultiScale Moisture and Temperature Observatory (TP-IMSO) was initiated to obtain a long-term, multiscale soil temperature and moisture data set that integrates site point, regional line, and spatial surface observation designs.

The TP-IMSO is composed of two automatic wireless transmission networks (spatial surface) over the Naqu and A'li regions, the Geographical Flow Observatory (GFO) of soil and vegetation features (regional line), and atmospheric and soil temperature and humidity vertical profile observations (site point) in the soil–atmosphere interface layer. This article introduces the project's motivation, scientific objectives, integrated experiment design, implementation, and data management and shows some initial results.

It was found that the elements of the TP-IMSO networks have a highly variable character. The soil moisture (SM) in the top layer (0–3 cm) is more variable than in other layers, and the largest standard deviation of all of the five layers occurs in July. According to the preliminary validation, the root-mean-square error (RMSE) of the remote sensing products ranges from 0.038 to 0.177 $\mathrm{cm}^3 \cdot \mathrm{cm}^{-3}$; and for the European Centre for Medium-Range Weather interim re-analysis data and National Centers for Environmental

Digital Object Identifier 10.1109/MGRS.2019.2924678
Date of current version: 2 March 2020

Prediction (NCEP) re-analysis data, the RMSE spans from 0.038 to 0.081 $cm^3 \cdot cm^{-3}$.

THE NEED FOR A MULTISCALE SOIL MOISTURE AND TEMPERATURE NETWORK

As a primary heat source in summer for Central Asia [36], [37], the TP directly affects regional weather and global climate patterns. SM is one of the key elements in the global water cycle and multispherical surface energy balance and exchange [2], [33]. Jung et al. [14] found that evapotranspiration has decreased since 1998 because of the limited moisture supply, which was determined based on available in situ data and remote sensing products. Land surface hydrometeorological data [17] and remote sensing products are also necessary in the calibration of climate and weather prediction models. However, the TP is in a widespread permafrost area. Hence, it is difficult to collect sufficient in situ data from the TP for modeling efforts, especially in the midwestern portion of the plateau. Conventional meteorological stations in the western and central TP are scarce. The number of national and regional meteorological stations in the TP is only 23.8% and 5.4% of the country's total stations, respectively. And there are few in situ observations of soil and atmospheric moisture and temperature profiles.

Recently, several experiments were carried out in the TP. The Multiscale Soil Temperature and Moisture Observation Network (TP-SMTMN) was established and described by [35]. The Heihe Watershed Allied Telemetry Experimental Research (HiWATER) project [16] was initiated on a smaller watershed to understand the processes and mechanisms of the ecohydrological system in an inland river basin. Three satellite validation sites on the plateau (Tibet-Obs) were established, namely, Maqu, Naqu, and Ngari, for validating microwave SM products [28]. The Tibet Observation and Research Platform (TORP), which focuses on atmosphere monitoring, was originally developed in 2005, covering SM and soil temperature in its parameter suite [19]. Unfortunately, except for TP-SMTMN and HiWATER, these measurements were not regularly collected at multiple scales but were sparsely distributed to provide a passive microwave remote sensing validation site (~25 km in average dimension).

The Tibet-Obs sample points were distributed randomly, as were the SM sites in HiWATER. The TP-SMTMN consisted of 56 sample sites, which were randomly distributed along the road layout at three observational scales: large network (1°), medium network (0.3°), and small network (0.1°) [35]. These observations, however, did not directly match the 25-km passive microwave SM products.

These four experiments were mainly conducted in complex landscapes. For example, the topographic effect was more significant in the TP-SMTMN; the land surface types in the Tibet-Obs included desert, vegetation, river, and other complex types; and in the TORP, a large proportion of surface water and a terrain transition from north to south can be found in the region. The HiWATER land surface types included crop, forest, scrubland, grasslands, urban and built up, barren and sparsely vegetated, snow and ice, and water bodies. Hence, a multiscale SM and temperature network is needed to support product validation and algorithm development for a homogeneous landscape (uniform surface characteristics) with well-matched pixels or grids.

Laterally, these in situ SM stations are point-scale measurements distributed across mesoscale footprints (~25 km), which is the approximate scale of most satellite microwave sensors. Vertically, the sensing depths of these satellite sensors are shallow, no more than 5 cm below the surface for an L-band radiometer. The absence of true SM values at the representative layer (~ <3.75 cm) of an X-band radiometer fundamentally limits the capacity to assess the quality of satellite SM products. The scientific observations for the soil dielectric character at the pixel scale are insufficient, as are the atmospheric measurements above the surface, including infrared skin temperature, air temperature, and relative humidity. These parameters are essential to understand the soil–atmosphere interface in the western TP.

Uncertainties in land surface models can be attributed to atmospheric forcing and surface parameter errors [9], [21]. There is no conclusion from the results of the Project for Intercomparison of Land Surface Parameterization Schemes and the Global Soil Wetness Project regarding which model is the most appropriate for simulating SM and other variables at the land surface. Shao et al. [29] and Henderson-Sellers [10] found that simulated SM results under different land surface parameterization schemes were significantly different. Srinivasan et al. [30] determined that no model among those participating in the Atmospheric Model Intercomparison Project can reproduce the interannual changes of the observed SM. Zhu et al. [40] established the calibration of several cosmic-ray SM sensors, although large-scale comparisons with remote sensing products require more numerous sensor networks than those available via these systems.

After validation of the products within the domain, satellite remote sensing provides a relatively reliable approach for observations of remote areas like the TP. SM has been retrieved from microwave remote sensing satellite platforms, as shown in Fujii and Koike and van der Velde et al. [31]. The past and present satellite sensors include

- the Scanning Multichannel Microwave Radiometer, launched in 1978
- the Special Sensor Microwave/Image, orbited in 1987
- the Tropical Rainfall Measuring Mission's (TRMM's) Microwave Imager, launched in 1997 by NASA and the Japan Aerospace Exploration Agency (JAXA)
- the Advanced Microwave Scanning Radiometer (AMSR-E) of the Earth Observation System, orbited in 2002
- the Microwave Radiometer Imager onboard the first satellite of China's *Fengyun-3* (*FY-3*), launched in 2008

- the L-band *Soil Moisture Ocean Salinity* (*SMOS*) satellite, orbited in 2009 by the European Space Agency (ESA)
- the *Soil Moisture Active Passive* (*SMAP*) satellite, launched in 2015 by NASA.

These missions and their satellite microwave radiometers can provide SM products at various spatial resolutions and can offer up long time-series SM products for studies on global climate change, water cycles, and multispherical exchange. However, the accuracy of the SM estimated from satellite sensors needs to be evaluated before practical application. Wagner et al. [32] and Rüdiger et al. [26] assessed satellite SM products through intercomparisons. Dorigo et al. [5] and Scipal et al. [27] also evaluated the error of global microwave SM data sets. Polcher et al. [25] compared the SM data retrieved from the ESA's *SMOS* with the output of the ORCHIDEE land surface model. Albergel et al. [1] studied the SM products of the Advanced Scatterometer (ASCAT) and *SMOS* against global ground-based in situ observations. Paulik et al. [24] validated the ASCAT soil wetness index products using the field data of the International Soil Moisture Network (ISMN) [12].

Dente et al. [4] examined the AMSR-E SM products and ASCAT soil wetness index products using the Maqu network. Chen et al. [3] also validated four SM products based on the AMSR-E data using the Naqu network, i.e., the NASA product [20], the JAXA product [8], [15], and the land parameter retrieval model C-band and X-band products based on a land surface parameter inversion model [22]. Zhao et al. [38] evaluated the accuracy of *SMOS* SM products on the TP. Zeng et al. [39] validated five SM products (AMSR-E, AMSR-2, ASCAT, EVC, and *SMOS*) using the Coordinated Enhanced Observing Period Asia–Australia Monsoon Project on the TP, Maqu, and Naqu network data. Dorigo et al. [6] evaluated the ESA Climate Change Initiative SM product using ISMN data. These results show that no product can meet the accuracy requirements on the TP without a local verification demonstration. The best method is to establish validation sites, including a dense network of representative locations, on the order of the interested scales [13].

To address these issues and provide a resource for future modeling and monitoring, a satellite pixel-oriented TP-IMSO was established to provide an integrated, long-term observation of the land surface and boundary layer by ground-based remote sensing facilities over the central and western TP. The TP-IMSO mainly aims to deepen understanding of how multiple satellite products on the TP can support studies on climate and land surface process models, the water cycle, the multispherical surface energy balance, and the exchange between the land surface and soil–atmosphere interface layer.

EXPERIMENTAL AREAS

The experimental areas are in the central and western TP, including two fixed automatic observation experimental areas with a wireless transmission network and two GFO experimental regions.

The first locality is in Nierong County, Naqu, with an area of 75 km × 75 km, on the Qiangtang grassland in the central TP, referred to as the *Naqu Soil Observatory* (*NSO*). The second site is in Geji county, A'li, with an area of 50 km × 50 km, on the semiarid grassland in the western TP, referred to as the *A'li Soil Observatory* (*ASO*), as shown in Figure 1. Both are instrumented with wireless transmission networks in land surface areas with different characteristics. The NSO area is unique alpine meadow grassland, without water bodies or urban areas, and is generally flat, with some rolling hills. The ASO location is characterized by a semiarid or desert grassland, wetlands, and one small water body and is also generally flat, with only some rolling hills. The elevation is between 4,400 and 5,200 m, with seasonal frozen soil. The soil surface starts its diurnal soil freeze/thaw cycle in November (Naqu) or October (A'li) and becomes fully frozen from December to February.

The A'li area is within the subcold arid climate zone and has an annual average rainfall of approximately 69 mm, with an average of 19 days of rain and snow. It has an annual average temperature of –2 °C, with a minimum temperature of –40 °C. Nierong county in Naqu is in the South Asian summer monsoon climate zone, and most precipitation occurs between June and September. With high elevation and low temperatures, the growing season is short, and the grass height can reach 10–15 cm. Therefore, the SM shows a remarkable seasonal variation [34].

In addition, two GFO experiments were initiated along the Lasa–Naqu–Changdu–Linzhi–Lasa and Linzhi–Lasa–Naqu–A'li routes in August, including many types of land cover, such as forest, shrubs, grassland, alpine meadow, desert, water bodies, snow and ice, and bare land.

NETWORK DESIGN

TIBETAN PLATEAU INTEGRATED MULTISCALE MOISTURE AND TEMPERATURE OBSERVATORY COMPOSITION AND DETERMINATION BASIS

THE INTEGRATED OBSERVATORY'S COMPOSITION

The TP-IMSO network is composed of the NSO, ASO, and GFO, the Naqu Climate Station (NCS), and an automatic weather station that is available and operated by the Geji Weather Bureau in the center of the ASO. The NCS was established in 2015 in the middle of the NSO, offering baseline reference data. To provide multipoint background information in wider regions for microwave SM validation, the GFO was conducted in the first few years after the deployment of the observatory.

DETERMINATION BASIS

The TP-IMSO network is designed according to the site point–regional line–spatial surface pattern. For example, the NCS and each site belong to a site point pattern, the GFO to a regional line pattern, and the NSO and ASO to a spatial

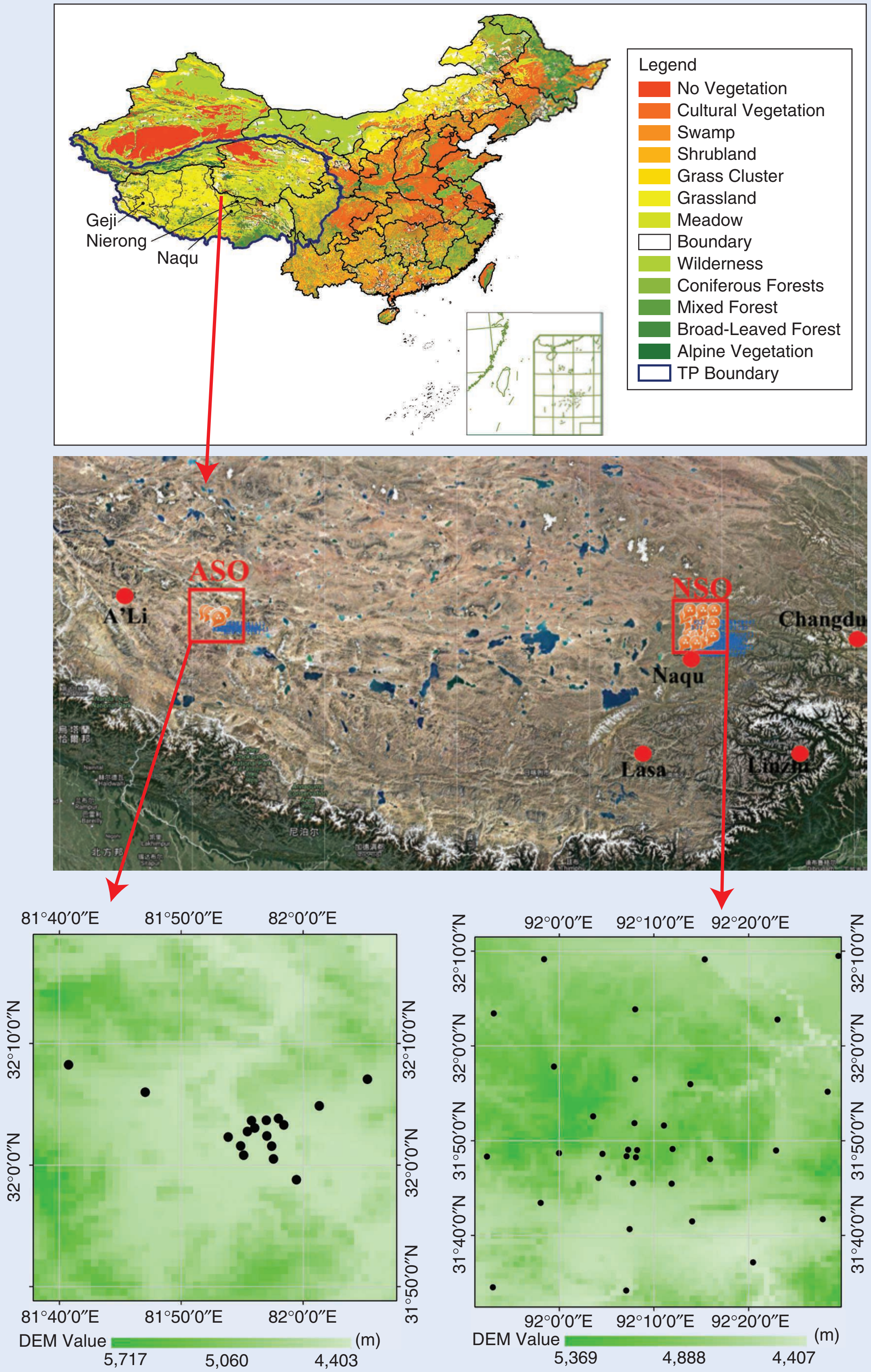

FIGURE 1. The location and environmental conditions of the TP-IMSO. DEM: digital elevation model.

surface pattern. The three patterns are integrated through the organic combination of observational elements.

Since microwave SM algorithms are greatly influenced by the optical thickness of vegetation and the dielectric constant of the soil, the NSO experimental area was selected and established in the typical seasonal frozen soil regions. Throughout Tibet, the vegetation cover is relatively uniform, and the terrain is relatively flat. The NSO region was chosen not only for the validation of multiple products but also, importantly, for the improvement of the product algorithm in evaluating the influence of the vegetation optical thickness and frozen soil.

To ensure that each site falls into 2 × 2 pure pixels, the SM product is first geocorrected, and four corner latitudes and longitudes of each pixel in the 25-km × 25-km scale are directly determined on the image. Then, the sites on other scales (1 km, 5 km, 15 km, and 75 km) are determined one by one, according to their distance from the four-corner site. A nested and satellite pixel-oriented site layout was established to use fewer sites to represent the actual situation of larger areas and scale down the SM products step by step. Hence, these characteristics are different from past experimental protocols.

The ASO experimental area is a mixed-pixel zone, with wetland and desertification grassland. To ensure the representativeness of the sites, they were established from wetland to desert grassland, centered on the wetland. And the density of the site is changed from dense to sparse.

Since the microwave SM product corresponding to the NSO experimental territory has a large pixel, there are few areas in Tibet that can meet the conditions of good vegetation and flat terrain. As for the A'li area in the western TP, the soil conditions around the wetlands are better, but they are relatively scattered. Hence, large-scale test sites are rare. Therefore, the two test areas (NSO and ASO) are easily determined by geostatistical methods from topographic, vegetation, and land use maps.

OBSERVED VARIABLES

Three categories of variables/parameters are observed: atmospheric, soil, and vegetation. The atmospheric state variables include air temperature and humidity at 2 m, wind direction and speed at 2 m, and precipitation at 3.5 m. The soil state variables include skin surface infrared radiation temperature and emissivity, 0-cm skin surface temperature, soil temperature and moisture at different depths, soil dielectric constant, soil texture, and soil organic carbon (SOC). As an important factor in passive microwave SM inversion in vegetated areas [11], SOC was considered in the design of this experiment. The vegetation state variables include vegetation type, vegetation coverage, surface infrared temperature, and emissivity. All of the observed variables are closely related to the inversion and inversion analysis of the SM. The sensors associated with these observed variables are listed in Table 1.

TABLE 1. THE OBSERVED VARIABLES AND SENSORS IN THE TP-IMSO.

OBSERVED VARIABLES	PHOTO	INSTRUMENT	MAJOR INSTRUMENT CHARACTERISTICS
Soil temperature and moisture (depth: 0–3 cm, 5 cm, 10 cm, 20 cm, 30 cm)		Soil Temperature and Moisture Sensor Decagon ECH$_2$O 5TM	Accuracy: apparent dielectric permittivity (ε_a): ±1 ε_a from 1 to 40 (soil range); ±15% from 40 to 80 (soil) Volumetric water content (VWC): using the Topps equation: ±0.03 $\text{cm}^3\cdot\text{cm}^{-3}$, typical in mineral soils that have an electrical conductivity <10 dS/m; using allocation-specific calibration: ±0.02 $\text{cm}^3\cdot\text{cm}^{-3}$ Temperature: ±1 °C Resolution: VWC: 0.0008 $\text{cm}^3\cdot\text{cm}^{-3}$ (0.08% VWC) from 0 to 50% VWC Temperature: 0.1 °C Range: VWC: 0 to 1 $\text{cm}^3\cdot\text{cm}^{-3}$; temperature: −40–50 °C Measurement time: 150 ms
0-cm surface temperature		Campbell Scientific 109 temperature probe	Sensor: BetaTherm 10K3A1 thermistor Measurement range: −50°–70 °C Accuracy: thermistor interchangeability error: <±0.36 °C over −25–50 °C, <±0.6 °C over −50–70 °C Survival range: −55–100 °C Linearization error: Steinhart and Hart equation used to calculate temperature; maximum error: 0.03 °C over −50–70 °C
Infrared radiation temperature (band: 8–14 μm)		Apogee infrared radiometer (SI-111)	Mean of differences from target: 0.002 °C Target temperature uncertainty (95% confidence) from −30–65 °C: 0.122 °C Maximum differences from target: 0.14 °C Minimum differences from target: −0.106 °C

(*Continued*)

TABLE 1. THE OBSERVED VARIABLES AND SENSORS IN THE TP-IMSO. (CONTINUED)

OBSERVED VARIABLES	PHOTO	INSTRUMENT	MAJOR INSTRUMENT CHARACTERISTICS
Infrared emissivity (five band)		Five-band thermal infrared radiometer (CE312)	France CIMEL Sensed temperature range: −80–50 °C (193.15–323.15K) Field of view: 10° or 7°, 3° Spectral band passes: 5 band: 8–14, 11.5–12.5, 10.5–11.5, and 8.2–9.2 μm Operating environment: −20–50 °C
Precipitation		Texas Electronics rain guage (TE525-MM)	Sensor type: tipping bucket/magnetic reed switch Material: anodized aluminum Temperature: 0–50 °C Resolution: 1 tip Volume per tip: 4.73 ml/tip (0.16 fl oz/tip) Rainfall per tip: 0.1 mm (0.004 in) Accuracy: up to 10 mm/h: ±1%; 10–20 mm/h: ±3%; 20–30 mm/h: ±5% Funnel collector diameter: 24.5 cm (9.66 in) Height: 29.21 cm (11.5 in)
Air temperature and humidity (instrument height: 2 m)		Campbell Scientific air temperature and humidity (HM-P155A)	Relative humidity: Sensor: HUMICAP 180R Measurement range: 0.8–100% relative humidity Accuracy: ±1–1.7%, depending on relative humidity Temperature: Sensor: PT100 RTD measurement range: −80–60 °C Accuracy: ±(0.055–0.0057 × temperature) °C
Wind speed and direction (instrument height: 2 m)		Campbell Scientific wind speed and direction (034b)	Wind speed: Range: 0–167 mi/h (0–75 m/s) Starting threshold: 0.9 mi/h (0.4 m/s) Accuracy: <22.7 mi/h: 0.25 mi/h (0.1 m/s) Accuracy >22.7 mi/h: ±1.1% of true Wind direction: Range: mechanical: 0–360°; electrical: 0–356°; starting threshold: 0.9 mi/h (0.4 m/s) Accuracy: ±4° Damping ratio: 0.25 standard (0.4–0.6 optional) Resolution: <0.5°
Soil dielectric constant	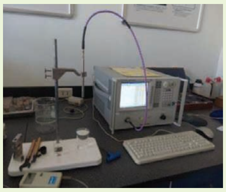	Keysight Technologies network analyzer (electrical)	Frequency range: 10–8.5/13.5/26.5 MHz; 43.5/50/67 GHz; up to 1.1 THz with extenders Best trace noise at 10 kHz 1 intermediate frequency bandwidth (IFBW) signal amplitude (decibel root mean square)/phase (degree root mean square): 0.0063/0.047 Best speed at 201 point 1 sweep, correction off: 5 ms (600 kHz IFBW)
SOC		Total organic carbon analyzer (Shimadzu TOC-VCPH)	Shimadzu Corporation Accuracy: the relative standard deviation of total carbon (TC), inorganic carbon (IC), and nonpurge organic carbon in liquid samples <1.5%, total nitrogen <3% Solid sample TC, IC <1%
Soil mechanical composition/soil texture		Laser particle size analyzer (Microtrac Inc. S3500)	Laser wavelength: 780 nm Particle size range: 2,000–0.02 μm Theoretical model: Mie scattering and nonspherical particle correction factor Precision: Spherical glass beads D50 = 642 μm, 0.7% Spherical glass beads D50 = 56 μm, 1.0% Spherical latex beads D50 = 0.4 μm, 0.6%

NAQU SOIL OBSERVATORY AND A'LI SOIL OBSERVATORY EXPERIMENTS

An array of base stations was established to collect the primary variables necessary for product validation and improvement.

MULTISCALE DEPLOYMENT

With 50 sites, the NSO and ASO were deployed over four successive summers, from 2014 to 2017. The latitudes and longitudes of all sites and background information are shown in Tables 2 and 3, respectively. Different deployment schemes were adopted by different land cover types in the NSO and ASO (Figure 2). For the NSO, the land cover and satellite pixel orientation required a nested, multiscale networking scheme in pure pixels. However, for the ASO, with a more diverse landscape, the random networking scheme was used.

The NSO experimental area [Figure 2(a)] is in the Qiangtang grassland and characterized by flat terrain, homogeneous grassland types, higher vegetation biomass, a gentle SM dynamic range, and a typical freeze/thaw cycle. Deployment of the sites began in August 2014, and the full set of 33 stations was completed by August 2015. The SM and temperature are measured across four spatial scales in the 2 pixel × 2 pixel arrangement. These scales are at 1, 5, 15, and 25 km. They extend to 75 km, with around five pixels. These data can be organized for land surface estimates matching a variety of hydrological modeling and microwave products for different purposes. The 1- and 5-km-scale data can match the resolutions of polar-orbiting and geostationary satellites, respectively. Currently, the 1- and 2-km-scale data are appropriate only for radar-based satellite products or aircraft/drone systems. A key feature of the NSO is that the alignment of multiple satellite SM products was considered to optimize nested intercomparisons between those products.

The ASO experimental area [Figure 2(b)] is in the A'li area of the western TP and characterized by complex terrain, multiple land cover types (desertification grassland, wetlands, and a small water body), and low vegetation biomass. It has a limited SM dynamic range and a typical freeze/thaw cycle. There was a total of 17 sites as of October 2016. The SM and temperature are measured at four spatial scales (3, 5, 10, and 25 km), with random deployment. These data also match the different scales of land hydrological modeling and passive and active microwave products. The 3-km-scale data are specifically developed to address the active–passive resolutions of such missions as *SMAP*.

At the 33 NSO sites, in addition to soil temperature and moisture measurements, many auxiliary parameters are measured, including infrared radiation temperature, emissivity, soil texture, soil dielectric constant, vegetation coverage, and vegetation type. The soil texture and organic matter content in 0 to 5 cm of soil at each site are measured by a laser particle-size analyzer and a total organic-carbon analyzer in the laboratory and are available in the observatory's metadata. These parameters can help to analyze the features of multiscale SM and temperature on the TP.

INSTRUMENT INSTALLATION AND DATA TRANSMISSION

SM and temperature are measured at five soil depths. One or two sensors are installed in the top layer, in 0–3 cm of soil, inserted from the surface at a 45° angle. The other sensors are inserted vertically at depths of 5, 10, 20, and 30 cm at each of the 33 stations. The installation is designed to match the sensing depths of most X-, C-, and L-band-based radiometers currently deployed, such as the FY, *SMOS*, *SMAP*, and ASCAT instruments. The data are recorded every 10–30 min, representing the prior 10–30-min average.

For the data transmission, each data logger is mounted in an enclosure box at a height of 1.5 m [Figure 3(a)], and data records are sent via wireless transmission network. To limit the damage to the installation from livestock and wildlife and interference from the public, a 1.5-m steel fence is installed around each site, which helps to provide a long-term, continuous data record.

The wireless transmission system aims for real-time remote monitoring of soil, vegetation, and meteorological changes distributed across the soil observatories. The sensor nodes communicate with the base station through wireless transmission techniques, i.e., general packet radio service (GPRS). To solve the problem of field instrument power supply in this cold area, a dual power-supply system was designed that contains a solar panel system and three parallel rechargeable battery systems [Figure 3(b)]. In the daytime, the solar panel charges the batteries and supplies power to the system. One of the three parallel rechargeable batteries works at night. Another five rechargeable batteries in the EM50 logger can also support continuous data measurement.

To ensure that the instrument can work normally in the winter, the dual power-supply system is used, which can channel some thermal energy to increase the surrounding temperature of the data logger so the internal temperature is maintained above 0 °C. The instrument status can be obtained through a cellular phone signal, including the status of the solar circuit, battery power, signal strength, instrument temperature, instrument working state, GPS positioning, and so forth. Two software platforms (see the "Data Management" section) for the wireless transmission system were developed and are able to automatically transmit and archive observed data and remotely access updates and alterations to the logger system, if necessary.

THE NAQU CLIMATE STATION

The NCS (Figure 4) is an automated climate and weather station to conduct a temperature and humidity vertical profile observation of a section from 30 cm underground to 3.5 m aboveground, defined in this article as the *soil–atmosphere interface layer*. This station provides valuable

TABLE 2. THE SITE INFORMATION FOR THE NAQU MULTISCALE OBSERVATORY NETWORK.

								SOIL TEXTURE			
SCALE	SITE ID	LONGITUDE/ LATITUDE	ELEVATION (m)	DEPTH (cm)	TPG	LAND COVER TYPE	SOC CONTENT (%)	CLAY (%)	SILT (%)	SAND (%)	START DATE
1 km	A1	92.12/31.8	5,043	0 to 3, 5, 10, 20, 30	Plain	Meadow grassland	4.33	3.77	52.35	43.88	August 2015
	A2	92.14/31.8	5,107	0 to 3, 5, 10, 20, 30	Plain	Meadow grassland	9.25	3.97	58.99	37.04	August 2015
	A3	94.14/31.82	5,009	0 to 3, 5, 10, 20, 30	Plain	Boundary between wetland and grassland	25.40	1.38	47.90	50.71	August 2015
	A4	92.12/31.82	4,969	0 to 3, 5, 10, 20, 30	Plain	Wetland	21.86	3.65	70.16	26.13	August 2015
5 km	B1	92.07/31.77	4,779	0 to 3, 5, 10, 20, 30	Plain	River wetland	2.77	1.77	41.57	56.66	August 2015
	B2	92.07/31.81	4,779	0 to 3, 5, 10, 20, 30	Plain	Boundary between wetland and grassland	20.22	3.48	66.90	29.62	August 2015
	B3	92.06/31.88	4,989	0 to 3, 5, 10, 20, 30	Plain	Wetland	9.65	3.85	45.00	50.45	August 2015
	B4	92.13/31.86	5,000	0 to 3, 5, 10, 20, 30	Slope	Boundary between wetland and grassland	10.89	1.58	34.70	63.72	August 2015
	B5	92.13/31.76	4,703	0 to 3, 5, 10, 20, 30	Plain	Wetland	19.31	2.53	60.14	37.32	August 2015
	B6	92.20/31.76	4,775	0 to 3, 5, 10, 20, 30	Plain	Meadow grassland	13.67	2.27	52.74	44.99	August 2015
	B7	92.20/31.82	5,074	0 to 3, 5, 10, 20, 30	Plain	Meadow grassland	12.18	2.94	57.57	39.50	August 2015
	B8	92.18/31.86	5,034	0 to 3, 5, 10, 20, 30	Plain	Wetland	13.28	3.60	63.51	32.89	August 2015
15 km	C1	91.97/31.72	4,703	0 to 3, 5, 10, 20, 30	Plain	Meadow grassland	16.08	3.85	56.46	39.69	August 2014
	C2	92.00/31.81	5,000	0 to 3, 5, 10, 20, 30	Plain	Grassland	22.09	3.94	57.77	38.22	August 2015
	C3	91.99/31.96	5,060	0 to 3, 5, 10, 20, 30	Plain	Meadow grassland	25.68	1.61	48.95	49.44	August 2015
	C4	92.12/31.68	4,779	0 to 3, 5, 10, 20, 30	Plain	Wetland	20.08	5.50	68.06	26.44	August 2015
	C5	92.13/31.94	4,880	0 to 3, 5, 10, 20, 30	Slope	Grassland	6.35	2.86	41.15	55.99	August 2015
	C6	92.23/31.71	N/A	0 to 3, 5, 10, 20, 30	Plain	Boundary between wetland and grassland	11.84	3.79	59.81	36.40	August 2014
	C7	92.26/31.8	4,991	0 to 3, 5, 10, 20, 30	Plain	Grassland	8.72	3.23	45.03	51.75	August 2015
	C8			0 to 3, 5, 10, 20, 30	Valley	Grassland	7.70	3.40	45.38	51.21	August 2014
25 km	D1	91.88/31.58	4,636	0 to 3, 5, 10, 20, 30	Plain	Grassland	5.22	10.3	76.61	13.08	August 2015
	D2	91.87/31.81	5,000	0 to 3, 5, 10, 20, 30	Plain	Grassland	4.08	1.77	20.57	77.66	August 2015
	D3	91.88/32.06	4,865	0 to 3, 5, 10, 20, 30	Plain	Meadow grassland	12.53	3.14	38.13	58.73	August 2015
	D4	92.13/32.07	4,952	0 to 3, 5, 10, 20, 30	Plain	Meadow grassland	22.20	2.25	42.75	54.81	August 2015
	D5	92.12/31.57	5,000	0 to 3, 5, 10, 20, 30	Plain	Meadow grassland	5.42	5.62	46.27	48.02	August 2015
	D6	92.34/31.62	4,464	0 to 3, 5, 10, 20, 30	Plain	Meadow grassland	3.80	4.67	55.00	40.32	August 2015
	D7	92.38/31.82	4,769	0 to 3, 5, 10, 20, 30	Plain	Boundary between wetland and grassland	26.60	1.97	55.54	42.50	August 2015
	D8	92.38/32.04	4,866	0 to 3, 5, 10, 20, 30	Plain	Grassland	10.12	3.40	41.83	54.77	August 2015

(Continued)

representative atmospheric and soil temperature and humidity profile data for the study of water and energy recycling in the soil–atmosphere interface layer. As there is no weather station in Nierong county, these data also help to develop and test retrieval models and determine appropriate climate parameterization in this region.

The NCS measures precipitation, wind speed and direction, air temperature and humidity at 2 m above the soil surface, five SM and temperature estimates (at 3, 5, 10, 20, and 30 cm below the soil surface), and the 0-cm surface temperature. The infrared radiation temperature (8–14 μm) is measured at 2 m (nadir) and 3.5 m, with 45° and a nadir angle. These parameters have a high correlation with SM and are helpful to analyze the factors that influence SM temporal variation.

GEOGRAPHICAL FLOW OBSERVATORY EXPERIMENT

The GFO experiment was conducted (Figure 5) during the summers of 2014–2016. It aimed to provide a unique data set in this harsh environment, capturing soil texture, SOC, soil dielectric constant, ground surface emissivity, and vegetation coverage, among other parameters. In the

TABLE 2. THE SITE INFORMATION FOR THE NAQU MULTISCALE OBSERVATORY NETWORK. (CONTINUED)

								SOIL TEXTURE			
SCALE	**SITE ID**	**LONGITUDE/ LATITUDE**	**ELEVATION (m)**	**DEPTH (cm)**	**TPG**	**LAND COVER TYPE**	**SOC CONTENT (%)**	**CLAY (%)**	**SILT (%)**	**SAND (%)**	**START DATE**
75 km	ELU	91.97/32.15	4,779	0–3, 5, 10, 20, 30	Plain	Meadow grassland	10.72	6.05	63.42	30.4	August 2014
	EMU	92.26/32.15	4,656	0–3, 5, 10, 20, 30	Slope	Meadow grassland	4.22	6.85	69.21	23.94	August 2014
	ERU	92.49/32.16	4,764	0–3, 5, 10, 20, 30	Plain	Boundary between wetland and grassland	16.44	2.74	46.64	50.61	August 2014
	ERM	92.47/31.92	4,746	0–3, 5, 10, 20, 30	Slope	Meadow grassland	7.12	4.76	49.18	46.06	August 2014
	ERD	92.46/31.7	4,600	0–3, 5, 10, 20, 30	Plain	Meadow grassland	5.68	3.34	43.45	52.96	August 2014

Elevation: elevation above mean sea level; TPG: location topography; clay: <2 μm: silt: 2–20 μm; sand: 20–2,000 μm.

TABLE 3. THE SITE INFORMATION FOR THE A'LI MULTISCALE OBSERVATORY NETWORK.

SCALE	**SITE ID**	**LONGITUDE/ LATITUDE**	**ELEVATION (m)**	**DEPTH (cm)**	**TPG**	**LAND COVER TYPE**	**START DATE**
3 km	A'li06	81.92/32.05	4,599	0 to 3, 5, 10, 20, 30	Plain	Wetland	November 2016
	A'li07	81.93/32.05	4,591	0 to 3, 5, 10, 20, 30	Plain	Wetland	November 2016
	A'li08	81.93/32.06	4,590	0 to 3, 5, 10, 20, 30	Plain	Junction between wetland and desert grassland	November 2016
	A'li09	81.95/32.06	4,589			Wetland	November 2016
	A'li12	81.95/32.04	4,596	0 to 3, 5, 10, 20, 30	Plain	Junction between wetland and desert grassland	November 2016
5 km	A'li10	81.97/32.06	4,590	0 to 3, 5, 10, 20, 30	Plain	Wetland	November 2016
	A'li11	81.97/32.05	4,585	0 to 3, 5, 10, 20, 30	Plain	Wetland	November 2016
	A'li13	81.96/32.03	4,597	0 to 3, 5, 10, 20, 30	Plain	Junction between wetland and grassland	November 2016
	A'li14	81.96/32.01	4,600	0 to 3, 5, 10, 20, 30	Plain	Junction between wetland and grassland	November 2016
10 km	A'li15	81.99/31.98	4,592	0 to 3, 5, 10, 20, 30	Plain	Desert grassland	November 2016
	A'li16	82.02/32.08	4,632	0 to 3, 5, 10, 20, 30	Plain	Desert grassland	November 2016
25 km	A'li02	81.78/32.10	4,641	0 to 3, 5, 10, 20, 30	Plain	Desert grassland	November 2016
	A'li03	82. 00/32.04	4,606	0 to 3, 5, 10, 20, 30	Plain	Desert grassland, fenced pasture	November 2016
	A'li04	81.91/32.03	4,604	0 to 3, 5, 10, 20, 30	Plain	Desert grassland, fenced pasture	November 2016
	A'li05	81.92/32.01	4,613	0 to 3, 5, 10, 20, 30	Plain	Desert grassland	November 2016
50 km	A'li01	81.68/32.14	4,811	0 to 3, 5, 10, 20, 30	Plain	Desert grassland	November 2016
	A'li17	82.09/32.12	4,687	0 to 3, 5, 10, 20, 30	Slope	Desert grassland	November 2016

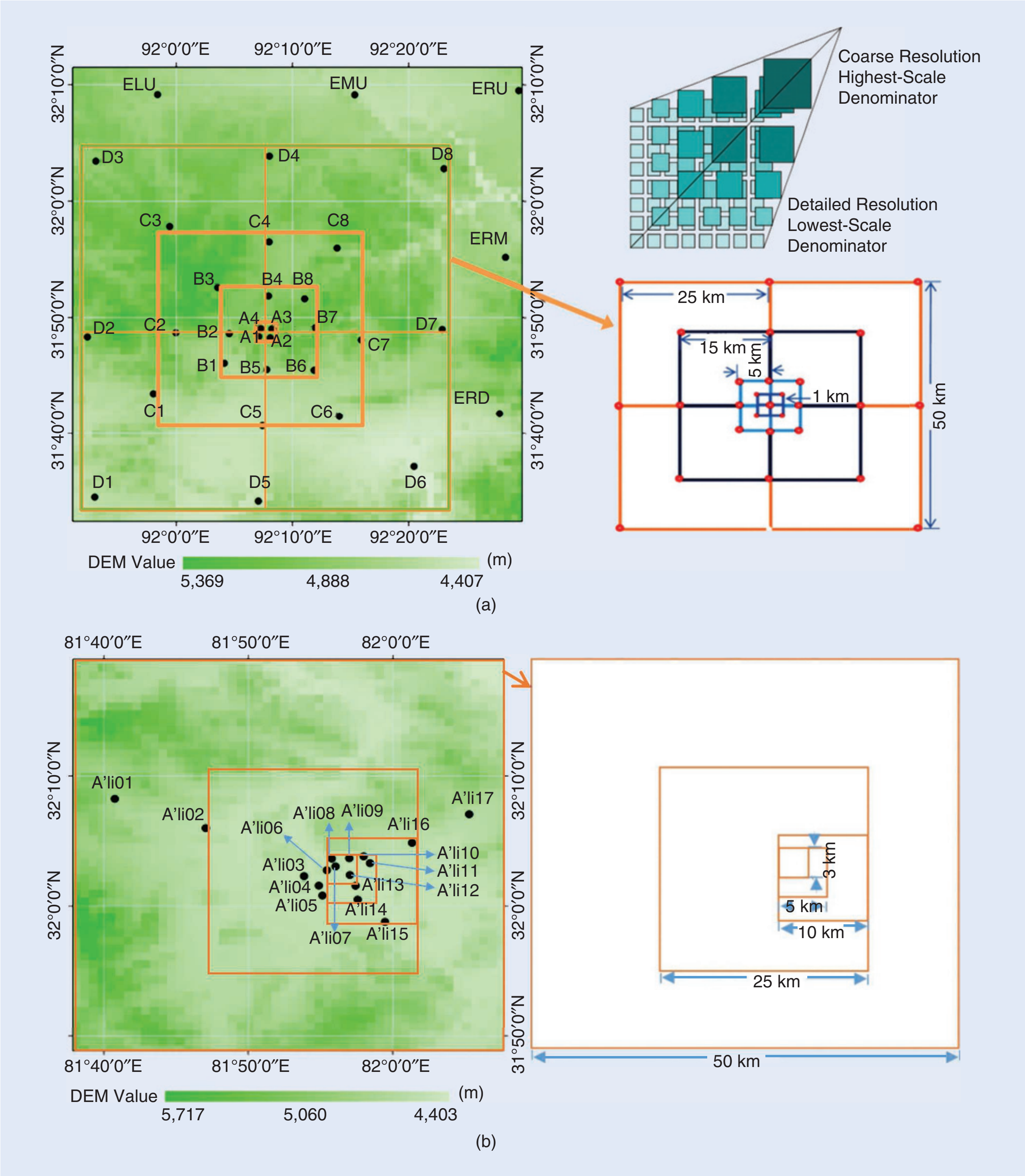

FIGURE 2. The multiscale site deployment of (a) the NSO and (b) the ASO.

larger experimental region, the main tasks included soil sampling, land cover surveying, vegetation mapping, and infrared emissivity measurement collection. Soil texture and organic matter content were also determined at each soil sample site with laboratory analyses.

The GFO experiment proceeded in three stages: 1) 28 July–5 August 2014, 2) 25 July–20 August 2015, 3) 14 August–2 September 2016. In the first and third stages, the soil sampling was conducted every 25–30 km. At the same time, the land cover type and vegetation coverage observations were conducted. Samples were also collected to determine soil texture, SOC, and the dielectric constant. In addition, the background data, such as slope, GPS position, and weather condition, were recorded. In the second and third stages, the emissivity measurement of different ground objects was added to the experiment.

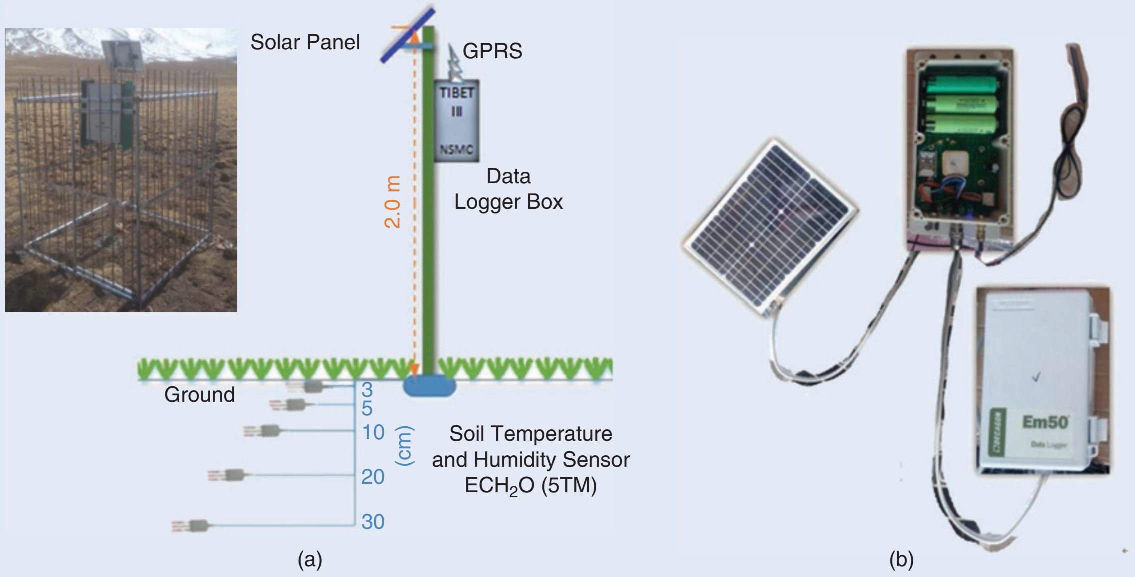

FIGURE 3. (a) The instrument installation and (b) the wireless transmission system at each site.

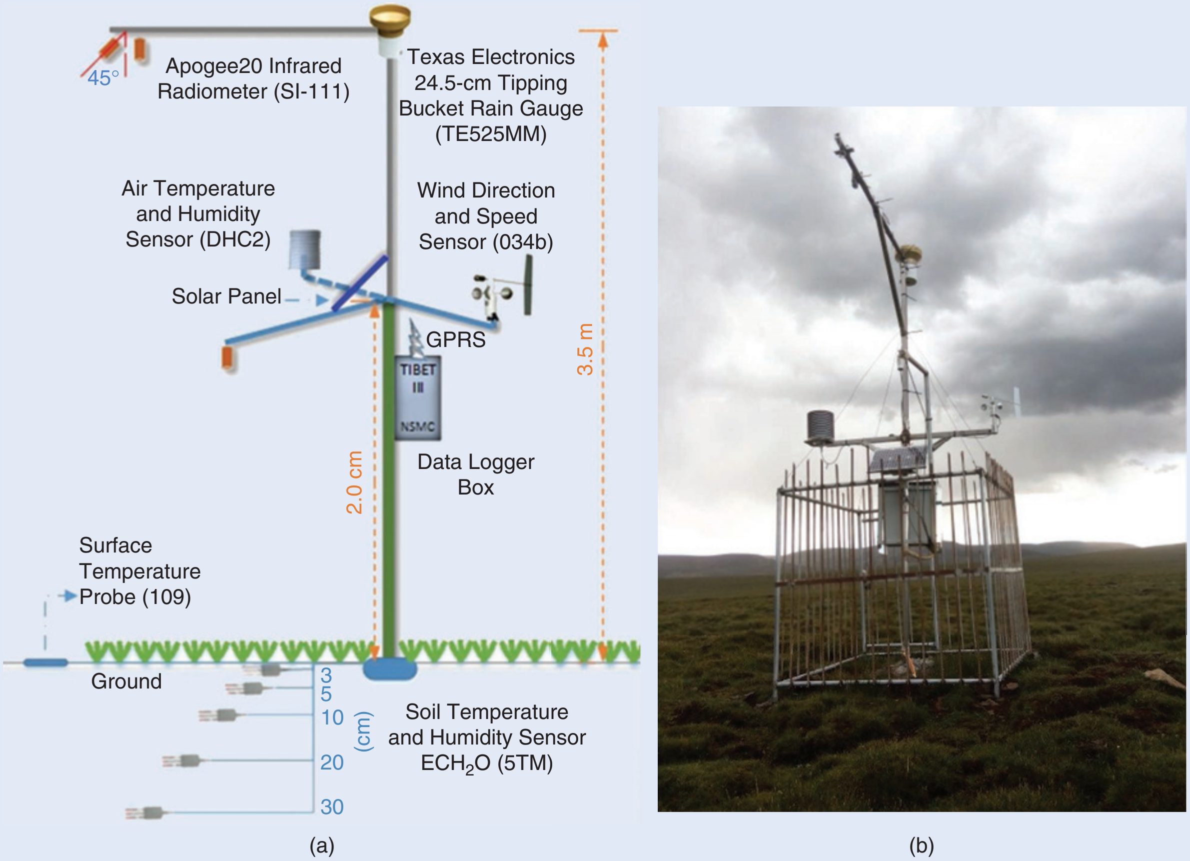

FIGURE 4. (a) A diagram and (b) a field photo of the instrument installation at the NCS.

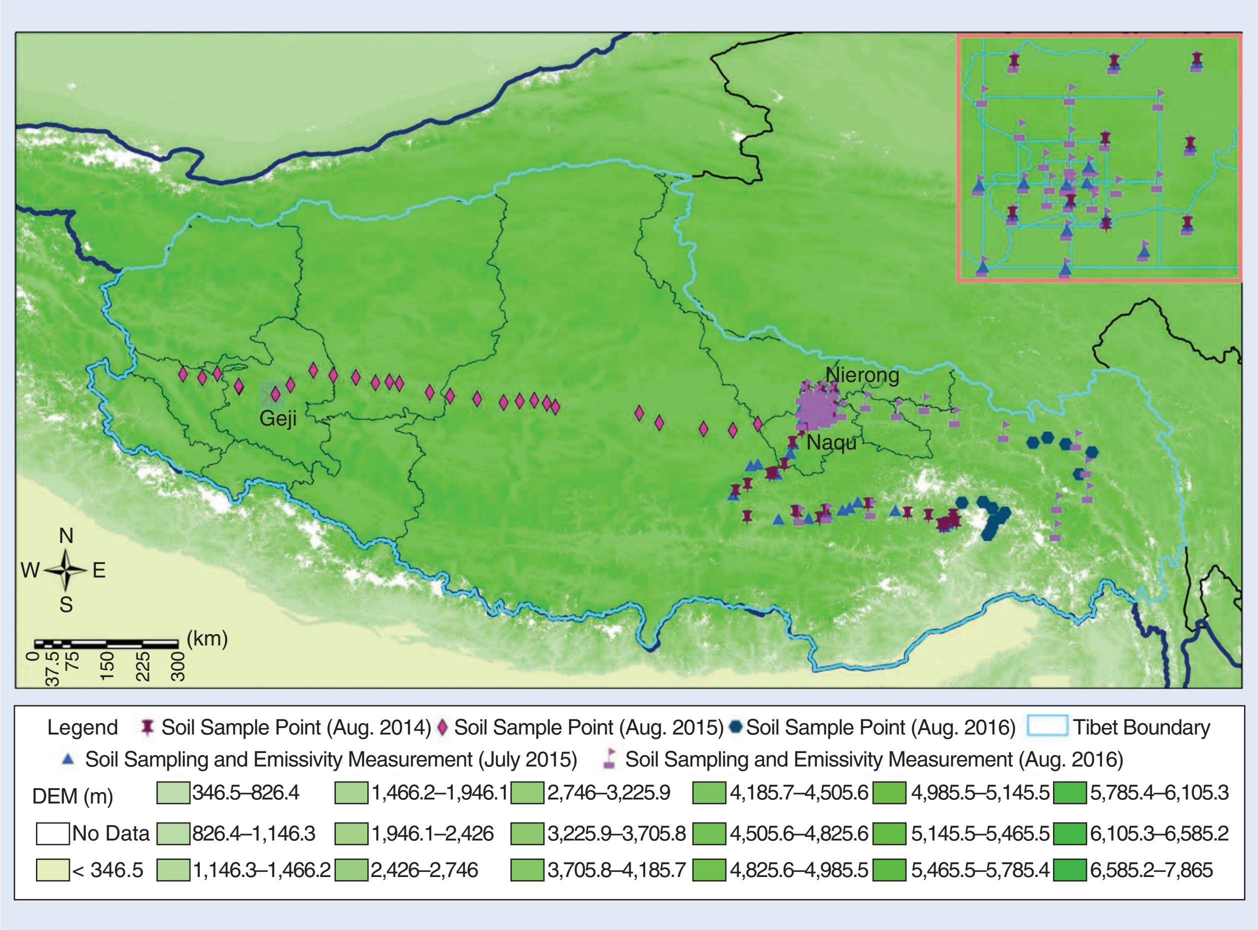

FIGURE 5. A diagram of the GFO experiment.

CALIBRATION OF SOIL SENSORS

The TP-IMSO uses 5TM capacitance probes manufactured by Decagon (http://www.decagon.com/). To accurately calibrate these sensors, an experiment was conducted that included both the effect of SOC and a correction based on gravimetrically collected soil samples, which is common for satellite validation programs. First, the SOC and soil properties (component and particle size) at each site were obtained for the organic carbon content V_{SOC} and the gravel content V_g in a unit volume calculation. The SM was calculated using the following [18]:

$$\theta = \frac{\sqrt{K_a}}{7.17 + 1.18\rho_b} - \frac{0.819 + 0.168\rho_b + 0.159\rho_b^2}{7.17 + 1.18\rho_b} \qquad (1)$$

$$\rho_b = (1 - V_{\mathrm{SOC}} - V_g)(1 - \theta_{m,\mathrm{sat}})\rho_p + V_{\mathrm{SOC}}\rho_{\mathrm{SOC}}, \qquad (2)$$

where

$$\rho_p = 2.65\ \mathrm{g \cdot cm^{-3}}, \quad \rho_{\mathrm{SOC}} = 0.13\ \mathrm{g \cdot cm^{-3}},$$
$$\theta_{m,\mathrm{sat}} = 0.489 - 0.00126 \times (\%\mathrm{sand}).$$

Second, SM is measured by the gravimetric method (converted to volumetric SM with bulk density) at varying SM conditions. The sensors are inserted into the soil and then dried by air in a laboratory to develop a calibration curve. Figure 6 shows the calibration equation, with an average RMSE of 0.037 $\mathrm{cm^3 \cdot cm^{-3}}$ and R^2 of 0.999.

DURATION AND FUTURE OF THE TIBETAN PLATEAU INTEGRATED OBSERVATORY

The TP-IMSO initially was deployed for four years, from 2014 to 2017, during which time an intensive observation campaign was conducted as a part of the GFO experiment. Intensive observation field work started in July 2014. Persistent in situ observation over the whole area would have lasted longer if funding had been available. Intensive observation periods are typically limited to the summer due to accessibility issues, and frozen soil limits the reliability of SM information.

DATA MANAGEMENT

Two software management systems were developed and copyrighted to effectively manage the TP-IMSO data (Figure 7). One is a multiscale network observation data remote management and real-time analysis system, i.e., the TP-IMSO Data Management System (DMAS). The other, the TP-IMSO Data Surveillance System (DSS),

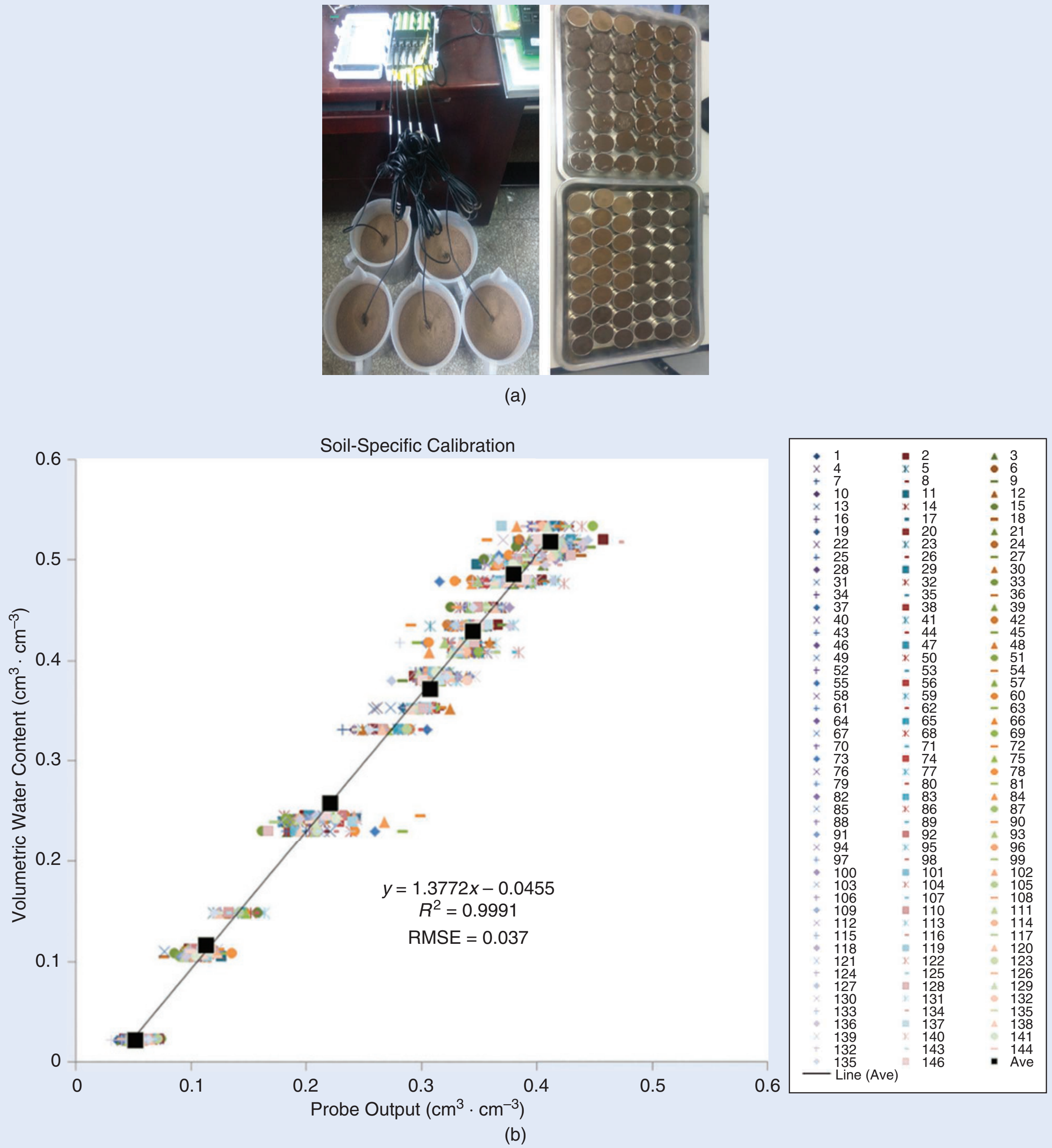

(a)

(b)

FIGURE 6. (a) The measurement and (b) a scatterplot of the sensor calibration by the gravimetric method with different soil water content samples.

provided real-time surveillance of the incoming data and instrument working status. The DMAS involves remote data collection, standardization, quality control, processing, warehousing, real-time analysis, and display. Quality control includes the elimination of invalid data and implementation of the calibration equations on the raw data.

The DSS provides real-time monitoring of the various apparatus, including the solar circuit, battery power, signal strength, GPRS online state, instrument temperature, instrument working status, GPS positioning, and so on. The online status of the instrument is obtained in

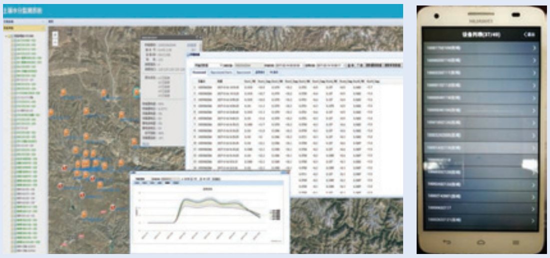

(a)

(b)

FIGURE 7. The software interfaces: (a) the TP-IMSO Data Management System and (b) the TP-IMSO Data Surveillance System.

real time by the wireless network. To quickly respond to abnormal conditions at the station, such as a power drop, an opening of the instrument box door, or the device temperature falling below a set value, an alert is sent via short message service to the instrument management personnel in a few seconds. The instruments' collection interval can be controlled by mobile phone short message command. For example, the acquisition time (10 min) can be easily changed to 5 or 30 min. This allows the in situ data to adapt to different time resolutions of the satellite data or assimilation systems and interesting weather events, which require higher-resolution data.

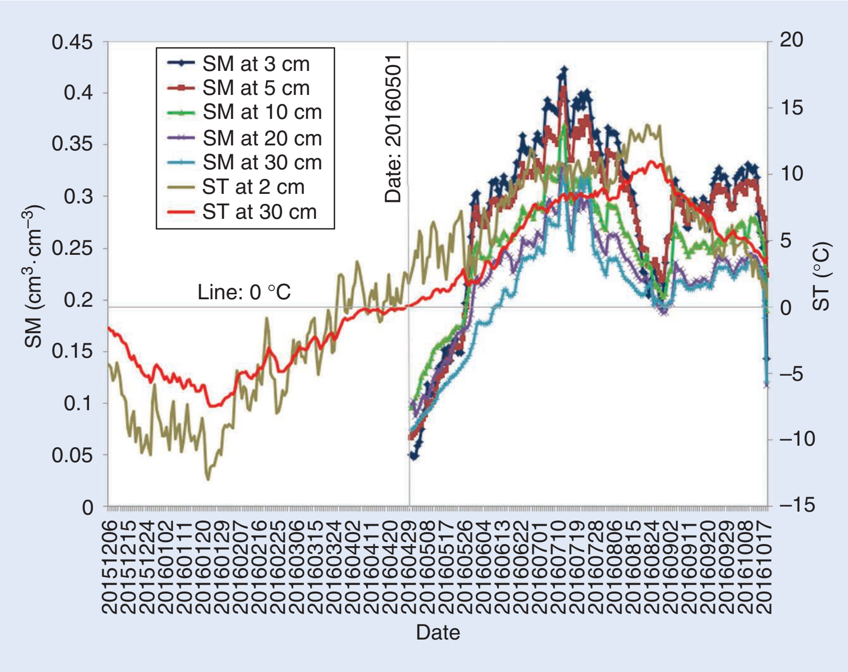

FIGURE 8. The variations of the averaged SM and soil temperature of multiple sites at different depths in the NSO. ST: soil temperature.

The TP-IMSO open data policy ensures that the experimental data are timely and adequately utilized. At the end of 2018, the protection period when observers can have priority in using original data lapsed. At that time, the TP-IMSO data were submitted to the data management and sharing platform constructed by TIPEX-III (http://data.cma.cn/tipex).

PRELIMINARY RESULTS

THE CHARACTERISTICS OF SEASONAL VARIATION

Figure 8 shows the variations of the average SM in multiple sites at different depths from May to November 2016 and the average soil temperature at 3 cm and 30 cm from December 2015 to November 2016 in the NSO. It can be seen that the soil temperature in the top layer started to reach 0 °C beginning on 27 March and, in the total layer (from 0 to 30 cm), completely reached 0 °C or more from 1 May. Hence, the 0–3-cm soil layer thawed from 27 March, and the total layer completely defrosted from 1 May. Due to the soil freezing before 1 May, the SM value from the sensors at different depths was no longer valid, and the data were removed. Due to the problem of GPRS wireless signals in some areas, some sites' data were temporarily unavailable for this analysis, but there were still 29 sites' data at hand for analysis and verification.

It can also be seen that the SM in the top layer is more variable than that at other depths. In April, soil water content starts to increase and then stabilizes for the short term. The main reason is that the ice in the soil melts during the daytime and freezes again at night during the freezing and thawing period (from late March to early May). Since the frozen soil maintains a large amount of water, the soil water content is high when it thaws. Hence, as the temperature rises continuously from early May, the SM of all layers rises very quickly since the ice completely melts and precipitation begins to increase. Therefore, the greatest SM recharge occurs in April and May. The SM gradient in the top layer first reverses in early May because of soil thawing. Through evaporation, the soil water turns to atmospheric vapor, which excites the conditions for the onset of the summer monsoon and plays an important role in the seasonal transition of the TP.

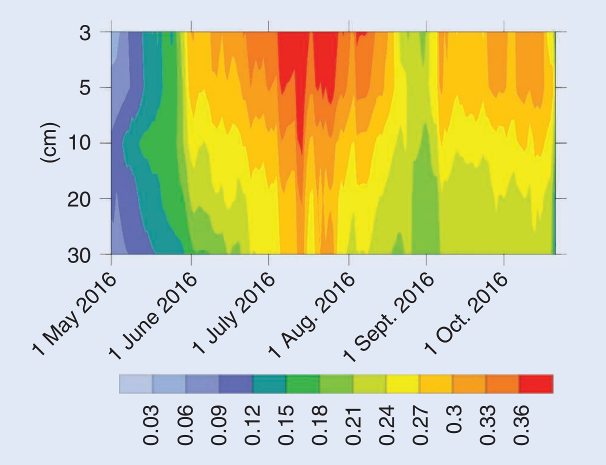

FIGURE 9. A cross section of the averaged SM at different depths in the NSO.

Three-quarters of the annual average precipitation on the TP is concentrated in the main flood season, from June to August, under the influence of the South Asian summer monsoon. With the arrival of the rainy season and the snow melting, the water content of the top soil stratum increases rapidly. From Figures 8 and 9, it can be seen that the SM decreases with depth in summer and autumn. The moisture is between 0.2 and 0.42 $cm^3 \cdot cm^{-3}$ in each layer, and the difference between the top soil layer and deep soil is 0.2 $cm^3 \cdot cm^{-3}$ in midsummer.

The average SM variations of multiple sites in each soil layer show two peaks, occurring in mid-July and mid-September. The maximum SM occurs in July (above 0.3 $cm^3 \cdot cm^{-3}$). In late August, it suddenly drops below 0.25 $cm^3 \cdot cm^{-3}$ in all layers. The main reasons are that the TP precipitation falls to fewer than 5 mm per day and the air temperature and soil evapotranspiration rise. The SM in late August is slightly lower than that of mid-July (Figures 8 and 9). With the increase of precipitation at the end of August, the SM rises again in early September. In mid-October, the precipitation and SM decrease significantly and simultaneously.

VARIABILITY ACROSS THE NETWORKS

The networks of the TP-IMSO demonstrate the highly variable character of elements on the TP. Although some stations are relatively close in distance, they present different time series. From Figure 10, it can be seen that the top SM in sites B1 and A4 are the largest (above 0.6 $cm^3 \cdot cm^{-3}$) in summer. In addition to B1 and A4, the SM at the 10-cm depth in site B5 is also greater. At 20-cm and 30-cm depths, the SM in B1 is much greater than that in other sites in summer. The largest SM difference among different sites reaches 0.6 $cm^3 \cdot cm^{-3}$ or more, due to different land types. For example, the B1 land type is a river wetland, and A4 is a typical wetland. For each layer, the SM at several sites could not represent the overall SM status in the area because of the large differences. In the climate system model, SM-related freezing and thawing processes and sensible heat calculations play an important role in model design and simulation results. The differences among various sites also indicated that it is necessary to use high-resolution grids in accurate climate simulation.

In Table 4, the standard deviation is used to represent the monthly variability among these sites. It can be seen that the largest standard deviation of all five depths appears in July, consistent with the results in Figure 10. In July, the SM is affected by precipitation and soil water permeability, and the largest difference among these sites appears. It is worth noting that the standard deviations at the 0–3-cm depth in October are larger than those in August, which might be related to the daily variations of the surface soil freeze/thaw process among different sites.

EVALUATION OF SOIL MOISTURE PRODUCTS AT COARSE SCALES

The TP-IMSO data set can be used for validating remote sensing products, climate models, and re-analysis products. For instance, the ERA-Interim re-analysis from the European Center for Medium-Range Weather Forecasts and the NCEP re-analysis outputs can be evaluated with the NSO's large- and medium-scale networks. Microwave SM products retrieved from AMSR-2, *SMOS*, TRMM, and *FY-3B/C* can be assessed with the medium-scale network data.

First, measurements at eight sites (ELU, EMU, ERU, ERM, ERD, C1, C6, and C8) of the NSO network established in 2014 are arithmetically averaged. And the remote sensing products at the 25 km × 25 km scale are validated by the averaged value of the SM in the top 3 cm of soil. The ascending and descending passes of satellite remote sensing data are evaluated separately. The average bias, maximum bias, RMSE, variance, mean relative error, squared correlation coefficient, and relative standard deviation are calculated, as shown in Table 5. The assimilation and re-analysis data were obtained on a daily basis from July to December 2014. The SM from the ERA-Interim analysis was evaluated by using the SM observations at 0–10 cm and 10–28 cm (the average of values at 10 and 30 cm), respectively.

Table 5 shows the preliminary results of comparing seven SM products derived from AMSR-2, *SMOS*, TRMM, and *FY-3B/C* ascending and descending signals, and ERA-Interim and NCEP re-analysis data from July to December 2014. Large biases between the five satellite products and the field observations can be detected. The RMSE ranges from 0.038 to approximately 0.177 $cm^3 \cdot cm^{-3}$ during the monsoon season, similar to previous study results [28], [35]. For ERA-Interim and NCEP re-analysis data, the RMSE spans from 0.038 to approximately 0.081 $cm^3 \cdot cm^{-3}$. There are high-value coefficients of determination (R^2) for these sites, indicating that these remote sensing platforms capture hydrologic dynamics and just need a refinement of retrieval algorithms for the unique circumstances of this environment. Future work should consider the high SOC impact on the soil dielectric permittivity and estimate the SM more accurately in the plateau environment.

DISCUSSION AND CONCLUSIONS

DISCUSSION

It is difficult to obtain comprehensive field observation data on the TP because of the spatiotemporal variation of SM and temperature and the complex topographic conditions. Obtaining the multiscale field data matching different satellite pixels is of profound significance to the technology, validation methods, and algorithm improvement of satellite remote sensing products. The multiscale observation strategy in this article is a new way to verify satellite and model products. According to comprehensive analysis of satellite remote sensing products, geographic information data, and the complex surface features of the TP, the observation layout is more suitable for the validation of satellite inversion and model products. The representative problem between site (point) and pixel (spatial) of satellite products is solved.

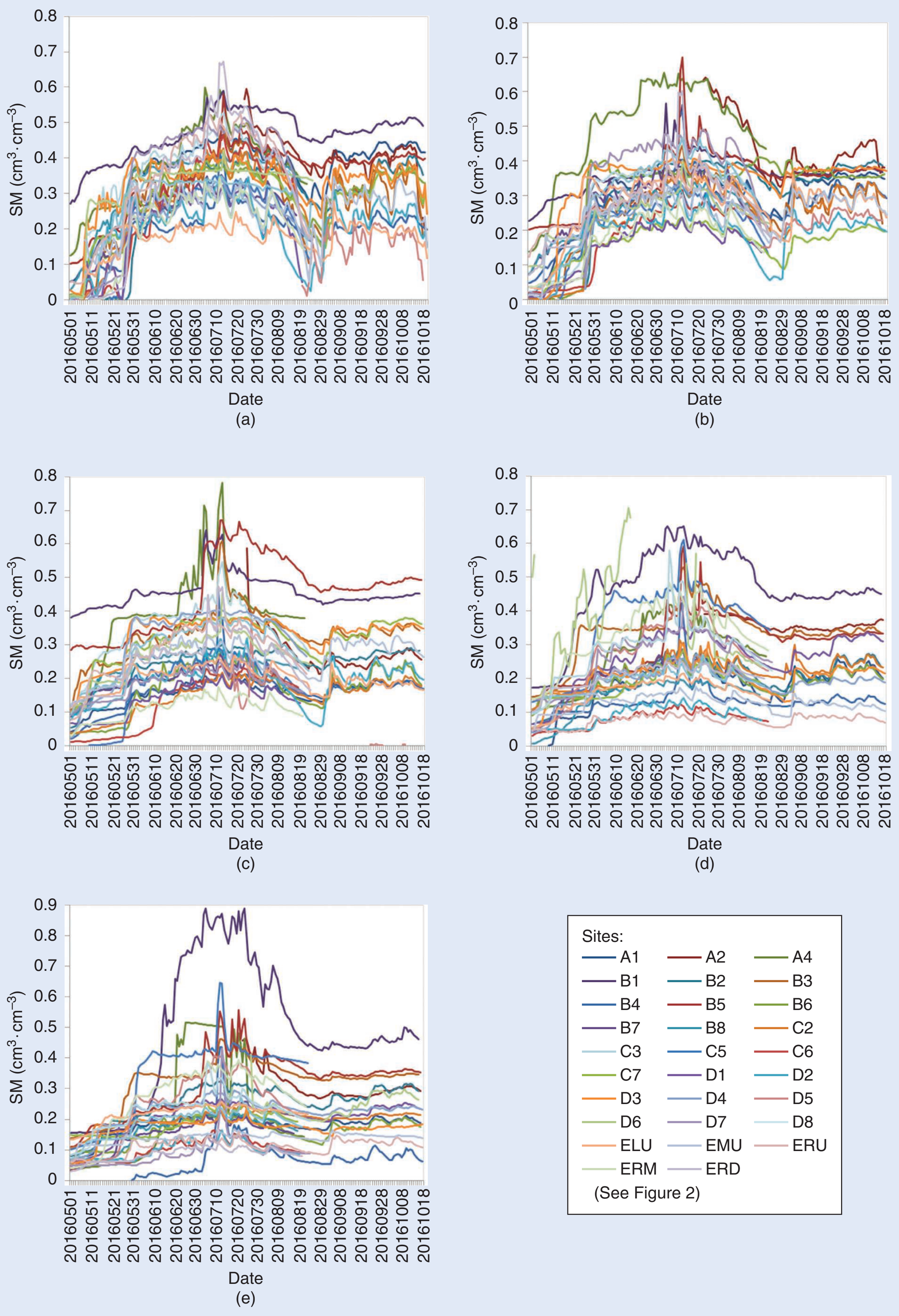

FIGURE 10. Different-depth SM time series at multiple sites in the NSO: (a) 3 cm, (b) 5 cm, (c) 10 cm, (d) 20 cm, and (e) 30 cm.

TABLE 4. THE STANDARD DEVIATIONS OF SM (cm^3·cm^{-3}) AT DIFFERENT DEPTHS IN DIFFERENT MONTHS.

	DEPTH				
MONTH	0–3 cm	5 cm	10 cm	20 cm	30 cm
May	0.0675	0.066	0.0825	0.0558	0.0466
June	0.0697	0.0793	0.0891	0.0977	0.0977
July	0.0845	0.0995	0.1149	0.1178	0.1446
August	0.0822	0.0825	0.0979	0.1007	0.1043
September	0.075	0.0603	0.0945	0.0948	0.0946
October	0.0833	0.0622	0.0977	0.0977	0.1005

The acquisition, monitoring, and transmission of field data on the TP were specially designed based on the experience and lessons of past experiments. The TP-IMSO network has high automation and precision, and it is an important resource for hydrologic parameter observations on the plateau. Adding the SM and temperature observations on the 0-to-3-cm top soil layer can reduce errors and uncertainties of verifying the SM and temperature products using 5-cm field data. Comprehensive observation of horizontal and vertical scales can not only help to validate the products but also be beneficial for improving product algorithms and analyzing influencing factors.

Of course, there are also some uncertainties in the TP-IMSO data. For example, in long-term observations, irregular calibration of the instrument is required. Consistency between different probes also needs to be considered. Unstable wireless signals and artificial damage can also lead to data loss. However, the TP-IMSO implements the current standards of the international community to enrich our knowledge in the harsh environmental conditions of the TP, meeting the needs of long-term, continuous, automatic observation.

CONCLUSIONS

A satellite pixel-oriented integrated, multiscale moisture and temperature observation experiment in the western and central TP was carried out for remote sensing and climate model application studies. The TP-IMSO is composed of two dense networks (the NSO and ASO) and a long-term climate station (the NCS). These studies were initiated for SM algorithm improvement and validation on the TP. The NSO and ASO constitute the core mission of the TP-IMSO. Data from the GFO experiment will contribute to algorithm improvement, and the NCS data will contribute to analysis of the factors that influence the land surface and atmosphere boundary layer.

Compared with other experiments on the TP, the TP-IMSO aims to answer scientific questions with more information integration at multiple satellite resolutions. It can provide a testbed for multisatellite products' validation and algorithm improvement and also support climate modeling or assimilation and land surface process studies, as it can capture multiscale soil properties in different land surface types.

By providing high-quality data, the TP-IMSO can greatly contribute to the international community in quantifying the roles of moisture and temperature in the multisphere interactions of the TP. The NSO, ASO, and NCS are run on a long-term basis, and more data are expected to become available in the near future. Scientists from all countries are welcome to participate in the field campaigns and use the data.

TABLE 5. AN EVALUATION OF SM PRODUCTS (cm^3·cm^{-3}).

	PRODUCTS	BIAS_AVE	BIAS_MAX	RMSE	VARIANCE	MRE	R^2	RSD	NUMBER
Image products	FY-3C-ASC	0.082	0.167	0.118	0.014	0.292	0.741	0.204	76
	FY-3C-DES	0.017	0.181	0.143	0.02	0.066	0.801	0.562	80
	FY-3B-ASC	0.044	0.496	0.135	0.018	0.129	0.734	0.534	78
	AMSR-2-ASC	−0.094	0.327	0.174	0.03	0.315	0.61	0.58	84
	AMSR-2-DES	−0.189	0.376	0.177	0.032	0.927	0.493	0.873	81
	TRMM-DY	0.036	0.168	0.128	0.016	0.086	0.891	0.302	87
	TRMM-NT	0.01	0.146	0.125	0.016	0.025	0.851	0.324	77
	SMOS-DY	0.014	0.294	0.145	0.021	0.053	0.483	0.533	31
	SMOS-NT	0.074	0.213	0.115	0.017	0.219	0.507	0.391	17
Re-analysis products	ERA_L07	0.005	0.135	0.038	0.001	0.014	0.713	0.117	380
	ERA_L10	0.047	0.133	0.038	0.001	0.143	0.786	0.117	380
	NCEP	0.116	0.317	0.081	0.007	0.318	0.309	0.222	124

Bias_Ave: average bias; Bias_Max: maximum bias; MRE: mean relative error; R^2: squared correlation coefficient; RSD: relative standard deviation.

The results show that the elements of the TP-IMSO network demonstrate a highly variable character. The SM in the top layer is more variable than that in other layers, and the largest standard deviation of all five depths appears in July. Through preliminary validation, the RMSE ranges from 0.038 to approximately 0.177 $cm^3 \cdot cm^{-3}$ in remote sensing products, and, in ERA-Interim and NCEP reanalysis data, the RMSE extends from 0.038 to approximately 0.081 $cm^3 \cdot cm^{-3}$.

ACKNOWLEDGMENTS

This work was jointly supported by the CMA Special Fund for Scientific Research in the Public Interest, The Third Tibetan Plateau Atmospheric Scientific Experiment (TIPEX-III) (GYHY201406001-01), and China's climate change special project, Remote Sensing Evaluation of the Effects of Climate and CO_2 Concentration Change on Alpine Vegetation (QHBH2014). At the end of 2018, a protection period lapsed in which observers could have priority in using original data. The validated data sets will be open to the domestic and international scientific communities for three to five months after the publication of this article. Meanwhile, the website (the Chinese version) for downloading the data (http://data.cma.cn/tipex) has been preliminarily built and will be further improved (with the English version). When users have problems downloading the data sets, they are encouraged to directly contact the corresponding authors, Lixin Dong and Shihao Tang. Also, we reaffirm the rules of open use of the data.

AUTHOR INFORMATION

Lixin Dong (dlxwater.student@sina.com) is with the Key Laboratory of Radiometric Calibration and Validation for Environmental Satellites, Beijing, and the National Satellites Meteorological Center, Beijing. He is a corresponding author for this article.

Shihao Tang (tangsh@cma.gov.cn) is with the Key Laboratory of Radiometric Calibration and Validation for Environmental Satellites, Beijing, and the National Satellites Meteorological Center, Beijing. He is a corresponding author for this article.

Michael H. Cosh (michael.cosh@usda.gov) is with the U.S. Department of Agriculture, Agricultural Research Service, Hydrology, and Remote Sensing Laboratory, Beltsville, Maryland.

Ping Zhao (zhaop@cma.gov.cn) is with the State Key Laboratory of Severe Weather, Chinese Academy of Meteorological Sciences, Beijing.

Pinting Lu (lupinting@163.com) is with the School of Geography and Remote Sensing, Nanjing University of Information Science and Technology, China.

Kanshe Zhou (zhoukanshe@163.com) is with the Tibet Climatic Center, Lasa, China.

Shuai Han (hans@cma.gov.cn) is with the National Meteorological Information Center, Beijing.

Min Min (minm5@mail.sysu.edu.cn) is with the School of Atmospheric Sciences, Sun Yat-sen University, and Key Laboratory of Tropical Atmosphere-Ocean System, Ministry of Education, and Southern Marine Science and Engineering Guangdong Laboratory, Zhuhai, China.

Na Xu (xuna@cma.gov.cn) is with the Key Laboratory of Radiometric Calibration and Validation for Environmental Satellites, Beijing, and the National Satellites Meteorological Center, Beijing.

Lin Chen (chenlin@cma.gov.cn) is with the Key Laboratory of Radiometric Calibration and Validation for Environmental Satellites, Beijing, and the National Satellites Meteorological Center, Beijing.

Fu Wang (wangfu@cma.gov.cn) is with the Key Laboratory of Radiometric Calibration and Validation for Environmental Satellites, Beijing, and the National Satellites Meteorological Center, Beijing.

REFERENCES

[1] C. Albergel et al., "Evaluation of remotely sensed and modeled soil moisture products using global ground-based in situ observations," *Remote Sens. Environ.*, vol. 118, pp. 215–226, Mar. 2012.

[2] G. Balsamo, P. Viterbo, and A. Beljaars, "A revised hydrology for the ECMWF model: Verification from field site to terrestrial water storage and impact in the integrated forecast system," *J. Hydrometeorol.*, vol. 10, pp. 623–643, June 2009.

[3] Y. Chen, K. Yang, J. Qin, L. Zhao, W. Tang, and M. Han, "Evaluation of AMSR-E retrievals and GLDAS simulations against observations of a soil moisture network on the central Tibetan Plateau," *J. Geophys. Res.: Atmospheres*, vol. 118, no. 10, pp. 4466–4475, 2013.

[4] L. Dente, Z. Vekerdy, J. Wen, and Z. Su, "Maqu network for validation of satellite-derived soil moisture products," *Int. J. Appl. Earth Observ. Geoinform.*, vol. 17, pp. 55–65, July 2012.

[5] W. Dorigo et al., "Error characterization of global active and passive microwave soil moisture datasets," *Hydrol. Earth Syst. Sci.*, vol. 14, no. 12, pp. 2605–2616, 2010.

[6] W. A. Dorigo et al., "Evaluation of the ESA CCI soil moisture product using ground-based observations," *Remote Sens. Environ.*, vol. 162, pp. 380–395, June 2015.

[7] H. Fujii and T. Koike, "Development of a TRMM/TMI algorithm for precipitation in the Tibetan Plateau by considering effect on land surface emissivity," *J. Meteorol. Soc. Japan*, vol. 79, no. 1B, pp. 475–483, 2001.

[8] H. Fujii, T. Koike, and K. Imaoka, "Improvement of AMSR-E algorithm for soil moisture estimation by introducing a fractional vegetation coverage dataset derived from MODIS data," *J. Remote Sens. Soc. Japan*, vol. 29, no. 1, pp. 282–292, 2009.

[9] Z. C. Guo, P. A. Dirmeyer, Z. Z. Hu, X. Gao, and M. Zhao, "Evaluation of the second global soil wetness project soil moisture simulations: 2. sensitivity to external meteorological forcing," *J. Geophys. Res.: Atmospheres*, vol. 111, Nov. 2006. doi:10.1029/2006JD007845.

[10] A. Henderson-Sellers, "Soil moistures immolation: Achievements of the RICE and PILPS inter-comparison workshop and future directions," *Global Planet. Change*, vol. 13, no. 1-4, pp. 99–115, 1996.

[11] R. Hida, A. Manns, A. Berg, and A. Colliander, "Soil organic carbon as a factor in passive microwave retrievals of soil water content over agricultural croplands," *J. Hydrometeorol.*, vol. 528, pp. 643–651, Sept. 2015.

[12] International Soil Moisture Network, 2013. [Online]. Available: http://ismn.geo.tuwien.ac.at/

[13] T. J. Jackson et al., "Validation of advanced microwave scanning radiometer soil moisture products," *IEEE Trans. Geosci. Remote Sens.*, vol. 48, no. 12, pp. 4256–4272, 2010.,

[14] M. Jung et al., "Recent decline in the global land evapotranspiration trend due to limited moisture supply," *Nature*, vol. 467, pp. 951–954, Oct. 2010.

[15] T. Koike et al., "Development of an Advanced Microwave Scanning Radiometer (AMSR-E) algorithm of soil moisture and vegetation water content," *Proc. Hydraulic Eng.*, vol. 48, no. 2, pp. 217–222, 2004.

[16] X. Li et al., "HeiHe Watershed Allied Telemetry Experimental Research (HiWATER): Scientific objectives and experimental design," *Bull. Amer. Meteorol. Soc.*, vol. 94, no. 8, pp. 1145–1160, 2013.

[17] H. Lu et al., "Improving land surface soil moisture and energy flux simulations over the Tibetan plateau by the assimilation of the microwave remote sensing data and the GCM output into a land surface model," *Int. J. Appl. Earth Observ. Geoinform.*, vol. 17, pp. 43–54, July 2012.

[18] M. A. Malicki, R. Plagge, and C. H. Roth, "Influence of matrix on TDR soil moisture readings and its elimination," in *Proc. Symp. Time Domain Reflectometry Environmental, Infrastructure, and Mining Applications*, Evanston, IL, U.S. Bureau Mines, Spec. Publ. SP 19-94, NTIS PB95-105789, Sept. 7–9, 1994, pp. 105–114.

[19] Y. M. Ma, S. Kang, L. Zhu, B. Xu, L. Tian, and T. Yao, "Roof of the world: Tibetan observation and research platform," *Bull. Amer. Meteorol. Soc.*, vol. 89, no. 10, pp. 1487–1492, 2008.

[20] E. G. Njoku and S. K. Chan, "Vegetation and surface roughness effects on AMSR-E land observations," *Remote Sens. Environ.*, vol. 100, no. 2, pp. 190–199, 2006.

[21] T. Oki, T. Nishimura, and P. Dirmeyer, "Assessment of annual runoff from land surface models using total runoff integrating pathways (TRIP)," *J. Meteorol. Soc. Japan*, vol. 77, no. 1B, pp. 235–255, 1999.

[22] M. Owe, R. De-Jeu, and T. Holmes, "Multi-sensor historical climatology of satellite derived global land surface moisture," *J. Geophys. Res.*, vol. 113, no. F01002, pp. 1–17, 2008. doi: 10.1029/2007JF000769.

[23] R. Panciera et al., "The Soil Moisture Active Passive Experiments (SMAPEx): Toward soil moisture retrieval from the SMAP mission," *IEEE Trans. Geosci. Remote Sens.*, vol. 52, no. 1, pp. 490–507, 2014.

[24] C. Paulik, W. Dorigo, W. Wagner, and R. Kidd, "Validation of the ASCAT Soil Water Index using in situ data from the International Soil Moisture Network International," *J. Appl. Earth Observ. Geoinform.*, vol. 30, pp. 1–8, Aug. 2014.

[25] J. Polcher, M. Piles, E. Gelati, A. Barella-Ortiz, and M. Tello, "Comparing surface-soil moisture from the SMOS mission and the ORCHIDEE land-surface model over the Iberian Peninsula," *Remote Sens. Environ.*, vol. 174, pp. 69–81, Mar. 2016.

[26] C. Rüdiger, J. C. Calvet, C. Gruhier, T. R. H. Holmes, R. A. M. de-Jeu, and W. Wagner, "An inter-comparison of ERS-Scat and AMSR-E soil moisture observations with model simulations over France," *J. Hydrometeorol.*, vol. 10, pp. 431–447, Apr. 2009.

[27] K. Scipal, T. Holmes, R. de-Jeu, V. Naeimi, and W. Wagner, "A possible solution for the problem of estimating the error structure of global soil moisture data sets," *Geophys. Res. Lett.*, vol. 35, Dec. 2008. doi:10.1029/2008GL035599.

[28] Z. Su et al., "The Tibetan Plateau observatory of plateau scale soil moisture and soil temperature (Tibet-Obs) for quantifying uncertainties in coarse resolution satellite and model products," *Hydrol. Earth Syst. Sci.*, vol. 15, no. 7, pp. 2303–2316, 2011.

[29] Y. Shao and A. Henderson-Sellers, "Validation of soil moisture simulation in land surface parameterization schemes with HAPEX data," *Global Planet. Change*, vol. 13, no. 1-4, pp. 11–46, 1996.

[30] G. Srinivasan et al., "Soil moisture simulations in revised AMIP models," *J. Geophys. Res.*, vol. 105, no. D21, pp. 26,635–26,644, Nov. 16, 2000.

[31] R. van der Velde, Z. Su, P. van Oevelen, J. Wen, Y. Ma, and M. Suhyb Salama, "Soil moisture mapping over the central part of the Tibetan Plateau using a series of ASAR WS images," *Remote Sens. Environ.*, vol. 120, pp. 175–187, May 2012. doi: 10.1016/J.RSE.2011.05.029.

[32] W. Wagner, K. Scipal, C. Pathe, D. Gerten, W. Lucht, and B. Rudolf, "Evaluation of the agreement between the first global remotely sensed soil moisture data with model and precipitation data," *J. Geophys. Res.: Atmospheres*, vol. 108, no. D19, p. 4611, 2003. doi: 10.1029/2003JD003663.

[33] K. Yang et al., "Response of hydrological cycle to recent climate changes in the Tibetan Plateau," *Climatic Change*, vol. 109, no. 3–4, pp. 517–534, 2011.

[34] M. Yang et al., "Diurnal freeze/thaw cycles of the ground surface on the Tibetan Plateau," *Chin. Sci. Bull.*, vol. 52, no. 1, pp. 136–139, 2007.

[35] K. Yang et al., "A multi-scale soil moisture and freeze-thaw monitoring network on the third pole," *Bull. Amer. Meteorol. Soc.*, vol. 94, no. 12, pp. 1907–1916, 2013. doi: 10.1175/BAMS-D-12-00203.1.

[36] D. Z. Ye and Z. C. Gu, "Influence of Tibet Plateau on East Asian atmospheric circulation and weather in China," *Chin. Sci. Bull.*, vol. 6, no. 2, pp. 29–33, 1955.

[37] D. Z. Ye, "Some physical factors for long term prediction," *Meteorology*, vol. 3, pp. 12–15, 1975.

[38] L. Zhao et al., "The scale-dependence of SMOS soil moisture accuracy and its improvement through land data assimilation in the central Tibetan Plateau," *Remote Sens. Environ.*, vol. 152, pp. 345–355, Sept. 2014.

[39] J. Y. Zeng, Z. Li, Q. Chen, H. Y. Bi, J. X. Qiu, and P. F. Zou, "Evaluation of remotely sensed and reanalysis soil moisture products over the Tibetan Plateau using in-situ observations," *Remote Sens. Environ.*, vol. 163, pp. 91–110, June 2015.

[40] X. Zhu et al., "Application of cosmic-ray neutron sensing to monitor soil water content in an alpine meadow ecosystem on the northern Tibetan Plateau," *J. Hydrometeorol.*, vol. 536, pp. 247–254, May 2016.

GRS

Preventing Forest Fires Through Remote Sensing

Achievements of the Prevention and Recovery of Forest Fires Emergency in the Mediterranean Area project

GIOVANNI LANEVE, LORENZO FUSILLI, GUIDO BERNINI, AND JUAN SUÁREZ BELTRAN

©ISTOCKPHOTO.COM/APIGUIDE

The three-year Space-Based Information Support for the Prevention and Recovery of Forest Fires Emergency in the Mediterranean Area (PREFER) project was devoted to creating a satellite-based service infrastructure capable of providing up-to-date information to support the preparedness, prevention, recovery, and reconstruction phases of the forest fires emergency cycle in the European Mediterranean region. The project, an initiative of the 7th Framework Programme for Research and Technological Development, was successfully completed at the end of 2015. However, the project's products were also made available to engaged users for the 2016 summer season.

The present article presents the initiative's achievements, emphasizing the most innovative information products developed in PREFER's framework. For these products, the

Digital Object Identifier 10.1109/MGRS.2019.2906948
Date of current version: 21 February 2020

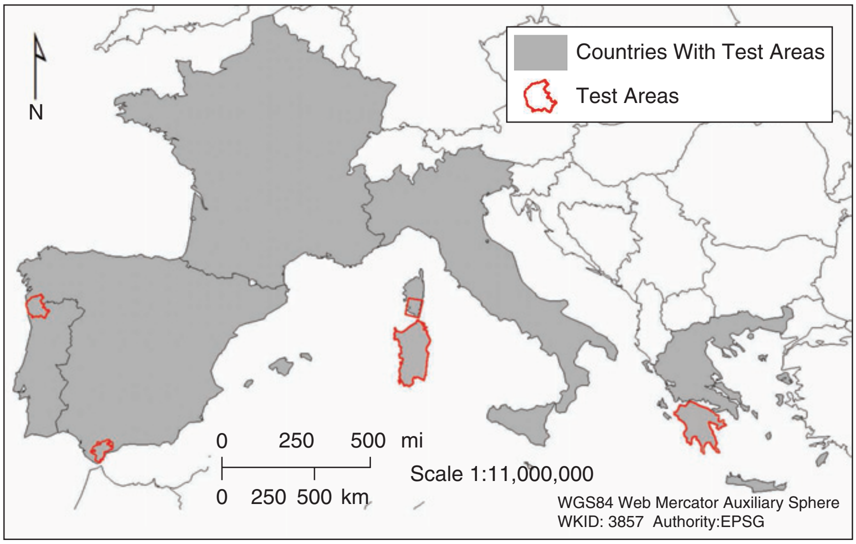

FIGURE 1. The countries where PREFER project partners are located and the project test areas.

methodology and validation results are introduced and discussed. The PREFER project was largely associated with the European Copernicus program (http://www.copernicus.eu/), the goal of which is to develop operational information services on a global scale, using both space- and ground-based monitoring systems, in support of environmental and security policy needs. This program aims to provide an increasingly broad user community with accurate, timely, and easily accessible information collected from satellites and in situ sensors, establishing a European capacity for Earth observation (EO). Copernicus delivers services in six main thematic areas: land, marine, atmosphere, climate change, emergency management, and security. A main objective of the PREFER project is to ensure and foster the complementarity of the EO information products portfolio with the EO products delivered by other ongoing Copernicus operational land and emergency services.

The project focuses its activities on the European Union (EU) Mediterranean region, namely, the five most fire-affected countries in southern Europe: France, Greece, Italy, Portugal, and Spain [1]. Every year in these countries, hundreds of thousands of hectares of forest are burned by fires. Approximately 500,000 ha per year are incinerated as a consequence of some 65,000 fires. Several conditions overlap that explain such a high fire incidence:

- the coincidence of the driest with the hottest season and the occurrence of wet and dry weather extremes throughout the year
- the coexistence of urban settlements, infrastructure networks, and vegetated areas (forest, agricultural, and uncultivated areas) in a complex, dense, and intimately interconnected patchwork
- diminished control over traditional practices involving fire as an instrument for land management and sanitization
- changes in land use that have occurred in recent decades [2], [3].

This article is devoted to introducing three products developed in the framework of project PREFER, namely, the Seasonal Fire Hazard Map (SFHM), Fuel Reduction Map (FRM), and Prescribed Burning Map (PBM). The computing methodology and validation results are described and discussed for each of these products, which belong to the group of innovations devoted to supporting the wildfire preparedness and prevention phases.

DATA AND METHODS

PREFER information products are available to stakeholders through the GeoServer project (http://www.prefer-copernicus.eu/). GeoServer allows users to consult the catalog, display available products on a virtual map, and select a part (region) of a layer on the map and download it through standard protocols and formats. A list of products presently available for the test areas (Figure 1), located in France (Corsica), Greece (Peloponnesus), Italy (Sardinia), Portugal (Minho), and Spain (Andalusia), is given in Table 1.

The project foresees the utilization of satellite optical images at medium, high, and very high spatial resolution (respectively, *MODIS/Terra* and *Aqua*; *Landsat* and *Spot*; and *Kompsat*, *RapidEye*, *Pleiades*, and so forth) and at a product refresh rate varying from high (days) to low (twice a month) to very low (once a year). Synthetic aperture radar images at very high spatial resolution (Cosmo-SkyMed, TanDEM-X, and the TerraSAR-X add-on for digital elevation measurement) are used in computing burned areas and digital elevation models (DEMs).

Table 1 provides a summary of the products that have been delivered by the project, according to each of the two project services [4]:

1) information support for the preparedness/prevention phase
2) information support for the recovery/reconstruction phase.

In this article, we focus on the following innovative products developed in the framework of the PREFER project:

- *FRM*: This is a high-spatial-resolution raster-format map of the areas where it would be useful to apply the practice of fuel reduction as a preventative treatment to mitigate the effects of a potential fire.
- *PBM*: This item provides a daily map of the areas where it would be useful to apply, under safe conditions, the prescribed fire practice as a preventative treatment to mitigate the effects of a potential fire.
- *SFHM*: This map provides a medium-resolution danger index with a temporal resolution of two to four weeks (updated during the fire season).

FUEL REDUCTION MAP

Regardless of the recognition that most fires in southern Europe are human caused (by accident, negligence, or arson) [5]—and that, therefore, awareness activities are required in this regard—it is known that particular environmental and meteoro-climatic conditions favor the spread of fire to areas away from the ignition point. The main ideas that have inspired the development of this map consist of defining factors that promote fire spread and identifying territorial units that have a higher probability of being affected by a fire. That is, the goal is to define a fire propagation probability (FPP) in the study area from which to extrapolate the territorial units more prone to be affected by fires. Based on these defined territorial units, an appropriate program can be planned for reducing the fuel load to lessen the dangerous effects of any future fire.

TABLE 1. THE PRODUCTS DELIVERED BY THE PREFER PROJECT.

INFORMATION SUPPORT FOR THE PREPAREDNESS/ PREVENTION PHASE	INFORMATION SUPPORT FOR THE RECOVERY/ RECONSTRUCTION PHASE
Fuel Map	Burn Scar Map: High Resolution
Daily Fire Hazard Index	Burn Scar Map: Very High Resolution Optical
Fire Vulnerability Map	Postfire Vegetation Recovery
Seasonal Risk Map	Damage Severity Map
SFHM	3D Fire Damage Assessment Map
FRM	
PBM	

Initially, the purpose of the FRM was to develop a product capable of providing multitemporal maps of areas to apply vegetation fuel reduction through prescribed burning practices. However, after meetings with representatives of fire management agencies, it became clear that confining fuel load reduction techniques to prescribed burning only was limiting and even conceptually misleading. In fact, if we take into consideration the rules governing the use of prescribed burning [6], [7], we note that, in several European countries, laws restrict or prohibit its use. Furthermore, some preliminary tests made during the development of the methodology indicated that, in some cases, the meteoro-climatic conditions for prescribed burning would occur for only a few days within the allowed time window (winter season), thus making it impossible to plan a prevention action based on intentional burning. Thus, we decided to develop an information product suitable to all techniques for reducing vegetation fuel load. These methods comprise those practices used in the field for reducing excessive and dangerous accumulation of natural fuel. They include [8]–[15]

- *Prescribed burning*: the deliberate use of fire in a given area under well-defined meteorological conditions
- *Mechanical treatment*: the modification or manual or mechanical removal of natural fuels, such as by cutting, crushing, or stacking
- *Other treatment*: the application of herbicides, introduction of biological controls, and pasturage.

The methodology introduced takes into account, first of all, geospatial elements, that is, all factors related to the territory

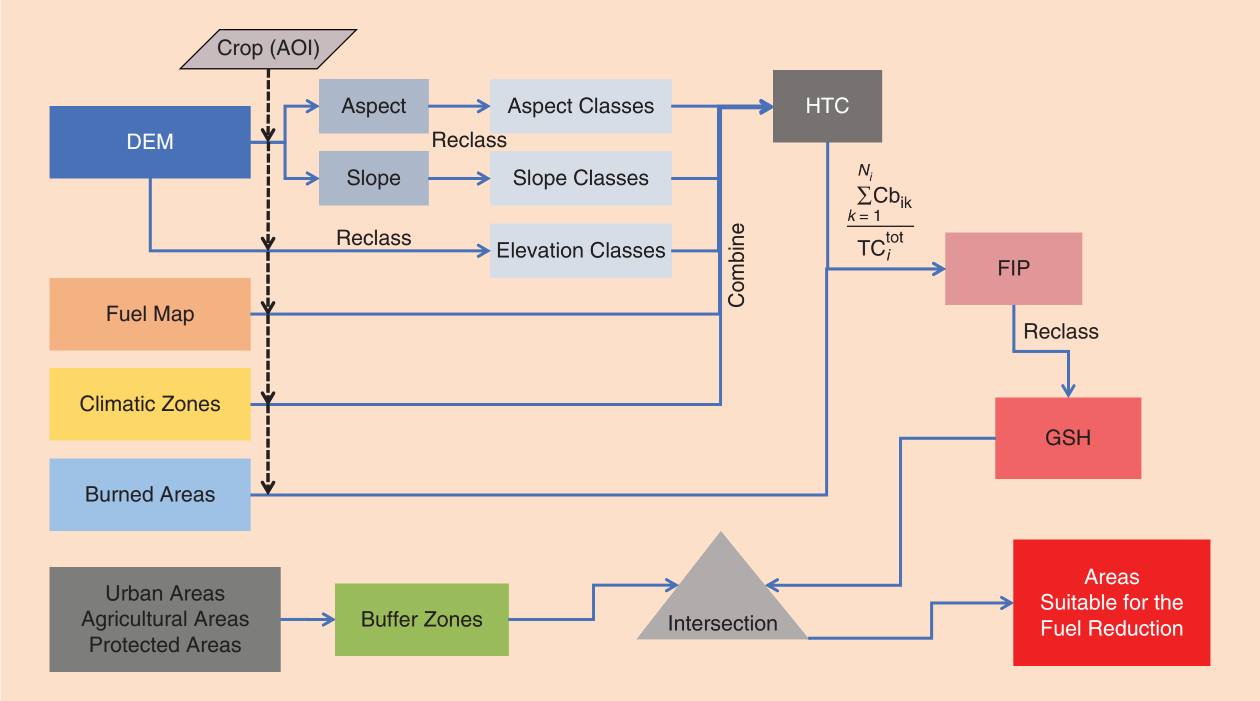

FIGURE 2. The workflow for the computation of the FRM. AOI: area of interest; FIP: fire ignition probability.

that may affect the onset and spread of fire (Figure 2). Four types were taken into account, grouped as follows:

- *Topographic factors*: altitude, slope, and aspect
- *Environmental factors*: fuel type and climate
- *Factors depending on fire incidence*: areas burned in the last five years (or later)
- *Land-use factors*: natural parks, forests, roads, urban areas, and agricultural areas.

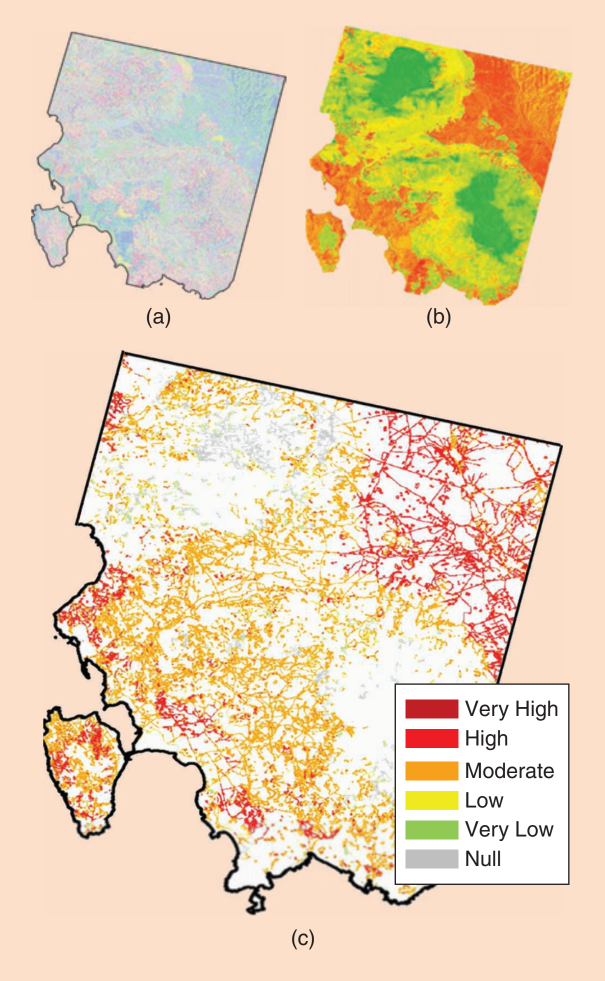

FIGURE 3. (a) A map of the HTCs computed for southwest Sardinia on the basis of environmental characteristics (topography, vegetation fuel type, and climatology). Each color corresponds to a different HTC. (b) The GSH derived by calculating the FPP for each HTC. (c) An FRM. The colors indicate the priority classes in terms of fuel reduction intervention (see legend).

TABLE 2. THE GSH CLASSES BASED ON THE FPP VALUES.

FPP VALUES	CLASS	GSH
> 0.1	5	Very high
0.1–0.01	4	High
0.01–0.001	3	Moderate
0.001–0.0001	2	Low
0.0001–0	1	Very low
0	0	Null

Topographic and environmental conditions are combined to compute a series of homogeneous territorial classes (HTCs), a kind of landscape classification in which each class represents a distinctive combination of the four factor groupings (Figure 3). Then, it is possible to calculate the FPP as

$$\mathrm{FPP}_i = \frac{\sum_{k=1}^{N_i} Cb_{ik}}{TC_i^{\mathrm{tot}}}, \quad (1)$$

where Cb_{ik} is the burned area of the kth fire within the ith HTC in hectares, T is the time range (five years or longer), N_i is the number of fires in the time range T in the type, and C_i^{tot} is the total area of the ith HTC.

The geospatial hazard (GSH) is obtained by reclassifying the FPP_i (that is, the FPP computed for the ith HTC) values into six classes, according to the ranges shown in Table 2. The values indicate the priority classes in terms of fuel reduction intervention.

The last step needed to obtain the final product (the FRM) consists of inserting protection buffer zones over the GSH around vulnerable areas (urban districts, agricultural areas, woodlands, parks and protected sites, roads, and so on) (Figure 3). This product is provided at the end of the fire season.

PRESCRIBED BURNING MAP

As already stated, the required fuel load reduction can be obtained using several techniques [8], [10]–[12]. If local statutes allow prescribed burning, it can be applied only under certain environmental conditions, ensuring that fuel reduction is achieved through a controlled, low-intensity fire. It needs to take place within specific ranges of some meteorological variables (Table 3), among which are wind speed, air temperature, relative humidity, number of days without rain, and moisture content of fine fuels. For European countries, these constraints have been defined in the framework of the Fire Paradox project [7], [13]–[15].

Then, the methodology must take into account the restrictions for the prescribed burning and develop a specific forecasting module. In this case, the analysis of the time factor predicts the optimum days for the prescribed burning. In other words, the technology should be able to foretell when the conditions expressed by the meteorological variables are all satisfied. Therefore, the output is a daily forecast map for the current and two following days of the areas where all the conditions that need to be satisfied are met (Figure 4).

For this purpose, an automatic procedure was implemented to generate daily maps using meteorological data provided by the forecasting model (COSMO-ME–Corsa 00) of the Italian Air Force's Meteorology and Climatology Center. This procedure carries out several actions every day, the main ones being

- downloading meteorological data via FTP
- resizing these data for each area of interest (AOI)
- converting data from Gridded Binary to GeoTIFF format
- resampling from 7 km to 250 m using a DEM
- computing the range values of temperature, humidity, wind, and total precipitation required for the application of the prescribed fire
- computing daily masks where the prescribed fire conditions are satisfied (GeoTIFF format)
- uploading maps via FTP and publishing them on the PREFER GeoServer.

The total processing time takes approximately 2 h. The starting time was set at 9 a.m. These maps are integrated with the product obtained from the geospatial computation module. In fact, only after overlapping and intersection of the time module (Figure 4) and geospatial module (Figure 3) is it possible to obtain full information about where and when to plan a prescribed burning intervention according to the prescription elements and the intervention priority (Figure 4).

SEASONAL FIRE HAZARD MAPS

Wildfires require effective prevention efforts and suppression preparation, based on a deep knowledge of the territory, fire behavior, and suppression system resources. When a fire has been ignited negligently or deliberately, its propagation depends on the vegetation status (in terms of both the dead and living fractions), meteorological conditions, and environmental factors. This is why daily fire hazard indices were developed.

Considering that a fire almost never occurs without human intervention in a given area, except under extreme weather conditions, it is necessary to account for the human factor in the definition of fire hazard [16]. This is normally done with the static (long-term) Fire Hazard Map, which usually takes into account the statistical spatial distribution of fires in the previous five to 10 years [16]–[19]. Of course, a statistical analysis based on previous fire seasons cannot consider the present season's weather conditions, which can differ from one year to another, or short-term (annual) changes in human behavior.

The methodology illustrated here aims to factor in the actual human and meteorological elements by developing a new index able to describe the conditions that may determine the onset and spread of a fire. Called the *Seasonal Fire Hazard Index* (see Figure 5), it results from the combination of the following information:

- *Natural factors*: These are further distinguishable as static elements (fuel map, slope, aspect, and climatic zone) and dynamic features (vegetation index, e.g., the Normalized Difference Vegetation Index; meteorological data; updated Fuel Map with burned areas; and the Daily Fire Hazard Index, or DFHI).
- *Human factors*: These are further distinguishable as static elements (urban areas, roads, fire statistics, and cultural factors) and dynamic components (actual fire season statistics).

The natural factors take into account the morphological characteristics (slope and aspect) and vegetation stress (based on a daily hazard index, averaged every 15 days). The DFHI is described in [20]–[23]. The human factors relate to accessibility, culture, and season. The accessibility element evaluates the number of people who are able to enter a zone (the more the possible people, the higher the probability of an accidental fire). The cultural determinant is based on fire occurrences during the last five to 10 years; it models a site's security. The seasonal factor is based on the actual fire trend in a season with respect to the average of the previous five to 10 years. At present, the actual fire trend can be evaluated using satellite-based active fire detection approaches like the Fire Information for Resource Management System [24], European Forest Fire Information System (EFFIS) [3], and System for Fire Detection [25]. In the near future, information on the actual wildfire trend could be provided directly by the fire management agencies if a near-real-time collection of active fires is implemented.

THE PROJECT FOCUSES ITS ACTIVITIES ON THE EUROPEAN UNION MEDITERRANEAN REGION, NAMELY, THE FIVE MOST FIRE-AFFECTED COUNTRIES IN SOUTHERN EUROPE: FRANCE, GREECE, ITALY, PORTUGAL, AND SPAIN.

The approach for the computation of this SFHM foresees the computation of an HTC following a procedure very similar to that used for an FRM (see previous discussion and Figure 2). In this case, data on fire ignition points instead of burned areas are used in the computation. In fact, a fire ignition probability (FIP_0) is obtained by combining the fire ignition points of the last five to 10 years with the morphologic (elevation, slope, and aspect), fuel, and climatic characteristics, as in the following:

$$\mathrm{FIP}_i = \frac{\sum_{k=1}^{N} F_{ik}}{C_i^{\mathrm{tot}}} \frac{A_{\mathrm{tot}}}{N}, \tag{2}$$

TABLE 3. THE TEMPORAL WINDOWS AND WEATHER CONDITION RANGES REGULATING THE APPLICATION OF PRESCRIBED BURNING FOR THE ITALIAN TEST AOI.

PRESCRIPTION ELEMENTS*	RANGE	OPTIMUM
Burn season	October–April	November–February
Wind speed	1–15 km/h	2–8 km/h
Air temperature	4–20 °C	6–15 °C
Relative humidity	30–80%	40%
Number of days since rain	Two to 10	Four to five

*According to the Fire Paradox.

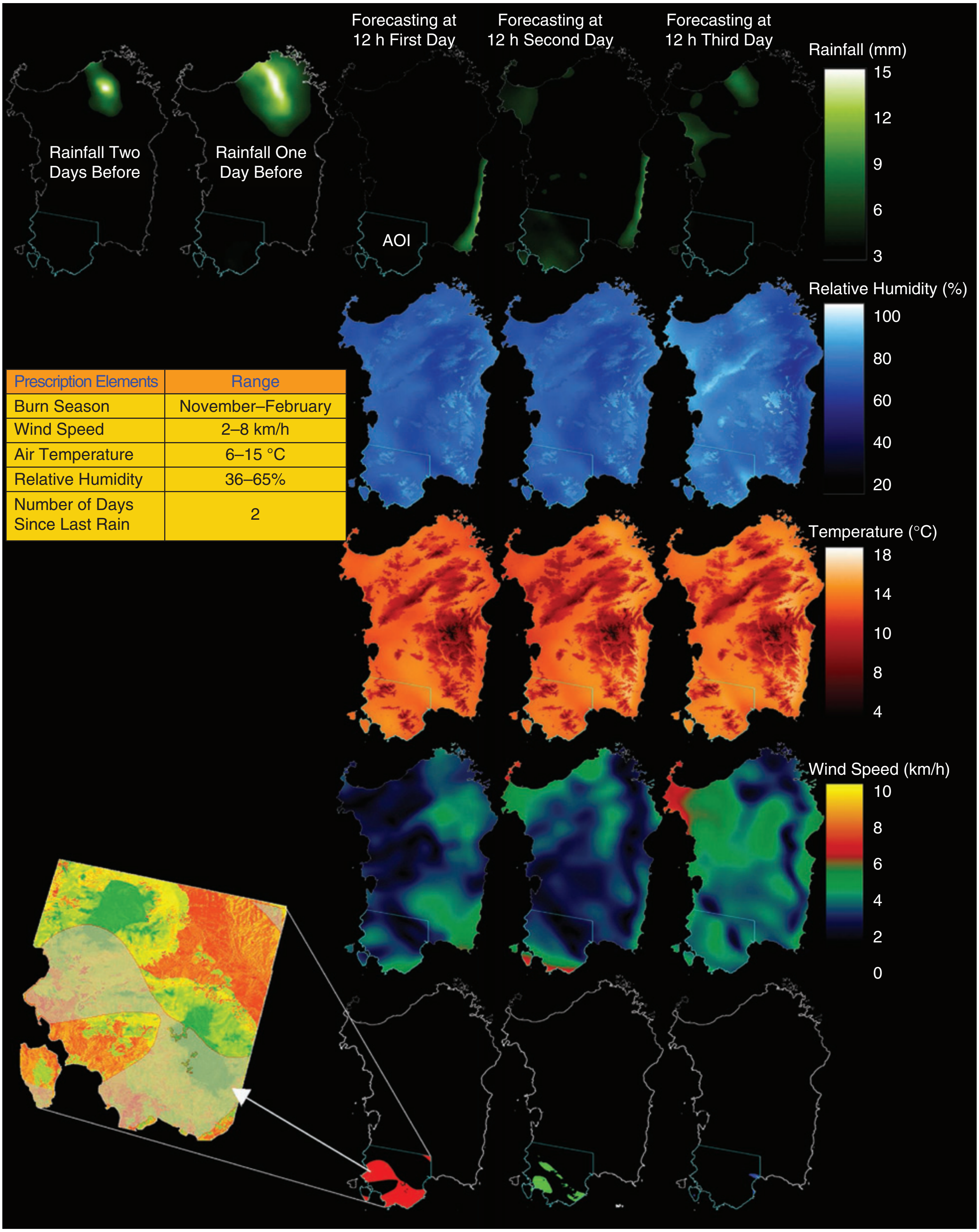

Prescription Elements	Range
Burn Season	November–February
Wind Speed	2–8 km/h
Air Temperature	6–15 °C
Relative Humidity	36–65%
Number of Days Since Last Rain	2

FIGURE 4. The forecasting of meteorological variables (rainfall, humidity, temperature, and wind speed) used daily to extract the conditions required for the prescribed burning. The overlap and intersection of the daily masks and FRM (lower left) provide the spatiotemporal information to know where (red, green, and blue areas) and when—present day (red area), the following day (green area), and the day after that (blue area)—it will be possible to plan the prescribed burning intervention.

where FIP_i is the FIP of the ith HTC, F_{ik} is the kth fire occurrence within the ith HTC, A_{tot} is the total area of the AOI, N is the total number of fires that occurred in the time range T (five years or longer) considered for computing the FIP map at the start of the season, and C_i^{tot} is the total area of the ith HTC.

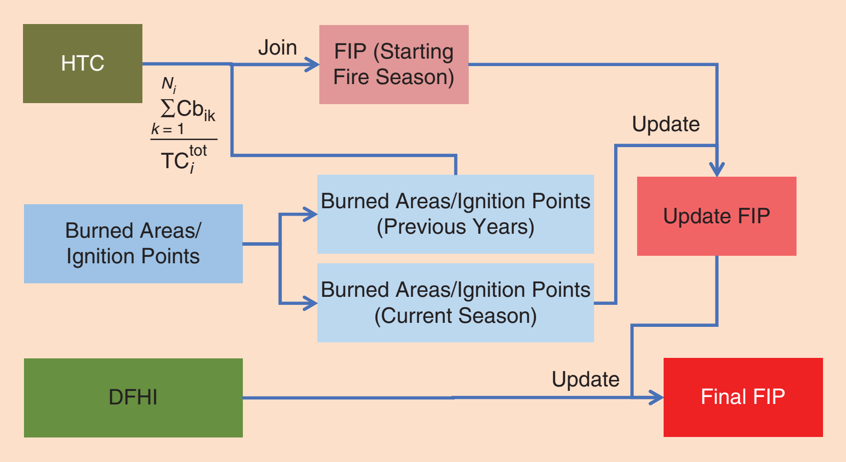

FIGURE 5. The forecasting workflow for the computation of the SFHM.

Then, the FIP values are grouped into five classes, number 1 being very low probability and number 5 very high (see Figure 6). This map is provided at the start of the fire season (1 June, in our case). During the fire season, the map is updated considering the fire events that occurred in the AOI during the preceding two weeks of the current season (i.e., fire events that occurred between 1 and 15 June). The updated version of FIP_0 (FIP_i) is calculated using (2), where the time range T is set to two weeks and N is the number of fires that occurred in the previous two weeks. The updating of the FIP map is computed by comparing the FIP_i with the FIP_0 map provided at the start of the season. The final output indicates the trend or the shift of the current fire season with respect to average long-term behavior (see Figure 6).

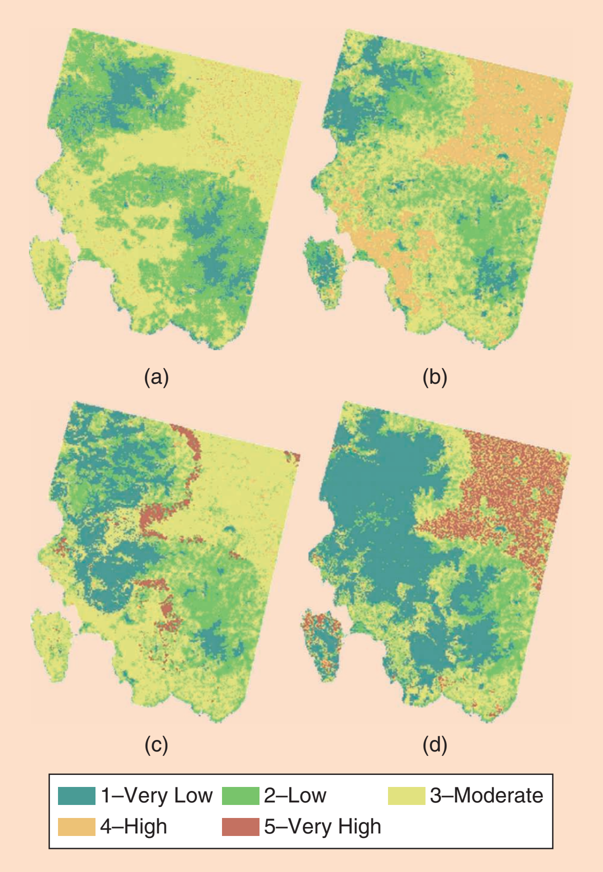

FIGURE 6. (a) The FIP computed at the start of the season (1 June) using eight years of fire data. Then, the FIP is computed every two weeks [(b) 28 June, (c) 12 July, and (d) 26 July] using the fire occurrences of the 2015 fire season.

The factor related to vegetation and meteorological conditions is introduced using the DFHI [20], [21], which takes into account vegetation status and actual weather conditions. The average DFHI ($\mathrm{DFHI}_{\mathrm{av}}$) is computed daily. How the actual average meteorological conditions (every two weeks), measured through the $\mathrm{DFHI}_{\mathrm{av}}$, enter into the seasonal hazard index computation is described later in the article. The averaged DFHI values for the AOI are computed for every couple of weeks, from 1 June to 31 October of, for instance, the previous eight years.

On the basis of these values, a long-term average $\mathrm{DFHI}_{\mathrm{long},i}$ and standard deviation σ_i are computed for each couple of weeks using the following:

$$\mathrm{DFHI}_{\mathrm{long},i} = \frac{\sum_{k=1}^{8} \mathrm{DFHI}_{av,i,k}}{8}$$

$$\sigma_i = \frac{1}{8} \cdot \sqrt{\sum_{k=1}^{8} (\mathrm{DFHI}_{av,i,k} - \mathrm{DFHI}_{\mathrm{long},i})^2}, \qquad (3)$$

where i is the ith two weeks of the fire season, defined as starting on 1 June and ending on 31 October; k is the kth year of the eight previous years considered; $\mathrm{DFHI}_{\mathrm{av}}$ is the daily DFHI value averaged every two weeks; and $\mathrm{DFHI}_{\mathrm{long}}$ is the DFHI value averaged on the two weeks of the previous eight years.

Now, the map of the FIP_0 is updated (SFHM_i) on the basis of the actual $\mathrm{DFHI}_{\mathrm{av}}$, following this rule:

- if the $\mathrm{DFHI}_{\mathrm{av}}$ computed in the two weeks of the present year is higher than $\mathrm{DFHI}_{\mathrm{long},i}$, then,
- if $\mathrm{DFHI}_{\mathrm{av}}(x,y) > (\mathrm{DFHI}_{\mathrm{long},i}(x,y) + \sigma_i(x,y)) \Longrightarrow \mathrm{SIFH}_i(x,y) = \mathrm{FIP}_i(x,y) + 1$;
- if the $\mathrm{DFHI}_{\mathrm{av}}$ is lower than $\mathrm{DFHI}_{\mathrm{long},i}$ and the FPI_i value in that pixel is higher than two, then,

- if $\mathrm{DFHI}_{\mathrm{av}} < (\mathrm{DFHI}_{\mathrm{long},i} - \sigma_i)$ and $\mathrm{FPI}_i(x,y) > 2 \Longrightarrow \mathrm{SFHM}_i(x,y) = FIP_i(x,y) - 1$,

where (x,y) define the coordinates of the pixel in the map.

RESULTS

These products were validated and demonstrated in 2015. In particular, the validation consisted of comparing the maps produced in 2014 with ground data provided by local authorities. The demonstration activity consisted of providing SFHMs, FRMs, and PBMs to potential users through the project's web server during the 2015 EU Mediterranean fire season (SFHMs) and the autumn/winter seasons (PBMs and FRMs), when the prescribed fire practice is allowed.

VALIDATION OF THE FUEL REDUCTION AND PRESCRIBED BURNING MAPS

The FRMs and PBMs were validated on the Italian and Portuguese AOIs using two approaches:

1) analysis of the spatial distribution of the fire events (burned areas) that occurred in the year following the publication of the product
2) using a fire behavior simulator (FARSITE) [26] to assess the fuel reduction effectiveness in ameliorating fire effects.

As noted previously, the GSH is calculated considering a reference period equal to or greater than the last eight fire seasons. For the two AOIs, the reference period was from 2005 to 2013. In the first approach, the distribution of the areas burned in 2014 was used to evaluate the spatial accordance between them and the GSH. The validation results are shown in Table 4. In both of the AOIs, 64% of the burned areas fell in class 4 (high GSH) and 33% in class 3 (Italy) or class 5 (Portugal).

TABLE 4. THE VALIDATION RESULTS FOR THE FRM.*

		ITALY		PORTUGAL	
CLASS	**GSH**	**HA**	**%**	**HA**	**%**
5	Very high	1	0	7,572	33
4	High	3,388	64	14,524	64
3	Moderate	1,751	33	580	3
2	Low	35	1	33	0
1	Very low	5	0	0.5	0
0	Null	153	3	103	0

*Courtesy of the local users involved in the project: the Civil Protection of the Regione Sardegna and the Instituto da Conservação da Natureza e das Florestas of Portugal.

Some fires that occurred in the 2014 fire season were considered to apply the second approach. In particular, two scenarios were simulated and the fire parameters retrieved. The first replicated the fire behavior in the actual situation without the application of any fuel reduction; the second simulated the same fire event, but assuming an environmental context corresponding to three different levels of fuel reduction treatment (low, moderate, and full).

The comparison between these two scenarios provides an estimate of the fuel reduction effectiveness in terms of fireline intensity, flame length, total burned area, and so forth. As an example, Table 5 shows some results, in terms of land cover burned, obtained by FARSITE simulations of a fire that occurred on 3 July 2014 in the Italian AOI.

In particular, Table 5 shows how, according to the simulation carried out using FARSITE, the burned area could be reduced by applying different grades of fuel reduction in the areas defined by the FRM, from 485 ha (corresponding to the actual case) to 13 ha, if the maximum grade of fuel load reduction was applied. The figures in Table 5 show the simulated polygons of the burned area for different levels of fuel reduction.

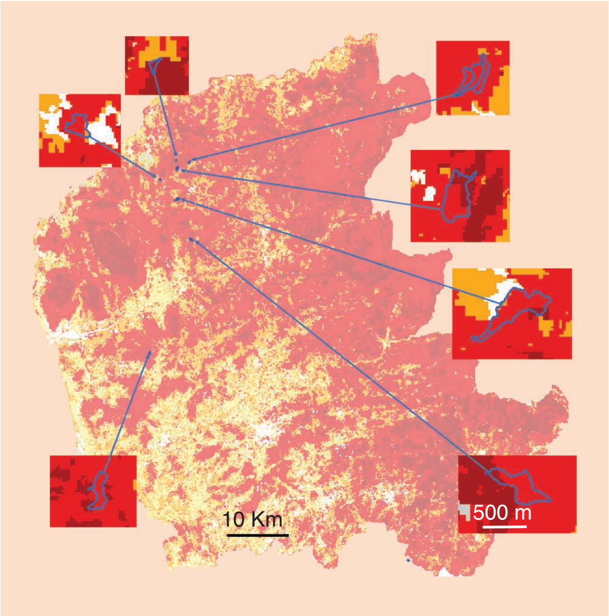

FIGURE 7. The prescribed burning areas superimposed on the FRM computed for the Minho region (Portugal).

Portugal is the only country out of those involved in the PREFER project that systematically adopts the prescribed burning technique to reduce fuel load as a method to mitigate fire hazard. The Instituto da Conservação da Natureza e das Florestas (ICNF) provided the polygons where the prescribed burning was performed in 2014 and 2015. Such polygons very well fit the GSH classes described by the FRM map. In fact, more than 97% of their surfaces fall into areas classified as high or very high GSH values (Figure 7). These results suggest the possibility of mitigating fire effects/damage through a policy of fire prevention based on fuel load reduction before the fire season. According to the ICNF, PBMs will be needed when it plans controlled burning on areas larger than those on which it is presently using the technique. In fact, the application of prescribed fires on small areas, as is now done,

TABLE 5. THE BURNED LAND COVER AFTER FARSITE SIMULATIONS.

		SIMULATED BURNED SURFACE (HA)		
LAND COVER	EFFECTIVE BURNED SURFACE (HA)	LOW FUEL REDUCTION	MODERATE FUEL REDUCTION	FULL REDUCTION OF FUEL LOAD
Garigue	165	136	136	0
Maquis shrubland	143	143	143	0
Agricultural land	114	59	24	13
Transitional woodland-shrub	20	10	10	0
Agro-forestry areas	20	19	9	0
Nonirrigated arable land	9	3	3	0
Natural grasslands	9	0	0	0
Vineyards	5	0	0	0
Total	485	370	353	13
		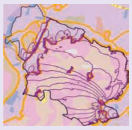	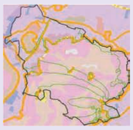	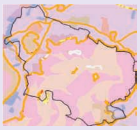

The time duration of the simulation corresponds to 4 h, 30 min. The colored lines (red, violet, green, and cyan) indicate the fire propagation for each simulation; the time step is 30 min. The orange and red bands indicate the buffer zones for the application of fuel load reduction.

is not very effective in reducing the incidence of wildfires in Portugal.

The first version of the FRMs was distributed at the end of the 2014 summer season for three demonstration areas (Andalusia, Minho, and Sardinia). A second version was released at the end of the 2015 summer season only for the Italian test area. This last product showed no significant changes over the previous version, only a slight increase in the areas with a high hazard, thus confirming the stability and the reliability of the product.

The PBMs were computed on the same three PREFER demonstration areas (Andalusia, Minho, and Sardinia). In particular, until 31 March 2016 (182 days after 1 October 2015), the demonstration phase produced 1,413 maps (three per day), 471 maps for each area over 157 days, that is, 86% of the total demonstration period. Maps were missing mainly because of some unexpected failures during the initial phase, the unavailability of meteorological data, and, in a few cases, a failure of the local Internet connection at the University of Rome.

VALIDATION OF SEASONAL FIRE HAZARD MAPS

Regarding SFHMs, their validation was carried out on test sites in Portugal and Sardinia using the fire occurrences of 2014. That year, in Portugal only, the number of fires was sufficient to achieve statistically significant results. Nine SFHMs were computed during the fire season. Table 6 shows the results, indicating that more than half of the hot spots are in areas corresponding to a very high hazard. According to the cumulative total number of hot spots, 90% correspond to high or very high hazard values.

TABLE 6. THE HOT SPOT DISTRIBUTION FOR EACH UPDATED MAP ACCORDING TO THE FIRE HAZARD INDEX (MINHO REGION, PORTUGAL).

WEEK/HAZARD	VERY HIGH	HIGH	MEDIUM	LOW	VERY LOW
1	0	0	0	0	0
2	1	0	0	0	0
3	6	1	0	0	0
4	0	1	0	0	0
5	0	0	6	0	0
6	0	97	7	2	0
7	294	38	51	6	0
8	118	28	3	1	0
9	23	87	1	0	0
Total hot spots	57.33%	32.68%	8.82%	1.17%	0%
Cumulative total	57.33%	90.01%	98.83%	100%	

Then, the SFHM product was also computed during the summer of 2015. The computation was carried out every two weeks in parallel with the generation of the DFHI, which is one of the dynamic inputs for the SFHM. The SFHM covers the period from 24 June to 30 September 2015. The SFHMs were computed on the same three project test sites: Andalusia, Sardinia, and Minho, as shown in Figure 8.

Figure 9 shows the products generated in the Minho region during the summer of 2015. A mere visual analysis of the results allows one to observe the spatiotemporal dynamics of the SFHM values, which proved to be a useful source of information for assessing fire hazard. A brief demonstration of the potential utility of this product is reported in Figure 10. In fact, this figure shows how, during the 2015 fire season, the distribution of the areas defined as high or very high hazard changed with respect to the statistical map provided at the start of the season based on historical data (the map of 1 June 2015 in Figure 9). This information could be very useful for adjusting the distribution of human resources and equipment in the territory. It should be recalled that, of the 47 fire occurrences reported by EFFIS in 2015 (from 4 April to 9 September) for the Minho region, 17 (36%) occurred 8–9 August.

LONG-TERM STATISTICS DO NOT ALLOW THE CAPTURE OF THE YEARLY FLUCTUATION OF METEOROLOGICAL CONDITIONS AND HUMAN BEHAVIOR CHANGES.

Figure 10 shows how the number of pixels classified as high or very high hazard reduces from 47% (that is, 47% of the Minho region) of the SFHM produced at the start of the season to 5–15% at the end of the fire season. Using the fire hazard map produced on the basis of a statistical analysis of the fire distribution in the previous 10 years, as has generally done up to now in several countries, the agencies involved in fire prevention activity are obliged to monitor 47% of the region. The new index updates this map by taking into account the actual distribution of fire (based on human behavior) and the specific meteorological conditions of the current year (the averaged DFHI). Doing so allows, in the particular case of the Minho region shown in Figure 10, the reduction of the area defined as high or very high hazard. This means that the area needing to be patrolled or monitored can be significantly reduced, allowing for saving money, personnel, and equipment.

In the other two test sites (in Italy and Spain), the results are less evident. In particular, in Spain (Andalusia), the fire hazard maintains a low level (a few pixels) during the entire period, whereas, in Italy (Sardinia), it oscillates between 25 and 5% during the fire season. Since the demonstration phase mainly aims at proving the capability of the PREFER infrastructure to provide this information in a timely and proper manner, this phase is not described in this article, which is devoted to a technical description of the innovative information for wildfire prevention management developed in the framework of this project.

CONCLUSIONS

The SFHM, FRM, and PBM products were developed during extensive research activity started several years ago and brought to an end in the framework of the PREFER project. Some brief conclusions on the activity devoted to validating and demonstrating the PREFER products described previously are reported now.

CONCLUSIONS ON SEASONAL FIRE HAZARD MAPS

The SFHM product responds to the need to take into account the human factor in the development of an effective fire hazard map (in Mediterranean Europe, more than 93% of fires are due to human intervention). Fire hazard maps based on statistical analysis of the fire distribution in the previous 10 or more years are capable of capturing, on average, the areas where the incidence of these phenomena is higher. However, long-term statistics do not allow the capture of the yearly fluctuation of meteorological conditions and human behavior changes due to, for instance, enforcement actions. The new index developed in the framework of the PREFER project does allow this, by

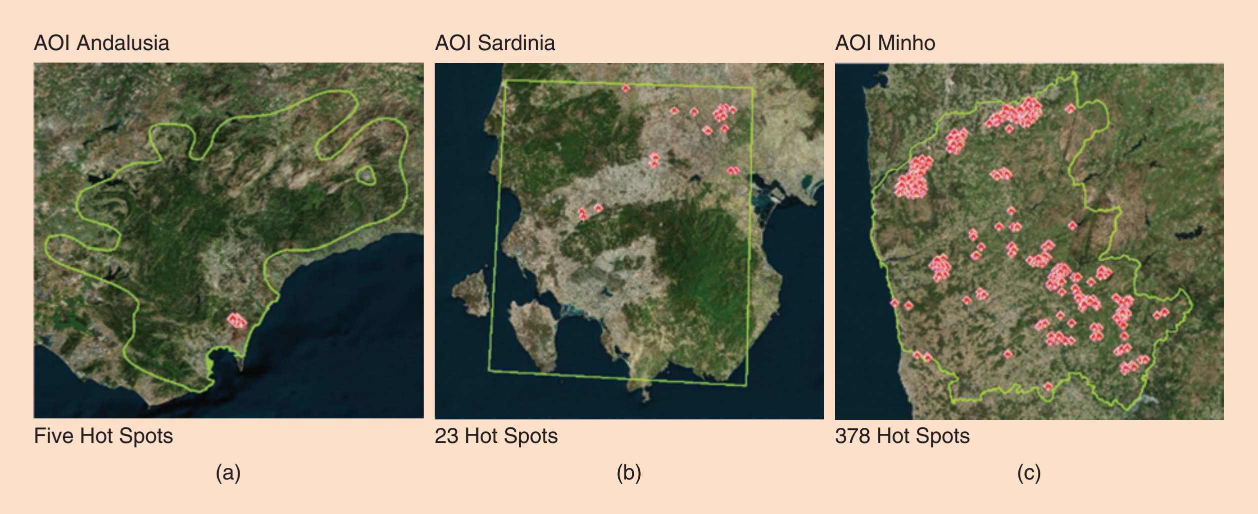

FIGURE 8. The geographic areas covered by the SFHM product overlaid by Fire Information for Resource Management System hot spots detected during the 2015 summer fire season: (a) Andalusia (Spain), (b) Sardinia (Italy), and (c) Minho (Portugal).

introducing short-term dynamics driven by actual fire occurrences (considering the fire events that occurred within a time span of two weeks) and the actual meteorological conditions (performing two-week averages of the daily weather situation). We can conclude the following from the demonstration activity:

- This innovative index exploits the recent increase in local authorities' speed in providing fire occurrence data and/or the high time frequency of hot spot information based on satellite images. In fact, such information can be used, together with meteorological data, to assess the actual characteristics of the present fire season with respect to previous ones from the point of view of human and climatic behavior.
- A brief demonstration of this is given in Figures 9 and 10. In fact, these figures show how, during the last fire season (2015), the distribution of the areas defined as high or very high hazard changes with respect to the static map provided at the start of the fire season based on historical data. This information could be very useful

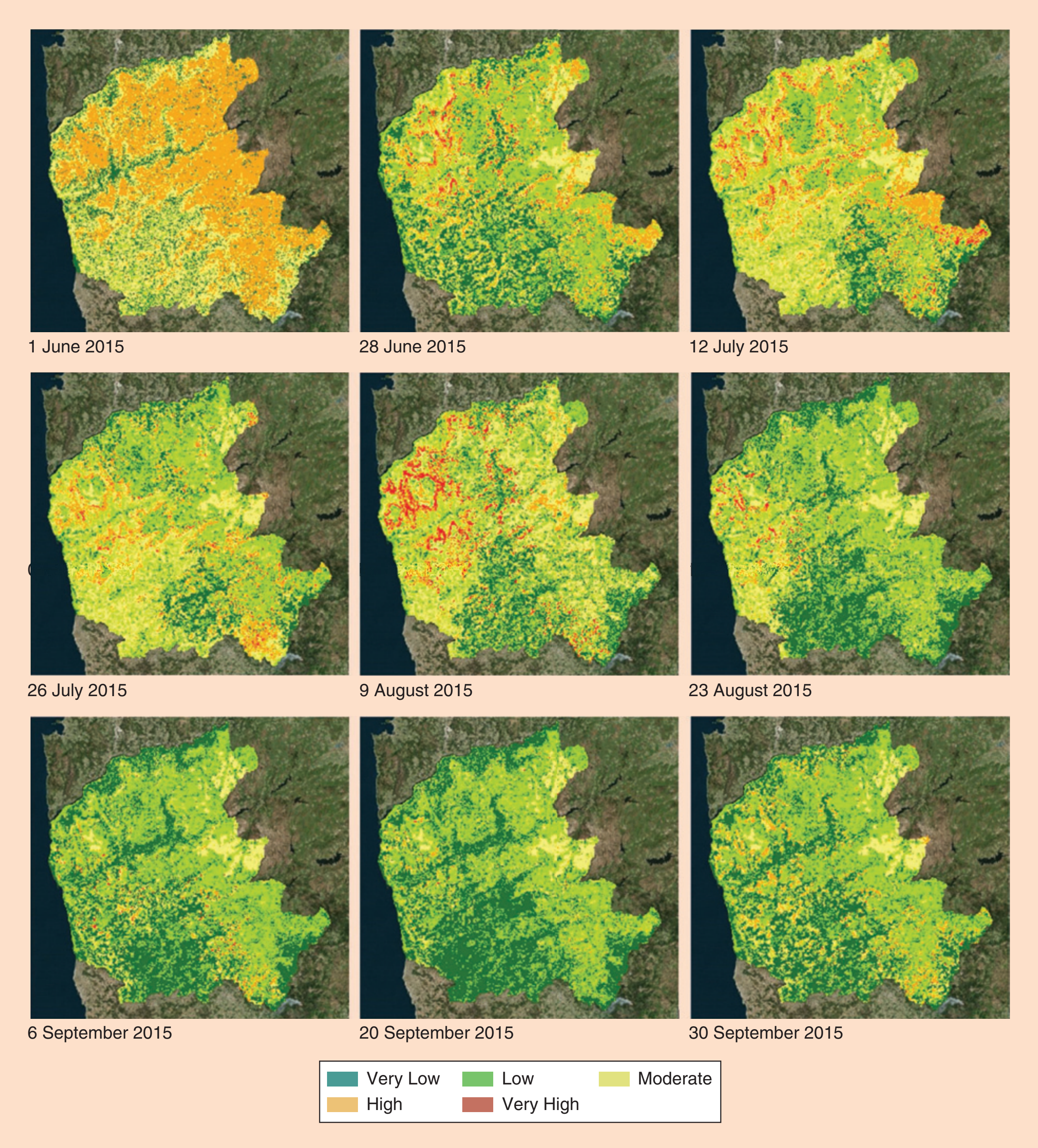

1 June 2015 | 28 June 2015 | 12 July 2015

26 July 2015 | 9 August 2015 | 23 August 2015

6 September 2015 | 20 September 2015 | 30 September 2015

FIGURE 9. A 2015 SFHM time series for the Minho (Portugal) AOI.

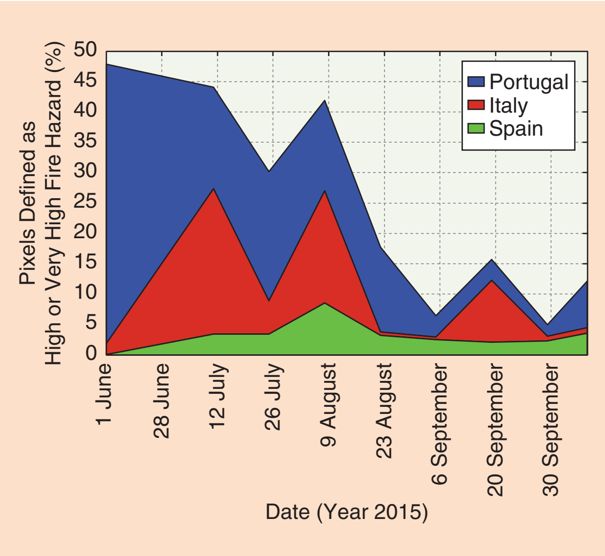

FIGURE 10. The variation of the area (percent of pixels) classified as high or very high fire hazard during the 2015 summer season in three of the PREFER test areas.

for adjusting the distribution of human resources and equipment in the territory.

CONCLUSIONS ON FUEL REDUCTION MAPS

Comparing the FRMs computed for the Italian AOI in Sardinia in 2015 and 2014, no remarkable changes were evident, except for a slight increase in the areas with a high hazard, thus confirming the stability and the reliability of the product.

The polygons of the prescribed burning performed in 2014 and 2015 in the Portuguese test area fit the GSH classes described by the FRM very well. In fact, over 97% of their surface falls into areas classified as having high or very high GSH values (Figure 7).

CONCLUSIONS ON PRESCRIBED BURNING MAPS

From the validation activities, we can conclude that the effectiveness of using prescribed burning to reduce fire incidence and large-fire risk was assessed starting from real fires and simulating the change in their behavior as different intensities of fuel reduction were applied (Table 5).

AUTHOR INFORMATION

Giovanni Laneve (giovanni.laneve@uniroma1.it) received his laurea degree in aeronautical engineering from the University of Naples, Italy, in 1985 and his laurea degree in aerospace engineering from Sapienza University of Rome, Italy, in 1988. From 1987 to 1991, he was a consultant at the San Marco Project Research Center, where he was involved in the San Marco 5 satellite mission control and data analysis. Since 1991, he has been an assistant professor with the Aerospace Engineering School of Sapienza University of Rome. He has produced more than 150 scientific papers. His past research activities targeted aeronomy, satellite thermal control, and mission design. Currently, his main research interests are in the areas of new algorithms for the exploitation of satellite images, satellite remote sensing applications for fire management, applications of satellite data for the African regions, and studies on environmental and disaster monitoring. He is a Member of the IEEE.

Lorenzo Fusilli (lorenzo.fusilli@uniroma1.it) graduated in geological sciences from Sapienza University of Rome, Italy. He has been involved in several sectors of multihyperspectral airborne and satellite remote sensing, especially in data preprocessing (calibration, geometric, and atmospheric correction), land cover and vegetation mapping of natural environments and inland water bodies, change detection, and time-series analysis of multisensor imagery. He has acquired experience in the spectral response of natural surfaces, classification procedures, algorithm performance assessment, satellite image processing to derive environmental parameters, and geographic information system applications. He participated in several calibration/validation campaigns conducted by the Instituto di Metodologie per l'Analisi Ambientale in the framework of national and international projects.

Guido Bernini (guido.bernini@uniroma1.it) received his B.S. degree in aerospace engineering in 2008 and his M.S. degree in astronautics engineering in 2012 from Sapienza University of Rome, Italy, where he is presently a Ph.D. student. His research field is remote sensing and the development of applications using multispectral satellite data. From 2011 to 2013, he was involved in the European Volcano Observatory Space Services project. From 2013 to 2014, he worked at the Institute of Methodologies for Environmental Analysis of the National Research Council of Italy on the Ionian Sea Water Quality Monitoring by Satellite Data research project. Since 2015, he has worked on the Space-Based Information Support for Prevention and Recovery of Forest Fire Emergency in the Mediterranean Area project, validating indices of severity damage (obtained from *Landsat* images) after forest fire events.

Juan Suárez Beltran (jusuarez@gmv.com) received his B.Sc. degree in geography from the Autonomous University of Madrid, Spain, in 1997. He has more than 18 years of experience in applied remote sensing, geoinformatics, and digital mapping. He has a strong background in satellite imagery procurement, preprocessing, analysis, and land features extraction and much experience in the development of Earth observation applications. Before joining GMV, he worked as a remote-sensing and geographic information system consultant at different geospatial consultancy companies. Early in his career, he worked as a research assistant at the Fire Ecology and Global Change Group, University of Castilla La Mancha, Spain. With the European Commission–Framework Project 5 Land Use Change Interactions With Fire in Mediterranean Landscapes project, his main duties entailed satellite-based fuel mapping, burned areas detection and time-series analysis, fire behavior modeling, implementation of meteorology- and satellite-based forest fire hazard indices, and investigation of fire impacts on ecosystems.

REFERENCES

[1] "Forest fires in Europe, Middle East and North Africa 2012," European Commission, Joint Research Centre, Ispra, Italy, Rep. EUR 26048 EN, 2013. [Online]. Available: https://effis.jrc.ec.europa.eu/media/cms_page_media/40/FireReport2012_Final_2pdf_2_qyaUkXu.pdf

[2] F. Moreira et al., "Landscape–wildfire interactions in southern Europe: Implications for landscape management," *J. Environ. Manag.*, vol. 92, no. 10, pp. 2389–2402, 2011.

[3] J. San-Miguel-Ayanz et al., "Comprehensive monitoring of wildfires in Europe: The European Forest Fire Information System (EFFIS)," in *Approaches to Managing Disaster: Assessing Hazards, Emergencies, and Disaster Impacts*, J. Tiefenbacher, Ed. London: InTech, 2012, pp. 87–105.

[4] G. Laneve et al., "PREFER FP7 project for the management of the pre- and post-fire phases: Presentation of the products," in Advances in Forest Fire Research, D. X. Viegas, Ed. Coimbra, Portugal: University of Coimbra, 2014. doi: 10.14195/978-989-26-0884-6.

[5] European Forest Fire Information System, "Annual fire reports," 2018. [Online]. Available: http://effis.jrc.ec.europa.eu/reports-and-publications/annual-fire-reports/

[6] G. Bovio and D. Ascoli, "Fuoco prescritto: Stato dell'arte della normativa italiana," *L'Italia Forestale e Montana*, vol. 67, no. 4, pp. 347–358, 2012.

[7] C. Montiel, "Fire use practices and regulation in Europe: Towards a fire frame work directive," in *Proc. 5th Int. Wildland Fire Conf.*, Sun City, South Africa, 2011.

[8] J. K. Agee and C. N. Skinner, "Basic principles of forest fuel reduction treatments," *Forest Ecology Manag.*, vol. 211, no. 1–2, pp. 83–96, 2005.

[9] P. M. Fernandes and H. S. Botelho, "A review of prescribed burning effectiveness in fire hazard reduction," *Int. J. Wildland Fire*, vol. 12, no. 2, pp. 117–128, 2003.

[10] M. Finney, "Design of regular landscape fuel treatment patterns for modifying fire growth and behavior," *Forest Sci.*, vol. 47, no. 2, pp. 219–228, 2001.

[11] E. Schelhaas, M. Cientiala, M. Lindner, G. J. Nabuurs, and J. Meyer, "Survey of technical and management-based mitigation measures in forestry," Impact of Environmental Agreements on the Common Agricultural Policy (MEACAP) Project Report, Sixth Framework Programme, Brussels, Belgium, Doc. Number MEACAP WP4 D13, 2006.

[12] G. Xanthopoulos, D. Caballero, M. Galante, D. Alexandrian, E. Rigolot, and R. Marzano, "Forest fuels management in Europe," U.S. Dept. Agriculture Forest Service, Washington, D.C., Proc. RMRS-P-41, 2006.

[13] "Towards integrated fire management—Outcomes of the European Project Fire Paradox," European Forest Institute Research, Joensuu, Finland, Rep. 23, 2010. [Online]. Available: https://www.ucm.es/data/cont/docs/530-2013-10-15-efi_rr23.pdf

[14] S. L. Stephens et al., "The effects of forest fuel-reduction treatments in the United States," *Bioscience*, vol. 62, no. 6, pp. 549–560, 2012.

[15] P. Fernandes and C. Loureiro, "Handbook to plan and use prescribed burning in Europe," Fire Paradox project, 2010. [Online]. Available: http://www.fireparadox.org/handbook_prescribed_burning_europe.php

[16] F. Tedim, G. Xanthopoulos, and V. Leone, "Forest fires in Europe: Facts and challenges," in *Wildfire Hazards, Risks, and Disasters*, 1st ed. Amsterdam, The Netherlands: Elsevier, 2014, pp. 77–99.

[17] E. Chuvieco, D. Riaño, J. W. Van Wagtendonk, and F. Morsdof, "Fuel loads and fuel type mapping," in *Wildland Fire Danger Estimation and Mapping: The Role of Remote Sensing Data*, E. Chuvieco, Ed. Singapore: World Scientific Publishing, 2003, pp. 119–142.

[18] G. Amatulli and A. Camia, "Exploring the relationships of fire occurrence variables by means of CART and MARS models," in *Proc. 4th Int. Wildfire Conf.*, Seville, Spain, 2007. [Online]. Available: http://citeseerx.ist.psu.edu/viewdoc/download?doi=10.1.1.571.8720&rep=rep1&type=pdf

[19] G. Laneve, L. Fusilli, P. Marzialetti, R. De Bonis, G. Bernini, and L. Tampellini, "Development and validation of fire damage-severity indices in the framework of the PREFER project," *IEEE J. Sel. Topics Appl. Earth Observ. in Remote Sens.*, vol. 9, no. 6, pp. 2806–2817, 2016.

[20] G. Laneve et al., "SIGRI Project: Products validation results," *J. Sel. Topics Appl. Earth Observ. in Remote Sens.*, vol. 7, no. 3, pp. 895–905, 2014.

[21] G. Laneve, M. Jahjah, F. Ferrucci, and F. Battazza, "SIGRI Project: The development of the fire vulnerability index," in *Proc. 34th Int. Symp. Remote Sensing Environment*, Sydney, Australia, 2011. [Online]. Available: http://www.isprs.org/proceedings/2011/ISRSE-34/

[22] G. Laneve, G. Bernini, L. Fusilli, P. Marzialetti, and B. Hirn, "Satellite-based products for supporting forest fires prevention and recovery in Europe," in *Proc. IEEE 16th Int. Conf. Environment and Electrical Engineering (EEEIC)*, 2016. doi: 10.1109/EEEIC.2016.7555460.

[23] G. Laneve, L. Fusilli, and G. Bernini. "Achievements of the PREFER project in the prevention phase of the forest fire management," in *Proc. IEEE Int. Geoscience and Remote Sensing Symp. (IGARSS)*, 2016, pp. 5765–5768.

[24] L. Giglio, W. Schroeder, and C. O. Justice, "The collection 6 MODIS active fire detection algorithm and fire products," *Remote Sens. Environ.*, vol. 178, pp. 31–41, June 2016.

[25] V. Di Biase and G. Laneve, "Geostationary sensor based forest fire detection and monitoring: An improved version of the SFIDE algorithm," *Remote Sens.*, vol. 10, no. 5, 2018. doi: 10.20944/preprints201801.0007.v1.

[26] M. A. Finney, "FARSITE: Fire area simulator—Model development and evaluation," U.S. Dept. Agriculture, Forest Service, Rocky Mountain Research Station, Ogden, UT, Res. Paper RMRS-RP-4 Revised, 2004.

GRS

Target Classification and Recognition for High-Resolution Remote Sensing Images

Using the parallel cross-model neural cognitive computing algorithm

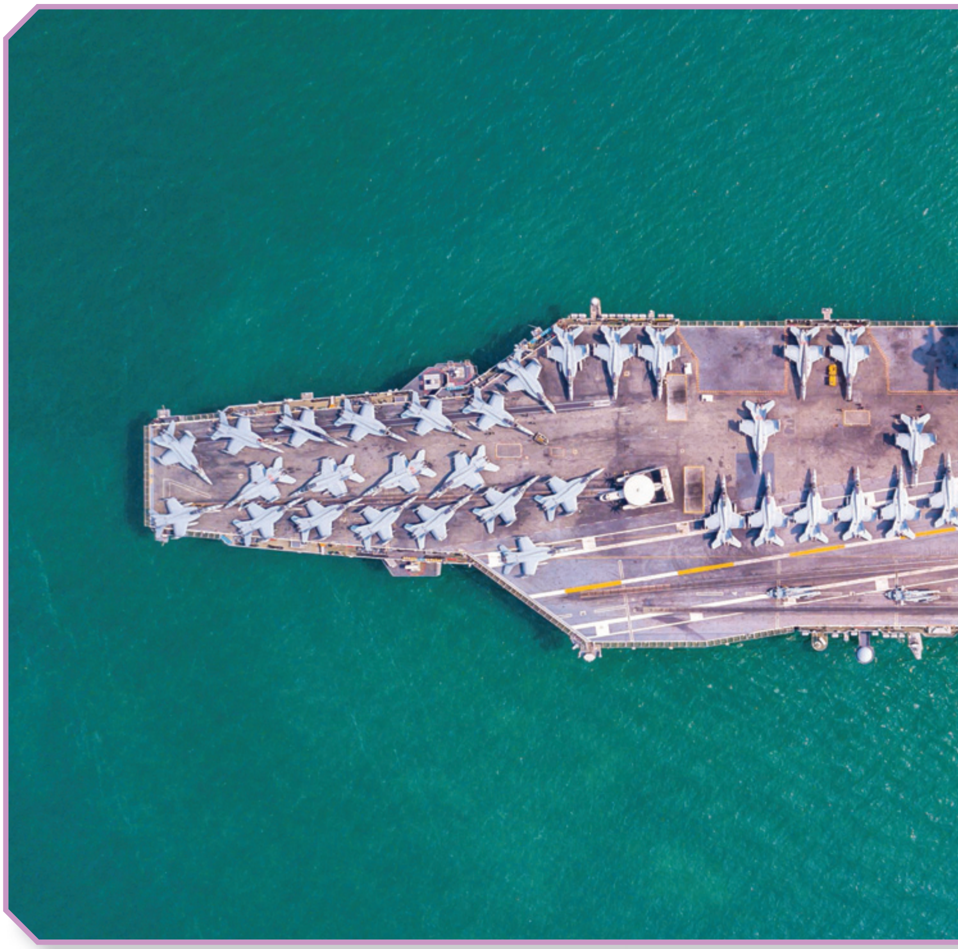

YANG LIU, YI XIE, WEI YANG, XIANYU ZUO, QIANG GE, AND BING ZHOU

Target classification and recognition (TCR) are important information-extraction techniques for high-resolution remote sensing images (HRIs). However, because methods with high accuracy usually have higher time complexity, the massive remote sensing image has brought great difficulties for real-time application. In this article, we propose a hybrid, heterogeneous parallel processing algorithm to improve the efficiency TCR based on the Cross-model Neural Cognitive Computing (CNCC) algorithm [parallel TCR based on MapReduce of hierarchical CNCC (PTCR-C)]. Parallel programming technologies used in this article include Open Multiprocessing (OpenMP), Compute Unified Device Architecture (CUDA), and the message passing interface (MPI). Experiments on public remote sensing image data sets show that the PTCR-C algorithm can effectively improve the efficiency of the original TCR algorithm. The PTCR-C algorithm has better augmented ability and provides the reference for further real-time TCR of remote sensing applications.

REDUCING TIME WITHOUT SACRIFICING ACCURACY

With the development of remote sensing technology, more HRIs are becoming available. HRIs have high spatial resolution, high spectral resolution, and high temporal resolution. However, information extraction algorithms from HRIs usually have high complexity [1].

Generally, target recognition of an HRI includes three target levels: category classification, type recognition, and model identification. These levels are determined by the

Digital Object Identifier 10.1109/MGRS.2019.2949353
Date of current version: 24 February 2020

resolution of the images, and the algorithms for each are essentially the same. Here, we do not distinguish among the three levels, which are collectively referred to as *TCR*. Meanwhile, more remote sensing applications use real-time TCR algorithms [2], [3].

The performance of the TCR algorithm must be improved, especially for HRI processing. High-performance parallel computing is a very effective tool for meeting the real-time requirements of TCR applications. The TCR algorithm of HRI is also very suitable for use with the data parallel method. TCR algorithms based on the CNCC framework deliver highly precise HRIs. The CNCC framework is a hierarchical multimedia neural cognitive computing model [4]. However, it also is highly complex and has high parallelism [5]. This article mainly focuses on how to improve the time efficiency of the CNCC-based TCR algorithm without sacrificing accuracy.


©SHUTTERSTOCK.COM/APIGUIDE

RELATED WORK

Parallel algorithms are grouped into three kinds of models, depending on structure: the data parallel model, message passing model, and shared variable model. From the perspective of algorithm design, parallel computing is often divided into data parallelism and task parallelism. In data parallelism, data are split into blocks and distributed to parallel computing nodes. The complex and time-consuming task is decomposed into a number of identical subtasks. In task parallelism, tasks are divided into some subtasks, which are assigned to parallel computing nodes for processing. Generally, the design of parallel algorithms includes four steps: partitioning, communication, agglomeration, and mapping.

Currently, many researchers studying HRIs focus on preprocessing algorithms. Yang et al. [6] presented a parallel computing paradigm based on multicore, parallel computing, pan-sharpening algorithms. Parallel processing is implemented on a workstation with two central processing units (CPUs) which can perform these processes up to 13.9 times faster than is possible with serial execution.

As for the problem of long training time for the convolutional neural network (CNN) on the Moving and Stationary Target Acquisition and Recognition (MSTAR) data set, Li et al. [7] proposed a fast method for the CNN using synthetic aperture radar (SAR) automatic target recognition. Tu et al. [8] proposed fast and accurate methods for target detection based on a multiscale saliency and active contour model, which can detect the small-scale target in HR SAR imagery. Meanwhile, Williams [9] proposed a fast, unsupervised algorithm for the detection of underwater targets in synthetic aperture sonar imagery. In recent years, object-based segmentation methods have been widely integrated for remote sensing image segmentation. Pan et al. proposed an object-based and heterogeneous segment filter CNN for HRI classification [10].

WITH THE DEVELOPMENT OF REMOTE SENSING TECHNOLOGY, MORE HRIS ARE BECOMING AVAILABLE.

TCR is an important intelligent technology in research on HRI information extraction. Some researchers have applied artificial intelligent algorithms to TCR. Guo et al. [11] found that deep learning is actually everywhere in remote sensing big data analysis, which can learn representative and discriminative hierarchical features from HRIs. Dong et al. [12] proposed target recognition in SAR images using unsupervised feature learning from an autoencoder and its variants based on NN architecture. Mou et al. [13] proposed an end-to-end, fully convolutional–deconvolutional network for unsupervised spectral–spatial feature learning of hyperspectral images. This network accommodates training in an end-to-end manner. Maggiori et al. [14] proposed an end-to-end framework for the dense, pixelwise classification of satellite imagery by CNNs. However, due to the complexity of the algorithm and the abundance of remote sensing data, high-performance algorithms must be used to intelligently extract remote sensing information to improve the speed of the algorithm.

Furthermore, spiking NNs and faster region-based CNNs are also used for HRI target [15] and change detection [16], respectively, and can achieve higher accuracy.

In general, HRI parallel processing can employ three modes: 1) MPI for multimachine parallel systems, 2) OpenMP for multicore parallel systems, and 3) CUDA for graphics processing unit (GPU) parallel systems. Guo et al. [17] proposed parallel computation of aerial target reflection of background infrared radiation, based on OpenMP, OpenACC, and CUDA, that can run on a multicore CPU or a many-core GPU platform. Some scholars have applied GPU technology to realize TCR for HRIs. Timchenko et al. [18] presented a method of parallel-hierarchical transformations for rapid recognition of dynamic images using GPU technology. Lokman et al. [19] proposed a CUDA-based platform method that can perform anomaly detection and target recognition gradually with hyperspectral images. Zhao et al. [20] proposed a fast framework of automatic recognition based on the visual attention model and bag of features for an airport target of a low-resolution remote sensing image in a complicated environment. A gradient-boosting random CNN for scene classification of remote sensing images was proposed by Zhang et al. [11]. This technique can effectively combine many deep NNs. In addition, fast field-programmable gate arrays are employed to implement computation of the pixel purity index of hyperspectral images [21]. In the future, high-performance parallel computing will become essential for remote sensing applications [22], [23].

THE PERFORMANCE OF THE TCR ALGORITHM MUST BE IMPROVED, ESPECIALLY FOR HRI PROCESSING.

The design of the software structure for HRI processing should be carefully considered. Wang et al. [24] introduced an architecture of parallel HRI processing software that includes MPI, the Geospatial Data Abstraction Library, and OpenCV. Due to the matrix structure of the image, high-resolution remote sensing imaging easily accommodates the use of Hadoop MapReduce technology for parallel processing. Recently, Hadoop was applied to the parallel analysis of HR remote sensing imaging [25]. It can effectively speed up for remote sensing applications. A proposed storage and processing scheme for HR remote sensing imaging based on Hadoop can be found in the literature [25], [26]. A parallel supervised land-cover classification system for hyperspectral and multispectral images was proposed by Garcia-Salgado et al. [27]. This system is highly accurate for classifying land and requires little image-processing time.

The size and number of remote sensing images are constantly increasing as resolutions of remote sensing images rise. As memory consumption increases, the performance of the multicore parallel processing algorithm falls. Communication among multimachines, multicores, GPUs, and CPUs is rather difficult. Data exchange and communications are classic issues that have been studied for a long time. Some researchers have proposed excellent solutions for exchanging data in parallel and distributed systems [28], [29]. However, data exchange and communication seriously affects the speedup and efficiency of parallel algorithms for HR remote sensing imaging. Therefore, it is important to determine how to split tasks and allocations in parallel TCR algorithms.

PARALLEL ANALYSIS OF CNCC-BASED TCR MODEL

In [5], we proposed a CNCC-based TCR algorithm. This algorithm has high TCR accuracy for HRIs, but it runs very slowly. We show here how the efficiency of the CNCC-based TCR algorithm for category classification, type recognition, and model identification can be improved. The CNCC-based TCR algorithm includes three major parts:

1) *Neural computing (NC) driven by bottom-up data*: This is a large matrix operation process of NC.
2) *Cognitive computing driven by top-down events*: This is a multitask process of cognitive computing.
3) *Reinforcement learning and model ensemble driven by goals*: This is the information-integration process of global computing.

The algorithm extracts the temporal–spatial sensation features using a deep-spiking convolutional neural network (DSCN) and extracts the temporal–spatial perception features using hierarchical latent Dirichlet allocation (HLDA). As showed in Figure 1, mapping DSCN and HLDA learning is the most time-consuming process. Both HLDA and DSCN need many iterations. Bottlenecks in the algorithm stem from such processes as back propagation (BP), DSCN conversion in DSCN training, and Gibbs sampling in HLDA training.

The heterogeneous parallel based on the GPU can be used to increase computing speed for large-scale matrix operation of NC. Multicore parallel techniques can be used to speed up the calculation for multitask processes of cognitive computing. For the information integration process of global computing, multimachine data parallel techniques can be used to speed up the calculation.

In the training of the DSCN, many components be processed in parallel, including neuron node activation, weight updating of the node, feature map computing, and message propagation. Both HLDA and DSCN have model parallelism. In addition, there is data parallelism in DSCN training and in the HLDA approximate algorithm of HLDA. We can use the GPU to accelerate BP for the convolution, subsampling, and Gibbs sampling of forward propagation in the DSCN.

Here, we use parallel computing to accelerate the process of temporal–spatial sensing and perception features, such as the parallel BP algorithm of the GPU-based DSCN, the parallel Gibbs sampling algorithm of OpenMP-based HLDA, and the parallel TCR algorithm of the hierarchical CNCC model based on MapReduce.

CNCC-BASED TCR ALGORITHM FOR HETEROGENEOUS PARALLEL PROCESSING

High-performance parallel computing is an important tool for improving the performance of HRI information extraction. Data parallel modeling and image segmentation are effective methods to realize the classification and recognition of HRIs. Image partitioning has only a small impact on classification and recognition for small-scale targets. In the worst case, a target may be split into four subblock images. Image partitioning can efficiently reduce false-detection rates and missed detection rates using a reasonable subblock image size and blocking overlapping for larger targets. For complex HRI processing algorithms, the task parallelism of the algorithm can be further considered.

The MPI+OpenMP+CUDA hybrid programming model [30] is a new hybrid multimachine, multicore, multithread, and multi-GPU parallel architecture. It offers the

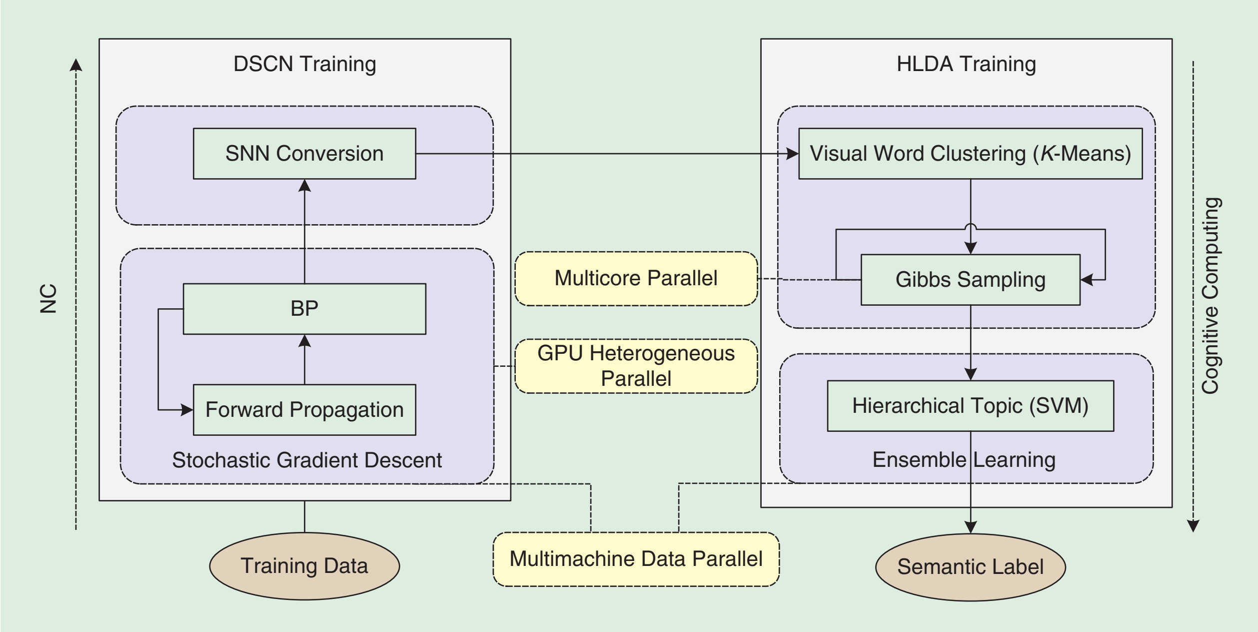

FIGURE 1. A diagram showing a parallel analysis of the hierarchical CNCC-based TCR model training. SNN: spiking NN; SVM: support vector machine.

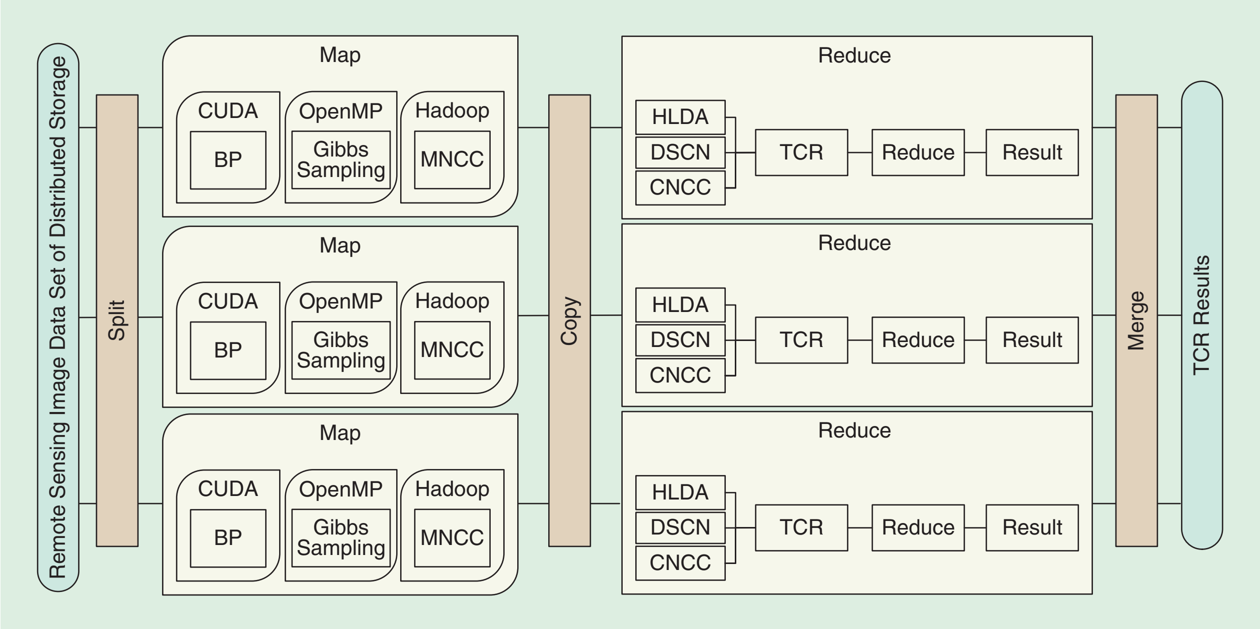

FIGURE 2. The parallel TCR architecture of the HRI based on hybrid heterogeneous implementation. MNCC: multimedia neural cognitive computing.

advantages of high performance at low cost and low consumption of energy. It has become the mainstream technology of new high-performance computing platforms. According to parallel analysis of the CNCC-based TCR algorithm, Figure 2 shows the parallel TCR of HR remote sensing imaging based on hybrid heterogeneous implementation. We use MPI+OpenMP+CUDA to design the parallel architecture. The algorithm is improved by the parallel method from three aspects, as follows:

1) The training data are split and stored in a distributed environment. The CNCC framework is trained using the MapReduce method in a multimachine parallel schema.
2) The DSCN model algorithm is improved through the use of a GPU and multicore to speed training in the computing node.
3) The hierarchical topic parameters are distributed into multiple machines, and, within each machine, Gibbs sampling is paralleled using OpenMP.

THE SIZE AND NUMBER OF REMOTE SENSING IMAGES ARE CONSTANTLY INCREASING AS RESOLUTIONS OF REMOTE SENSING IMAGES RISE.

PARALLEL BP ALGORITHM OF GPU-BASED DSCN

Over the past few years, the field of GPU-based high-performance computing in radiotherapy has experienced rapid developments. A new research area, general-purpose GPU (GPGPU) [31], [32], has emerged in large-scale parallel computing. With this technology, multiple single instructions on multiple threads are composed of multiple stream processors in the GPU. GPGPU programming generally considers the data as an image. It packages data into a "texture," and computing tasks are mapped to a texture-rendering process [33].

For the stochastic gradient descent algorithm of large-scale deep NNs, the model can be copied and distributed on multiple servers. Both models and data are processed by a parameter's server [34]. It has a very good performance on the nonconvex optimization problem with the self-adaptive learning rate Adagrad [35] and momentum [36]. We split the parallel part of the DSCN model and improve the training speed of convolution by using a GPU. The pseudocode for this variant is presented in Algorithm 1.

PARALLEL GIBBS SAMPLING ALGORITHM OF OPENMP-BASED HLDA

According to the basic architecture of parallel computing, some technologies are used to improve computing efficiency

ALGORITHM 1. DPB-G PSEUDOCODE.

```
Input: Training data {M,Y}
Output: DSCN parameters
split data {M,Y} to k parts (k is the number of GPUs) and distribute {$M_k$,$Y_k$} to k GPUs, respectively
Initial spiking neural network$_0$ and the parameters are distributed to k GPUs.
Repeat
    Parfor parallel Do on GPU
        // Forward propagation of GPU message
        Select sample {$M_k$,$Y_k$}, according to the leaky integrate and fire neuron model, generate the spike image $S_k$, and convert to the GPU matrix as network input: $S_g$ = gpuArray($S_k$)
        For each layer of the network Do
            In the convolution layer, each $W \times H$ patch is transformed with 1D row vector to input $S_{g,l-1}$. The matrix [$W \times H$, $K \times K \times D$] is composed by row vector. The D convolution kernel of $K \times K$ dimensions transforms 1D column vector, and matrix [$M$, $K \times K \times D$] is composed by column vector. The convolution of the 3D matrix is replaced by GPU multiplication of the 2D matrix, then feature maps $outMap_{g,l}$ are generated.
            In the pooling layer, each feature map $outMap_{g,l}$ is downsampled to compute $S_{g,l+1}$ by GPU matrix.
        End For
        The output $O_g$ is computed, minimum-variance $\delta$ is computed by $O_g$ minus real values $Y_k$.
        Weights are calculated layer by layer in the GPU and converted to conventional matrix $\Delta W_{k,l}$ = gather($\Delta W_{g,l}$), sent $\Delta W_{k,l}$ to main process.
    End Parfor
    // DSCN model synchronization: backpropagation (BP) residual and updating the global DSCN model
    According to the minimizing the residual, weights matrix are adjusted by BP method.
    Updating weights: $W_l \leftarrow \mathrm{W}_{k,l} + \eta \sum_k (\Delta W_{k,l})/K$, and new iterative model $DSCN_p$ is generated.
    Distribute weight $W_l$ and new model $DSCN_p$
Until error meets demand
Return DSCN model and parameters
```

in the single-machine environment, such as multicore computing based on OpenMP [17] and heterogeneous computing based on GPU [18]. The multimachine message passing mechanism is often considered for distributed clusters, such as MPI [30] and others. Meanwhile, the OpenMP, the most popular standard for homogeneous computing, is unsuitable for nonshared memory systems in the multimachine cluster. In the multithread environment, the MPI is needed to solve synchronization and mutex among the processes.

Gibbs sampling, a Markov-chain Monte Carlo method to perform inference, is a CPU computing-intensive algorithm [37]. The Gibbs sampling algorithm for HLDA can be accelerated by OpenMP. In Gibbs sampling of HLDA training, the training samples, doc-topic matrix, and word-topic matrix are stored in shared memory. The performance of the sampling algorithm is improved by multicore technology based on static load balancing. The pseudocode for this variant is presented in Algorithm 2.

PARALLEL TCR ALGORITHM OF THE HIERARCHICAL CNCC MODEL BASED ON MAPREDUCE

At present, heterogeneous platforms have many computing platforms, such as MPI, OpenMP, Open Computing Language (OpenCL), Hadoop, and Spark. Generally, Hadoop is a distributed system framework, which is suitable for offline and large-scale data batch processing. Spark is a kind of computing framework based on memory and iteration. In addition, MATLAB has multiprocess processing ability based on MPI, GPU, Parfor, and MapReduce technology. It has a parallel computing tool box and can easily verify the parallel algorithm.

As a fast-growing parallel programming model, MapReduce has a well-defined interface and runtime library. It hides low-level details and reduces the difficulty of parallel programming. MapReduce can easily realize automatic large-scale parallel computing tasks. MapReduce provides a good solution for HRI parallel processing [38], [39]. HR remote sensing imaging is a big data consumer not only in terms of storage volume. Key problems of HRI parallel research are data storage, parallel processing, and system management. Hadoop-distributed file systems store very large files by stream data access mode [40]. Hadoop provides solutions for distributed storage of HRIs, because it has high throughput and strong fault tolerance.

HIGH-PERFORMANCE PARALLEL COMPUTING IS AN IMPORTANT TOOL FOR IMPROVING THE PERFORMANCE OF HRI INFORMATION EXTRACTION.

The Hadoop platform was employed to improve the TCR algorithm of the hierarchical CNCC framework by MapReduce. First, the parallel part of the hierarchical CNCC framework and training sample was split for a distributed computing environment. Second, each datum and model was distributed to multiple nodes by a mapping process based on dynamic load balance. The local model was trained using the local multicore heterogeneous computing environment in each node. Finally, the results were combined by key-value pairs

ALGORITHM 2. HLDA PARALLEL GIBBS SAMPLE BASED ON OPENMP (HPGS-O) PSEUDOCODE.

```
Input: Training image $M$ and the visual word clustering center $A$ of the sensation features of the training image $M$
Output: HLDA parameters
    //Data and HLDA model parameter's distribution
    The visual word $A$ is divided into $p$ parts $A_p$ according to the layer of the DSCN
    $A_p$, topic-image matrix $N_{kjp}$, visual word-topic matrix $N_{wkp}$, $\alpha_{kp}$, and initial parameter $\beta$, $\gamma$ and $\eta$ of HLDA model are distributed
    to $p$ process.
    Repeat
        #pragma omp parallel for each subprocess $p$
            Sampling local topic $Z_p$: iterate local DPB-Gibbs ($A_p$, $Z_p$, $N_{kjp}$, $N_{wkp}$, $\alpha_{kp}$, $\beta$, $\gamma$, $\eta$)
            Send $N_{wkp}$ and $\alpha_{kp}$ to main process
        endfor
        // HLDA model synchronization: merging global topic, updating global statistics matrix
        Update: $N_{wk} \longleftarrow N_{wk} + \Sigma p(N_{wkp} - N_{wk})$
        Update: $\alpha_k \longleftarrow (\Sigma_p \alpha_{kp})/P$
        Sampling: $\alpha_k$, $\gamma$, $\eta$
        Distribute: $N_{wk}$, $a_k$, $\gamma$, $\eta$
    Until meet iteration conditions
Return HLDA model and parameters.
```

with the reducer process. In this way, the fast iterative training of the hierarchical CNCC framework is realized. Mainly pseudocode steps of this phase are outlined in Algorithm 3.

PARALLEL TCR EXPERIMENT AND ANALYSIS

EXPERIMENTAL ENVIRONMENT AND PARAMETERS

The Sugon high-performance cluster system was employed for a parallel experiment. Table 1 describes the software and hardware environment of the experiment. The main parameters of the NN include network depth (number of hidden layers), network width (number of hidden layer neurons), network topology structure, and activation function of neurons. The training emphasis of the NN is the adjustment of weight. For general NNs, the model structure is as follows: input layer × hidden layer × output layer, where the number of nodes in the input layer is equal to the feature dimension of input data, and the number of nodes in the output layer is equal to the number of classification categories. Given training samples and semantic labels, the number of nodes in the input and output layers has been determined, so the key point of the structural design of the NN is to determine the number of layers and nodes in hidden layers. However, the structural design of the DSCN lacks theoretical support at present and is mostly based on experience.

For the design of network depth, it is generally considered that the depth of network is related to the level of feature abstraction. The more hidden layers designed for the network, the stronger the fitting, the lower the model error, and the higher the accuracy. However, too many hidden layers easily complicate the network and make it difficult to train.

For the design of network width, it is generally considered that the network width is related to the number of features in each layer. The larger the number of hidden layer nodes, the stronger the fitting ability of the network, but this easily leads to poor generalization ability of the model; the smaller the number of hidden layer nodes, the worse

ALGORITHM 3. PARALLEL TCR BASED ON MAPREDUCE OF HIERARCHICAL CNCC (PTCR-C) PSEUDOCODE

```
Input: Media {$M$, $Y$}
Output: CNCC model and parameters
Initialize $CNCC_0$ model and parameters
Split process: training data $M$ is divided into $n$ parts {$M_n$, $Y_n$}.
Initialization $CNCC_0$, parameters, and training data {$M_n$, $Y_n$} are distributed to $n$ nodes in the cluster.
While ($Epochs<MaxNum$ || $er < \varepsilon$)
    Repeat parallel Do in $n$ nodes
        //DSCN mapper process:
        In the computing node, call Algorithm 1 DSCN parallel BP based on GPU: local {$M_n$, $Y_n$}$\longrightarrow$local DSCN parameters $DSCN_n$
        The key-value pairs <$Key_{s,n}$, $Val_{s,n}$> are generated by $DSCN_n$ ,weight $W_n$, and so on.
    Until meet DSCN iteration conditions
    // DSCN reducer process
    Receive key-value pairs <$Key_{s,n}$, $Val_{s,n}$> of $DSCN_n$
    Iterative and update global network weights $W \longleftarrow W_n + \eta\sum n(\Delta W_n)/K$, update global DSCN
    Distribute new network weight $W$ and iterative model $DSCN_s$
    Call K-means algorithm, then visual word clustering center is parallel computed: $DSCN_n \longrightarrow$local visual word $A_n$
    The topic-image matrix $N_{kjn}$, visual word-topic matrix $N_{wkn}$, $\alpha_{kn}$, and initial parameter $\beta$, $\gamma$ and $\eta$ of HLDA model are distributed to $n$ process.
    Repeat parallel Do in $n$ process
        // HLDP mapper process
        On computing node, call Algorithm 2 HPGS-O: $A_n \longrightarrow$local $N_{wkn}$, topic of visual word $Z_n$, $\alpha_{kn}$, $\gamma$, $\eta$
        The key-value pairs <$Key_{h,n}$, $Val_{h,n}$> are generated $HLDA_n$ model $N_{wkn}$, topic of visual word $Z_n$, $\alpha_{kn}$, $\gamma$, $\eta$, and so on
        // HLDP reducer process: HLDA model synchronization, merging global topics, and updating global statistics matrix
        Receive $HLDA_n$ key-value pairs <$Key_{h,n}$, $Val_{h,n}$>
        Update: $N_{wk} \longleftarrow N_{wk} + n(N_{wkn} - N_{wk})$
        Update: $\alpha_k \longleftarrow (\sum_n \alpha_{kn})/N$
        Sampling: $\alpha_k$, $\gamma$, $\eta$
        Distribute: $N_{wk}$, $\alpha_k$, $\gamma$, $\eta$
    Until meet HLDA iteration conditions
    Call parallel training algorithm of SVM:topic of visual words $Z_n \longrightarrow SVM_n$
End While
Return CNCC model (DSCN, HLDA, SVM) based on DSCN_HTM integration.
```

the ability to obtain information, which cannot reflect the rules of data sets.

Considering the types of classification and recognition, the size of data set images, the number of different types of images, and the size of the data set, according to the experimental results, the DSCN was designed with a different structure on the three data sets. Table 2 shows the data set parameter information of the DSCN. Here, I@28 × 28 indicates that the input layer's size is 28 × 28, O@5 indicates that the output layer size is 7, 16C5@24 × 24 indicates the conventional layer size has 16 kernels with size 5 × 5, and 16S2@12 × 12 indicates that the pooling layer has 16 filters with size 2 × 2, and so on. The DSCN includes an HR ship TCR (HSTCR) data set and an MSTAR data set. Both the HSTCR and MSTAR data sets are augmented by the object-oriented and multiscale target data augmentation algorithm [5] and Alex's algorithm.

The HSTCR data set was made up of our establishment ship's visible light images from Google Earth, which mostly comprise HR satellite imagery from *Landsat-7*, *Landsat-8*, *Wordview-II*, and the *DigitalGlobe Quickbird*, which is roughly 65-cm pan-sharpened (65-cm panchromatic at nadir, 2.62-m multispectral at nadir). The targets of HSTCR data set types include military and civilian ships. Military ships include destroyers and aircraft carriers, while civilian ships include oil tankers, bulk carriers, and container ships. The image size is 256 × 256. The number of samples is 10,500 in the train data set, and the number of samples is 2,100 in test data set. Figure 3 illustrates some examples of HSTCR images.

The MSTAR data set was obtained by the X-band (9.6-GHz) HH-polarization SAR sensor with spatial resolution of 0.3 × 0.3 m in support of the DARPA-sponsored MSTAR program. The MSTAR data consist of three classes and seven types of vehicles: the BMP2 (9563, 9566, c21), BTR70 (c71), and T72 (132, 812, s7) with several configuration variations for each class. The original image size is 128 × 128. The vehicle's image is taken in spotlight mode at 15° and 17° depression angles over 360° of aspect angles. Figure 4 shows one subset of the MSTAR data that consists of three classes and seven types of military targets. The number of samples is 30,287 in the 15° Alex augmentation train data set, and the number of samples is 1,622 in the 17° Alex augmentation test data set.

PARALLEL EXPERIMENTS OF GPU-BASED DSCN ALGORITHM

Since GPU memory capacity and the size of the registration matrix have a great influence on acceleration, the three data sets are used with different batch sizes to validate the DSCN parallel backpropagation based on GPU (DPB-G) algorithm efficiency. Table 3 shows the average running time of the GPU-based DSCN iterations in different batch sizes. The relationship between the single iteration of batch size and the speedup on the GPU-based DSCN algorithm is shown in Figure 5. The algorithm has the fastest speed on the MSTAR data set and the slowest speed on the HSTCR data set. This is because the DSCN structure is different on each of the three data sets. Among the two data sets, the MSTAR data set has the smallest image size and the least storage for model training, while the HSTCR data set has the largest image size and the largest storage for model training. The limitations of GPU memory, larger demand on GPU memory, and more frequent data exchanges between system memory (random-access

TABLE 1. THE SOFTWARE AND HARDWARE ENVIRONMENT FOR PARALLEL ALGORITHM.

NAME	PARAMETER
Master node	Xeon E5-2620v2 × 2, 12 core, 2.1 GHz, 64-GB DDR3
Compute node 1–9	Xeon E5-2680v2 × 2, 20 cores, 2.8 GHz, 128-GB DDR3, Nvida Tesla K20 × 2, 5 GB × 2, CUDA core 2,496 × 2
Storage node	20 TB, 7,200 rpm, 32-GB cache
Switch of cluster	InfiniBand FDR, 56 G, 4.032 Tb/s
Switch of disk array	Storage area network 8-Gb fiber channel
Switch of network	Ethernet 1,000 M
Operating system	Red Hat Enterprise Linux server release 6.5 (Santiago)
Input–output management software	Sugon cluster monitoring and management system Gridview 3.0
Compute node software	MATLAB 8.5.0.197613 (R2015a), MATLAB parallel computing toolbox (MPCT) 6.6, MATLAB distributed computing server (MDCS) 6.6, ComputeCapability 3.5

TABLE 2. THE MODEL PARAMETER OF THE EXPERIMENT FOR PARALLEL EXPERIMENTS.

PARAMETER NAME	PARAMETER VALUES
DSCN structure in MSTAR data set	I@64 × 64-16C5@60 × 60-16S6@10 × 10-32C7@4 × 4-32S4@1 × 1-O@5
DSCN structure in HSTCR data set	I@128 × 128-16C5@124 ×124-16S4@31 × 31-32C7@25 × 25-32S5@5 × 5-O@7
HSTCR data set batch size of the sample	1,000
Number of new samples per time	500
Maximum iterative number epochs of incremental	100
Maximum iterative number epochs of reinforcement	100
Minimum error ε of reinforcement	0.01

memory) and GPU memory cause the algorithm to slow down. The reduction in absolute time is substantial. For example, CPU processing needs to spend 168.393 s on the HSTCR data set when the batch size equals 4,096. However, it spends only 40.831 s on the GPU. So, GPU operation can significantly enhance training efficiency of the DSCN.

PARALLEL EXPERIMENTS OF OPENMP-BASED HLDA ALGORITHM

Considering such factors as task allocation and process communication, the HLDA parallel Gibbs sample based on the OpenMP (HPGS-O) algorithm was tested with the process numbers and the sizes of the training sample.

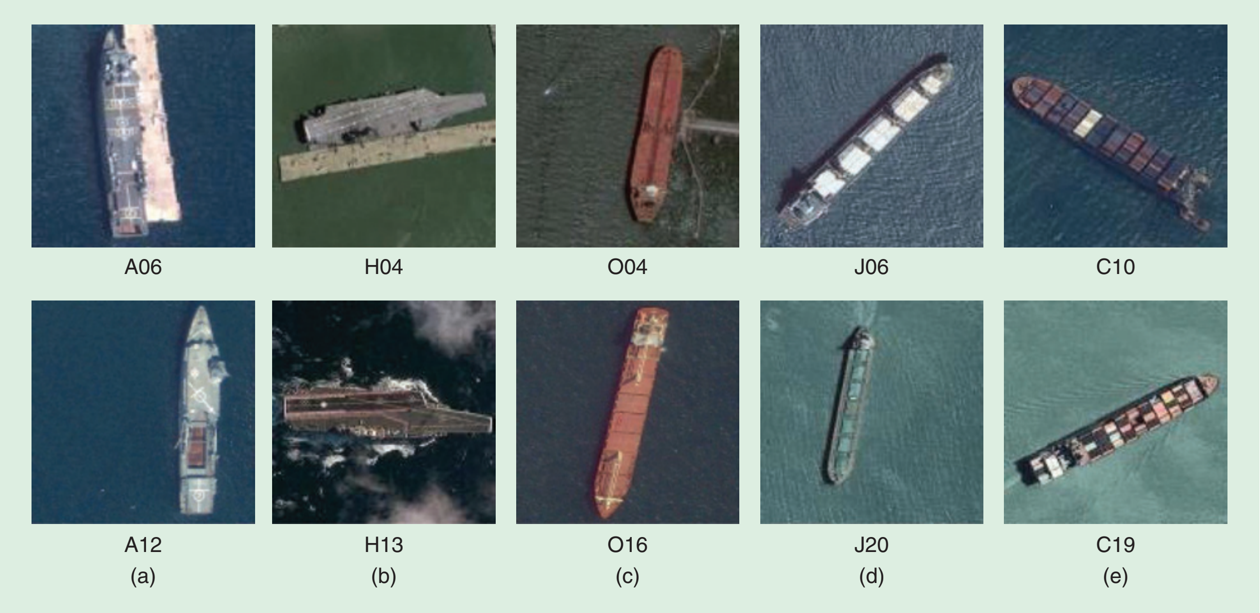

FIGURE 3. Optical images of five ships in the HSTCR data set: (a) destroyers, (b) aircraft carriers, (c) oil tankers, (d) bulk carriers, and (e) container ships.

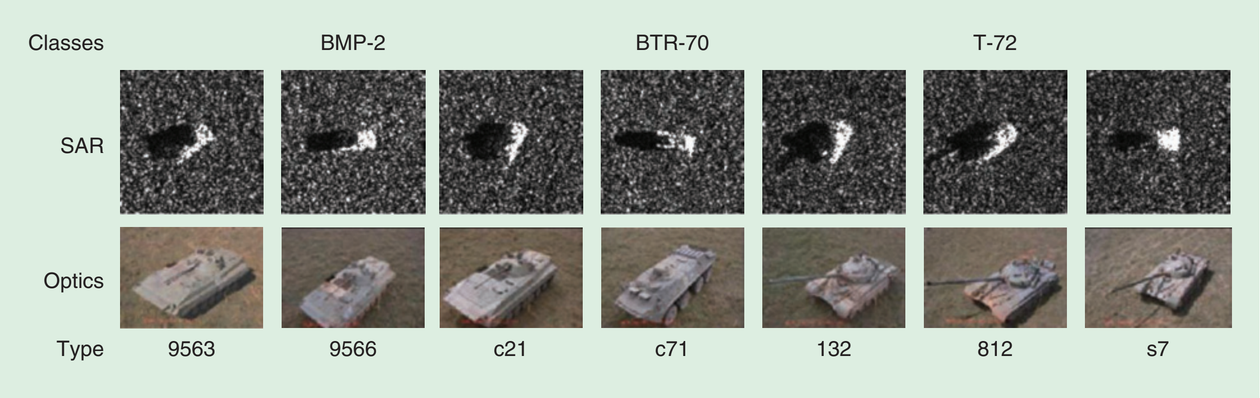

FIGURE 4. Seven tactical target vehicles in the MSTAR data set.

TABLE 3. THE TRAINING RESULTS OF DSCN ON GPU IN DIFFERENT BATCH SIZES.

BATCH SIZE	64	128	256	512	1,024	2,048	4,096
MSTAR-CPU time (s)	0.296	0.518	1.001	2.114	5.015	14.597	44.629
MSTAR-GPU time (s)	0.452	0.769	1.403	2.63	5.117	10.194	19.958
MSTAR speedup	0.66	0.67	0.71	0.8	0.98	1.43	2.24
HSTCR-CPU time (s)	2.179	4.225	8.427	17.032	34.946	74.764	168.393
HSTCR-GPU time (s)	3.344	3.74	6.739	11.191	19.287	27.598	40.831
HSTCR speedup	0.65	1.13	1.25	1.52	1.81	2.71	4.12

Table 4 shows the process average running time in the process number of Gibbs sampling of HLDA in the multicore algorithm. Here the number of batch training samples is 1,024. Figure 6 shows the increasing speed of parallel HLDA when data sets are split. The highest speed of the algorithm can be increased by 12 times on the HSTCR data set. But, for MSTAR data sets, the increased speed of the algorithm remains constant when data sets are distributed on seven cores because of the large communication overhead between processes.

PARALLEL TCR EXPERIMENT OF HIERARCHICAL CNCC FRAMEWORK BASED ON MAPREDUCE

To verify the efficiency of the parallel hierarchical CNCC-based TCR algorithm, the PTCR-C algorithm is tested with the iteration number, the core numbers in the single host, and the node number on three data sets. Table 5 shows the relationship between the node's number of CNCC framework distributions and the average training time on the multimachine. Here the number of the iteration's epoch is 10, the batch size of training is 4,096, and the number of processes in single-node kernels is 16. The algorithm spends about 10 h on the MSTAR data set and more than 12 h on the HSTCR data set. Figure 7 shows the relationship between the number of nodes and the increase in speed. The experiment demonstrated that, for the HSTCR and MSTAR data sets, the TCR parallel algorithm achieved speeds 39.49 and 65.58 times faster than the base speed when nodes are assigned to 16 and 28, respectively. With the increase of communication overhead between nodes, the speed of the algorithm does not increase as much.

For 10 iterations, the recognition accuracy of TCR is improved by 0.25% on the MSTAR data set. However, the recognition accuracy of TCR is reduced by 12.28% on the HSTCR data set. This may be because the model has not yet been trained to be optimal on the HSTCR data set.

THE RECOGNITION PRECISION OF THE PARALLEL CNCC-BASED TCR ALGORITHM

To verify the influence of parallel TCR algorithms on precision, the original sequential algorithm and the improved parallel algorithm were tested on the three data sets. Table 6 shows the experimental results' iteration number and average precision (AP) of recognition. Here the number of iterations is set in epochs from one to 10 times, respectively. Figure 8 shows the relationship between the iteration number and the AP of parallel TCR.

The results show that the parallel acceleration effect has a greater impact on the HSTCR and MSTAR data sets. After 10 iterations, the precision of parallel TCR is basically sequential running time on the MSTAR data set. However, the precision of parallel TCR shows an upward trend with the increase in the iteration number on the HSTCR data set. This is because some factors tremendously affect recognition, including data set size, object complexity, and target resolution. Generally, the parallel algorithm can effectively improve the efficiency of the hierarchical CNCC-based TCR algorithm.

CONCLUSIONS

This article analyzed and summarized the progress of the HRI parallel processing algorithms and makes a parallel analysis of the CNCC-based TCR algorithm. Aiming at the bottleneck problem of the TCR algorithm, we propose the DPB-G, HPGS-O, and PTCR-C algorithms. These adapt a multimachine, multicore, and GPU heterogeneous parallel technique. The experimental results show that our algorithms can greatly improve efficiency without loss of recognition precision.

To realize the higher speeds for the TCR algorithm, the parameters need careful selection and reasonable configuration. This is especially true for the structure design of the

TABLE 4. THE GIBBS SAMPLING OF HLDA ON A MULTICORE ENVIRONMENT.

KERNELS/PROCESS	1	2	4	6	8	16
MSTAR time (min)	3.888	1.469	0.705	0.559	0.536	0.641
MSTAR speedup	—	2.65	5.51	6.96	7.25	6.06
HSTCR time (min)	3.834	1.403	0.616	0.441	0.39	0.314
HSTCR speedup	—	2.73	6.22	8.69	9.83	12.2

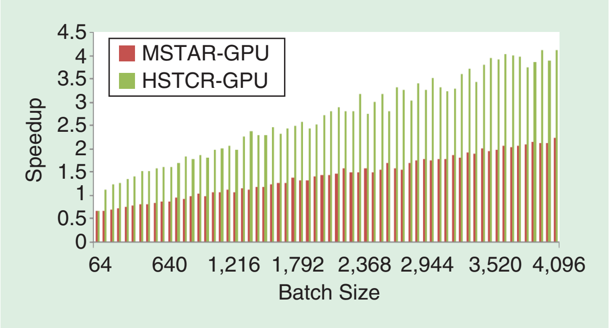

FIGURE 5. A graph showing the relationship of batch size and speedup on the DPB-G algorithm.

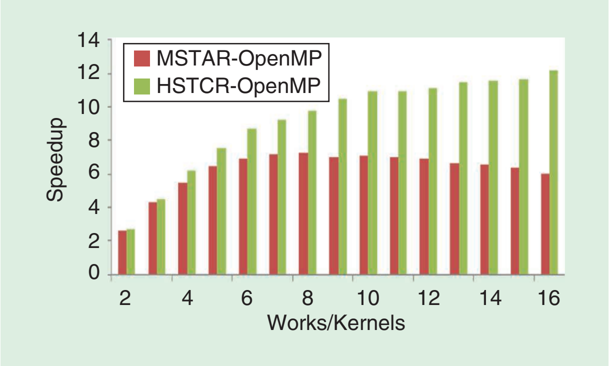

FIGURE 6. A graph showing increases in HPGS-O algorithm speedup on different data sets.

deep NN and the selection of training parameters. For the DPB-G algorithm, the main factors that affect the speed increase are image size, GPU performance (such as the available memory of GPU, MaxThreadsPerBlock), and the number of GPU threads. For the HPGS-O algorithm, the main factors affecting speed are image size and node performance, such as the total memory capacity, the number of threads of the CPU, and the capacity of the cache. For the PTCR-C algorithm, the main factors affecting speed are image size, communication bandwidth of the network, and node performance. This is because the parallel TCR algorithm is limited by the problem of scale, size, and hardware environment and the overhead of process communication.

GENERALLY, THE PARALLEL ALGORITHM CAN EFFECTIVELY IMPROVE THE EFFICIENCY OF THE HIERARCHICAL CNCC-BASED TCR ALGORITHM.

The iterations have little effect in terms of the AP of the parallel TCR algorithm on the data sets with the large number of the train samples, and it has more effect on the training data sets with the small number of train samples and large image size. Overall, under the premise of ensuring high recognition accuracy, our proposed parallel algorithm can greatly improve the speed of TCR.

Fast TCR is also an important focus of research for automatic or semiautomatic remote sensing image interpretation of HR Earth-observing systems. Both the fast parallel and high precision of TCR methods have significant value for theoretical and practical applications in military and civilian fields. Due to the limited length of this article, only optical image and the SAR image experiments were presented. To improve the robustness of the TCR

TABLE 5. MULTIMACHINE EXECUTION TIME OF CNCC-BASED TCR TRAINING ON DIFFERENT DATA SETS.

NODES/WORKS	1	2	4	8	16	32	64	128	216
MSTAR time (h)	10.237	2.292	0.726	0.274	0.157	0.14	0.202	0.362	0.59
MSTAR speedup	—	4.47	14.1	37.4	65.39	73.28	50.57	28.3	17.34
HSTCR time (h)	12.342	2.846	0.983	0.446	0.313	0.377	0.624	1.177	1.944
HSTCR speedup	—	4.34	12.55	27.7	39.49	32.7	19.78	10.49	6.35

TABLE 6. THE ITERATIONS AND AVERAGE PRECISION AP OF RECOGNITION OF PARALLEL CNCC-BASED TCR.

EPOCHS	1	2	3	4	5	6	7	8	9	10
Sequential AP in MSTAR (%)	15.25	30.75	66.25	82.5	80	81	82	90.5	89	90
Parallel AP in MSTAR (%)	7	15.25	15.25	34.5	45.5	53.25	55.5	86	87.5	89.75
Sequential AP in HSTCR (%)	38.14	36.84	38.25	37.51	37.98	37.19	54.93	54.43	57.9	59.86
Parallel AP in HSTCR (%)	29.5	41.18	52.96	48.82	55.21	57.43	57.96	73.62	76.81	72.14

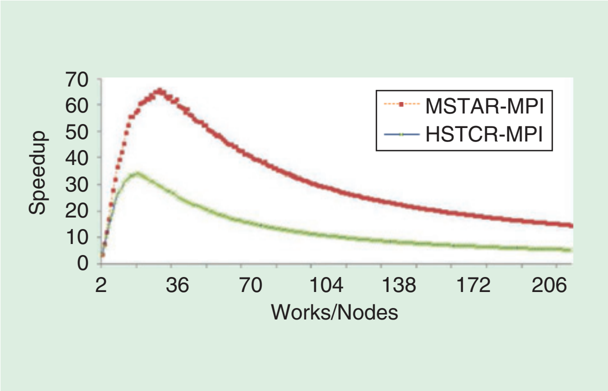

FIGURE 7. A graph showing the relationship of the parallel nodes and speedup in the PTCR-C algorithm.

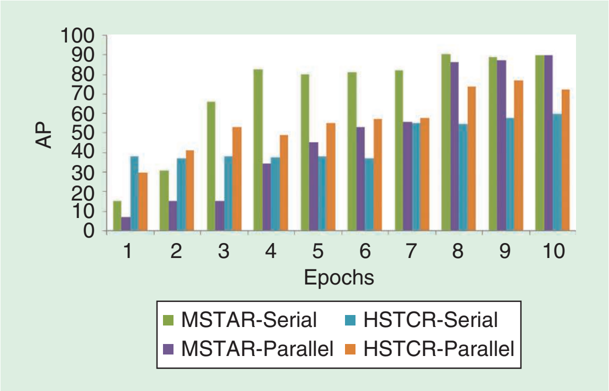

FIGURE 8. A graph showing the relationship of iterates and AP of hierarchical CNCC-based parallel TCR.

algorithm, it is necessary to explore the TCR performance of the algorithm in applications involving hyperspectral and infrared remote sensing images.

ACKNOWLEDGMENTS

This work was supported by the National Natural Science Foundation of China (grants 61806074 and U1704122), the Key Research and Promotion Projects of Henan Province (grants 192102210096 and 182102210242), and the Science and Technological Research of Key Projects of Henan Province (grants 172102110006 and 182102110065).

AUTHOR INFORMATION

Yang Liu (ly.sci.art@gmail.com) received his B.S. degree from Changchun University of Science and Technology, China, in 1996 and his M.S. and Ph.D. degrees from Henan University, Kaifeng, China, in 2008 and 2016, respectively. He is an associate professor and master's supervisor at the College of Computer Science and Information Engineering, Henan University. His current research interests include brain-inspired computing (i.e., multimedia neural cognitive computing, cross-model neural cognitive computing, multisource cross-modal target recognition, and audiovisual cross-media semantic retrieval) and temporal–spatial information high-performance computing in remote sensing.

Yi Xie (34971750@qq.com) received his B.S degree from Changzhou University, China, in 2005 and his M.S degree in Henan University, Kaifeng, China, in 2011. He is currently working toward his Ph.D. degree at the College of Environment and Planning at Henan University. His current research interests include remote sensing information processing, spatial analysis, optimization, and application.

Wei Yang (yang0sun@gmail.com) received his B.S. degree from the Department of Computer Science, Xinyang Normal University, China, in 2005 and his M.S. and Ph.D. degrees from the School of Computer Science and Technology, Harbin Institute of Technology, China, in 2008 and 2011 respectively. Currently, he is an associate professor at Henan University, Kaifeng, China. His research interests include machine learning and deep learning.

Xianyu Zuo (mncc.zxy@hotmail.com) received his B.S degree in computational mathematics from Henan Normal University, China, in 2003, and his Ph.D. degree in computational mathematics from the Graduate School of China Academy of Engineering Physics, Beijing, in 2012. Currently, he is an associate professor at Henan University, Keifeng, China. His research interests include parallel computing and remote sensing image processing.

Qiang Ge (gq101@139.com) received his B.S. and M.S. degrees from the School of Computer and Information Engineering, Henan University, Keifeng, China, in 2002 and 2005, respectively. He received his Ph.D. degree from the National Engineering Research Center for E-Learning, Huazhong Normal University, Wuhan, China, in 2011. Currently, he is an associate professor at Henan University. His research interests include atmospheric remote sensing and spatial information processing.

Bing Zhou (zhoub1631@163.com) received his B.S. degree from the School of Computer Science, Northwestern Polytechnical University, Xi'an, China, in 1997 and his M.S. and Ph.D. degrees from the School of Electronics and Information Engineering, Xi'an Jiaotong University, China, in 2000 and 2004, respectively. Currently, he is an associate professor at Henan University, Keifeng, China. His research interests include parallel computing and spatial information processing.

REFERENCES

[1] Y. B. Huang, "Infrastructural development for farm-scale remote sensing big data service," *Multispectral, Hyperspectral, and Ultraspectral Remote Sensing Technology, Techniques and Applications VII*. vol. 10780, A. M. Larar, M. Suzuki, and J. Wang, Eds. Bellingham, WA: SPIE, 2018.

[2] T. Long et al., "High resolution radar real-time signal and information processing," *China Commun.*, vol. 16, pp. 105–133, Feb. 2019.

[3] L. L. Yu, Q. X. Yang, and L. M. Dong, "Aircraft target detection using multimodal satellite-based data," *Signal Processing*, vol. 155, pp. 358–367, Feb. 2019.

[4] Y. Liu, Research on the brain-inspired cross-media neural cognitive computing framework. 2018. [Online]. Available: arXiv:1805.01385

[5] Y. Liu and F. Zheng, "Object-oriented and multi-scale target classification and recognition based on hierarchical ensemble learning," *Comput. Elect. Eng.*, vol. 62, pp. 538–554, 2017.

[6] J. H. Yang, J. X. Zhang, and G. M. Huang, "A parallel computing paradigm for pan-sharpening algorithms of remotely sensed images on a multi-core computer," *Remote Sensing*, vol. 6, no. 7, pp. 6039–6063, July 2014.

[7] X. Li, C. Li, P. Wang, Z. Men, and H. Xu, "SAR ATR based on dividing CNN into CAE and SNN," in *Proc. 2015 IEEE 5th Asia-Pacific Conf. Synthetic Aperture Radar (APSAR)*, pp. 676–679.

[8] S. Tu and Y. Su, "Fast and accurate target detection based on multiscale saliency and active contour model for high-resolution SAR images," *IEEE Trans. Geosci. Remote Sens.*, vol. 54, no. 10, pp. 5729–5744, Oct. 2016.

[9] D. P. Williams, "Fast target detection in synthetic aperture sonar imagery: A new algorithm and large-scale performance analysis," *IEEE J. Ocean. Eng.*, vol. 40, no. 1, pp. 71–92, Jan. 2015.

[10] X. Pan, J. Zhao, and J. Xu, "An object-based and heterogeneous segment filter convolutional neural network for high-resolution remote sensing image classification," *Int. J. Remote Sens.*, vol. 40, no. 15, pp. 5892–5916, Aug. 2019.

[11] L. Zhang, L. Zhang, and B. Du, "Deep learning for remote sensing data: A technical tutorial on the state of the art," *IEEE Geosci. Remote Sens. Mag.*, vol. 4, no. 2, pp. 22–40, 2016.

[12] G. Dong, G. Liao, H. Liu, and G. Kuang, "A review of the autoencoder and its variants: A comparative perspective from target recognition in synthetic-aperture radar images," *IEEE Geosci. Remote Sens. Mag.*, vol. 6, no. 3, pp. 44–68, 2018.

[13] L. C. Mou, P. Ghamisi, and X. X. Zhu, “Unsupervised spectral-spatial feature learning via deep residual conv-deconv network for hyperspectral image classification,” *IEEE Trans. Geosci. Remote Sens.*, vol. 56, no. 1, pp. 391–406, Jan. 2018.

[14] E. Maggiori, Y. Tarabalka, G. Charpiat, and P. Alliez, “Convolutional neural networks for large-scale remote-sensing image classification,” *IEEE Trans. Geosci. Remote Sens.*, vol. 55, no. 2, pp. 645–657, Feb. 2017.

[15] Y. Liu, K. Cai, M. H. Zhang, and F. B. Zheng, “Target detection in remote sensing image based on saliency computation of spiking neural network,” in *Proc. 2018 IEEE Int. Geoscience and Remote Sensing Symp.*, pp. 2865–2868.

[16] Q. Wang, X. D. Zhang, G. Z. Chen, F. Dai, Y. F. Gong, and K. Zhu, “Change detection based on faster R-CNN for high-resolution remote sensing images,” *Remote Sensing Lett.*, vol. 9, no. 10, pp. 923–932, 2018.

[17] X. Guo, J. Wu, Z. Wu, and B. Huang, “Parallel computation of aerial target reflection of background infrared radiation: Performance comparison of OpenMP, OpenACC, and CUDA implementations,” *IEEE J. Sel. Topics Appl. Earth Observ. and Remote Sens.*, vol. 9, no. 4, pp. 1653–1662, Apr. 2016.

[18] L. Timchenko, A. Yarovyy, N. Kokriatskaia, I. Ivasyuk, and A. Denysova, “Application of parallel-hierarchical transformations for rapid recognition of dynamic images based on GPU technology,” in *Proc. 2nd Int. Conf. Advances Computer Science and Engineering (CSE 2013)*, Los Angeles, CA, 2013, pp. 224–228. doi: 10.2991/cse.2013.51.

[19] G. Lokman and G. Yilmaz, “Anomaly detection and target recognition with hyperspectral images,” in *Proc. 2014 22nd Signal Processing and Communications Applications Conf.*, 2014, pp. 1019–1022.

[20] D. Zhao, J. Shi, J. Wang, and Z. Jiang, “Saliency-constrained semantic learning for airport target recognition of aerial images,” *J. Appl. Remote Sensing*, vol. 9, no. 1, pp. 096058–096073, May 4, 2015. doi: 10.1117/1.JRS.9.096058.

[21] J. Guo, Y. S. Li, K. Liu, J. Lei, and K. Y. Wang, “Fast FPGA implementation for computing the pixel purity index of hyperspectral images,” *J. Circuits Syst. Comput.*, vol. 27, no. 3, pp. 84–89, Mar. 2018. doi: 10.3969/j.issn.1000-565X.2014.01.015.

[22] A. Plaza, Q. Du, Y. L. Chang, and R. L. King, “High performance computing for hyperspectral remote sensing,” *IEEE J. Sel. Topics Appl. Earth Observ. and Remote Sens.*, vol. 4, no. 3, pp. 528–544, Sept. 2011.

[23] C. A. Lee, S. D. Gasster, A. Plaza, C. I. Chang, and B. Huang, “Recent developments in high performance computing for remote sensing: A review,” *IEEE J. Sel. Topics Appl. Earth Observ. and Remote Sens.*, vol. 4, no. 3, pp. 508–527, Sept. 2011.

[24] X. Y. Wang, Z. H. Li, and S. Gao, “Parallel remote sensing image processing: Taking image classification as an example,” in *Proc. Computational Intelligence and Intelligent Systems: 6th Int. Symp.*, Wuhan, China, 2012, pp. 159–169.

[25] X. Y. Wang, G. Q. Li, W. Y. Yu, and Q. Zou, “Research on method for massive pixel-level remote sensing image processing based on Hadoop,” *Applied Mechanics and Materials*, vol. 333–335, pp. 1224–1230, 2013.

[26] N. Golpayegani and M. Halem, “Cloud computing for satellite data processing on high end compute clusters,” in *Proc. 2009 IEEE Int. Conf. Cloud Computing*, pp. 88–92.

[27] B. P. Garcia-Salgado, V. I. Ponomaryov, S. Sadovnychiy, and M. Robles-Gonzalez, “Parallel supervised land-cover classification system for hyperspectral and multispectral images,” *J. Real-Time Image Processing*, vol. 15, no. 3, pp. 687–704, Oct. 2018.

[28] H. Ma and Z. Wang, “Distributed data organization and parallel data retrieval methods for huge laser scanner point clouds,” *Comput. Geosci.*, vol. 37, pp. 193–201, Feb 2011.

[29] H. Zhou, X. Yang, H. Liu, and Y. Tang, “GPGC: A grid-enabled parallel algorithm of geometric correction for remote-sensing applications,” *Concurrency Computation-Practice Experience*, vol. 18, pp. 1775–1785, Dec. 15, 2006.

[30] C. T. Yang, C. L. Huang, and C. F. Lin, “Hybrid CUDA, OpenMP, and MPI parallel programming on multicore GPU clusters,” *Comput. Physics Commun.*, vol. 182, no. 1, pp. 266–269, Jan. 2011.

[31] J. D. Owens et al., “A survey of general-purpose computation on graphics hardware,” *Comput. Graph. Forum*, vol. 26, no. 1, pp. 80–113, 2007.

[32] J. D. Owens, M. Houston, D. Luebke, S. Green, J. E. Stone, and J. C. Phillips, “GPU computing,” *Proc. IEEE*, vol. 96, no. 5, pp. 879–899, May 2008.

[33] M. Garland et al., “Parallel computing experiences with CUDA,” *IEEE Micro*, vol. 28, no. 4, pp. 13–27, July–Aug. 2008.

[34] J. Dean et al., “Large scale distributed deep networks,” in *Proc. Advances in Neural Information Processing Systems*, 2012, pp. 1223–1231.

[35] J. Duchi, E. Hazan, and Y. Singer, “Adaptive subgradient methods for online learning and stochastic optimization,” *J. Mach. Learning Res.*, vol. 12, pp. 257–269, 2011.

[36] E. D. Rumelhart, E. G. Hinton, and J. R. Williams, “Learning representations by back-propagating errors,” *Nature*, vol. 323, no. 6088, pp. 533–536, 1986.

[37] D. Newman, A. Asuncion, P. Smyth, and M. Welling, “Distributed algorithms for topic models,” *J. Mach. Learning Res.*, vol. 10, pp. 1801–1828, Aug. 2009.

[38] J. Dean and S. Ghemawat, “MapReduce: A flexible data processing tool,” *Commun. ACM*, vol. 53, no. 1, pp. 72–77, Jan. 2010.

[39] J. Dean and S. Ghemawat, “MapReduce: Simplified data processing on large clusters,” *Commun. ACM*, vol. 51, no. 1, pp. 107–113, Jan. 2008.

[40] R. C. Taylor, “An overview of the Hadoop/MapReduce/HBase framework and its current applications in bioinformatics,” in *Proc. 11th Annu. Bioinformatics Open Source Conf. (BOSC)*, 2010, pp. 1–6. doi: 10.1186/1471-2105-11-S12-S1.

GRS

ORHAN EROGLU, DYLAN R. BOYD, AND MEHMET KURUM

The Signals of Opportunity Coherent Bistatic Scattering Simulator

A free open source framework

Signals of opportunity (SoOp) has the potential to offer cost-effective global remote sensing for land applications. Because of the complexity of SoOp scattering over land, comprehensive bistatic scattering models and simulators can help demonstrate its feasibility. To investigate this potential, we have developed a generalized, fully polarimetric forward model: the SoOp Coherent Bistatic Scattering (SCoBi) model. We have also developed a simulator framework, employing the SCoBi model to create an analysis environment for a community of researchers, scientists, and users with little or no electromagnetic background. We aim to enable studying and analyzing new SoOp methods with varying configurations; determining the optimal cases for specific missions; and generating, visualizing, and analyzing test data with the help of SCoBi.

The SCoBi framework currently implements SoOp analyses over bare or vegetated terrains, where soil can be modeled as a single-layered or multilayered dielectric medium. The software is free and open source under the GNU General Public License (GPL) and is compatible with the MATLAB development environment. It obtains several inputs for bistatic configuration, such as bistatic geometry, transmitter and receiver antenna characteristics, ground structure, and user preferences, through a set of user-friendly graphical user interface (GUI) windows. It generates the simulated direct received field and power as well as the specular reflection coefficient and reflectivity outputs. It also provides basic analysis functions, such as plotting reflectivity as a function of simulation parameters, including a transmitter's elevation angle and the volumetric soil moisture (VSM). This article describes the SCoBi simulator in detail and provides case studies for the Earth science community.

Digital Object Identifier 10.1109/MGRS.2019.2916071
Date of current version: 21 September 2020

DEVELOPMENT OF THE SCOBI MODEL

The SoOp approach has emerged in recent years because of its potential for global-scale microwave remote sensing in Earth science applications. This approach is based on receiving the reflected signals of existing transmitters such as navigation or communication satellites scattered along the Earth's surface in a bistatic geometry. Because a dedicated transmitter is not needed, SoOp enables high spatiotemporal microwave remote sensing through the use of small satellite constellations. Depending on the geolocation of the specular point between the transmitter and the receiver, SoOp receivers can collect valuable information for both land- and ocean-based geophysical properties, realizable through comprehensive inverse retrievals.

Advances over the past two decades in SoOp applications for remote sensing of the ocean have resulted in the launch of a few satellite missions. For instance, the first dedicated spaceborne Global Navigation Satellite System Reflectometry (GNSS-R) receiver was a secondary payload on board the U.K. Disaster Monitoring Constellation [1]. It has demonstrated the potentiality of GNSS-R for remote sensing of ocean, ice, and land geophysical parameters [2]. The United Kingdom's *Technology Demonstration Satellite-1* was launched in 2014 with an improved secondary GNSS-R payload to demonstrate SoOp's ocean remote sensing feasibility [3]. NASA's Cyclone Global Navigation Satellite System (CYGNSS) mission was launched in December 2016 to improve weather predictions by estimating ocean winds between 38° S and 38° N latitudes [4]–[6]. CYGNSS has eight small satellites each with four channels in orbit, and it has a mean revisit time of 7 h. The constellation records a considerable amount of land observation data as well, which are publicly available. Nevertheless, SoOp land remote sensing has yet to demonstrate the same technology readiness as ocean remote sensing. The major reason is the lack of bistatic land models that sufficiently account for the effects of many land geophysical parameters (for example, surface and root-zone soil moisture, vegetation biomass, surface roughness, topography, and snow water equivalent) on SoOp observables.

Only a few studies have introduced forward models to deal with bistatic geometries over bare soil or vegetated terrains. These models can be grouped into two categories based on their method: radiative transfer theory (originating from the law of energy conservation) or analytical wave theory (in conjunction with distorted Born approximation). The known radiative transfer models are as follows: Bistatic–Michigan Microwave Canopy Scattering (Bi-MIMICS) [7]; an extension of the Tor Vergata model [8]; the Soil and Vegetation Reflection Simulator, which is another model employing Tor Vergata [9]; and an extension of Bi-MIMICS [10], [11]. The Coherent Bistatic Scattering Model [12], on the other hand, is based on analtyical wave theory. Some of these studies utilize a previously developed monostatic model and extend it to the bistatic geometry [7], [10], [11]. Another exploits a monostatic coherent model [12] (the others are intrinsically bistatic).

Each of these studies considers diverse ground conditions and covers some microwave spectrum bands and polarizations. For instance, Liang et al. applied their model to tree canopies at the L, C, and X bands with linear polarization [7]. Ferrazzoli et al. performed forest biomass analysis at the L band (GNSS-R) with circular polarization [8]. Pierdicca et al. studied bare soil and vegetated terrains at the L band with circular polarization [9]. Two studies were applied to the L band (GNSS-R) with combinations of linear and circular polarizations [10], [11]. Thirion-Lefevre et al. performed a P-band analysis with linear polarization [12]. In addition to these models, an open source GPS multipath simulator [13] based on a coherent forward multipath model is used for near-surface reflectometry and positioning applications [14]. It is a comprehensive GPS analysis toolbox that can produce signal-to-noise ratio, carrier phase, and code pseudorange observables.

TABLE 1. THE SCoBi IN A NUTSHELL.

EFFECTS	CHARACTERISTICS
Polarimetric	Fully polarimetric
	Combination of linear/circular polarizations
Antenna	Custom antenna patterns
	Cross-polarization coupling
	Beam divergence
	Polarization mixing
	Orientation
Configuration	Altitude
	Spreading loss over vegetation layer
Interferometric	Complex voltage
	Orientation
	Beamforming
Multilayer	Complex dielectric media
	Stratified layer division
	Vegetation and subsurface scattering
Vegetation	Mix vegetation
	Seasonal effects

We have recently developed a generalized, fully polarimetric bistatic forward model for the purpose of creating a comprehensive SoOp analysis environment. The model was originally called the *SCoBi for Vegetated Terrains* (*SCoBi-Veg*) [15], [16]; however, it is now applicable for vegetated and bare soil terrains, where the ground structure can be single- or multilayered in either case. Hence, the model will be referred as *SCoBi* starting with this study. As its name suggests, it is a coherent model based on analytical wave theory.

The SCoBi model, as shown in Table 1, considers the antenna characteristics, polarimetric effects, and configuration influences, in particular, because such models are commonly used for ground-based and low-altitude airborne simulations, where these factors significantly impact bistatic deliverables. For instance, it takes into account any combination of polarizations (linear and circular) in conjunction with antenna effects, such as polarization mismatch and crosstalk. It also incorporates the antenna altitude, orientation, and voltage pattern as well as interferometric effects, such as complex voltage and beamforming. The SCoBi model applies analytical wave theory in conjunction with the distorted Born approximation to account for the vegetation layer. Hence, it allows users to analyze the phase as well as the amplitude information through a single scattering assumption. The model is capable of simulating the complex field and received power (modified Stokes vectors converted from the complex field quantities) constructed by three contributions: direct (the line-of-sight distance between the transmitter and the receiver), coherent (the shortest multipath distance in the specular direction), and diffuse (scattered waves from the entire scene due to the vegetation scatterers). The diffuse term is acquired through a Monte Carlo scheme that generates a sufficient number of realizations for canonical scatterers within the vegetation canopy. One can refer to [16] for an exhaustively theoretical explanation of the SCoBi model. SCoBi was recently validated by P-band SoOp reflectometry measurements over land, through simulations of measured field data collected at Purdue University's Agronomy Center for Research and Education during the 2017 growth season [17]. Bare soil measurements during this season showed consistent results between the measured and simulated reflectivity values. In the near future, the SCoBi model will be employed to cross-validate the measurements obtained by drone- and tower-based multifrequency receievers built in-house as well as small satellite missions such as CYGNSS [4] and SoOp P-band Investigation (SNoOPI) [18].

This article describes the free and open source SCoBi simulator framework, which we have further developed by employing the SCoBi model. The principal motivation for open sourcing such a simulator is to create a medium for the Earth science community, including researchers, scientists, and even end users with little to no electromagnetic background, for the following reasons:

1) to study new SoOp methods under changing configurations
2) to analyze existing or newly developed methods in detail
3) to determine optimal cases for specific applications/missions
4) to generate, visualize, and analyze test data.

From this point, SCoBi has the potential to contribute to the reproducibility of scientific efforts, technology validations, and replicability of our simulation studies. SCoBi is also intended to optimize the time and effort spent by Earth science researchers on bistatic forward modeling needs. To acquire these objectives, the SCoBi simulator framework is released under the GPL.

THE SCOBI MODEL SIMULATOR FRAMEWORK

The distribution package of the SCoBi release can be accessed through GitHub [19] and is shown in Figure 1. The package consists of design, docs, and source folders as well as the license file (COPYING.txt) and brief introduction (README.md) documentation. The design folder includes the architectural design of the SCoBi framework created by using the Sparx Systems' Enterprise Architect tool. The docs folder currently contains only the manuals folder, which includes the SCoBi user's manual [20], developer's manual [21], and a quick-start guide [22]. The source folder contains both the input and lib folders. The input folder includes the system, configuration, Rx_antenna_pattern, and vegetation folders. Each of these folders includes some number of default input files with the distribution. The details of these files are discussed in the section "Input Files."

This section describes the features, available analysis types, inputs, and outputs of the SCoBi simulator framework. The simulator predicts fully polarimetric reflections over vegetated or bare terrains, where the ground is assumed to be flat and have a smooth-to-moderate surface roughness level. The ground structure can be modeled as single-layered or multilayered slabs of dielectric constants for surface or root-zone analysis, respectively. Therefore, the framework currently provides bistatic analyses over vegetated and bare soil terrains with surface-only (single-layered) or multilayered ground structures. A major difference between the current simulator and the original SCoBi-Veg model [16] is that diffuse scattering is not included in the current simulator. We decided to open-source the simulator without methods for calculating diffuse scattering because of significant findings based on recent simulation studies [16], [23] that demonstrated the dominance of coherent contributions over incoherent scattering even for ground-based configurations in the case of forested or agricultural terrain over a flat, smooth surface. For instance, terrains with a root-mean-square height (RMSH) roughness below 2.5 cm for the L band could generate coherent reflections with respect to the Rayleigh roughness criterion, and the SCoBi model is still capable of calculating the diffuse term despite this feature not being implemented in the current simulator. The diffuse-scattering feature will be added to the existing simulator in a future update for the purpose of applying SCoBi for terrains with topographic relief and high roughness levels.

The simulator calculates bistatic scattering for the most-common SoOp configuration, which consists of a transmitter far away from Earth. The receiver model is a ground-based or low-altitude passive instrument that acts as a reflectometer for the transmitted signals from long distances. A general bistatic geometry considered by SCoBi is depicted in Figure 2. The figure shows a satellite transmitter, a ground-based receiver,

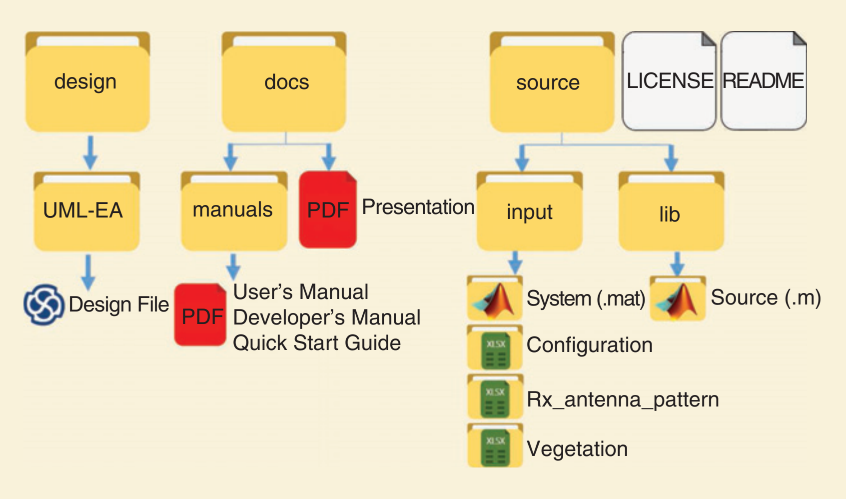

FIGURE 1. The SCoBi distribution package. The icons represent individual files, and the folder-enclosed icons represent folder names with several files. UML-EA: Unified Modeling Language–Enterprise Architect.

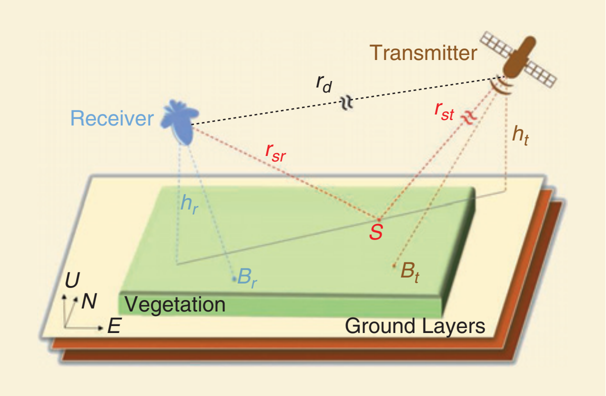

FIGURE 2. The general bistatic geometry. U: up; N: north; E: east.

a multilayer soil profile, and a vegetation layer. The local east-north-up coordinate system is depicted. In the figure, S represents the specular reflection point, and h_r and h_t represent the receiver and transmitter altitudes, respectively. In fact, h_r is not required for reflectivity analysis, but it can be given as an input for received power calculations. B_t and B_r represent the boresight (main beam) directions of the transmitter and receiver, respectively. The transmitter incidence angle (θ_{0t}) is defined as the angle between the transmitter's boresight direction and the nadir. Although this angle is used for bistatic geometry computations, SCoBi prompts the user to input the transmitter's elevation angle, which is a complement of the incidence angle to 90°.

The transmitter azimuth angle (φ_{0t}) is defined as the angle between the transmitter's local x-axis and local north. The receiver zenith observation (θ_{0r}) and azimuth observation (φ_{0r}) angles are defined in a way similar to the incidence and azimuth angles, respectively, of the transmitter. The defined azimuthal angles of the transmitter and receiver are converted into Cartesian coordinates to use in computations after input acquisition. The range term r_d denotes the line-of-sight distance between the transmitter and the receiver, r_{st} is the distance between the specular point and the transmitter, and r_{sr} stands for the distance between the specular point and the receiver.

The SCoBi simulator gets several inputs for the analysis type of interest and simulation specifications through a set of user-friendly GUI windows. It is applicable over a wide range of the microwave spectrum with any combination of linear and circular polarizations between the transmitter and receiver. It has a few constraints on the other hand. For instance, vegetation analysis is applicable from the P- to S-bands due to the employment of the distorted Born approximation [16]. The application domain of the SCoBi simulator can be explained considering the analysis types and input sets as follows.

SCOBI MODEL ANALYSIS TYPES

The SCoBi simulator was developed as a framework to make it easily expandable for new analysis types. Currently, it provides vegetation or bare soil analyses over single-layered or multilayered ground structures. In addition, the ground model assumes a flat, smooth surface without topographic relief. SCoBi can be extended by adding other capabilities, such as snow, topography, permafrost, and wetlands. Figure 3 shows the analysis selection window of the SCoBi simulator, the initial window that welcomes the user when SCoBi is accessed by running the runSCoBi.m file under the /source/lib folder of the distribution package. This window has eight buttons representing analysis types. The first four of these are currently ready to use; the next four show how this framework can be extended in the future.

FIGURE 3. The SCoBi analysis selection window.

For instance, as a further development, the SCoBi model could be enabled to account for snow cover in conjunction with vegetation cover. In addition, the smooth-ground assumption of the current model will be revised to consider diffuse scattering over highly rough ground, making possible a topography analysis. The currently active selection buttons (forest, agriculture, soil, and root zone) provide an easy way to select the SoOp analysis of interest and prepare the simulator with default inputs (provided for each analysis type in the software release) or recently used inputs of that analysis type. In other words, the choice made in the analysis selection window does not make any change in the use of SCoBi other than filling entries with default or recently used input values; the user should determine the appropriate input set for the analysis type selected.

SCoBi opens the simulation inputs window after one of the analysis types is selected, as displayed in Figure 4. This GUI window maintains the same layout for all analysis types. However, the visibility of the GUI elements is managed based on the corresponding default or recently used inputs.

SCOBI MODEL INPUTS

SCoBi allows the user to determine a large number of input parameters to specify the bistatic geometry, scene characteristics, transmitter and receiver antenna specifications and orientations, and dynamic scene conditions. The simulator receives the simulation inputs with the help of a GUI window, called the *simulation inputs window*, as seen in Figure 4. In fact, we have created a SCoBi user's manual [20] and a set of tutorial videos [24] to help visualize what the parameters within the simulation inputs window represent and how changing these parameters affects the input structure of the configuration inputs, antenna pattern, and vegetation input files discussed later in this article. In addition, we briefly describe the separate input groups on the simulation inputs window in the following.

ANALYSIS SELECTION BUTTONS

These buttons are included for the sake of allowing users to load the default or recently used inputs for the different analysis types at any time without returning to the analysis selection window.

SIMULATION SETTINGS

The simulation settings panel includes the main setting parameters that determine the output directory name, simulation mode, ground cover, and preferences. The campaign

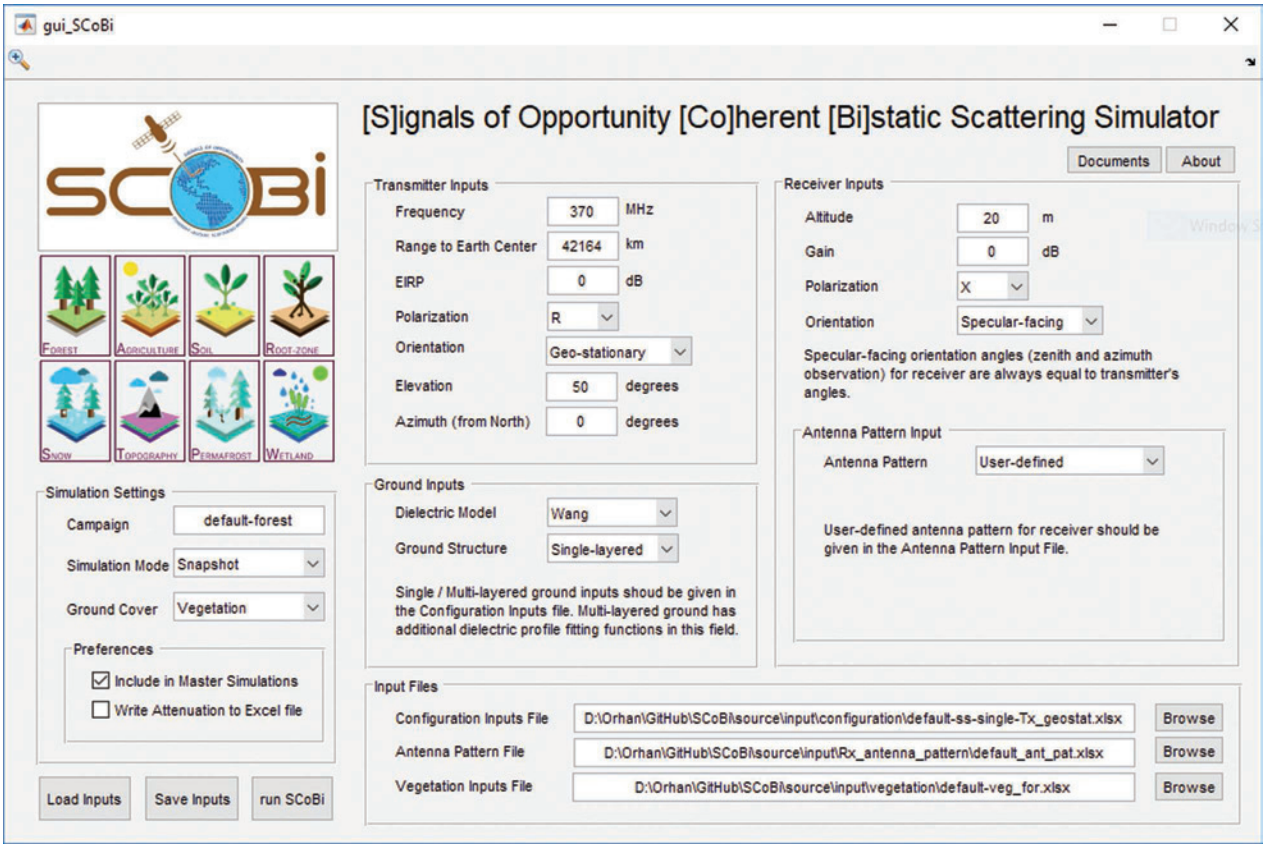

[S]ignals of Opportunity [Co]herent [Bi]static Scattering Simulator

Transmitter Inputs
Frequency: 370 MHz
Range to Earth Center: 42164 km
EIRP: 0 dB
Polarization: R
Orientation: Geo-stationary
Elevation: 50 degrees
Azimuth (from North): 0 degrees

Receiver Inputs
Altitude: 20 m
Gain: 0 dB
Polarization: X
Orientation: Specular-facing

Specular-facing orientation angles (zenith and azimuth observation) for receiver are always equal to transmitter's angles.

Antenna Pattern Input
Antenna Pattern: User-defined

User-defined antenna pattern for receiver should be given in the Antenna Pattern Input File.

Simulation Settings
Campaign: default-forest
Simulation Mode: Snapshot
Ground Cover: Vegetation

Preferences
☑ Include in Master Simulations
☐ Write Attenuation to Excel file

Ground Inputs
Dielectric Model: Wang
Ground Structure: Single-layered

Single / Multi-layered ground inputs shoud be given in the Configuration Inputs file. Multi-layered ground has additional dielectric profile fitting functions in this field.

Input Files
Configuration Inputs File: D:\Orhan\GitHub\SCoBi\source\input\configuration\default-ss-single-Tx_geostat.xlsx
Antenna Pattern File: D:\Orhan\GitHub\SCoBi\source\input\Rx_antenna_pattern\default_ant_pat.xlsx
Vegetation Inputs File: D:\Orhan\GitHub\SCoBi\source\input\vegetation\default-veg_for.xlsx

FIGURE 4. The SCoBi simulation inputs window.

field expects any character input and is combined with the time stamp of the simulation to generate the simulation output name. One of the most significant features of the SCoBi simulator, the simulation mode enables snapshot and time-series analyses. The former simulates every combination of varying configurations and scene dynamics, such as transmitter elevation and azimuth angles, VSM, and RMSH, to easily generate large numbers of simulated data sets. The latter allows the user to run temporal analyses, with every simulation iteration considering a corresponding set of dynamic parameters in conjunction with time stamps. The default input files use a day-of-year (DoY) numbering system.

The simulation mode selection affects the content of the configuration inputs file, as described in the section "Input Files." Ground cover allows the user to perform an analysis over a vegetated or bare soil terrain. If having vegetation cover is selected, then SCoBi requires a vegetation inputs file from the user, which is described later. The SCoBi user can also select among a few preferences, such as including a simulation in a master logging option or performing it as temporary as well as writing vegetation attenuation to an Excel file.

ACTION BUTTONS

The simulation inputs window houses three action buttons: load inputs, save inputs, and run SCoBi. The first is used for loading an existing system input (.mat extension) into the simulation inputs window. The second can be used to save the current input parameter values on the simulation inputs window as a SCoBi system input file with the .mat extension. The run SCoBi button allows the user to run a simulation with the inputs given in the simulation inputs window.

TRANSMITTER INPUTS

This panel consists of editable text fields and pop-up menus to determine the transmitter characteristics and orientation of the SCoBi simulations. The user can input the transmitter's operating frequency, range to Earth's center, and effective isotropic radiated power (EIRP) from this panel. The operating frequency should be chosen appropriately from the microwave spectrum based on the analysis requirements. The range should be determined taking into account the SCoBi simulator's assumption that the transmitter is a satellite far away from Earth. The EIRP is included in the inputs to account for its offset effect on the received power.

The transmitter can be chosen for right-hand circular polarization (RHCP), left-hand circular polarization, X-polarized, or Y-polarized. In the SCoBi model, the y-axes of the antennas are considered parallel to the ground plane; thus, Y-polarization stands for H-polarization (horizontal). X-polarization accounts for the V-polarization (vertical) because the *x*-axes of the antennas are complementary-perpendicular to their *y*-axes. The orientation of the transmitter allows the user to include either a geostationary or variable-orientation satellite. The orientation selection also makes changes in the preparation of the configuration inputs file such that the elevation and azimuth angles of a variable-orientation transmitter should be given in that file. On the other hand, the angles of a geostationary transmitter can be directly given in the simulation inputs window. The transmitter's boresight and specular directions are assumed to be the same in the SCoBi model because the transmitter is far away from Earth and these directions differ by a small angular difference. However, in the future, the system can be extended to input the real transmitter orbit dynamics. Another potential future extension to SCoBi could account for geosynchronous transmitter orientation as well.

RECEIVER INPUTS

The content and purpose of this panel are similar to those of the transmitter inputs. The receiver altitude and gain are given as inputs for the power calculations. The polarization of the receiver can be chosen in the same way as the transmitter. The receiver orientation can be specular facing or fixed. For specular-facing orientation, the main beam axis of the receiving antenna always faces the specular reflection point; thus, the receiver's zenith observation and azimuth observation angles are equal to the transmitter's incidence and azimuth angles, respectively. This orientation is aimed at directly analyzing any SoOp configuration's angular sensitivity for varying incidence angles by minimizing the antenna pattern effects and polarization mismatch, which might significantly dominate the ground-based observations.

The fixed orientation makes the receiver boresight direction always look at a fixed point, and fixed orientation angles (zenith and azimuth observation) can be given directly in the simulation inputs window. These receiver orientations enable ground-based analysis; however, the SCoBi simulator can be extended for low-altitude airborne instruments by adding a variable receiver orientation just as the transmitter inputs panel allows. In this case, the varying receiver orientation angles can be given in the configuration inputs files like the transmitter so that, for example, time-series analysis from the observation of an airborne receiver with variable roll, pitch, and yaw can be performed.

The final receiver input parameter is antenna pattern selection. SCoBi currently provides two different antenna pattern specification methods: user defined and generalized Gaussian. The user-defined antenna pattern definition is a powerful feature that allows users to employ both simulated and measured antenna radiation patterns by simply providing the normalized voltage pattern values to the system [such that theta (θ) angles span 180°, while phi (ϕ) angles span 360°]. The normalized voltage pattern of the antenna (copolarization and cross polarization for dual ports) may be measured in an anechoic chamber or generated in any antenna modeling tool and fed into SCoBi as the antenna pattern file (described in section "Input Files.") The second option for defining the antenna pattern, the generalized Gaussian, simply generates a 3D-symmetrical antenna pattern with side lobes. This option allows inputs, i.e., half-power beamwidth, side-lobe levels, and cross-polarization levels, to be provided directly on the GUI window.

GROUND INPUTS

This panel is used for deciding on the ground dielectric model and layer structure. The SCoBi simulator offers the option of using the dielectric models proposed by Dobson et al. [25], Mironov and Fomin [26], or Wang and Schmugge [27]. The ground can be modeled as single- or multilayered. The former provides a ground surface analysis only, whereas the latter is especially useful for root-zone analyses. The selection of the ground structure changes the content of the configuration inputs file, as described in the following section. SCoBi offers unprecedented strength because it allows both vegetation and bare soil analysis to be run over either single-layered or multilayered ground structures. The remaining ground inputs, such as soil texture or multilayer discretization, are provided through the configuration inputs file.

The simulation inputs window shows four different dielectric profile generation methods when the ground structure is multilayered. The user can choose from one to all of these methods when generating dielectric profiles and simulating GNSS-R observables (such as reflectivity) for these profiles. The discrete slab option can be selected to make SCoBi calculate the midpoint between each pair of VSM measurements within the soil layer. The user-defined soil moisture is then assumed to represent the soil moisture for the entire layer. For instance, for a VSM profile defined at points 5, 10, 20, and 40 cm within the soil moisture profile, the VSM at 5 cm will be representative of the calculated layer extending from 0 to 7.5 cm, the VSM value at 10 cm will represent values from 7.5 to 15 cm, the VSM value at 20 cm will represent values from 15 to 30 cm and the VSM value at 40 cm will represent the VSM from 30 cm to (40 cm + the bottom layer size). The bottom layer size (*zB*) is defined on the ground sheet of the configuration inputs file, which is described in the section "Input Files." The other available fit functions include second-order polynomial, third-order polynomial, and logistic regression fit. When any of these are selected, the value for *delZ*, defined on the ground sheet of the configuration inputs file, is used to generate a series of points from the top of the soil moisture profile ($z = 0$) to the bottom.

INPUT FILES

The SCoBi simulator runs the simulations through the simulation inputs window. The input parameters within this window are saved as a system input file with a .mat extension whenever a simulation is run or the user saves the input. The default system input files (forest, agriculture, soil, and root zone) are stored in the directory .\source\input\system\. (also shown in Figure 1).

Additional input files fed into the simulations are Microsoft Excel files. The need for these files and their contents may differ depending on the given inputs through the simulation inputs window. A comprehensive visualization and explanation of these Excel input files and their interactions with SCoBi can be found in the user's manual [17] and tutorial videos [20] and are described as follows.

CONFIGURATION INPUTS FILE

This file is required in every simulation and consists of two Excel spreadsheets: dynamic and ground. The dynamic spreadsheet defines the variable parameters, which may be given changing values with every simulation. The variable parameters include time stamps (DoYs), azimuth and elevation angles of the transmitter, RMSH roughness, and VSM. The ground spreadsheet includes the parameters defining ground texture and multilayering. The simulation mode, transmitter orientation, and ground structure selections determine the preparation of the content of this file. For example, the multilayered soil moisture profile is defined using both the dynamic and ground sheets of the configuration inputs file. On the ground sheet, values for soil bulk density, sand ratio, and clay ratio at multiple locations within the soil profile should be given; the single-layered ground case requires only one value for each of these parameters. Values for the air layer size (*zA*), bottom layer size (*zB*), and layer discretization (*delZ*) are also defined; these are not included in a single-layered simulation. Similar to values recorded by soil moisture data loggers, the dynamic sheet lists the VSM at different layer depths for a multilayered ground structure. When a time-series analysis is performed, each row is a different point in time, as denoted by the DoY column. Thus, the dynamic sheet lists the different VSM measurements as a function of time. Further advanced details are provided in the user's manual [20]. In addition, a number of default configuration inputs files accompany the SCoBi software distribution to help users understand the configurations needed to prepare this file for different analysis types in the following directory of the SCoBi download package: .\source\input\configuration\.

ANTENNA PATTERN FILE

This file is required only if the receiver antenna pattern is selected as user defined. Otherwise, the simulation inputs window disables the corresponding parts that allow input to this file. It consists of four spreadsheets—gnXX, gnXY, gnYX, and gnYY—that hold the normalized voltage pattern values for copolarization and cross polarizations for dual ports. The default antenna pattern file that comes with the SCoBi software distribution can be found in the following directory of the downloaded package: .\source\input\Rx_antenna_pattern\.

VEGETATION INPUTS FILE

This file is required only if the ground cover is selected as vegetation. Otherwise, the simulation inputs window disables the corresponding parts that allow the user to input this file. It consists of two spreadsheets: layers and kinds. The layers spreadsheet should provide detailed information about the vegetation layer thicknesses and the content of each individual layer. Vegetation cover can be divided into a number of layers by defining separate layer thicknesses for the purpose of placing scatterers, called *kinds* (leaf, branch, trunk, or needle), into different layers. For each vegetation layer row, the subsequent columns following the thickness column should define the content (involved constituent kinds) of the layer specified by the row. Detailed information about these kinds, such as the dimensions, densities, orientation, and dielectric constants, should be given in the kinds spreadsheet. New vegetation inputs files other than the default ones can be prepared following the user's manual [20]. Default files for forest and agricultural analysis come with the SCoBi release under the directory .\source\input\vegetation\.

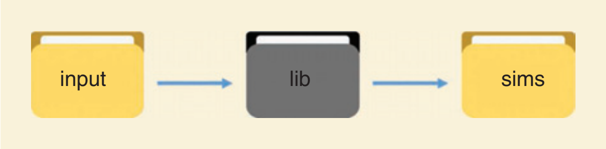

FIGURE 5. The black-box relationship between the input, lib, and output folders from the user's perspective.

SCoBi MODEL OUTPUTS

The basic relationship among the inputs, the SCoBi sourcecode (lib folder), and the outputs is, from the user's perspective, similar to the use of a black-box tool, as presented in Figure 5. In other words, the SCoBi user prepares the inputs and runs the simulator interacting with only the runSCoBi.m function. SCoBi, then, uses the inputs (both system input and Excel inputs) and generates the corresponding simulation outputs under the ./source/sims directory. It generates the complex field and real-valued power results for the directly received signals as well as reflection coefficient and reflectivity values for the specular reflection contribution. The SCoBi outputs can also be used to calculate the received power due to the specular reflection contribution. The sizes of the resulting matrices depend on the simulation inputs (snapshot or time-series simulation) and the number of varying values for dynamic system parameters.

The current SCoBi simulator version has a limited number of analysis functions, such as plotting reflectivity as a function of transmitter elevation angle or VSM. These initial plotting functions are provided to help users easily visualize the reflectivity; however, the simulator outputs are ready to be analyzed for phase or amplitude as well. Further details about the SCoBi outputs and analysis features can be found in the user's manual [20] and the tutorial videos [24].

CASE STUDIES

The default inputs of the system are aimed at allowing the user to easily learn the use of the SCoBi system and the differences between analyses. They enable performing four different case studies with the initial distribution package as well: forest, agriculture, soil, and root zone. In this section, the case studies are given with only the reflectivity results. However, advanced users can further analyze the bistatic phase, interferometry, reflection coefficient, or received power. Moreover, the effects of varying custom antenna patterns and specifications (polarization, polarization mismatch and crosstalk, orientation, and altitude) as well as different vegetation statistics on the reflectivity can be studied.

FOREST

The default input for the forest analysis, as seen in Figure 4, allows for a P-band simulation over a forested terrain of deciduous Paulownia trees. It considers a geostationary communication satellite operating at the P-band (370 MHz). It simulates a ground-based, *X*-polarized receiver that has an altitude of 20 m. A single-layered ground structure is modeled in this forest case. The vegetation layer is designed to resemble a Paulownia forest and so includes trunks, branches, and leaves along with statistics of dimensions, densities, orientation, and dielectric characteristics coming from in situ measurement data [28]. This example is described comprehensively in the SCoBi user's manual [20]. The simulated reflectivity as a function of VSM values used in these simulations is shown in Figure 6.

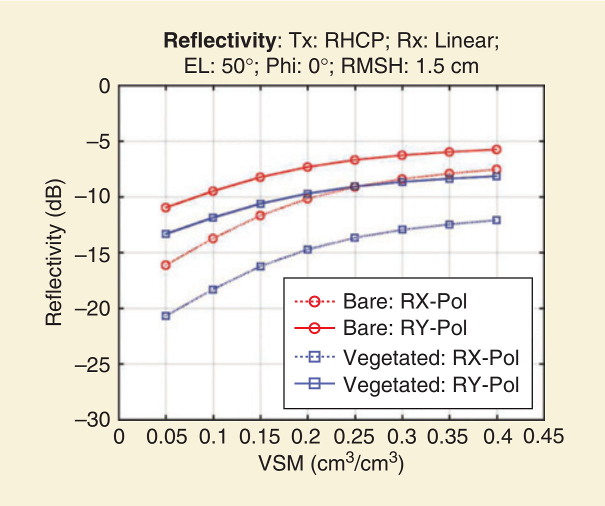

FIGURE 6. Reflectivity as a function of VSM for the default forest inputs. The transmitter elevation angle is 50°, and the surface RMSH roughness is 1.5 cm. Tx: transmitter; EL: elevation; RX-Pol: RHCP-to-X polarization; RY-Pol: RHCP-to-Y polarization.

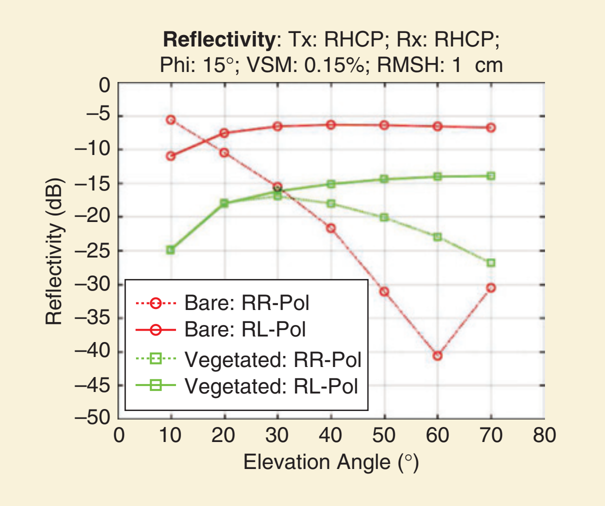

FIGURE 7. Reflectivity as a function of transmitter elevation for the default agricultural inputs. The transmitter's azimuth angle is 15°, VSM is 0.15 cm^3/cm^3, and the surface RMSH roughness is 1 cm.

AGRICULTURE

The default input for the agriculture analysis considers an agricultural field, where vegetation inputs enable modeling of the corn constituents. The transmitter is a GNSS satellite that operates at L1A band (1,575.42 MHz). The ground structure and receiver are similar to those of the forest defaults except that an RHCP antenna is assumed. The vegetation layer inputs are prepared considering the real-world statistics of the corn stalks, leaves, and cobs. This agriculture input configuration has been exploited in a corn simulation study, where GNSS-R responses to dynamic scene conditions are quantified [23]. This example is explored in greater detail in the SCoBi user's manual [20]. The simulated reflectivity as a function of the transmitter elevation angle is illustrated in Figure 7.

SOIL

The default input for the soil analysis allows the simulation of a P-band SoOp configuration over bare soil. The ground is considered to be single layered; hence, this analysis covers a surface reflection scenario. This setup employs the same transmitter as the default agriculture input and the same receiver as the forest input. The main purpose of the default soil inputs is to enable the performance of an L-band time-series analysis over a bare soil terrain. Further details about this example are included in the SCoBi user's manual [20].

ROOT ZONE

The default input for the root-zone analysis is quite different from that for the previous analyses because it represents a multilayered soil profile. A multilayered bare soil terrain is considered in this default input for the sake of simplicity. However, any root-zone analysis may include vegetation cover as well. The default input uses the same transmitter satellite as the forest analysis. It considers a similar receiver as well, but the receiver now has a set of fixed orientation angles. A detailed example is explored in the SCoBi user's manual [20].

SCoBi MODEL ARCHITECTURE

The SCoBi simulator framework was developed by an iterative and incremental development process, including requirements analysis, design, implementation, testing, and deployment. For instance, the requirements analysis took place mostly during the creation of the SCoBi model [16] over several years, and then the simulator framework was designed, implemented, and tested with increments. However, many iterations have been performed on the requirements, design, and implementation based on the results of the tests and findings of the studies [16], [23] undertaken for the preliminary SCoBi versions. Our tests demonstrated the verification of the SCoBi simulator framework. In other words, tests show that the simulator meets the requirements of the SCoBi model. The validation of SCoBi is mature, to some degree, because the simulated results are compared and shown to be in agreement with several experimental studies [16], [23]. The multilayered ground simulations for bare soil and vegetated terrains are currently being used for validation purposes [17] for the SNoOPI project [18]. CYGNSS-based reflectivity derivations [4] over homogenous and known terrain conditions, such as agricultural fields, are currently being compared to SCoBi-generated reflectivity values during our ongoing research [29]. Moreover, airborne and tower data collection campaigns are planned for further experimental validation in the near future. For this purpose, observatory data are currently being collected over several terrains using in-house-built drone-based receivers. We will handle the maintenance of the SCoBi product for scheduled improvements (such as improving exception-handling mechanisms or adding new SoOp analysis types), user requests, and possible scientific collaborations.

The SCoBi source code was implemented in the MATLAB R2017a environment; however, it is compatible with the versions above MATLAB R2015a (the oldest version that SCoBi was tested with) within the MS Windows Operating System (64-bit Windows 10). SCoBi does not require additional MATLAB toolboxes or plugins. MATLAB was chosen for the development because of its common use among researchers, efficient handling of the matrices, simple scripting features, and plotting capabilities. Both the structural and behavioral design models of the SCoBi software can be found in the Sparx Systems' Enterprise Architect design file shown in Figure 1. However, the SCoBi design details can be explained as follows.

STRUCTURAL DESIGN

The SCoBi architectural design is mainly achieved using the procedural programming principles MATLAB intrinsically supports. However, object-oriented programming (OOP) design and implementation principles are also utilized, as needed, for advanced design, data encapsulation, manipulation, code organization and readability, and maintenance purposes. Combining two design approaches offers the enumerated advantages of the OOP design while exploiting MATLAB's procedural scripting capabilities. For instance, the simulation engine (runSCoBi.m) is operated only by a MATLAB procedure (function) implementation, whereas the dynamic and static system parameters are handled with the help of several classes with singleton pattern features.

The software packages within the source code are determined with respect to the relational hierarchy between each software entity (MATLAB functions or classes). Each package consists of several functions and/or classes. The Unified Modeling Language (UML) package diagram for the SCoBi source code (/source/lib/) packages is represented in Figure 8. The runSCoBi.m function is directly beneath the lib package. It uses several packages to perform specific tasks to compute the model's output; for instance, the gui package obtains the user inputs for simulations, the init and param packages initialize the simulation parameters using the information (inputs) from the gui package, and the main package performs every simulation iteration. The main package uses the param package to manipulate parameters-related tasks, the bistatic package to handle the bistatic geometry, the ground package to account for ground operations (dielectric calculation and specular reflection), the multilayer and vegetation packages (if involved in a simulation), and the products package to create and store simulation outputs. There are information flows from the bistatic, ground, multilayer (if included), and vegetation (if included) packages to the products package.

The SCoBi design file (created in Enterprise Architect) also includes the UML class model of the software (lib package). In fact, class models are dedicated to the class instances in the OOP designs; however, this model is employed to depict the entire structural relations (usage, information flow, or inheritance) between the source code entities (MATLAB functions and classes). Although this is not a valid use of the class model, it can help developers understand the general structure of SCoBi. Because the overall SCoBi class model is highly complicated, class models are also provided for the runSCoBi.m and mainSCoBi.m functions, which are the simulation engine and simulation iterator functions, respectively. These two models show only the dedicated function and its first-degree relations with the other source code entities.

BEHAVIORAL DESIGN

UML behavioral diagrams, such as sequence and activity diagrams, are specialized to demonstrate the dynamic aspects of software programs. The UML activity diagrams are used to show the temporal flow of the SCoBi simulator. The SCoBi design file contains activity diagrams for both the simulation engine and simulation iterator because these two deal with the overall flow. The SCoBi simulator framework always starts by running the runSCoBi.m function. The activities and the decisions performed as part of this function are pictured in Figure 9. In summary, the simulation engine receives the user inputs, initializes the parameters and simulation by using these inputs (with the help of input validation controls), and calls the simulation iterator (mainSCoBi.m) after writing the simulation reports.

The runSCoBi.m determines the required number of simulation iterations for a chosen simulation using the parameters manager class. This is because the simulation mode, whether snapshot or time-series, in conjunction with the system and configuration inputs may change the number of total simulation iterations. Details of this phenomenon are described in both the user's manual [20] and the tutorial videos [24]. The simulation engine then runs the simulation iteration function (mainSCoBi.m) for the number of simulations.

The simulation iteration function, mainSCoBi.m, is always the same regardless of the analysis type. However, the analysis type and input selections affect the package usage and procedure calls within mainSCoBi.m. For instance, a vegetation analysis requires SCoBi to use the software package called *vegetation* and to call several related procedures, such as the propagation calculation.

The flow of the mainSCoBi.m function is shown with the help of a UML activity diagram in Figure 10. Because

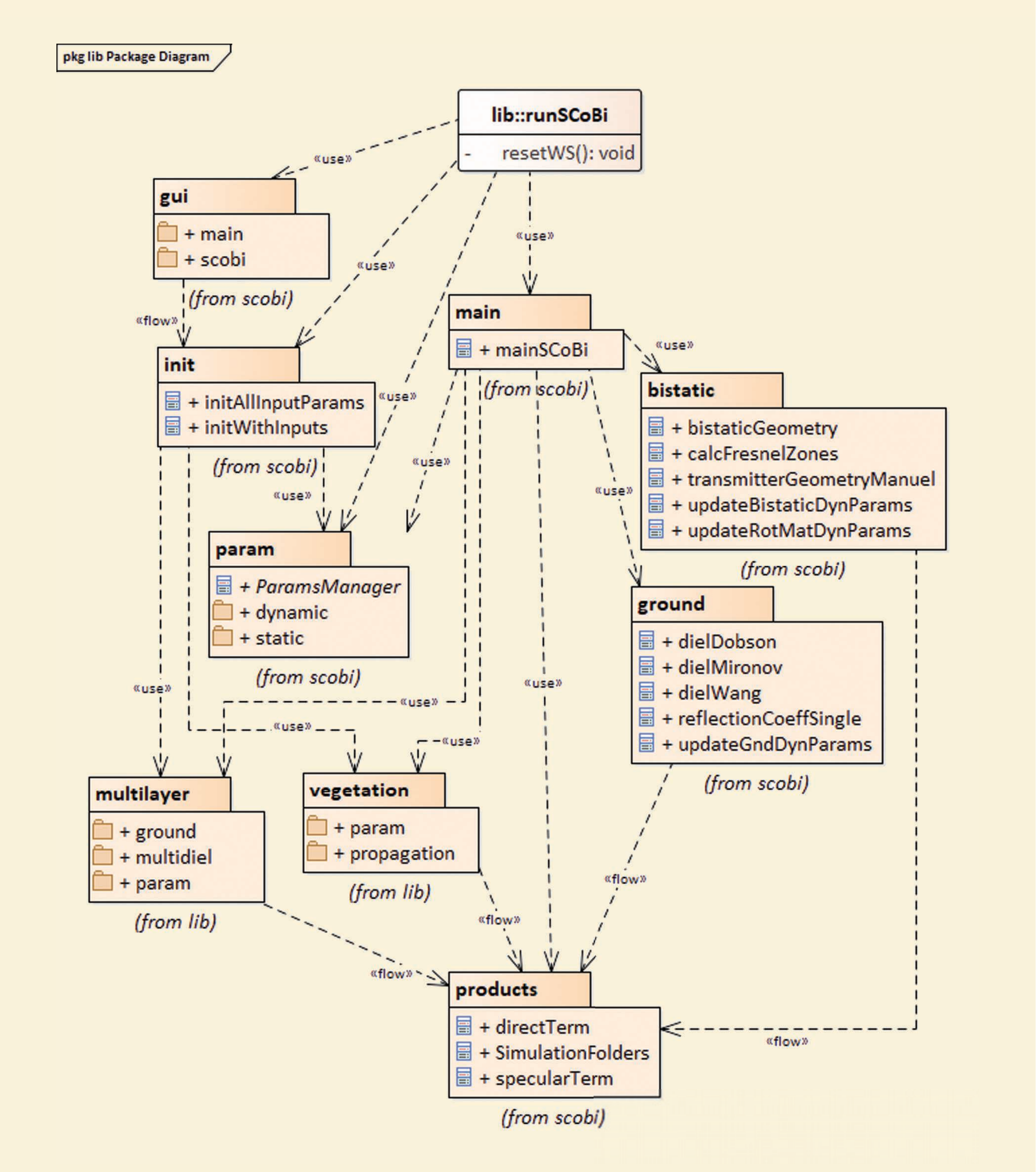

FIGURE 8. The SCoBi lib package diagram.

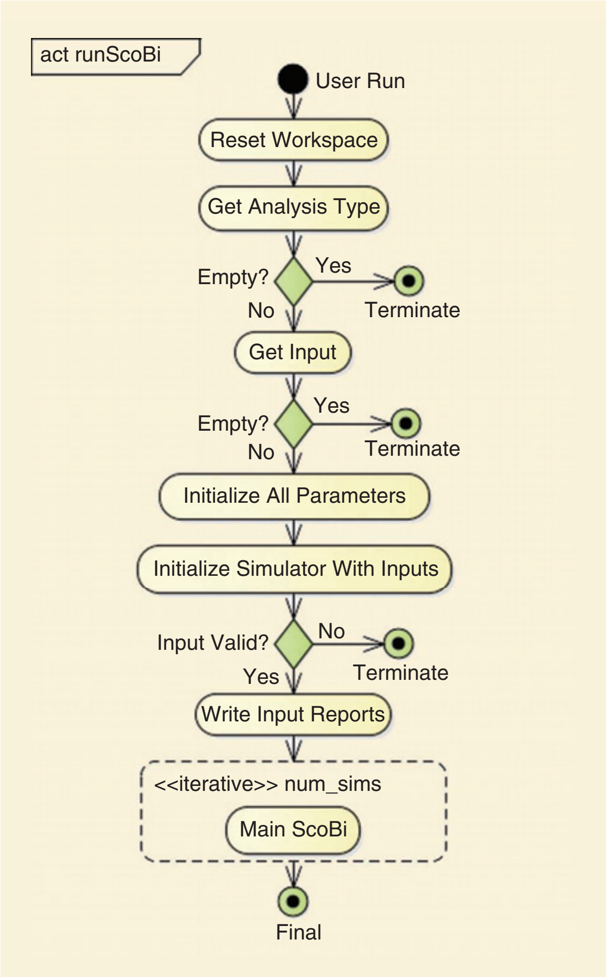

FIGURE 9. The runSCoBi.m (simulation engine) activity diagram.

this function is called for in every iteration of the simulation engine, it handles the updates and calculations related to the iterative steps. For instance, it starts by updating the dynamic parameters for the bistatic geometry and ground surface. These updates are needed in each iteration because the simulation inputs may contain changing transmitter orientation angles and land geophysical parameters, such as VSM and RMSH. If the ground structure is multilayered, the multilayer dielectric profiles are computed. If the ground cover is vegetation, the vegetation propagation is calculated; furthermore, the vegetation attenuation values are written into an Excel file if chosen by the user. The polarization rotation matrices for the local antenna coordinate systems must also be updated due to changes in the bistatic geometry during each iteration. Finally, the current iteration prepares to generate the SoOp deliverables (the direct and specular contributions) for the parameters in the iteration and stores the calculations incrementally to the simulation outputs.

FUTURE DEVELOPMENTS

The SCoBi simulator was designed with the intention to foster a community of developers who may advance the modeling and simulation capabilities for SoOp over land applications. The framework is designed to simplify the implementation of new features for the simulator. A developer's manual is included as part of the SCoBi distribution package to encourage and assist developers in extending this SoOp simulator.

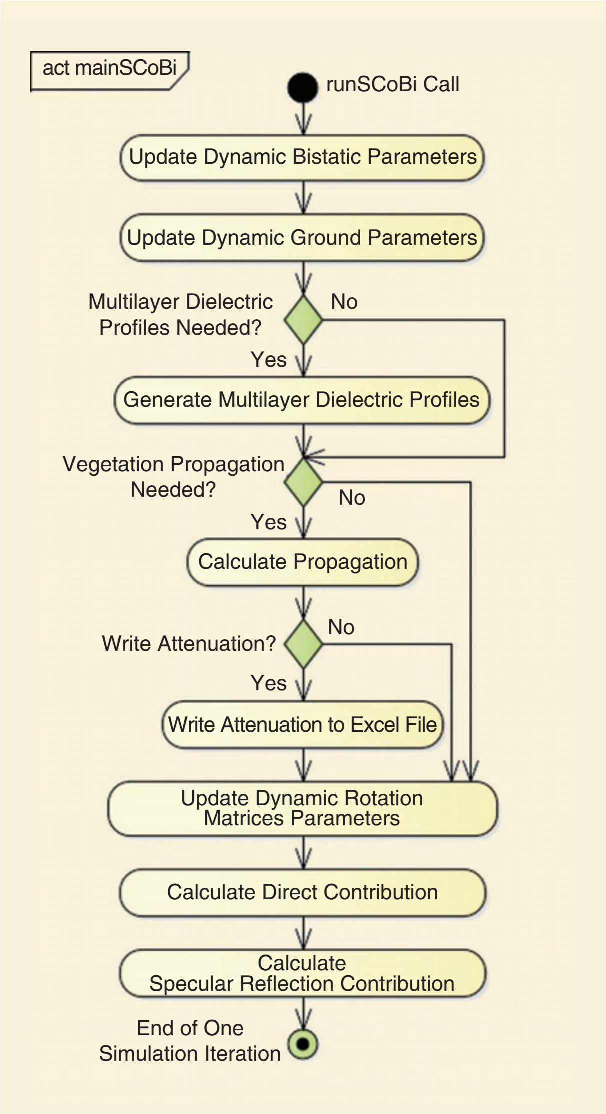

FIGURE 10. The mainSCoBi.m (simulation iteration function) activity diagram.

Potential future extensions to the SCoBi framework are twofold: improvements made by its initial developers and improvements made by the community for specific needs. We aim to organize future extensions in two directions: improving the structure of the SCoBi framework and adding new capabilities. Implementing advanced exception-handling mechanisms is one potential major structural improvement to strengthen the current architecture, although the current SCoBi provides several handling techniques, such as input manipulation (regulation) and use of management classes. Batch running without any GUI window could be another objective to make SCoBi more flexible for fast-analysis purposes.

The second class of improvements we aim to include in future versions involves enlarging SCoBi's features. For instance, the visualization capabilities are as significant as the generation of the simulated observables. We plan to release the plotting options for time-series analysis over multilayered grounds as well as provide user-friendly GUI windows for visualization purposes.

SCoBi can also be extended in response to the Earth science community's needs. Such extensions can be made by us at the request of users, through collaborations, or based on future users' and developers' own initiatives. To illustrate, diffuse scattering, which is already handled by the SCoBi model [16], might be added to the simulator if any specific need arises, although we believe diffuse contribution is far from dominating SoOp land observables. In addition, the SCoBi forward model possesses many capabilities not yet utilized by the SCoBi simulator, although the current distribution contains many novel tools and features. For instance, the model supports the use of new antenna pattern methods; thus, a new antenna pattern generation, such as cosine to power n, can be added to the framework. Similarly, geosynchronous transmitters, a new ground dielectric model, or a new plotting function can be incorporated into the framework. For those who try to extend SCoBi alone, the SCoBi developer's manual and UML designs can help. A major extension could be the implementation of one of the unimplemented analysis types. For example, snow cover on the ground, topographic relief to the current scattering calculations, permafrost analysis within the root zone, or wetland analysis can be introduced to the model.

CONCLUSIONS

A new fully polarimetric coherent SoOp simulator was introduced for the Earth science community. It has unprecedented capabilities, such as supporting any combination of polarizations, taking into account significant antenna characteristics (polarization crosstalk and mismatch, different antenna pattern methods, and so forth), handling vegetation and multilayered soil analysis simultaneously, supporting multiple models for soil dielectric calculations, and enabling interferometric analysis by providing the complex field quantities. It simulates direct and specular reflection contributions on bistatically received signals. It is released with a set of built-in plotting functions. Furthermore, it has a user-friendly GUI, it is free and open source, and it offers a user's manual [20] and developer's manual [21] together with a set of tutorial videos [24].

The SCoBi simulator framework is aimed at creating an environment wherein both lifelong researchers and newcomers to SoOp reflectometry can investigate new methods for SoOp Earth science applications. It can be exploited by researchers, scientists, and even end users with little to no electromagnetic background. SCoBi has the potential to allow users to study new SoOp techniques, make analyzing SoOp methods in detail possible, help determine optimal configurations for directed use, and enable generating, visualizing, and analyzing large amount of simulated test data.

AUTHOR INFORMATION

Orhan Eroglu (oe79@msstate.edu) received his B.S. degree in computer engineering from Bogazici University, Istanbul, Turkey, in 2009 and his M.S. degree in computer engineering from the Turkish Air Force Academy, Aeronautics and Space Technology Institute, Istanbul, in 2013. He worked as a senior researcher in the Informatics and Information Security Research Center, Scientific and Technological Research Council of Turkey, between 2009 and 2016. He is a Ph.D. student with the Information Processing and Sensing Laboratory, Electrical and Computer Engineering Department, Mississippi State University. His research interests include data analysis and machine learning in signals of opportunity remote sensing applications. He is a NASA Earth and Space Science Fellow with his study "Unveiling CYGNSS Land Signatures for High Spatiotemporal Soil Moisture Estimation." He is a Student Member of the IEEE.

Dylan R. Boyd (db1950@msstate.edu) received his B.S. degree in electrical and computer engineering from Mississippi State University (MSU) in 2017. He is a Ph.D. student with the Information Processing and Sensing Laboratory, Electrical and Computer Engineering Department, MSU. His research interests include investigating multifrequency signals of opportunity sources for Earth science parameter inverse problems. He is a Student Member of the IEEE.

Mehmet Kurum (kurum@ece.msstate.edu) received his B.S. degree in electrical and electronics engineering from Bogazici University, Istanbul, Turkey, in 2003 and his M.S. and Ph.D. degrees in electrical engineering from George Washington University, Washington, D.C., in 2005 and 2009, respectively. He held a post-doctoral position with the Hydrological Sciences Laboratory, NASA Goddard Space Flight Center, Greenbelt, Maryland. In 2016, he became an assistant professor with the Information Processing and Sensing Laboratory, Department of Electrical and Computer Engineering, Mississippi State University. His research interests include microwave and millimeter-wave remote sensing, radio frequency sensors and systems, machine learning, smartphone sensing, and signals of opportunity. He was a recipient of the Leopold B. Felsen Award for excellence in electromagnetics in 2013 and the International Union of Radio Science (URSI) Young Scientist Award in 2014. He serves as an Early Career Representative for the International URSI Commission F (Wave Propagation and Remote Sensing). He is a Senior Member of the IEEE.

REFERENCES

[1] S. Gleason et al., "Detection and processing of bistatically reflected GPS signals from low earth orbit for the purpose of ocean

remote sensing," *IEEE Trans. Geosci. Remote Sens.*, vol. 43, no. 6, pp. 1229–1241, 2005.

[2] S. Gleason, M. Adjrad, and M. Unwin, "Sensing ocean, ice and land reflected signals from space: Results from the U.K.-DMC GPS reflectometry experiment," in *Proc. 2005 ION GNSS Technical Meeting*, pp. 11–16.

[3] G. Foti et al., "Spaceborne GNSS reflectometry for ocean winds: First results from the U.K. TechDemoSat-1 mission," *Geophys. Res. Lett.*, vol. 42, no. 13, pp. 5435–5441, 2015.

[4] C. S. Ruf et al., "The CYGNSS nanosatellite constellation hurricane mission," in *Proc. IEEE Int. Geosci. Remote Sens. Symp.*, 2012, pp. 214–216.

[5] C. S. Ruf et al., "New ocean winds satellite mission to probe hurricanes and tropical convection," *Bull. Am. Meteorol. Soc.*, vol. 97, no. 3, pp. 385–395, 2016.

[6] R. Rose, S. Gleason, and C. Ruf, "NASA CYGNSS Mission Update; A pathfinder for operational GNSS scatterometry remote sensing applications," in *Proc. 31st Annu. AIAA/USU Conf. Small Satellites*, 2017, pp. 1–10.

[7] P. Liang, L. E. Pierce, and M. Moghaddam, "Radiative transfer model for microwave bistatic scattering from forest canopies," *IEEE Trans. Geosci. Remote Sens.*, vol. 43, no. 11, pp. 2470–2483, 2005.

[8] P. Ferrazzoli, L. Guerriero, N. Pierdicca, and R. Rahmoune, "Forest biomass monitoring with GNSS-R: Theoretical simulations," *Adv. Space Res.*, vol. 47, no. 10, pp. 1823–1832, 2011.

[9] N. Pierdicca, L. Guerriero, R. Giusto, M. Brogioni, and A. Egido, "SAVERS: A simulator of GNSS reflections from bare and vegetated soils," *IEEE Trans. Geosci. Remote Sens.*, vol. 52, no. 10, pp. 6542–6554, 2014.

[10] X. Wu and S. Jin, "GNSS-Reflectometry: Forest canopies polarization scattering properties and modeling," *Adv. Space Res.*, vol. 54, no. 5, pp. 863–870, 2014.

[11] X. Wu, S. Jin, and J. Xia, "A forward GPS multipath simulator based on the vegetation radiative transfer equation model," *Sensors (Switzerland)*, vol. 17, no. 6, 2017.

[12] L. Thirion-Lefevre, E. Colin-Koeniguer, and C. Dahon, "Bistatic scattering from forest components. Part I: Coherent polarimetric modelling and analysis of simulated results," *Waves Random Complex Media*, vol. 20, no. 1, pp. 36–61, Feb. 2010.

[13] F. G. Nievinski and K. M. Larson, "An open source GPS multipath simulator in Matlab/Octave," *GPS Solut.*, vol. 18, no. 3, pp. 473–481, 2014.

[14] F. G. Nievinski and K. M. Larson, "Forward modeling of GPS multipath for near-surface reflectometry and positioning applications," *GPS Solut.*, vol. 18, no. 2, pp. 309–322, 2014.

[15] M. Kurum, M. Deshpande, A. T. Joseph, P. E. O'Neill, R. H. Lang, and O. Eroglu, "Development of a coherent bistatic vegetation model for Signal of Opportunity applications at VHF/UHF-bands," in *Proc. IEEE Geoscience and Remote Sensing Symp. (IGARSS)*, 2017, pp. 4894–4896.

[16] M. Kurum, M. Deshpande, A. T. Joseph, P. E. O'Neill, R. Lang, and O. Eroglu, "SCoBi-Veg: A generalized bistatic scattering model of reflectometry from vegetation for signals of opportunity applications," *IEEE Trans. Geosci. Remote Sensing*, vol. 57, no. 2, pp. 1049–1068, 2018.

[17] J. L. Garrison et al., "Remote sensing of root-zone soil moisture using I- and P-band Signals of Opportunity: Instrument validation studies," in *Proc. IEEE Geoscience Remote Sensing Symp.*, 2018, pp. 8305–8308.

[18] J. L. Garrison et al., "SNOOPI: A technology validation mission for P-band reflectometry using signals of opportunity," in *Proc. IGARSS 2019–2019 IEEE Int. Geoscience and Remote Sensing Symp.*, 2019, pp. 5082–5085. doi: 10.1109/IGARSS.2019.8900351.

[19] O. Eroglu, D. R. Boyd, and M. Kurum, "SCoBi v1.0.0 release package," Accessed on: Nov. 6, 2018. [Online]. Available: https://github.com/impresslab/SCoBi

[20] O. Eroglu, D. R. Boyd, and M. Kurum, "SCoBi user's manual," Accessed on: Nov. 6, 2018. [Online]. Available: https://github.com/impresslab/SCoBi/blob/master/docs/manuals/SCoBi-User_Manual-v1_0.pdf

[21] O. Eroglu, D. R. Boyd, and M. Kurum, "SCoBi developer's manual," Accessed on: Nov. 6, 2018. [Online]. Available: https://github.com/impresslab/SCoBi/blob/master/docs/manuals/SCoBi-Developer_Manual-v1_0.pdf

[22] O. Eroglu, D. R. Boyd, and M. Kurum, "SCoBi quick start guide," Accessed on: Nov. 6, 2018. [Online]. Available: https://github.com/impresslab/SCoBi/blob/master/docs/manuals/SCoBi-Quick_Start_Guide-v1_0.pdf

[23] O. Eroglu, M. Kurum, and J. E. Ball, "Response of GNSS-R on dynamic vegetated terrain conditions," *J. Sel. Topics Appl. Earth Observ. and Remote Sensing*, to be published.

[24] D. R. Boyd, O. Eroglu, and M. Kurum, "SCoBi tutorial videos," Accessed on: Nov. 6, 2018. [Online]. Available: https://www.youtube.com/playlist?list=PLpNPNnGsHon7WyQ8IkK6odma0wsqjfZi4

[25] M. C. Dobson, F. F. Ulaby, M. T. Hallikainen, and M. A. El-Rayes, "Microwave dielectric behavior of wet soil - Part II: Dielectric mixing models," *IEEE Trans. Geosci. Remote Sens.*, vol. 23, no. 1, pp. 35–46, 1985.

[26] V. L. Mironov and S. V. Fomin, "Temperature dependable microwave dielectric model for moist soils," in *Proc. PIERS*, 2009, pp. 23–27.

[27] J. R. Wang and T. J. Schmugge, "An empirical model for the complex dielectric permittivity of soils as a function of water content," *IEEE Trans. Geosci. Remote Sens.*, vol. GE-18, no. 4, pp. 288–295, 1980.

[28] M. Kurum, R. H. Lang, P. E. O'Neill, A. T. Joseph, T. J. Jackson, and M. H. Cosh, "A first-order radiative transfer model for microwave radiometry of forest canopies at L-band," *IEEE Trans. Geosci. Remote Sens.*, vol. 49, no. 9, pp. 3167–3179, 2011.

[29] O. Eroglu and M. Kurum, "Unveiling CYGNSS land signatures for high spatiotemporal soil moisture estimation," in *2018 NESSF Awards: Projects awarded funding under the NASA Earth and Space Science Fellowship (NESSF) Program 2018*, 2018 NASA Earth and Space Science Fellowship Program, Washington, D.C., grant 80NSSC18K1329, 2018.

XIAO XIANG ZHU, JINGLIANG HU, CHUNPING QIU, YILEI SHI, JIAN KANG, LICHAO MOU,
HOSSEIN BAGHERI, MATTHIAS HÄBERLE, YUANSHENG HUA, RONG HUANG, LLOYD HUGHES,
HAO LI, YAO SUN, GUICHEN ZHANG, SHIYAO HAN, MICHAEL SCHMITT, AND YUANYUAN WANG

So2Sat LCZ42

A benchmark data set for the classification of global local climate zones

Gaining access to labeled reference data is one of the great challenges in supervised machine-learning endeavors. This is especially true for an automated analysis of remote sensing images on a global scale, which enables us to address global challenges, such as urbanization and climate change, using state-of-the-art machine-learning techniques. To meet these pressing needs, especially in urban research, we provide open access to a valuable benchmark data set, So2Sat LCZ42, which consists of local-climate-zone (LCZ) labels of approximately half a million *Sentinel-1* and *Sentinel-2* image patches in 42 urban agglomerations (plus 10 additional smaller areas) across the globe.

This data set was labeled by a group of domain experts following a carefully designed workflow and evaluation process. We conducted rigorous quality assessment with independent label voting by domain experts, which is rarely done in other labeled remote sensing data sets. The data set achieved an overall confidence of 85%. We believe this is a first step toward an unbiased, globally distributed data set for urban growth monitoring using machine-learning methods, because LCZ analysis provides a rather objective measure compared with many other semantic land-use and land-cover classification systems. It measures morphology, compactness, and height of urban areas, which are less dependent on human activity and culture. Furthermore, such large-scale labeled data with uncertainty measures can serve as a benchmark for cutting-edge machine-learning research specific to Earth observation (EO), such as automatic topology learning, data fusion, modeling uncertainties in machine learning, and many more. This data set can be accessed at http://doi.org/10.14459/2018mp1483140.

THE NEED FOR LOCAL-CLIMATE-ZONE LABELS

The production of land-use/land-cover (LULC) maps at large or even global scales is an essential task in the field of remote sensing. These maps can provide valuable input for many societal questions, such as understanding human poverty or climate change, supporting the conservation of biodiversity and ecosystems, and providing stakeholder information for disaster management and sustainable urban development [1].

Urbanization is undoubtedly the most important megatrend in the 21st century after climate change. Currently, half of humanity—3.5 billion people—lives in cities. Shockingly, one billion of them still live in slums. Therefore, sustainable urban development has become one of the 17 sustainable development goals of the United Nations. Today, sustainable development increasingly depends on the successful management of urban growth, especially in developing countries, where the pace of urbanization is projected to be the fastest, according to *World Urbanization Prospects: The 2018 Revision* [2]. LULC maps enable us to describe, track, and manage urban growth in an objective and consistent manner.

Examples of global LULC products created by the remote sensing community include the Global Urban Footprint [3], [4], produced from synthetic aperture radar (SAR) data acquired by the TanDEM-X mission; the Global Human Settlement Layer, created from global, multitemporal archives of fine-scale satellite imagery, census data, and volunteered geographic information [5]; and the Finer Resolution Observation and Monitoring of Global Land Cover and GlobeLand30 data sets, generated from 30-m-resolution *Landsat* data [6]. This list is not exhaustive; however, these products all provide semantic labels of urban and nonurban or even more specific classes. These semantic labels are often subjective (to human interpretation) and culture-dependent. For example, the definitions of urban and nonurban areas might be drastically different in Europe and Africa and from person to person.

LOCAL CLIMATE ZONES IN GLOBAL URBAN MAPPING

For consistent analysis across the globe, an objective and culture-independent classification scheme for urban areas

Digital Object Identifier 10.1109/MGRS.2020.2964708
Date of current version: 21 September 2020

is pressingly needed. After extensive research, we turned to LCZs, which were originally developed for metadata communication of observational urban heat island studies [7]. There are 17 classes in the LCZ classification scheme; 10 are built classes and seven are natural classes. They are based on climate-relevant surface properties on the local scale, which are mainly related to 3D surface structures (e.g., the height and density of buildings and trees), surface cover (e.g., vegetation or paving), and anthropogenic parameters (such as human-based heat output).

A schematic drawing of the 17 classes is shown in Figure 1(a). The 10 urban classes describe the morphology of the area, including the density and height of the buildings as well as the percentage of impervious surface. The urban classes are mostly shown in red, with decreasing intensities as the building density and height decrease from compact high-rise to open low-rise. Figure 1(b) shows the LCZ classification of Vancouver, Canada, created by the authors. The dark red part marked by the yellow rectangle is downtown Vancouver, where most of Vancouver's high-rise buildings are located. The light red part of the classification map is mostly low-rise residential houses. As a reference, the Google image of this area in Figure 1(c).

Because the LCZ classes are defined by their physical properties, they are generic and applicable to cities across the world, offering the potential to compare different areas of various cities with trenchant distinctions representing the heterogeneous thermal behavior within an urban environment [8]. In addition to the increasing impact on worldwide climatological studies, such as the cooling effect of green infrastructure and microclimatic effects on town peripheries [9]–[18], researchers have recently started to use the LCZ approach to classify the internal structure of urban areas, providing promising information for various applications, such as infrastructure planning, disaster mitigation, health and green-space planning, and population assessment [19], [20]. The remote sensing community also addressed this topic by organizing the 2017 IEEE Geoscience and Remote Sensing Society Data Fusion Contest, which had the goal of LCZ classification [21].

RELATED WORK IN LOCAL-CLIMATE-ZONE CLASSIFICATION

COMMUNITY-BASED LOCAL-CLIMATE-ZONE MAPPING

A significant part of the existing development of LCZ classification is community-based, large-scale LCZ mapping using freely available *Landsat* data and software [23]–[25]. The World Urban Database and Portal (WUDAPT) [22], a community-driven initiative, was organized by researchers to map high-quality LCZ maps worldwide. Within this framework, currently, almost 100 cities worldwide have been mapped with moderate quality, providing sufficient detail for certain model applications [26]. LCZ maps of tens of cities, after undergoing quality assessment and generation of metadata, are now openly available at the WUDAPT portal. More recently, LCZs of Europe are being mapped as part of the WUDAPT project, with data from *Sentinel-1*, *Sentinel-2*, and the Defense Meteorological Program Operational Linescan System Nighttime Lights product [27].

These community-based efforts mark the first step toward a more synergetic cooperation among researchers. However, multiple studies have reported that the quality of the produced LCZ maps is inconsistent [28], [29], as the procedures strongly rely on the knowledge of individual volunteers. For example, the methods of community-based LCZ mapping mainly consist of 1) labeling of reference data in Google Earth and 2) classification using shallow learning algorithms, such as random forest (RF) in geographic information system software, a process detailed in [8].

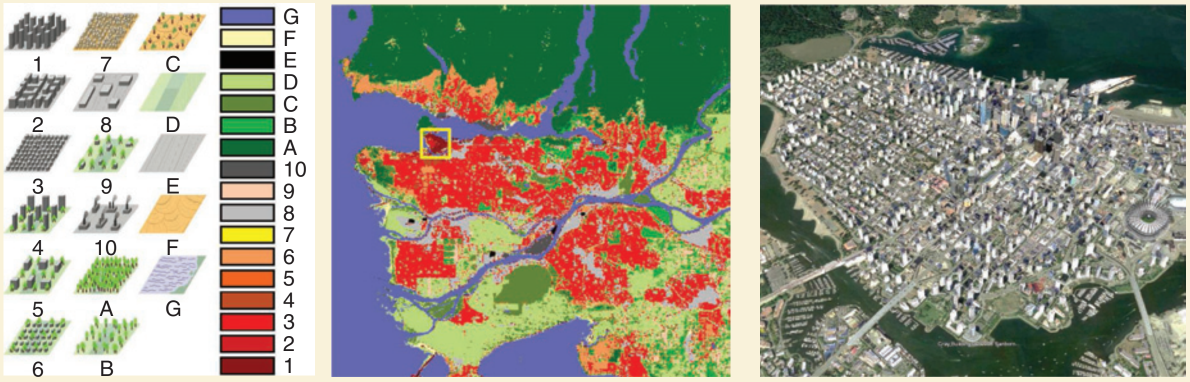

(a) (b) (c)

FIGURE 1. (a) A schematic drawing of the 17 LCZ classes. (Source: modified from the World Urban Database and Portal [22].) (b) An LCZ classification map of Vancouver, Canada, created by the authors. (c) A Google image of downtown Vancouver, where most of the high-rise buildings are located. The yellow rectangle in (b) map marks the downtown areas. (a) was modified from the WUDAPT [22].

ALGORITHMIC DEVELOPMENT

Therefore, significant development is still needed to achieve global LCZ mapping because of the lack of high-quality labels and transferable classifiers for worldwide deployment. There are various promising classifiers for LCZ recently proposed by different research groups, including RF, support vector machines (SVMs) [30], canonical correlation forests [31], [32], rotation forests [21], gradient-boosting machines [33], and ensembles of multiple classifiers [34]. The data used are mainly satellite data in the optical and microwave ranges, such as *Landsat*, *Sentinel-1*, and *Sentinel-2* images.

Recently, fusing of multisource data, such as satellite images and Google Street View, has also been investigated for LCZ classification [35]. Deep learning certainly played an important role in LULC using remote sensing data [36]. Multiple algorithms based on convolutional neural networks, such as residual neural network and ResNeXt, [35], [37]–[42] have been developed. These approaches provide satisfying results for specific areas. However, according to [8], [26], and [43], regional variations in vegetation and artificial materials as well as significant variations in cultural and physical environmental factors cause large intraclass variability of spectral signatures. One existing effort to further improve LCZ classification results is developing more robust machine-learning models with high generalization ability to facilitate efficient upscaling in a reasonable time frame [27], [43]. Deep-learning-based models have been shown to have better generalization ability; thus, they can be better exploited for LCZ classification [36], [40].

Despite active algorithmic development, the global transferability of a machine-learning LCZ model requires a large quantity of globally distributed and reliable reference data as a first step. Such a data set is nonexistent in the community; this task is addressed in this article.

CONTRIBUTIONS OF THIS ARTICLE

THE DATA SET

To answer the pressing need for LCZ training data sets, we carefully selected and labeled 42 urban agglomerations plus 10 additional smaller areas across all of the continents (except Antarctica) around the globe. Their geographic distribution can be seen in Figure 2. Many polygons in those cities were manually labeled by the authors. By projecting these labels to the corresponding coregistered *Sentinel-1* and *Sentinel-2* images, we obtained 400,673 pairs of corresponding *Sentinel-1* SAR and *Sentinel-2* multispectral image patches with LCZ labels. An impression of the *Sentinel* image patch pairs in the data set can be seen in Figure 3. However, the actual patches in the data set have a dimension of 320 × 320 m, which is smaller than the visualization in Figure 3. Accompanying this article, we provide open access to this high-quality So2Sat LCZ42 data set to the research community. This is meant to foster the development of fully automatic classification pipelines based on modern machine-learning approaches and support the accelerated use of LCZ mapping at global scale.

IMPROVED LABELING WORKFLOW

We found that merely following the definition of LCZs in [9] and the labeling process mentioned in WUDAPT is not optimal for a joint labeling activity by a group of people because of the vague definitions of some LCZ classes. To ensure the highest possible quality of the result, we designed a rigorous labeling workflow and decision rules, shown in Figure 4 and “Decision Rule of Local-Climate-Zone Labeling,” respectively. Meetings were conducted before and during the labeling process to calibrate our understanding of the definitions of the 17 classes. Afterward, the labeling

FIGURE 2. The locations of the 42 main cities (green dots) and 10 additional cities (orange dots) included in the So2Sat LCZ42 data set. (Source: Microsoft Bing Maps.)

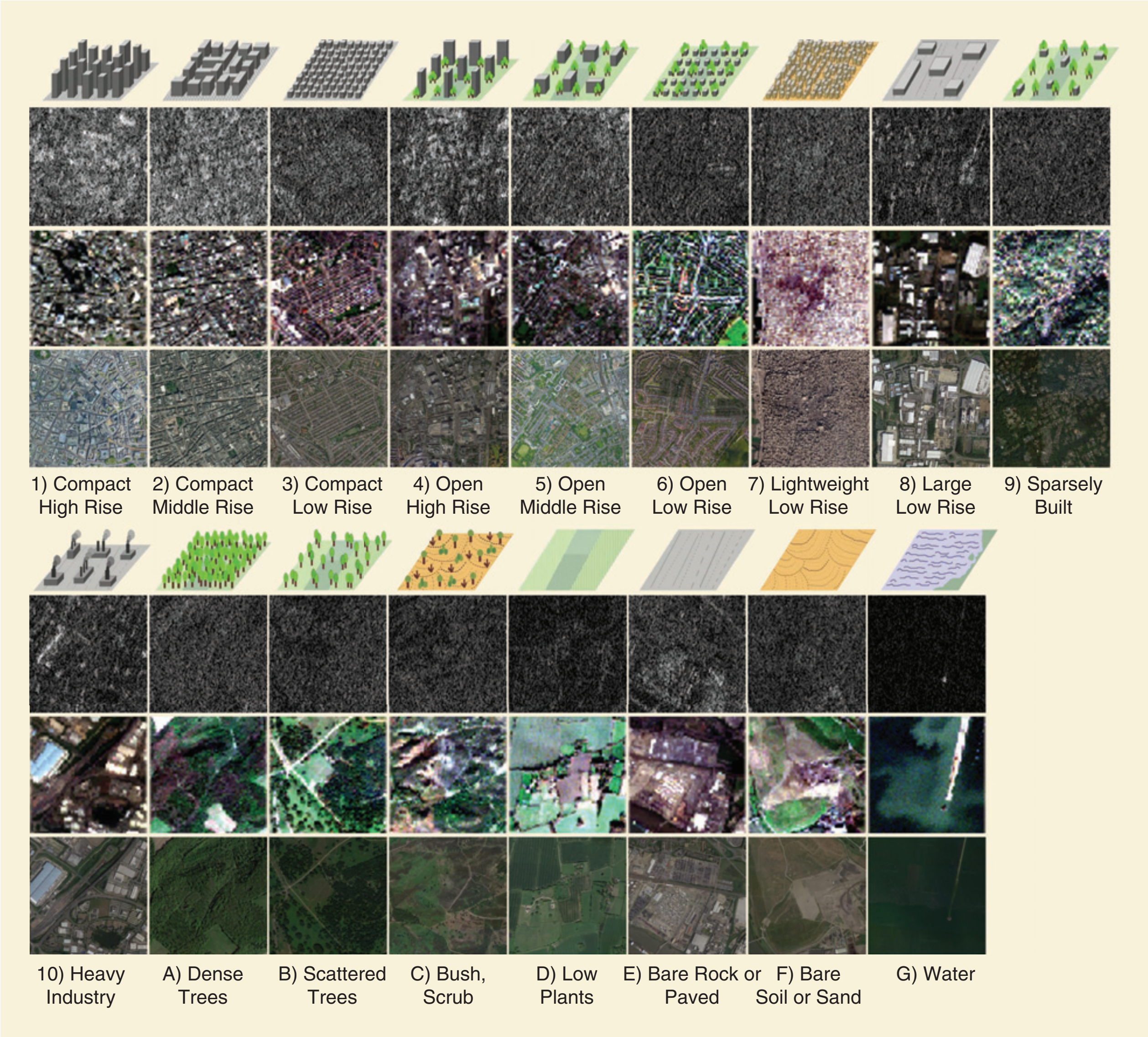

FIGURE 3. Examples of *Sentinel-1* and *Sentinel-2* image scenes of the 17 LCZ classes. In each LCZ, the upper image is the intensity (in decibels) of the *Sentinel-1* scene; the middle image is the corresponding *Sentinel-2* scene in red, green, blue; and the lower image is the high-resolution aerial image from Google as a reference. This figure shows the typical urban morphology of each LCZ class and the content observable by *Sentinel-1* and *Sentinel-2*. For visualization purposes, the image scenes are much larger than the actual patches (32 × 32 pixels) in the So2Sat LCZ42 data set.

results from each member of the labeling crew were visually inspected by a different person to spot obvious errors. Finally, we conducted a quantitative evaluation of the label quality. The entire rigorous labeling processing took approximately 15 person-months.

RIGOROUS LABEL-QUALITY ASSESSMENT

Similar to any remote sensing product, reference labels must have error bars to indicate their trustworthiness, but such a quality measure rarely appears in data sets of remote sensing image labels. As mentioned previously, we conducted a rigorous quantitative evaluation of 10 cities in the data set by having a group of remote sensing experts cast 10 independent votes on each labeled polygon, to identify possible errors and assess human labeling accuracy. “Human confusion matrices” per polygon and per pixel were created, where the confidence of individual classes can be seen. In general, our human labels achieve 85% confidence. This confidence number can serve as a reference accuracy for the machine-learning models trained on this data set.

So2Sat LCZ42 DATA SET CREATION

A four-phase labeling process was designed to maximize label consistency and minimize human error, consisting of learning, labeling, visual validation, and quantitative validation phases (Figure 4). The detailed procedures for each phase are introduced in this section. We also prepared the corresponding *Sentinel-1* and *Sentinel-2* images of the 52 areas, and proper preprocessing procedures were performed on the two types of images.

CREATING THE LABELS

LEARNING PHASE

The learning phase aims at creating a standard for team members who conduct the labeling (referred to as the *labeling crew*). The reasons are twofold. First, the definition of LCZ classes (given in [9] and listed in Table 1) are not mutually disjoint (e.g., class 3, compact low-rise, and class 8, large low-rise), and their union does not describe the entirety of Earth's surface. That is, that some areas do not fall into any of the LCZ classes, and some can be categorized according to multiple classes. Second, interpretations of the definitions by different individuals still differ from each other.

The labeling crew started by building a visual impression of different LCZ classes by viewing aerial images on Google Earth and then moved toward a quantitative understanding of each class. As a result, we constructed a quantitative-labeling decision rule according to the literal definition. This is shown in Figure S1. An examination of the labeling learning course was conducted before actual labeling began, for which everyone in the labeling crew cast a vote on many selected scenes. Ambiguous scenes were selected and discussed to calibrate everyone's understanding.

LABELING PHASE

The labeling phase followed a standard procedure defined in the WUDAPT project [22]. First, each member of the labeling crew claimed a few cities among the 52 cities and defined a region of interest (ROI) within each selected city by drawing a rectangle of approximately 50 × 50 km around the city center in Google Earth. Second, polygons enclosing different LCZ classes were manually delineated in Google Earth. These polygons are the preliminary labels. Afterward, *Landsat 8* images covering the ROI were prepared.

After this preparation, an RF classifier was trained using the *Landsat 8* images and the preliminary LCZ labels to produce an LCZ classification map of the specific city. This classification map and the satellite image on Google Earth served as auxiliary data for cross-checking the correctness and completeness of the LCZ labels. The details are explained as follows.

- *Correctness*: The crew visually inspected discrepancies between the classification maps and the labels of the polygons. If a mismatch was found for a labeled polygon, the crew inspected the satellite image on Google Earth and corrected the given label if necessary. This process was repeated until no noticeable discrepancy between the classification map and label was found.
- *Completeness*: The labeling crew cross-checked the classification result with the satellite image on Google Earth in unlabeled areas to find negative samples. For example, dense forest might be classified as water because of the lack of a dense forest label. The labeling crew then labeled those negative samples of dense forest and included them in the whole label data set. This hard-negative mining procedure was carried out iteratively until no noticeable discrepancies between the classification maps and Google Earth images in unlabeled areas were found.

The classification maps produced during the manual labeling process were employed only to provide guidance to the labeling crew and were not used in the final data. All LCZ labels in the final provided reference data fully relied on manual human annotation.

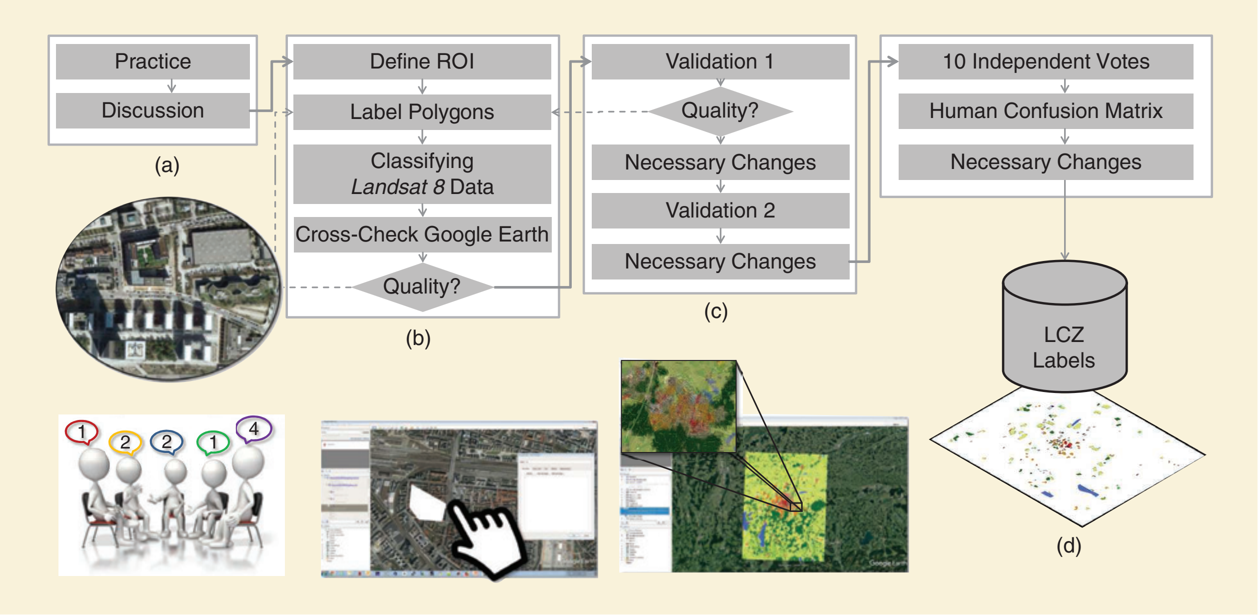

FIGURE 4. The four-phase labeling project, showing the (a) learning, (b) labeling, (c) first validation, and (d) second validation phases.

Decision Rule of Local-Climate-Zone Labeling

The decision rule consists of seven hierarchical questions:

A) Is it homogeneous for at least five pixels of 100 × 100 m?

B) Is the building footprint large?

C) Does any obvious industrial feature exist (such as oil tanks, cranes, or conveyor belts)?

D) What is the building height?
  - D1. Up to three floors
  - D2. Three to 10 floors
  - D3. Ten floors and higher.

E) For D1, what is the building surface fraction?
  - E1. Between 20% and 40%
  - E2. Smaller than 20%
  - E3. Between 40% and 70%.
  - E4. Light material built with a surface fraction of larger than 60%

F) For D2, is the building surface fraction larger than 40%?

G) For D3, is the building surface fraction larger than 40%?

The percentage is estimated by experts with a 100 × 100-m polygon drawn on Google Earth. The building height is decided by experts using any available information, such as a 3D model, satellite images, or photos (Figure S1).

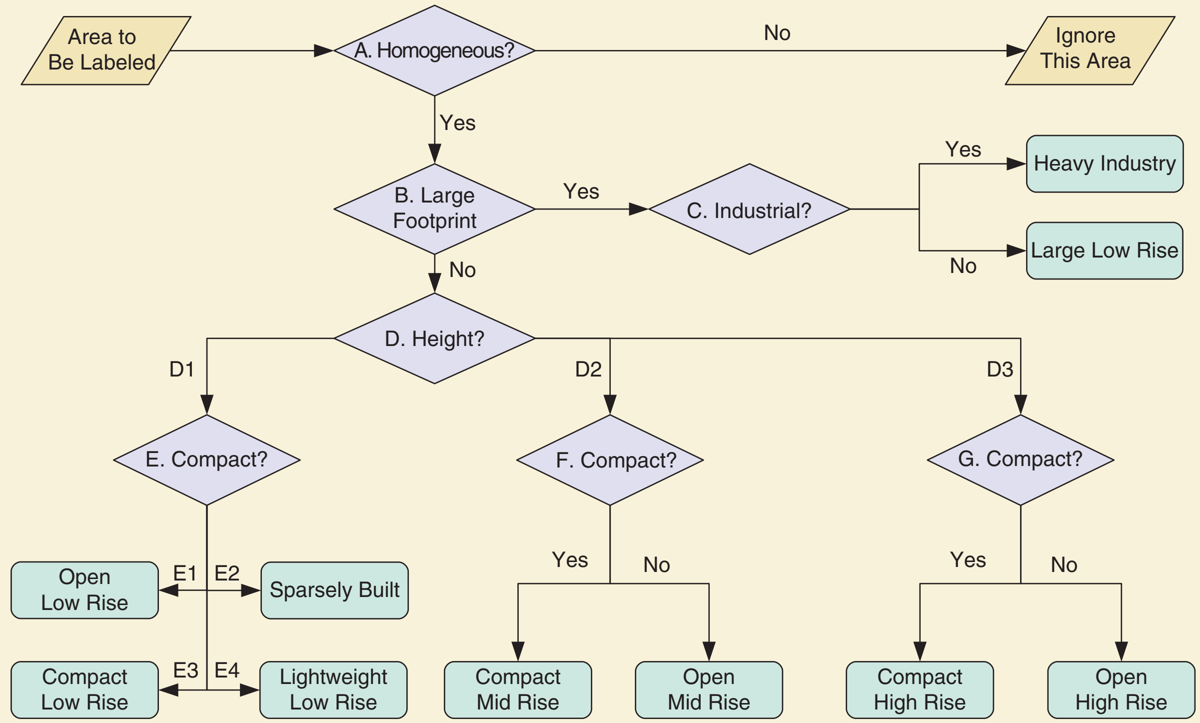

FIGURE S1. A flowchart of the labeling decision rule, which identifies one scene with seven decisions.

VISUAL QUALITY-CONTROL PHASE

Despite a clear quantitative definition that was agreed on by the labeling crew in the learning phase, personal bias and outliers still existed in the labeling result. Therefore, a manual inspection was required before quantitative validation to adjust personal biases and decrease the inevitable human mistakes. After the labeling phase, two persons other than the individual who labeled the polygons sequentially and independently validated the labels, as demonstrated in step C of Figure S1. These two persons were responsible for visually inspecting two types of signals in the classification map: 1) obvious outliers, such as water being classified as a dense high-rise building, and 2) a normal compactness-centric pattern of urban areas, that is, the compactness of urban buildings decreases from the city center toward the suburbs. If the obvious outliers cover a comparatively large area, a polygon with the correct label must be added. If an abnormal compactness pattern appears, the validation requires a detailed inspection, which often leads to adding polygons or correcting labels of existing polygons. We found that visual validation gave us a significant indication of label quality.

LABEL POSTPROCESSING

After obtaining labeled LCZ polygons, we discovered that the following postprocessing procedures were necessary.

- *Polygon shrinking*: Although all of the polygons were correctly labeled, some polygons in a given LCZ class were drawn in close proximity to another LCZ class. This might cause erroneous labels on the pixels close to the borders of the polygon when the polygon is rasterized, especially when using a large ground-sampling distance

(GSD). For example, the GSD of an LCZ-label map defined in our research is 100 m. A pixel in the label map that is too close to the boundary of two LCZs may cover both LCZ classes. To avoid this, the polygons of all nonurban LCZ classes except water (that is, classes A–F) were shrunk by 160 m. We chose a distance of 160 m because this corresponds to half of the patch size (16 pixels) of the *Sentinel-1* and *Sentinel-2* image patches in the So2Sat LCZ42 data set. For class G (water), the shrinking distance is only 10 m, given that the width of many rivers is on the order of hundreds of meters.

- *Class balancing*: For those vector-format polygon labels in machine learning of EO images to be used, they must be rasterized into image format in certain geographic coordinate systems. We used GeoTIFF format and local Universal Transverse Mercator (UTM) coordinates. However, the polygons of nonurban LCZ classes (i.e., classes A–G) tend to be much larger in area than those of urban classes, because the percentage of nonurban areas is naturally larger and they are much easier for humans to label. This results in many more pixels (samples) for nonurban classes. To balance the number of samples among all of the LCZ classes, for each city, we reduced the number of samples of each of the nonurban classes (A–G) to N_m, where N_m is the maximum number of samples from the urban classes (i.e., classes 1–10). If the number of samples of certain nonurban classes was less than N_m, those classes remained untouched. The samples of the urban classes were not reduced because they are difficult to label. In this way, we were able to balance the different LCZ classes.

QUANTITATIVE QUALITY CONTROL AND VALIDATION PHASE

The maximum accuracy achievable by any supervised learning procedure depends not only on the chosen algorithm but also on the quality of the training data. Therefore, we conducted quantitative evaluation on 10 European cities in the data set by having a group of remote sensing experts cast 10 independent votes on each labeled polygon to assess human labeling accuracy and identify possible remaining errors. Despite the huge labor cost, we believe this is essential for EO data and products to provide an error bar to users. This label evaluation procedure is discussed in detail in the "Label Evaluation" section.

PREPARING THE SENTINEL-1 *DATA*

The *Sentinel-1* mission provides an open access global SAR data set. We used the *Sentinel-1* VV–VH dual-Pol single-look complex (SLC) level 1 data via the Copernicus Open Access Hub [50] employing an automatic script developed by the authors based on SentinelSat [51].

A series of preprocessing steps was applied to the *Sentinel-1* data using the graph processing tool in the European Space Agency's Sentinel Application Platform (SNAP) toolbox. The detailed configurations of the preprocessing are listed as follows.

TABLE 1. THE BUILDING TOTAL, PERVIOUS, AND IMPERVIOUS SURFACES OF EACH CLASS [9] AND THE HEIGHT ABOVE THE GROUND.

CLASS	BUILDING SURFACE (%)	PERVIOUS SURFACE (%)	IMPERVIOUS SURFACE (%)	HEIGHT ABOVE GROUND (M)
1. Compact, high rise	40–60	0–10	40–60	>25
2. Compact, mid rise	40–70	0–20	30–50	10–25
3. Compact, low rise	40–70	0–30	20–50	2–10
4. Open, high rise	20–40	30–40	30–40	>25
5. Open, mid rise	20–40	20–40	30–50	10–25
6. Open, low rise	20–40	30–60	20–50	2–10
7. Lightweight, low rise	60–90	0–30	0–20	2–10
8. Large, low rise	30–50	0–20	40–50	2–10
9. Sparsely built	10–20	60–80	0–20	2–10
10. Heavy industry	20–30	40–50	20–40	2–10
A. Dense trees	0–10	90–100	0–10	>3
B. Scattered tree	0–10	90–100	0–10	>3
C. Bush, scrub	0–10	90–100	0–10	1–2
D. Low plants	0–10	90–100	0–10	<1
E. Bare rock or paved	0–10	0–10	90–100	0
F. Bare soil or sand	0–10	90–100	0–10	0
G. Water	0–10	90–100	0–10	0

- *Apply orbit profile*: This module downloads the latest released orbit profile so that a precisely geocoded product can be achieved.
- *Radiometric calibration*: Radiometry is employed to compute the backscatter intensity using sensor calibration parameters in the metadata. The output is set to a complex-valued image to preserve the relative phase between VV and VH channels.
- *TOPSAR deburst*: For each polarization channel, the *Sentinel-1* IW product has three swaths. Each swath image consists of a series of bursts. The TOPSAR deburst merges all of these bursts and swaths into a single SLC image.
- *Polarimetric speckle reduction*: Speckle reduction was conducted by using the SNAP-integrated refined Lee filter. An unfiltered version is also included in the data set.
- *Terrain correction*: Terrain correction eliminates the distortion introduced by topographical variations. To accomplish the correction, the SRTM digital elevation model was used to provide height information. The data were resampled

to a 10-m GSD by nearest-neighbor interpolation. The data were geocoded into the WGS84/UTM coordinate system of the corresponding city with a GSD of 10 m.

To summarize, the *Sentinel-1* data in the So2Sat LCZ42 data set contain the following eight real-valued bands:

- real part of the unfiltered VH channel
- imaginary part of the unfiltered VH channel
- real part of the unfiltered VV channel
- imaginary part of the unfiltered VV channel
- intensity of the refined Lee-filtered VH channel
- intensity of the refined Lee-filtered VV channel
- real part of the refined Lee-filtered covariance matrix off-diagonal element
- imaginary part of the refined Lee-filtered covariance matrix off-diagonal element.

PREPARING THE SENTINEL-2 *DATA*

We employed Google Earth Engine (GEE) to create cloud-free *Sentinel-2* images [44]. The overall workflow, based on the GEE Python application programming interface, consisted of the following three main steps.

- *Querying step*: loading *Sentinel-2* images from the catalogue
- *Scoring step*: calculating a cloud-related quality score for each loaded image
- *Mosaicking step*: mosaicking the selected images based on the meta-information generated in the preceding modules.

More details can be found in [45].

Sentinel-2 images contain bands B2, B3, B4, and B8 with 10-m GSD; bands B5, B6, B7, B8a, B11, and B12 with 20-m GSD; and bands B1, B9, and B10 with 60-m GSD. In the So2Sat LCZ42 data set, the 20-m bands were upsampled to 10-m GSD, and bands B1, B9, and B10 were discarded because they mostly contain data related to the atmosphere and, thus, bear little relevance to LCZ classification. To summarize, the *Sentinel-2* data in the So2Sat LCZ42 data set contain the following 10 real-valued bands:

- band B2, 10-m GSD
- band B3, 10-m GSD
- band B4, 10-m GSD
- band B5, upsampled to 10 m from 20-m GSD
- band B6, upsampled to 10 m from 20-m GSD
- band B7, upsampled to 10 m from 20-m GSD
- band B8, 10-m GSD
- band B8a, upsampled to 10 m from 20-m GSD
- band B11, upsampled to 10 m from 20-m GSD
- band B12, upsampled to 10 m from 20-m GSD.

CONTENT OF THE So2Sat LCZ42 DATA SET

By projecting the labels to the coregistered *Sentinel-1* and *Sentinel-2* images, we can extract *Sentinel-1* and *Sentinel-2* image patch pairs with the corresponding LCZ labels. We define the dimension of the image patches in the So2Sat LCZ42 data set as 32 × 32 pixels, which corresponds to a physical dimension of 320 × 320 m. To create nonoverlapping patches, we sampled the labeled polygons with a 320 × 320-m grid, where the grid nodes are the center of each image patch. We obtained 400,673 pairs of *Sentinel* image patches. The volume of the whole data set is approximately 56 GB.

For machine-learning purposes, the data set was split into a training set, a testing set, and a validation set, which consist of 352,366; 24,188; and 24,119 pairs of image patches, respectively. The training set comprises all of the image patches of 32 cities plus the 10 add-on areas in the city list. See "City List of the So2Sat LCZ42 Data Set" for the full list of cities). The remaining 10 cities are distributed across all of the continents and culture regions of the world. For each, we split the labels of each LCZ class into the western and eastern halves of a city to form the testing and validation sets, respectively. Therefore, all three data subsets are geographically separated from each other, despite our having drawn the testing and validation sets from the same list of cities.

LABEL EVALUATION

The maximum accuracy achievable by any supervised learning procedure depends not only on the chosen algorithm but also on the quality of the training data [46]. In the Human Influence Experiment (HUMINEX), Bechtel et al. [28] recently showed the difficulties associated with having human experts assign LCZ classes. Therefore, evaluating the labels that are the result of human expert knowledge is of vital importance for further use of the data set in the training of classification algorithms for large-scale automatic LCZ mapping.

THE EVALUATION SET

For the evaluation, we chose a subset of 10 European cities (Table 2) from the group of cities we labeled. The choice was based on the following three rationales:

- All of our labeling experts have lived in Europe for a significant number of years. This ensures familiarity with the general morphological appearance of European cities.
- Google Earth provides detailed 3D models for the 10 cities, which is of great help in determining the approximate heights of urban objects. This is necessary to be able to distinguish among the low-rise, mid-rise, and high-rise classes.

City List of the So2Sat LCZ42 Data Set

Cities used for training: Amsterdam, Beijing, Berlin, Bogota (added on), Buenos Aires (added on), Cairo, Cape Town, Caracas (added on), Changsha, Chicago (added on), Cologne, Dhaka (added on), Dongying, Hong Kong, Islamabad, Istanbul, Karachi (added on), Kyoto, Lima (added on), Lisbon, London, Los Angeles, Madrid, Manila (added on), Melbourne, Milan, Nanjing, New York, Paris, Philadelphia (added on), Qingdao, Rio de Janeiro, Rome, Salvador (added on), São Paulo, Shanghai, Shenzhen, Tokyo, Vancouver, Washington (D.C.), Wuhan, Zurich.

Cities used for testing and validation: Guangzhou, Jakarta, Moscow, Mumbai, Munich, Nairobi, San Francisco, Santiago de Chile, Sydney, Tehran.

- As previously mentioned, LCZ labeling is very labor intensive. Reducing the evaluation set to 10 cities allowed us to generate more individual votes per polygon for better statistics.

Unfortunately, few European cities contain LCZ class 7 (lightweight, low rise), which mostly describes informal settlements (e.g., slums). Therefore, we included the polygons of class 7 for an additional nine cities that are representative of the nine major non-European geographical regions of the world (Table 3).

EVALUATION STRATEGY AND RESULTS

For the evaluation experiment, 10 remote sensing experts (hereafter referred to as the *label validation crew*), who were already trained in applying the LCZ scheme to annotate urban areas, were provided with .kml files containing the polygons of the original So2Sat LCZ42 data set, but without labels. They were then asked to reassign an LCZ class to every polygon, using Google Earth as the labeling environment. After all of the relabeled .kml files were submitted, both polygon-wise and pixel-wise evaluations between the original labels and the votes newly cast by the label validation crew were carried out in the form of confusion matrices, which combine the validation results of the 10 European cities (Table 2) and the slum areas of the additional nine non-European cities (Table 3). These confusion matrices are displayed in Figure 5(a) and (b).

In addition, majority voting was carried out for each polygon; that is, each polygon was reassigned to the class for which a majority of the label validation crew had voted, although we kept the original label in case there was a draw between this original class and another major class. The polygon-wise and pixel-wise confusion matrices between these final labels and the votes of the label validation crew can be seen in Figure 5(c) and (d).

TABLE 2. THE 10 EUROPEAN CITIES SELECTED FOR QUANTITATIVE LABEL EVALUATION.

CITY	COUNTRY
Amsterdam	The Netherlands
Berlin	Germany
Cologne	Germany
London	United Kingdom
Madrid	Spain
Milan	Italy
Munich	Germany
Paris	France
Rome	Italy
Zurich	Switzerland

TABLE 3. THE ADDITIONAL NINE CITIES WHOSE POLYGONS OF CLASS 7 (LIGHTWEIGHT, LOW RISE) WERE USED FOR THE EVALUATION.

CITY	GEOGRAPHIC REGION
Guangzhou, China	East Asia
Islamabad, Pakistan	Middle East
Jakarta, Indonesia	Southeast Asia
Los Angeles, United States	North America
Melbourne, Australia	Oceania
Moscow, Russia	Eastern Europe
Mumbai, India	Indian subcontinent
Nairobi, Kenya	Sub-Saharan Africa
Rio de Janeiro, Brazil	Latin America

INTERPRETATION OF THE EVALUATION RESULTS

The confusion matrices in Figure 5 show the following.

- There is no significant difference between the polygon-wise and pixel-wise results, which indicates that the polygons are evenly distributed with respect to size.
- The majority voting step helped slightly improve the label confidences. Before the refinement, 11 of the 17 LCZ classes provided a confidence of more than 80%; after the refinement, this confidence level held for 13 classes.
- In general, confusion among the urban classes is slightly higher than among the nonurban classes.
- The classes with the most confidence are 8 (large, low rise), A (dense trees), D (low plants), and G (water), with classes 2 (compact, mid rise) and E (bare rock/paved) following close behind.
- The classes with the least confidence are 3 (compact, low rise), 7 (lightweight, low rise), and C (bush, scrub), with classes 4 (open, high rise) and 9 (sparsely built) following behind. The main sources of confusion for these classes are summarized in Table 4.

These experiences go hand in hand with the findings of Bechtel et al. [28], who also found that LCZ classes A (dense trees), D (low plants), G (water), 2 (compact, mid rise), 6 (open, low rise), and 8 (large, low rise) were recognized consistently well by all operators, whereas classes 9 (sparsely built) and B (scattered trees) were reported as difficult to classify. Classes 1 (compact, high rise), 4 (open, high rise), 7 (lightweight, low-rise), and C (bush, scrub) were not present in most of their study cities and, thus, not discussed in detail.

Based on the major sources of confusion summarized in Table 4, all of these discrepancies appear fairly reasonable: apparently, it is difficult even for human experts to distinguish the vaguely defined characteristics “open” and “compact” as well as “mid rise” and “high rise.” In addition, sparsely built environments are understandably frequently confused with open low-rise neighborhoods, as is bush/scrubland with scattered trees and low plants.

Given the accordance with the findings of Bechtel et al. [28], the semantic subtleties of the LCZ classification scheme as well as a mean class confidence of approximately 80%

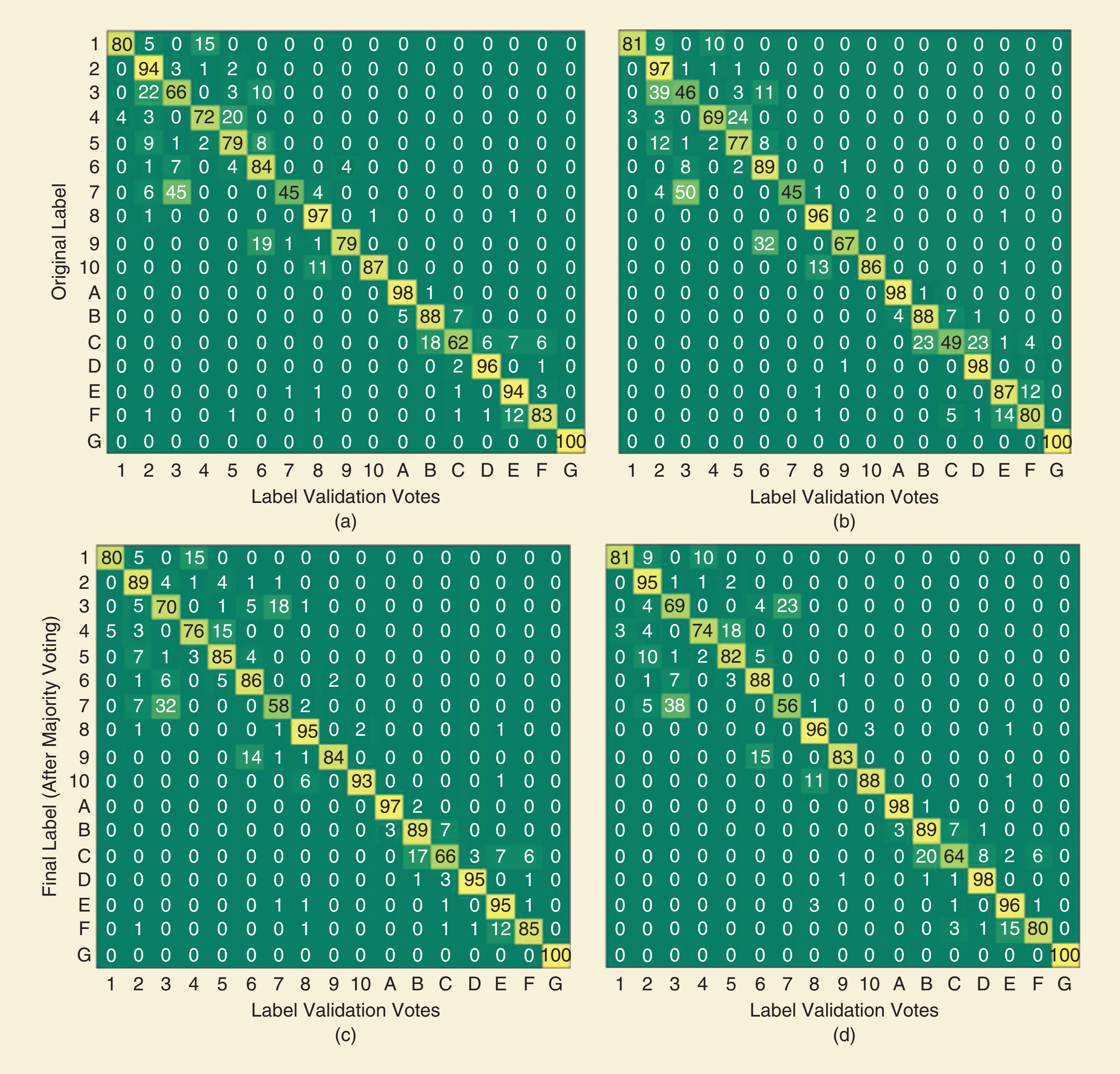

(a)

	1	2	3	4	5	6	7	8	9	10	A	B	C	D	E	F	G
1	80	5	0	15	0	0	0	0	0	0	0	0	0	0	0	0	0
2	0	94	3	1	2	0	0	0	0	0	0	0	0	0	0	0	0
3	0	22	66	0	3	10	0	0	0	0	0	0	0	0	0	0	0
4	4	3	0	72	20	0	0	0	0	0	0	0	0	0	0	0	0
5	0	9	1	2	79	8	0	0	0	0	0	0	0	0	0	0	0
6	0	1	7	0	4	84	0	0	4	0	0	0	0	0	0	0	0
7	0	6	45	0	0	0	45	4	0	0	0	0	0	0	0	0	0
8	0	1	0	0	0	0	0	97	0	1	0	0	0	0	1	0	0
9	0	0	0	0	0	19	1	1	79	0	0	0	0	0	0	0	0
10	0	0	0	0	0	0	0	11	0	87	0	0	0	0	0	0	0
A	0	0	0	0	0	0	0	0	0	0	98	1	0	0	0	0	0
B	0	0	0	0	0	0	0	0	0	0	5	88	7	0	0	0	0
C	0	0	0	0	0	0	0	0	0	0	0	18	62	6	7	6	0
D	0	0	0	0	0	0	0	0	0	0	0	0	2	96	0	1	0
E	0	0	0	0	0	0	1	1	0	0	0	0	1	0	94	3	0
F	0	1	0	0	1	0	0	1	0	0	0	0	1	1	12	83	0
G	0	0	0	0	0	0	0	0	0	0	0	0	0	0	0	0	100

(b)

	1	2	3	4	5	6	7	8	9	10	A	B	C	D	E	F	G
1	81	9	0	10	0	0	0	0	0	0	0	0	0	0	0	0	0
2	0	97	1	1	1	0	0	0	0	0	0	0	0	0	0	0	0
3	0	39	46	0	3	11	0	0	0	0	0	0	0	0	0	0	0
4	3	3	0	69	24	0	0	0	0	0	0	0	0	0	0	0	0
5	0	12	1	2	77	8	0	0	0	0	0	0	0	0	0	0	0
6	0	0	8	0	2	89	0	0	1	0	0	0	0	0	0	0	0
7	0	4	50	0	0	0	45	1	0	0	0	0	0	0	0	0	0
8	0	0	0	0	0	0	0	96	0	2	0	0	0	0	1	0	0
9	0	0	0	0	0	32	0	0	67	0	0	0	0	0	0	0	0
10	0	0	0	0	0	0	0	13	0	86	0	0	0	0	1	0	0
A	0	0	0	0	0	0	0	0	0	0	98	1	0	0	0	0	0
B	0	0	0	0	0	0	0	0	0	0	4	88	7	1	0	0	0
C	0	0	0	0	0	0	0	0	0	0	0	23	49	23	1	4	0
D	0	0	0	0	0	0	0	0	1	0	0	0	0	98	0	0	0
E	0	0	0	0	0	0	0	1	0	0	0	0	0	0	87	12	0
F	0	0	0	0	0	0	0	1	0	0	0	0	5	1	14	80	0
G	0	0	0	0	0	0	0	0	0	0	0	0	0	0	0	0	100

(c)

	1	2	3	4	5	6	7	8	9	10	A	B	C	D	E	F	G
1	80	5	0	15	0	0	0	0	0	0	0	0	0	0	0	0	0
2	0	89	4	1	4	1	1	0	0	0	0	0	0	0	0	0	0
3	0	5	70	0	1	5	18	1	0	0	0	0	0	0	0	0	0
4	5	3	0	76	15	0	0	0	0	0	0	0	0	0	0	0	0
5	0	7	1	3	85	4	0	0	0	0	0	0	0	0	0	0	0
6	0	1	6	0	5	86	0	0	2	0	0	0	0	0	0	0	0
7	0	7	32	0	0	0	58	2	0	0	0	0	0	0	0	0	0
8	0	1	0	0	0	0	1	95	0	2	0	0	0	0	1	0	0
9	0	0	0	0	0	14	1	1	84	0	0	0	0	0	0	0	0
10	0	0	0	0	0	0	0	6	0	93	0	0	0	0	1	0	0
A	0	0	0	0	0	0	0	0	0	0	97	2	0	0	0	0	0
B	0	0	0	0	0	0	0	0	0	0	3	89	7	0	0	0	0
C	0	0	0	0	0	0	0	0	0	0	0	17	66	3	7	6	0
D	0	0	0	0	0	0	0	0	0	0	0	1	3	95	0	1	0
E	0	0	0	0	0	0	1	1	0	0	0	0	1	0	95	1	0
F	0	1	0	0	0	0	0	1	0	0	0	0	1	1	12	85	0
G	0	0	0	0	0	0	0	0	0	0	0	0	0	0	0	0	100

(d)

	1	2	3	4	5	6	7	8	9	10	A	B	C	D	E	F	G
1	81	9	0	10	0	0	0	0	0	0	0	0	0	0	0	0	0
2	0	95	1	1	2	0	0	0	0	0	0	0	0	0	0	0	0
3	0	4	69	0	0	4	23	0	0	0	0	0	0	0	0	0	0
4	3	4	0	74	18	0	0	0	0	0	0	0	0	0	0	0	0
5	0	10	1	2	82	5	0	0	0	0	0	0	0	0	0	0	0
6	0	1	7	0	3	88	0	0	1	0	0	0	0	0	0	0	0
7	0	5	38	0	0	0	56	1	0	0	0	0	0	0	0	0	0
8	0	0	0	0	0	0	0	96	0	3	0	0	0	0	1	0	0
9	0	0	0	0	0	15	0	0	83	0	0	0	0	0	0	0	0
10	0	0	0	0	0	0	0	11	0	88	0	0	0	0	1	0	0
A	0	0	0	0	0	0	0	0	0	0	98	1	0	0	0	0	0
B	0	0	0	0	0	0	0	0	0	0	3	89	7	1	0	0	0
C	0	0	0	0	0	0	0	0	0	0	0	20	64	8	2	6	0
D	0	0	0	0	0	0	0	0	1	0	0	1	1	98	0	0	0
E	0	0	0	0	0	0	0	3	0	0	0	0	1	0	96	1	0
F	0	0	0	0	0	0	0	0	0	0	0	0	3	1	15	80	0
G	0	0	0	0	0	0	0	0	0	0	0	0	0	0	0	0	100

FIGURE 5. The confusion matrices (values as percentages) of the original and final labels (refined by majority voting) versus the votes cast by the label validation crew for the polygons of the evaluation cities selected in Tables 2 and 3: (a) polygon-wise assessment of the original labels, (b) pixel-wise assessment of the original labels, (c) polygon-wise assessment of the final labels, and (d) pixel-wise assessment of final labels.

before refinement by majority voting and 85% after refinement, the So2Sat LCZ42 data set can be considered a reliable source of labels for the training of machine-learning procedures aimed at automated LCZ mapping on a larger scale.

BASELINE CLASSIFICATION ACCURACY

To provide a baseline for achievable LCZ classification accuracy, we performed classification on the So2Sat LCZ42 data set using popular classifiers, including classical RFs, SVMs [30], and an attention-based ResNeXt, as proposed in [47] and [48]. The employed RF consists of 200 trees, and the max_depth is set to 10, with the other parameters set to the default. A radial basis function kernel is chosen for the SVM in the experiment. The depth of the ResNeXt is 29 layers, and the convolutional block attention module is plugged into each of the residual blocks. For RF and SVM, the pixel values of the patches are converted into vectors, using the statistical measures (maximum, minimum, standard deviations, and mean) of each band. All of the classifiers are trained using the training set and tested on the validation set.

The resulting accuracy based on the *Sentinel-2* images in the So2Sat LCZ42 data set can be seen in Table 5. The accuracy measures include overall accuracy, averaged accuracy, and the kappa coefficient. In addition, weighted accuracy, introduced in [28], is considered, because it gives user-defined weights to confusions between different classes. For example, misclassifying compact high rise as compact

TABLE 4. THE MAIN SOURCES OF CONFUSION FOR THE LCZ CLASSES WITH LESS CONFIDENCE.

LOW CONFIDENCE CLASS	MAJOR CONFUSION CLASSES
3. Compact, low rise	2. Compact, mid rise 6. Open, low rise
4. Open, high rise	5. Open, mid rise
7. Lightweight, low rise	3. Compact, low rise
9. Sparsely built	6. Open, low rise
C. Bush, scrub	B. Scattered trees D. Low plants

TABLE 5. THE CLASSIFICATION ACCURACY FROM THREE BASELINE METHODS, WITH *SENTINEL-2* IMAGES IN THE PROPOSED DATA SET.

METHOD	OA	WA	AA	KAPPA
RF	51%	87%	31%	0.46
SVM	54%	88%	36%	0.49
ResNeXt-CBAM	61%	92%	51%	0.58

AA: averaged accuracy; CBAM: convolutional block attention module OA: overall accuracy; WA: weighted accuracy.

middle rise is less critical than mistaking compact high rise for water and, thus, should be penalized less.

DISCUSSION

The goal of this article is to provide documentation about a large benchmark data set for LCZ classification from *Sentinel-1* and *Sentinel-2* satellite data. Since the *Sentinel* data are openly available for the whole globe, the main intention of the data set is to enable the training of models that can be generalized to any unseen areas of the world. This is ensured by sampling the data from 52 cities located on all inhabited continents. In spite of these promising characteristics, two major challenges must be noted.

First, LCZs are sometimes hard to distinguish. As the label validation results shown in the "Label Evaluation section" illustrate, it is extremely difficult to distinguish some LCZ classes, even if human experts investigate several data sources (such as high-resolution optical imagery and 3D building models like those available in Google Earth). This especially holds for the distinction of different height levels in compact areas, but it is also true for open areas, which comprise both open land/vegetation and building structures. This must be acknowledged as a natural limitation when tackling LCZ mapping with remote sensing data. The limitation can be solved only by combining remote sensing data with other data sources, such as information from social media data.

Second, learning a generic LCZ prediction model is challenging. As described in the "Content of the So2Sat LCZ42 Data Set" section, the test and training sets are completely disjunct, with the test cities being distributed across the 10 major cultural regions of the inhabited world. Therefore, results achieved on this data set can be considered a good measure of how well the trained model would generalize to completely unseen data. In this regard, overall accuracies between 50% and 60% can already be considered promising—especially for a target scheme comprising 17 difficult-to-distinguish classes. Nevertheless, there is still room for improvement, as usually an accuracy of at least approximately 85% to 90% is required for land-cover mapping purposes, according to Anderson [49].

We hope that the community is eager to tackle these challenges and puts the So2Sat LCZ42 data set to good use to achieve significant progress in the global mapping of cities into LCZs.

CONCLUSIONS AND OUTLOOK

This article introduced a unique data set that contains manually labeled LCZ reference data as well as coregistered *Sentinel-1* and *Sentinel-2* image patch pairs for more than 42 cities and 10 smaller areas across the six inhabited continents on Earth. The article described the carefully designed labeling process and a rigorous evaluation procedure that ensures the quality of the data set. Despite the fact that each LCZ class is quantitatively defined in the original article, we discovered that several LCZ classes can be easily confused with each other, because the height and percentage of pervious surface of these classes cannot be easily distinguished by the human eye from aerial images during labeling. This renders the entire labeling process highly labor intensive.

Still, we were able to achieve an average class confidence of 85% through our human evaluation procedure with independent voting by 10 experts. Hence, this data set is a reliable source for the training of machine-learning procedures, and it can be considered a challenging and large-scale data fusion and classification benchmark data set for cutting-edge machine-learning methodological developments. Examples for possible research directions include the following.

- Since we have provided the label confusion matrix, the question of how to introduce such prior knowledge into machine learning, deep learning models in particular, is an interesting direction.
- Due to culture-induced diversity existing in the data, transferability of the models will be a key to achieving good classification results on a global scale.
- Radar and optical data have completely different yet partially complementary characteristics. Developing methods to fuse them in an optimal way or select appropriate features from such diverse data sources is of general interest to the remote sensing community.
- Thanks to the large scale of the proposed benchmark data set, it can serve as a test bed for the development of efficient training techniques.

Our vision in the near future is to produce a global LCZ classification map using multisensory remote sensing images, which will be made available to the community. Such geographic information seems trivial for developed countries, but it is still very scarce on the global scale. For example, the city of Lagos, Nigeria (population: 21 million), does not have a quality 3D city model. Therefore, a quality LCZ classification map will become the firsthand information source for urban building volume and distribution. A global LCZ map will strongly boost urban geographic research and help us develop a better understanding of global urbanization. For this purpose, we invite everyone to contribute by using this data set and developing new, sophisticated algorithms.

ACKNOWLEDGMENTS

This research was funded by the European Research Council (ERC) under the European Union's Horizon 2020 research and innovation programme under grant ERC-2016-StG-714087(So2Sat, project website: http://www.so2sat.eu/), Helmholtz Association under the framework of the Helmholtz Artificial Intelligence Cooperation Unit–Local Unit "Munich Unit @Aeronautics, Space and Transport (MASTr)," and Helmholtz Excellent Professorship "Data Science in Earth Observation–Big Data Fusion for Urban Research."

AUTHOR INFORMATION

Xiao Xiang Zhu (xiaoxiang.zhu@dlr.de) received her M.Sc. degree, Dr.-Ing. degree, and habilitation in the field of signal processing from the Technical University of Munich (TUM), Germany, in 2008, 2011, and 2013, respectively. She is currently a professor for signal processing in Earth observation (EO) at TUM and the head of the department's EO Data Science at the Remote Sensing Technology Institute, German Aerospace Center. Since 2019, she has been co-coordinating the Munich Data Science Research School. She is also leading the Helmholtz Artificial Intelligence Cooperation Unit–Research Field "Aeronautics, Space and Transport." Her main research interests are remote sensing and EO, signal processing, and machine learning and data science, with a special application focus on global urban mapping. She is an associate editor of *IEEE Transactions on Geoscience and Remote Sensing*. She is a Senior Member of the IEEE.

Jingliang Hu (jingliang.hu@dlr.de) received his B.Sc. degree in geographic information systems from the Chengdu University of Technology, China, in 2011, the M.Sc. degree in cartography and geographic information system from Wuhan University, China, in 2014, and the M.Sc. degree in space science and technology from the Technical University of Munich (TUM), Germany, in 2014, where he is currently pursuing the Ph.D. degree in signal processing in Earth observation. Since July 2015, he has been a research associate with the Remote Sensing Technology Institute, German Aerospace Center, Germany. His research interests include topological data analysis, data fusion, machine learning, and deep learning.

Chunping Qiu (chunping.qiu@tum.de) is with Signal Processing in Earth Observation, Technical University of Munich, Germany.

Yilei Shi (yilei.shi@tum.de) is with the chair of Remote Sensing Technology, Technical University of Munich, Germany.

Jian Kang (jian.kang@tum.de) was with Signal Processing in Earth Observation, Technical University of Munich, Germany when conducting the work reported in this article.

Lichao Mou (lichao.mou@dlr.de) is with Signal Processing in Earth Observation, Technical University of Munich, Germany.

Hossein Bagheri (hossein.bagheri@tum.de) is with Signal Processing in Earth Observation, Technical University of Munich, Germany.

Matthias Häberle (matthias.haeberle@dlr.de) is with the Remote Sensing Technology Institute, German Aerospace Center.

Yuansheng Hua (yuansheng.hua@tum.de) is with the Remote Sensing Technology Institute, German Aerospace Center.

Rong Huang (rong.huang@tum.de) was with Signal Processing in Earth Observation, Technical University of Munich, Germany, when conducting the work reported in this article.

Lloyd Hughes (lloyd.hughes@tum.de) is with Signal Processing in Earth Observation, Technical University of Munich, Germany.

Hao Li (hao.li@uni-heidelberg.de) was with Signal Processing in Earth Observation, Technical University of Munich, Germany, when conducting the work reported in this article.

Yao Sun (yao.sun@dlr.de) is with the Remote Sensing Technology Institute, German Aerospace Center.

Guichen Zhang (guichen.zhang@tum.de) was with Signal Processing in Earth Observation, Technical University of Munich, Germany, when conducting the work reported in this article.

Shiyao Han (shiyao.han@tum.de) was with Signal Processing in Earth Observation, Technical University of Munich, Germany, when conducting the work reported in this article.

Michael Schmitt (m.schmitt@tum.de) received his Dipl.-Ing. (university) degree in geodesy and geoinformation, his Dr.-Ing. degree in remote sensing, and his habilitation in data fusion from the Technical University of Munich (TUM), Germany, in 2009, 2014, and 2018, respectively. Since 2015, he has been a senior researcher and deputy head at the professorship for Signal Processing in Earth Observation at TUM; in 2019, he was additionally appointed as an adjunct teaching professor at the Department of Aerospace and Geodesy of TUM. In 2016, he was a guest scientist at the University of Massachusetts, Amherst. His research focuses on image analysis and machine learning applied to the extraction of information from remote-sensing observations. In particular, he is interested in remote sensing data fusion with a focus on synthetic aperture radar and optical data. He is a cochair of the International Society for Photogrammetry and Remote Sensing Working Group I/3 "SAR and Microwave Sensing."' He frequently serves as a reviewer for a number of renowned international journals and conferences and has received several Best Reviewer awards. He is an associate editor of *IEEE Geoscience and Remote Sensing Letters*. He is a Senior Member of the IEEE.

Yuanyuan Wang (y.wang@tum.de) received his B.Eng. degree (with honors) in electrical engineering from Hong Kong Polytechnic University in 2008 and his M.Sc. and Dr. Ing. degrees from the Technical University of Munich (TUM), Germany, in 2010 and 2015, respectively. In June and July 2014, he was a guest scientist with the Institute of Visual Computing, ETH Zürich, Switzerland. He is currently with the Signal Processing in Earth Observation (EO), TUM, and the Department of EO Data Science, German Aerospace Center, Weilheim, Germany, where he leads the working group Big SAR Data. His research interests include optimal and robust parameters estimation in multibaseline interferometric synthetic aperture radar (SAR) techniques, multisensor fusion algorithms of SAR and optical data, nonlinear optimization with complex numbers, machine learning in SAR, and high-performance computing for big data. He received a Best Reviewer award for *IEEE Transactions on Geoscience and Remote Sensing* in 2016. He is a Member of the IEEE.

REFERENCES

[1] H. Taubenböck, T. Esch, A. Felbier, M. Wiesner, A. Roth, and S. Dech, "Monitoring urbanization in mega cities from space," *Remote Sens. Environ.*, vol. 117, pp. 162–176, 2012. doi: 10.1016/j.rse.2011.09.015.

[2] "World urbanization prospects: 2018 revision," United Nations, New York, 2018.

[3] T. Esch et al., "TanDEM-X mission–new perspectives for the inventory and monitoring of global settlement patterns," *J. Appl. Remote Sens.*, vol. 6, no. 1, p. 061702, 2012. doi: 10.1117/1.JRS.6.061702.

[4] T. Esch et al., "Urban footprint processor: Fully automated processing chain generating settlement masks from global data of the TanDEM-X mission," *IEEE Geosci. Remote Sens. Lett.*, vol. 10, no. 6, pp. 1617–1621, 2013. doi: 10.1109/LGRS.2013.2272953.

[5] M. Pesaresi et al., "A global human settlement layer from optical HR/VHR RS data: Concept and first results," *IEEE J. Sel. Topics Appl. Earth Observ. Remote Sens.*, vol. 6, no. 5, pp. 2102–2131, 2013. doi: 10.1109/JSTARS.2013.2271445.

[6] Y. Ban, P. Gong, and C. Gini, "Global land cover mapping using earth observation satellite data: Recent progresses and challenges," *ISPRS J. Photogramm. Remote Sens.*, vol. 103, no. 1, pp. 1–6, 2015. doi: 10.1016/j.isprsjprs.2015.01.001.

[7] I. D. Stewart, "Local climate zones: Origins, development, and application to urban heat island studies," presented at the Annu. Meeting American Association of Geographers, Seattle, WA, Apr. 11–16, 2011.

[8] B. Bechtel et al., "Mapping local climate zones for a worldwide database of the form and function of cities," *ISPRS Int. J. Geo-Inf.*, vol. 4, no. 1, pp. 199–219, 2015. doi: 10.3390/ijgi4010199.

[9] I. D. Stewart and T. R. Oke, "Local climate zones for urban temperature studies," *Bull. Amer. Meterol. Soc.*, vol. 93, no. 12, pp. 1879–1900, 2012. doi: 10.1175/BAMS-D-11-00019.1.

[10] I. D. Stewart, T. R. Oke, and E. S. Krayenhoff, "Evaluation of the 'local climate zone' scheme using temperature observations and model simulations," *Int. J. Climatol.*, vol. 34, no. 4, pp. 1062–1080, 2014. doi: 10.1002/joc.3746.

[11] D. Fenner, F. Meier, B. Bechtel, M. Otto, and D. Scherer, "Intra and inter local climate zone variability of air temperature as observed by crowdsourced citizen weather stations in Berlin, Germany," *Meteorol. Z.*, vol. 26, no. 5, pp. 525–547, 2017. doi: 10.1127/metz/2017/0861.

[12] S. J. Quan, F. Dutt, E. Woodworth, Y. Yamagata, and P. P.-J. Yang, "Local climate zone mapping for energy resilience: A fine-grained and 3D approach," *Energy Procedia*, vol. 105, pp. 3777–3783, May 2017. doi: 10.1016/j.egypro.2017.03.883.

[13] J. A. Quanz, S. Ulrich, D. Fenner, A. Holtmann, and J. Eimermacher, "Micro-scale variability of air temperature within a local climate zone in Berlin, Germany, during summer," *Climate*, vol. 6, no. 1, p. 5, 2018. doi: 10.3390/cli6010005.

[14] R. Kotharkar and A. Bagade, "Evaluating urban heat island in the critical local climate zones of an Indian city," *Landsc. Urban Plan.*, vol. 169, no. 2018, pp. 92–104, 2018. doi: 10.1016/j.landurbplan.2017.08.009.

[15] J. Geletič, M. Lehnert, S. Savić, and D. Milošević, "Inter-/intra-zonal seasonal variability of the surface urban heat island based on local climate zones in three central European cities," *Build. Environ.*, vol. 156, pp. 21–32, June 2019. doi: 10.1016/j.buildenv.2019.04.011.

[16] C. B. Koc, P. Osmond, A. Peters, and M. Irger, "Understanding land surface temperature differences of local climate zones based on airborne remote sensing data," *IEEE J. Sel. Topics Appl. Earth Observ. Remote Sens.*, vol. 11, no. 8, pp. 2724–2730, 2018. doi: 10.1109/JSTARS.2018.2815004.

[17] C. B. Koc, P. Osmond, A. Peters, and M. Irger, "Mapping local climate zones for urban morphology classification based on airborne remote sensing data," in *Proc. 2017 IEEE Joint Urban Remote Sensing Event (JURSE)*, pp. 1–4. doi: 10.1109/JURSE.2017.7924611.

[18] J. Geletič, M. Lehnert, P. Dobrovolný, and M. Žuvela-Aloise, "Spatial modelling of summer climate indices based on local climate zones: Expected changes in the future climate of Brno, Czech republic," *Clim. Chang.*, vol. 152, nos. 3–4, pp. 487–502, 2019. doi: 10.1007/s10584-018-2353-5.

[19] A. Wicki and E. Parlow, "Attribution of local climate zones using a multitemporal land use/land cover classification scheme," *J. Appl. Remote Sens.*, vol. 11, no. 2, p. 026001, 2017. doi: 10.1117/1.JRS.11.026001.

[20] H. C. Ho et al., "Spatial variability of geriatric depression risk in a high-density city: A data-driven socio-environmental vulnerability mapping approach," *Int. J. Environ. Res. Public Health*, vol. 14, no. 9, p. 994, 2017. doi: 10.3390/ijerph14090994.

[21] N. Yokoya et al., "Open data for global multimodal land use classification: Outcome of the 2017 IEEE GRSS data fusion contest," *IEEE J. Sel. Topics Appl. Earth Observ. Remote Sens.*, vol. 11, no. 5, pp. 1363–1377, 2018. doi: 10.1109/JSTARS.2018.2799698.

[22] WUDAPT. Accessed on: Nov. 16, 2018. [Online]. Available: http://www.wudapt.org/lcz/lcz-framework/

[23] G. Mills, J. Ching, L. See, B. Bechtel, and M. Foley, "An introduction to the WUDAPT project," in *Proc. 9th Int. Conf. Urban Climate*, Toulouse, France, 2015, pp. 20–24.

[24] B. Bechtel et al., “CENSUS of cities: LCZ classification of cities (Level 0)—Workflow and initial results from various cities,” in *Proc. 9th Int. Conf. Urban Climate*, Toulouse, France, 2015.

[25] J. Hidalgo et al., “Comparison between local climate zones maps derived from administrative datasets and satellite observations,” *Urban Clim.*, vol. 27, pp. 64–89, Mar. 2019. doi: 10.1016/j.uclim.2018.10.004.

[26] B. Bechtel et al., “Generating WUDAPT level 0 data–current status of production and evaluation,” *Urban Clim.*, vol. 27, pp. 24–45, Mar. 2019. doi: 10.1016/j.uclim.2018.10.001.

[27] M. Demuzere, B. Bechtel, A. Middel, and G. Mills, “Mapping Europe into local climate zones,” *PLoS ONE*, vol. 14, no. 4, p. e0214474, 2019. doi: 10.1371/journal.pone.0214474.

[28] B. Bechtel et al., “Quality of crowdsourced data on urban morphology: The human influence experiment (HUMINEX),” *Urban Sci.*, vol. 1, no. 2, p. 15, 2017. doi: 10.3390/urbansci1020015.

[29] C. Ren, R. Wang, M. Cai, Y. Xu, Y. Zheng, and E. Ng, “The accuracy of LCZ maps generated by the world urban database and access portal tools (WUDAPT) method: A case study of Hong Kong,” in *Proc. 4th Int. Conf. Countermeasure Urban Heat Islands*, Singapore, 2016, pp. 1–11.

[30] Y. Xu, C. Ren, M. Cai, N. Y. Y. Edward, and T. Wu, “Classification of local climate zones using ASTER and Landsat data for high-density cities,” *IEEE J. Sel. Topics Appl. Earth Observ. Remote Sens.*, vol. 10, no. 7, pp. 3397–3405, 2017. doi: 10.1109/JSTARS.2017.2683484.

[31] C. Qiu, M. Schmitt, P. Ghamisi, and X. X. Zhu, “Effect of the training set configuration on Sentinel-2-based urban local climate zone classification,” in *Proc. Int. Archives of the Photogrammetry, Remote Sensing and Spatial Information Sciences*, 2018, pp. 931–936. doi: 10.5194/isprs-archives-XLII-2-931-2018.

[32] J. Hu, P. Ghamisi, and X. Zhu, “Feature extraction and selection of Sentinel-1 dual-pol data for global-scale local climate zone classification,” *ISPRS Int. J. Geo-Inf.*, vol. 7, no. 9, p. 379, 2018. doi: 10.3390/ijgi7090379.

[33] S. Sukhanov, I. Tankoyeu, J. Louradour, R. Heremans, D. Trofimova, and C. Debes, “Multilevel ensembling for local climate zones classification,” in *Proc. 2017 IEEE Int. Geoscience and Remote Sensing Symp. (IGARSS)*, pp. 1201–1204. doi: 10.1109/IGARSS.2017.8127173.

[34] N. Yokoya, P. Ghamisi, and J. Xia, “Multimodal, multitemporal, and multisource global data fusion for local climate zones classification based on ensemble learning,” in *Proc. 2017 IEEE Int. Geoscience and Remote Sensing Symp. (IGARSS)*, pp. 1197–1200. doi: 10.1109/IGARSS.2017.8127172.

[35] G. Xu, X. Zhu, N. Tapper, and B. Bechtel, “Urban climate zone classification using convolutional neural network and ground-level images,” *Prog. Phys. Geogr., Earth Environ.*, vol. 43, no. 3, pp. 410–424, 2019. doi: 10.1177/0309133319837711.

[36] X. X. Zhu et al., “Deep learning in remote sensing: A comprehensive review and list of resources,” *IEEE Geosci. Remote Sens. Mag.*, vol. 5, no. 4, pp. 8–36, 2017. doi: 10.1109/MGRS.2017.2762307.

[37] C. Qiu, M. Schmitt, L. Mou, and X. X. Zhu, “Urban local climate zone classification with a residual convolutional neural network and multi-seasonal Sentinel-2 images,” in *Proc. 10th IAPR Workshop on Pattern Recognition in Remote Sensing*, 2018, pp. 1–5. doi: 10.1109/PRRS.2018.8486155.

[38] C. Qiu, M. Schmitt, P. Ghamisi, L. Mou, and X. X. Zhu, “Feature importance analysis of Sentinel-2 imagery for large-scale urban local climate zone classification,” in *Proc. 2018 IEEE Int. Geoscience and Remote Sensing Symp. (IGARSS)*, pp. 4681–4684. doi: 10.1109/IGARSS.2018.8517732.

[39] C. Qiu, L. Mou, M. Schmitt, and X. X. Zhu, “Local climate zone-based urban land cover classification from multi-seasonal Sentinel-2 images with a recurrent residual network,” *ISPRS J. Photogramm. Remote Sens.*, vol. 154, pp. 151–162, Aug. 2019. doi: 10.1016/j.isprsjprs.2019.05.004.

[40] C. Yoo, D. Han, J. Im, and B. Bechtel, “Comparison between convolutional neural networks and random forest for local climate zone classification in mega urban areas using Landsat images,” *ISPRS J. Photogramm. Remote Sens.*, vol. 157, pp. 155–170, Nov. 2019. doi: 10.1016/j.isprsjprs.2019.09.009.

[41] Y. Fu et al., “Mapping impervious surfaces in town–rural transition belts using Chinas GF-2 imagery and object-based deep CNNs,” *Remote Sens.*, vol. 11, no. 3, p. 280, 2019. doi: 10.3390/rs11030280.

[42] H. Jing et al., “Effective classification of local climate zones based on multi-source remote sensing data,” in *Proc. IGARSS 2019–2019 IEEE Int. Geoscience and Remote Sensing Symp.*, pp. 2666–2669. doi: 10.1109/IGARSS.2019.8898475.

[43] M. Demuzere, B. Bechtel, and G. Mills, “Global transferability of local climate zone models,” *Urban Clim.*, vol. 27, pp. 46–63, Mar. 2019. doi: 10.1016/j.uclim.2018.11.001.

[44] N. Gorelick, M. Hancher, M. Dixon, S. Ilyushchenko, D. Thau, and R. Moore, “Google earth engine: Planetary-scale geospatial analysis for everyone,” *Remote Sens. Environ.*, vol. 202, pp. 18–27, July 2017. doi: 10.1016/j.rse.2017.06.031.

[45] M. Schmitt, L. H. Hughes, C. Qiu, and X. X. Zhu, “Aggregating cloud-free Sentinel-2 images with google earth engine,” *ISPRS Ann. Photogramm., Remote Sens. Spat. Inf. Sci.*, vol. IV-2/W7, pp. 145–152, Sept. 2019. doi: 10.5194/isprs-annals-IV-2-W7-145-2019.

[46] C. E. Brodley and M. A. Friedl, “Identifying mislabeled training data,” *J. Artif. Intell. Res.*, vol. 11, no. 1, pp. 131–167, 1999. doi: 10.1613/jair.606.

[47] S. Xie, R. Girshick, P. Dollár, Z. Tu, and K. He, “Aggregated residual transformations for deep neural networks,” in *Proc. IEEE Conf. Computer Vision and Pattern Recognition*, 2017, pp. 1492–1500. doi: 10.1109/CVPR.2017.634.

[48] S. Woo, J. Park, J.-Y. Lee, and I. So Kweon, “CBAM: Convolutional block attention module,” in *Proc. European Conf. Computer Vision*, 2018, pp. 3–19. doi: 10.1007/978-3-030-01234-2_1.

[49] J. R. Anderson, “Land-use classification schemes: Used in selected recent geographic applications of remote sensing,” *Photogramm. Eng.*, vol. 37, no. 4, pp. 379–387, 1971.

[50] European Space Agency, “Copernicus open access hub.” Accessed on: 2018. [Online]. Available: https://scihub.copernicus.eu/

[51] sentinelsat, “sentinelsat,” GitHub. Accessed on: 2018. [Online]. Available: https://github.com/sentinelsat/sentinelsat

GRS

IRENA HAJNSEK

Technical Committees Survey Results

The IEEE Geoscience and Remote Sensing Society (GRSS) has established a number of technical committees (TCs) to actively promote discussion and advances in areas of members' technical interests. Activities of the TCs include networking within their respective scientific topic, organizing thematic workshops, educating young professionals, and organizing special sessions at the IEEE International Geoscience and Remote Sensing Symposium (IGARSS) as well as hosting committee meetings open to all IGARSS participants.

To improve networking activities and reconsider the scientific topics covered by our TCs, a member survey was performed at the beginning of 2020. The survey was based on three main questions: 1) asking how familiar TC members are with its activities and the technical topic, 2) getting members' opinions concerning potential topics not currently covered by a TC, and 3) inquiring about suggestions for possible improvements with regard to activities and technical content.

The following offers a brief summary of the main outcomes of the survey, presented separately for each TC.

EARTH SCIENCE INFORMATICS

Manil Maskey, NASA Marshall Space Flight Center, United States
Peter Baumann, Jacobs University, Germany
Weiguo Han, University Corporation for Atmospheric Research/NOAA, United States

The GRSS Earth Science Informatics (ESI) TC provides a venue for informatics professionals to exchange ideas and share knowledge. It aims at advancing the application of informatics to geosciences and remote sensing, assessing technology to support data stewardship and management, and promoting best practices and lessons learned.

The main technical areas supported by the ESI TC include cloud computing, big data, machine learning, visualization, data search and discovery, web services, standards, data cubes, the semantic web, data stewardship, and geographic information systems. The survey results (Figure 1) show that TC members are familiar with the ESI TC technical areas; however, data cubes and the semantic web are seen as areas that can be improved.

The survey also showed that TC members are interested in other, relatively new concepts, including

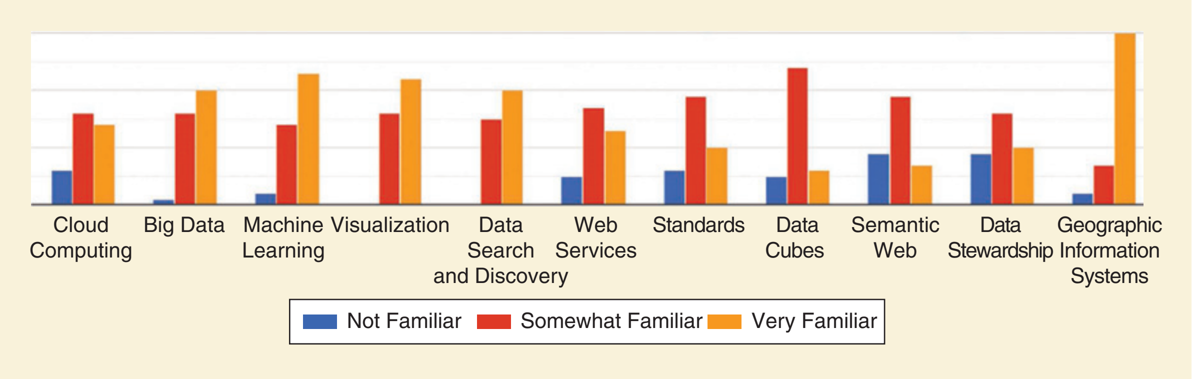

FIGURE 1. Survey findings for the ESI TC.

Digital Object Identifier 10.1109/MGRS.2020.3014541
Date of current version: 21 September 2020

analysis-ready data, 3D vision, machine learning on synthetic aperture radar (SAR), spatial data science, and LiDAR point clouds. TC members are willing to contribute toward broadening the ESI TC technical areas with these concepts.

Additionally, members suggested that the TC should communicate more often via webinars and newsletters. The ESI TC looks forward to member suggestions for improving activities and member engagement going forward.

FREQUENCY ALLOCATIONS IN REMOTE SENSING

Paolo de Matthaeis, NASA Goddard Space Flight Center, United States
Roger Oliva Balague, Zenithal Blue Technologies, Spain
Tobias Bollian, German Aerospace Center (DLR), Oberpfaffenhofen

The main objective of the GRSS Frequency Allocations in Remote Sensing (FARS) TC is to interface between the GRSS community and the radio frequency (RF) regulatory world.

Approximately one quarter of FARS TC members participated in the survey. The interest of TC members is almost evenly spread across all frequency bands, with particular emphasis on the L, C, and X bands (Figure 2).

As for field of expertise (Figure 3), FARS TC members are more expert in RF interference (RFI) algorithms for passive instruments than for active. Most members are quite familiar with airborne instruments and data but not as much with unmanned aerial vehicles (UAVs). As expected, members' knowledge is focused on hardware and scientific data and applications rather than on telecommunications or data links. A good number have a basic understanding of spectrum management.

Other fields proposed by our members to be covered by the FARS TC include Global Navigation Satellite System reflectometry (GNSS-R), antenna engineering, and government policy. Interesting suggestions for future activities were also given such as providing more public outreach with media engagement or even YouTube videos and assisting in educating policy makers about the impact of RFI for passive sensing.

Finally, it is encouraging to see that more than half of survey participants are interested in joining a FARS First Responders group established to respond to frequency regulatory proposals.

INSTRUMENTATION AND FUTURE TECHNOLOGIES

Jose Marquez Martinez, Airbus Defense, United Kingdom
Delwyn Moller, University of Auckland, New Zealand
Marwan Younis, DLR, Oberpfaffenhofen

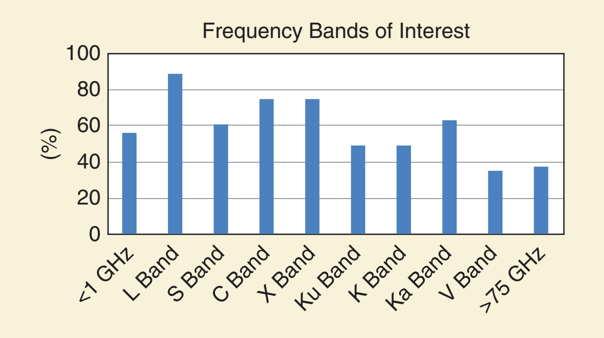

FIGURE 2. FARS TC members' interest in different frequency bands.

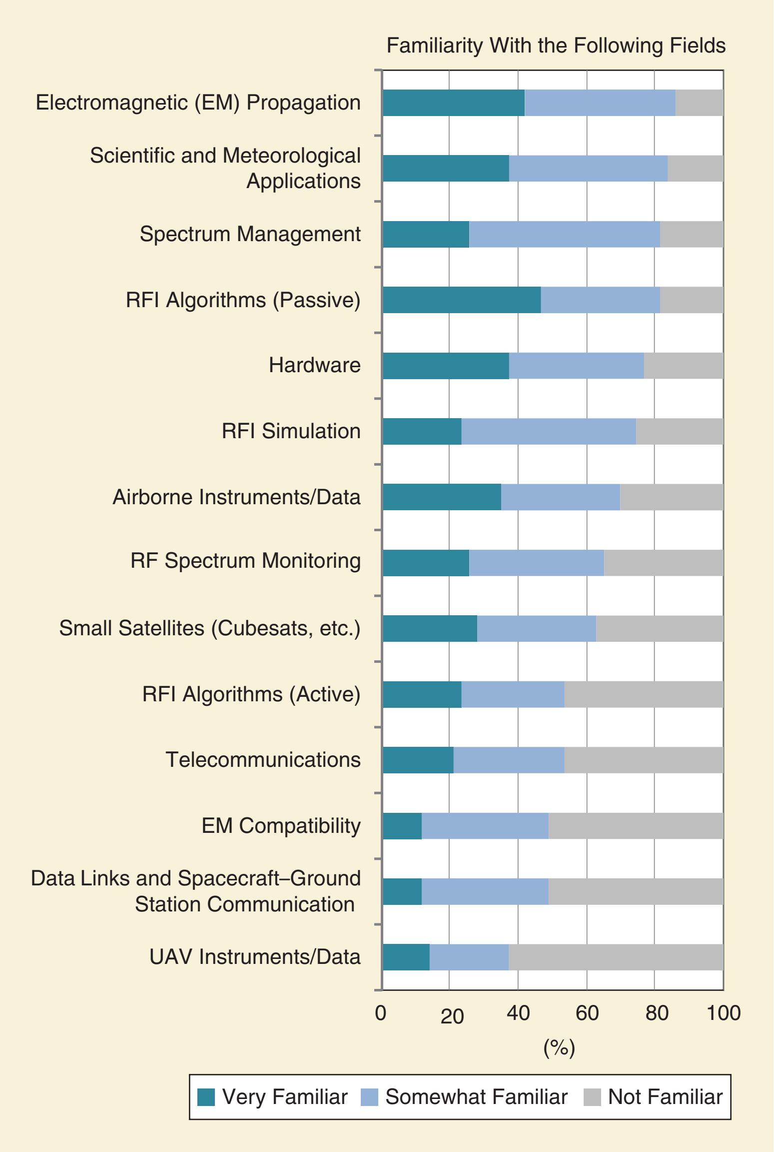

FIGURE 3. FARS TC members' designated fields of expertise.

The GRSS Instrumentation and Future Technologies (IFT) TC has established as its goal "to foster international cooperation in advancing the state of the art in geoscience remote sensing instrumentation and technologies to improve knowledge for the betterment of society and the global environment".

The main objectives of the IFT TC are as follows:

- assess the current state of the art in remote sensing instruments and technology
- identify new instrument concepts and relevant technology trends
- recognize enabling technologies for future instruments.

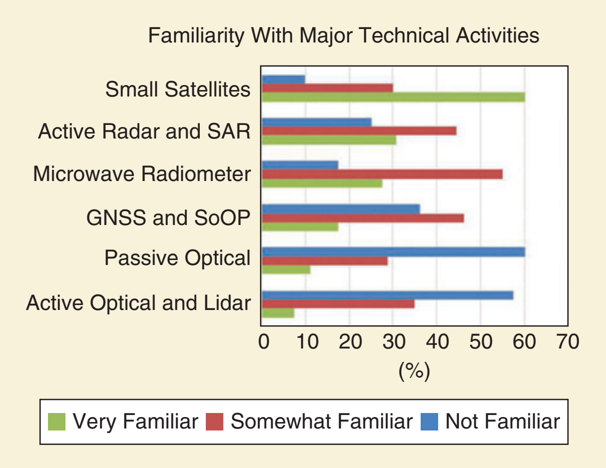

FIGURE 4. IFT TC member's familiarity with technical areas. SoOP: signals of opportunity.

The committee also actively promotes and provides insight into institutions and industry involved in remote sensing instrument and technology development.

The results of the survey (Figure 4) show that IFT TC members are primarily familiar with microwave systems and small satellites. It is also significant to note that >55% express no familiarity at all with optical systems—a point to address and improve in the future.

The survey also revealed that IFT TC members are mainly involved in new instrument concepts (65%) and that we are not properly reaching members with experience on hardware technology (Figure 5). Our members pointed out that cognitive sensing and low-cost, real time systems should be considered as topics relevant to the IFT TC.

The IFT TC survey had a response rate of around 15%. It also revealed that the engagement of our members is variable, with similar results for members who want to contribute significantly and those just interested in receiving the newsletter.

IMAGE ANALYSIS AND DATA FUSION

Naoto Yokoya, RIKEN, Japan
Ronny Hänsch, DLR, Oberpfaffenhofen
Pedram Ghamisi, HZDR Dresden, Germany

The GRSS Image Analysis and Data Fusion (IADF) TC serves as a global, multidisciplinary network for geospatial image analysis (e.g., machine learning, deep learning, image and signal processing, and big data) and data fusion (e.g., multisensor, multiscale, and multitemporal data integration). It aims at connecting people and resources, educating students and professionals, and promoting theoretical advances and best practices in image analysis and data fusion.

Examples of the main technical activities of the IADF TC are the GRSS Data and Algorithm Standard Evaluation (DASE) website, organization of the Data Fusion Contest (a scientific challenge held annually since 2006), and organization of EarthVision (a workshop on large-scale computer vision for remote sensing imagery held in conjunction with the Conference on Computer Vision and Pattern Recognition, one of the major computer vision conferences). The survey results show that TC members are quite familiar with all these activities and, at least to some extent, actively participate in them (Figure 6).

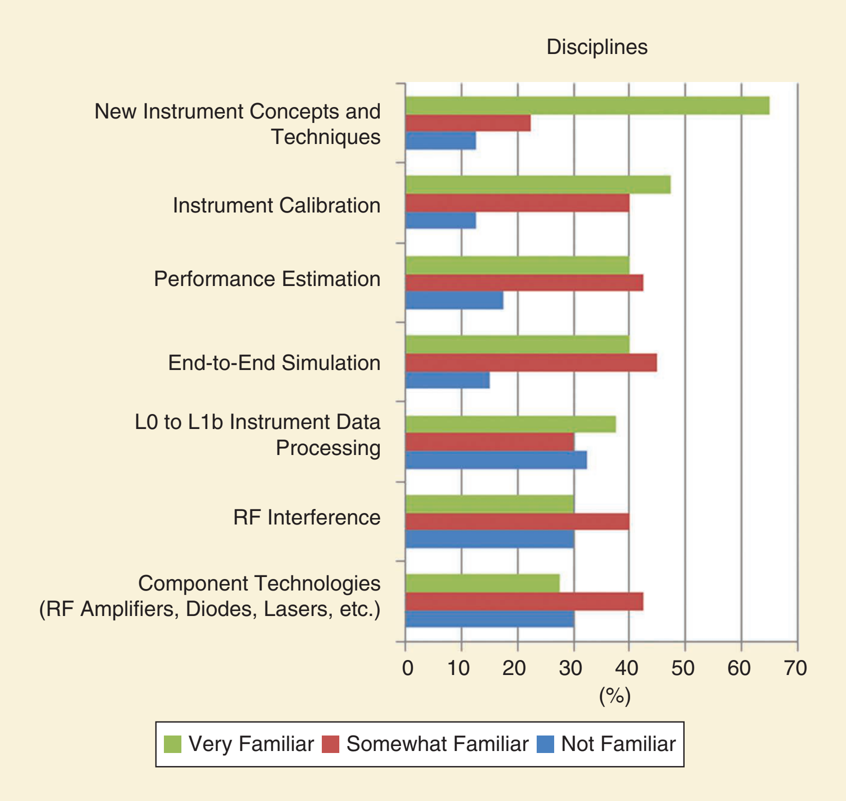

FIGURE 5. IFT TC members' involvement in disciplinary areas.

The survey also showed that TC members are very well acquainted with the core topics of machine learning (e.g., deep learning, object detection, and semantic segmentation) as well as high-level image processing (e.g., segmentation, feature extraction, and restoration), while there is only medium familiarity with low-level image processing topics (e.g., compression and quantization). This illustrates that the majority of IADF TC members come from machine learning and computer vision topics, which are very well represented by current IADF activities.

However, TC members also feel that sensor-specific topics as well as the regression of bio/geophysical parameters are underrepresented. Further suggestions were to increase the relevance of TC activities for industry, further encourage code and data sharing, and increase outreach to other scientific communities. As a result, the IADF TC established three working groups to diversify the topics addressed by the TC, increased the information content of the monthly newsletter, established an industry sponsorship for EarthVision, and initiated a redesign of the DASE website to address the most current developments in the machine learning-based analysis of remotely sensed images.

GEOSCIENCE SPACEBORNE IMAGING SPECTROSCOPY

Uta Heiden, DLR, Oberpfaffenhofen
Cindy Ong, CSIRO, Australia
Jens Nieke, European Space Agency, The Netherlands

The mission of the GRSS Geoscience Spaceborne Imaging Spectroscopy (GSIS) TC is to share information about operating and future spaceborne imaging spectroscopy missions as a means of initiating new partnerships among national space agencies, commercial spaceborne imaging spectroscopy data providers, research institutions, and the user community. One of the main tasks is to build the knowledge base required for imaging spectroscopy missions and enable the uptake of spaceborne imaging spectroscopy by the geoscientific community. With an increasing number of missions going operational, coordinating calibration and validation to ensure interoperability among missions, best practice mission implementation, and mass data management challenges are required.

To provide a vivid and informative platform for knowledge and news exchange, a short member questionnaire was developed. It started with the question "how familiar are you with the TC's major technical activities?" to learn about the current effectiveness of the GSIS TC. In summary, 7.4% of members replied, representing a balanced share of expertise. Additionally, a variety of applications are covered (Figure 7), including classical fields such as geology, mineralogic mapping, and mine-face imaging; terrestrial environmental fields such as vegetation productivity, forestry, biodiversity, and soils; atmospheric fields; urban applications; aquatic environmental applications such as research on detection of pollution; and issues related to space and security.

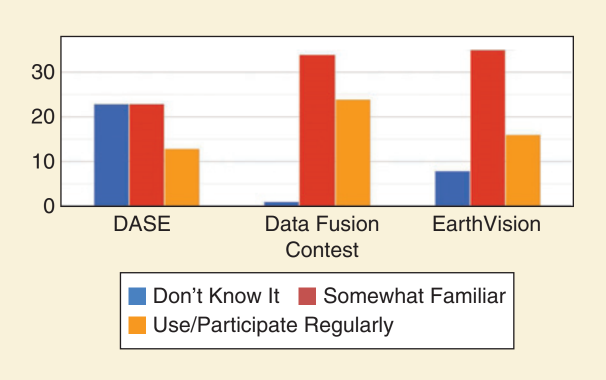

FIGURE 6. IADF TC members' familiarity with current TC activities.

Several pertinent fields of interest that have not yet been considered a focus of the GSIS TC were also identified, such as the development of lab and/or in situ spectral databases for sensor calibration and validation, astronomy, the large field of target anomaly and change detection, and spectral-based detection of surfaces. Members also considered the more methodological fields of hyperspectral pan-sharpening and unmixing, which are of high interest.

Further suggestions include bringing different application fields together, since data sets and methodological strategies are very similar and exchange of experiences can be mutually beneficial. These suggestions strengthen the path taken by the GSIS TC to invest in data harmonization and calibration activities and motivate expansion of activities toward various geoscientific application domains. Another suggestion was to strengthen links with other relevant networks such as the Committee on Earth Observation Satellites Working Group on Calibration and Validation and the IEEE P4000 initiative. In fact, this link is already well established but may need more visibility and communication. Finally, continuing with the organization of workshops, sessions, and courses was emphasized.

In summary, the TC determined to follow the path of data calibration/validation to ensure better data harmonization and thus provide the basis for bringing different applications together.

MODELING IN REMOTE SENSING

Sharmila Padmanabhan, Jet Propulsion Laboratory, NASA, United States
Rob Sundberg, Spectral Sciences Inc., United States
Jean Phillippe Gastellu-Etchegorry, CESBIO, France

The mission of the GRSS Modeling in Remote Sensing (MIRS) TC is to serve as a technical and professional forum for advancing the science of predicting remotely sensed observations from first principles theory. The MIRS TC addresses the technical space between basic EM theory and data collected by remote sensing instruments. It focuses on models and techniques used to make geometric, volumetric, and material composition descriptions of a scene along with their EM attributes (e.g., scattering, absorption, emission, optical bidirectional reflectance distribution function, dielectric properties, etc.) and then predict for a given remote sensing instrument the resulting observation.

The survey indicated that MIRS TC members are most familiar with forward modeling, followed by EM, SAR, radiative transfer, and optical modeling (Figure 8). Members suggested that consideration be given to adding the following modeling topics:

- soil modeling
- geology and mineralogy modeling
- vegetation fluorescence
- land surface modeling
- water resources management (hydrological modeling)
- GNSS-R bistatic modeling.

In general, the responses showed the need for more member interaction, including the exchange of field campaign results for testing different models, which can then be generalized so that members may cooperate and publish together. Moreover, a database can be established for committee members, in addition to an open blog or even a Github devoted to exchanging ideas among working

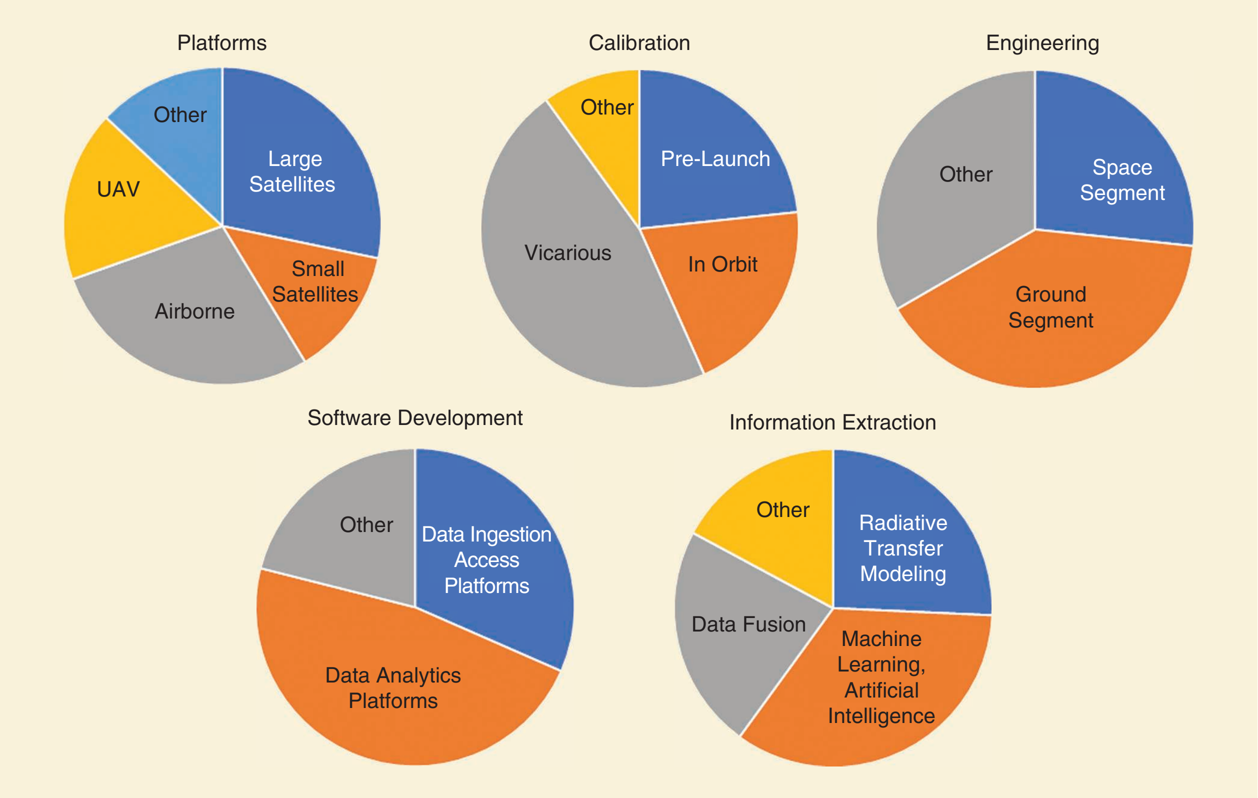

FIGURE 7. Results of the GSIS TC member survey.

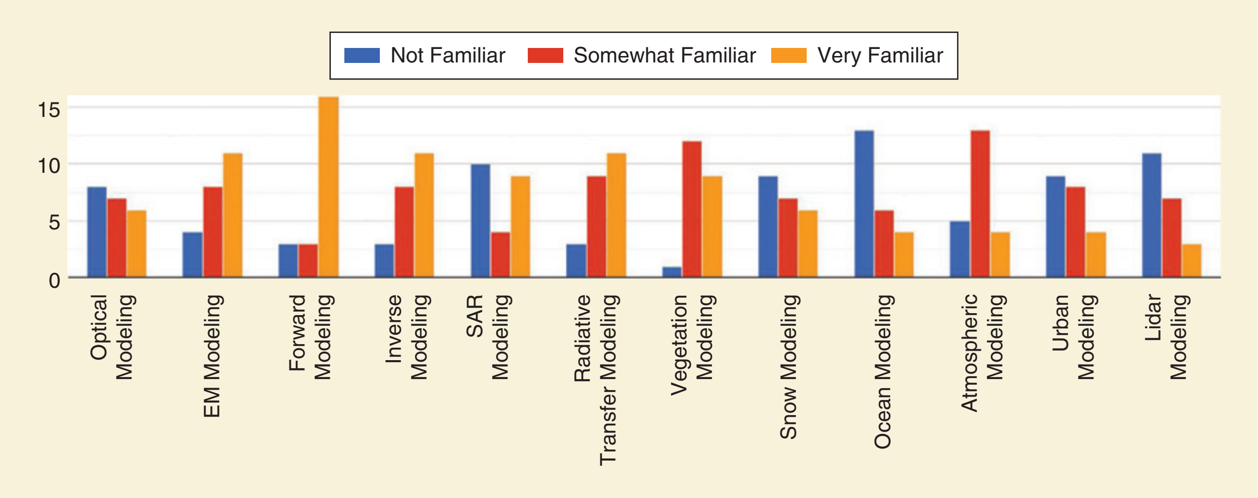

FIGURE 8. Results of the MIRS TC member survey about familiarity with aspects of the field.

groups focused on a few major fields. There were suggestions to 1) organize webinars for better communication, 2) initiate panel discussions during professional conferences for the promotion of remote sensing science, 3) extend applications of radiative transfer modeling to other fields such as Earth system modeling, 4) advance multimodel intercomparison projects, and 5) have regular as well as frequent special sessions during IGARSS as well as special issues involving the Joint Surveillance and Target Attack Radar System. Publishing a newsletter to keep members informed about TC activities was supported by most members who filled out the survey.

SUMMARY

Each survey to gather feedback from GRSS TC members about improving TC activities and getting more members involved was a very valuable action for the TC chairs. Many suggestions have been received on how to improve the TCs' operation and extend their profile portfolio.

The feedback can be grouped into four categories:

- *Education*: develop educational courses for members, and also nonmembers, to make the TCs more visible
- *Communication*: have more sustained reporting on activities and international boards
- *Networking*: increase platforms to provide opportunities for member exchanges
- *Participation*: generate contests on wider topics to involve TC members and nonmembers.

Out of the collected suggestions, actions have been formulated and will be taken into account to improve the TCs' operation. On this point, we thank all participants for their contribution and valuable inputs. For more information about the GRSS TCs, please visit http://www.grss-ieee.org/community/technical-committees/.

AUTHOR INFORMATION

Irena Hajnsek (irena.hajnsek@dlr.de) is with ETH Zürich, Switzerland, and the German Aerospace Center, Oberpfaffenhofen, Germany. Hajnsek is vice-president of GRSS Technical Activities

---

SIRI JODHA S. KHALSA

Progress on Standards Development for Remote Sensing in the Geosciences

The rapid development and deployment of new remote sensing instrumentation is transforming the way we acquire and interpret information on all aspects of environmental and human activity. This is driving the need for technical standards that support the processing, management, analysis, and quality assessment of data from these sources. The IEEE Geoscience and Remote Sensing Society (GRSS) Standards for Earth Observations (SEO) Technical Committee (TC) was created in 2017 to support this need. To date, it has sponsored four standards development projects, with two new projects starting soon. This article highlights the scope of each and looks at future directions.

CREATING STANDARDS

A standards development organization (SDO) exists to provide the environment, rules, and governance necessary to facilitate the fair and equitable development of standards and to assist in the distribution and maintenance of the resulting standards. SDOs such as the IEEE Standards Association (IEEE-SA), the International Electrotechnical Commission, the International Organization for Standardization (ISO), the European Machine Vision Association (EMVA), and the Open Geospatial Consortium all operate in a similar fashion, but each has its own policies and procedures that help ensure the integrity of the standards development process.

The motivation for developing a standard begins with a specific challenge such as the need for consolidation (there are too many options), the need for interoperability among systems, or the need for consistency to allow comparison among options. These can originate from industry, government, or academia.

The development of a new standard is typically triggered by a formal request submitted to an SDO for review and evaluation. Once approved, the sponsor recruits and assembles a collaborative team, or working group, to begin the standards development process. working groups

Digital Object Identifier 10.1109/MGRS.2020.3015309
Date of current version: 21 September 2020

comprise individuals and/or entities (people, companies, organizations, nonprofits, and government agencies) who volunteer to support the development of standards.

Each participant in a working group typically brings specific interests as a producer, consumer, or regulator of a particular material, product, process, or service. Working group officers oversee the standards development project in adherence to SDO rules and procedures [1]. The GRSS SEO (GSEO) TC initiated the IEEE-SA GRSS Standards Committee, which is overseeing the following projects.

CHARACTERIZING AND CALIBRATING HYPERSPECTRAL IMAGERS (P4001)

CHAIR: CHRIS DURELL, LABSPHERE, INC.

This project seeks to define procedures and terminology for the absolute characterization of hyperspectral imagers to ensure proper performance for the intended application. The focus is on visible, near-infrared (IR), and short-wave IR sensors (a wavelength range of 300–2,500 nm) using silicon-, indium gallium arsenide-, or mercury cadmium telluride-based focal plane arrays in pushbroom or scanning configurations. The standard will be applicable to instruments deployed on spaceborne, airborne, handheld, or benchtop platforms (see Figure 1). The P4001 project has three subgroups working on terminology, testing and characterization, and data structures.

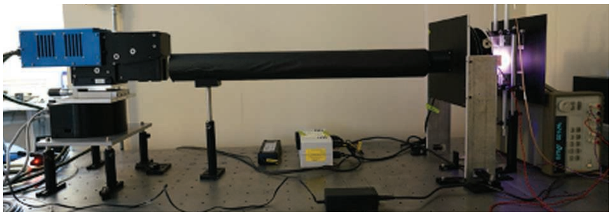

FIGURE 1. The setup for the measurement of point spread function to characterize coregistration and resolution. (Photo courtesy of David Allen.)

TERMINOLOGY ACTIVITIES

The current working draft of terminology includes terms in the following categories: spectral, spatial, signal/radiometric, and system/operational. Where possible, each term references the existing definitions from ISO, IEEE, and EMVA standards. An extended discussion on the definition of *hyperspectral* concluded that it should not include a minimum-wavelength range in the definition. However, a maximum spectral-sampling interval and a minimum number of bands were considered important to the definition of what a hyperspectral imager is.

CHARACTERIZATION ACTIVITIES

The radiometric characteristics deemed important to specify in the standard include properties such as noise, saturation, spectral responsivity, and geometric variation (vignetting and so on). The subgroup is currently discussing two alternatives for predicting signal-to-noise ratio and saturation as well as the scaling/invariance properties of the various characteristics to make direct comparison of hyperspectral imagers easier.

DATA STRUCTURES ACTIVITIES

This subgroup is looking at requirements coming from these communities of interest: geoscience and remote

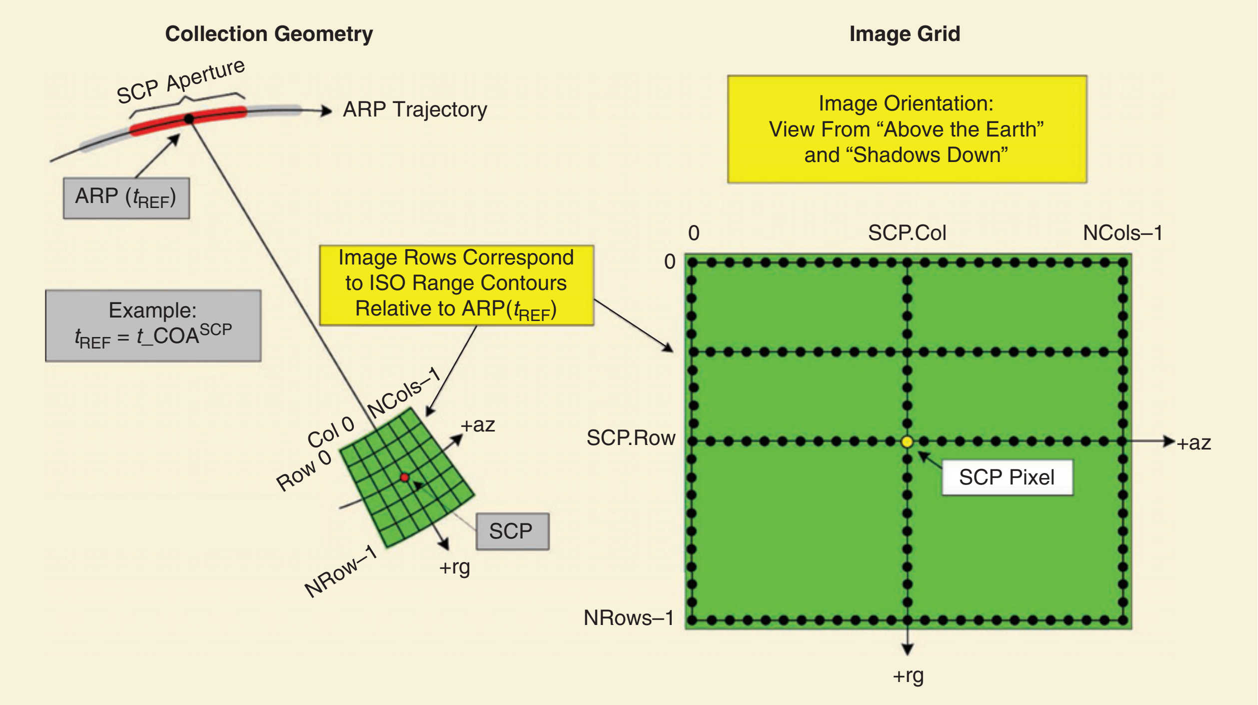

FIGURE 2. SAR collection geometry. (Image courtesy of Leland Pierce.) SCP: scene center point; ARP: aperture reference point.

sensing, laboratories, industry, defense, and security. The subgroup is proposing to develop at least two profiles of a metadata schema: one for a remote sensing application, which would leverage existing ISO/TC211 standards, and a simpler one having high market pressure, perhaps for hyperspectral images in industrial applications. A spectral National Imagery Transmission Format (NITF) implementation profile might be considered as an additional profile for the geointelligence community.

A METADATA MODEL FOR SYNTHETIC APERTURE RADAR DATA (P4002)

CHAIR: LELAND PIERCE, THE UNIVERSITY OF MICHIGAN

The P4002 group is working on a common data model for synthetic aperture radar (SAR) data, driven by the need for generic SAR processing tools that can work with data from multiple sensors having different formats (see Figure 2). This is timely, as the number of SAR data providers is growing, e.g., Sentinel and NASA-ISRO SAR, as well as *ICEYE*, *Capella*, and similar small satellite (sat) constellations. The initial focus is on single-look complex data, the base data level for most SAR products. The project began by looking at elements of the ISO 19115 and 19159-3 standards and then at the sensor-independent complex data (SICD) specification from the U.S. National Geospatial-Intelligence Agency. The latter is perhaps the most modern, complete standard for SAR metadata; thus, the current effort is aimed at aligning SICD with ISO/TC211 elements.

DESCRIBING GNSS REFLECTOMETRY DATA SETS (P4003)

CHAIR: HUGO CARREÑO-LUENGO, THE UNIVERSITY OF MICHIGAN

This effort seeks to develop a standard for data and metadata content arising from spaceborne GNSS-reflectometry (GNSS-R) missions (see Figure 3). Within the scope are

- the terminology used to describe GNSS-R data and derived products
- the structure and content of the data products, such as units of measure, data organization, data encoding, and data storage format
- metadata describing the lineage, methods, and algorithms applied to the data; parameters related to the

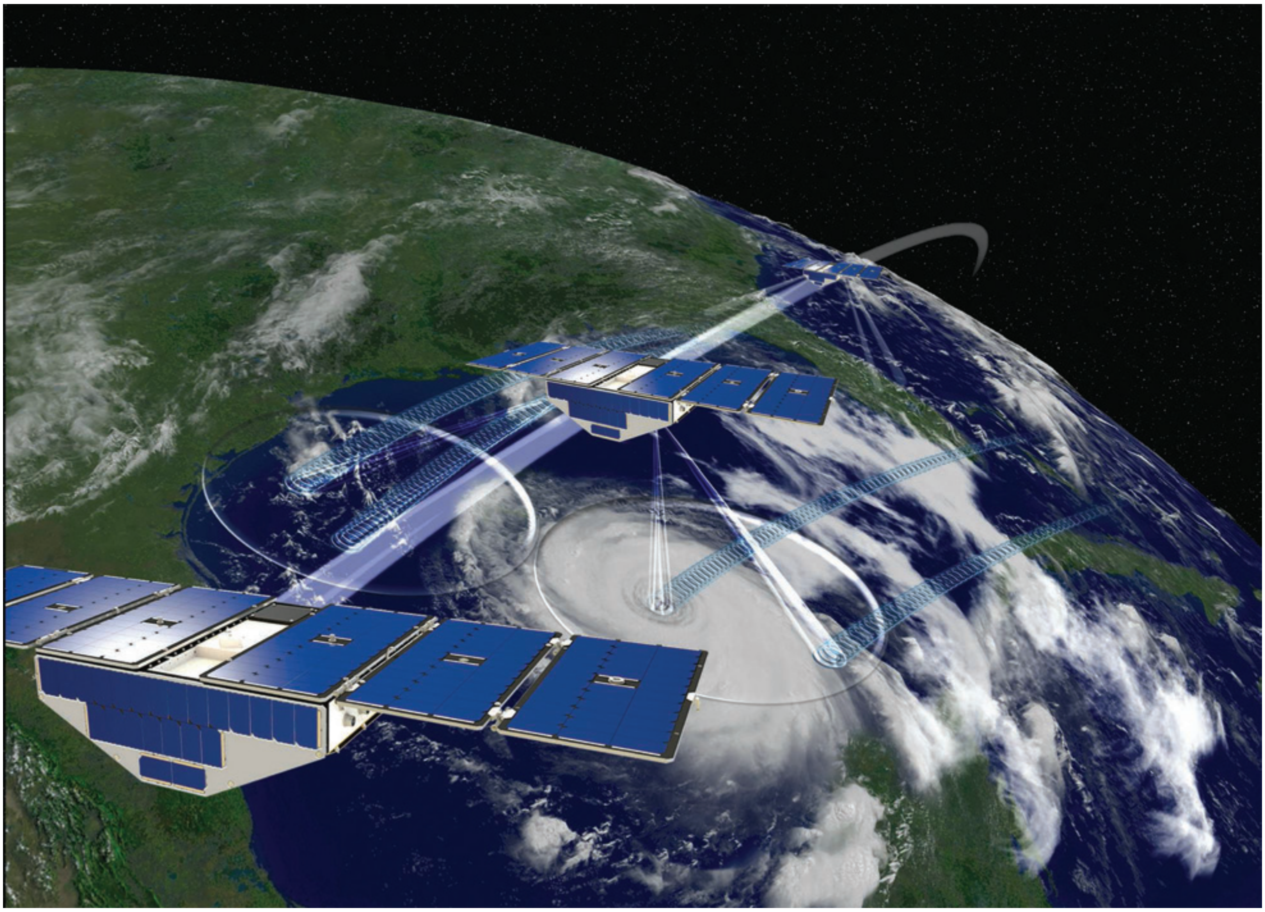

FIGURE 3. NASA's *CyGNSS* reflectometry constellation. (Image courtesy of Chris Ruf.)

algorithms, citation information, instrument calibration, and characterization; and description of the input signals.

A user guide will also be part of this standard, which will be particularly useful for first-time users of GNSS-R data. The standard should prove valuable to GNSS-R payload and sensor developers, the producers of GNSS-R data, the facilities that archive and distribute GNSS-R data, and the developers of data-processing software.

A secondary goal is to provide guidance on the design of level-2 data products to a degree of uniformity across different GNSS-R data sets. It is hoped that this will help solve problems related to products having different data terminologies, units of measures, encodings, and so on, which often require writing new software to deal with each particular data set.

CALIBRATION PROCEDURES FOR MICROWAVE RADIOMETERS (P4004)

CHAIR: DEREK HOUTZ, THE SWISS FEDERAL RESEARCH INSTITUTE WSL

Due to the weak signals typically encountered in microwave remote sensing, the instruments used employ high-gain receiver chains requiring frequent calibration. The P4004 group is working on a standard describing calibration procedures for the microwave radiometers used in geoscience remote sensing applications (see Figure 4). The frequency range being addressed encompasses 300 MHz–1 THz. The standard will not address radiometer calibration for use in other fields, such as radio astronomy, medicine, or security.

The intent is to publish the standard as an IEEE Recommended Practice. It will address

- the terminology in use in the field of radiometer calibration, such as *absolute uncertainty*, *traceable*, *intercalibration*, *vicarious calibration*, and so on
- ground, airborne, and spaceborne radiometers and their respective calibration techniques
- free-space calibration and single-mode (e.g., guided-wave) calibrations
- the calibration of total-power, Dicke-switched, and differential radiometer architectures
- the calibration of polarized radiometers, including full Stoke's radiometers
- the referencing of brightness temperature units to the fundamental constants and the unit Kelvin.

Absolute calibration requirements will vary depending on the application and platform, e.g., short-life CubeSats and operational weather missions versus measurements for climate data records, where detector stability, frequency drift, solar intrusion, and so forth must be considered. Also, different architectures (Dicke, total power, differential correlating, and interferometric), detector types (diode and bolometer), detection types (heterodyne, direct-detect, and digital), polarizations, calibration methods, load/reference types, and scan geometry will be considered. Full end-to-end calibration as well as partial calibration procedures will be addressed.

STANDARD PROTOCOL AND SCHEME FOR MEASURING SOIL SPECTROSCOPY (P4005)

CHAIR: EYAL BEN-DOR

The newest GRSS-sponsored standards project seeks to define protocols and schemes for sensors and measurement methods in creating, comparing, and utilizing soil spectral libraries derived from hyperspectral data (see Figure 5). The goal is to improve how soils are monitored and mapped worldwide. Such a standard will improve the process of merging, comparing, and utilizing soil-spectral libraries from different sources. The standard will also help in evaluating the scheme used in generating soil spectra, which is necessary before performing quantitative analyses based on hyperspectral data.

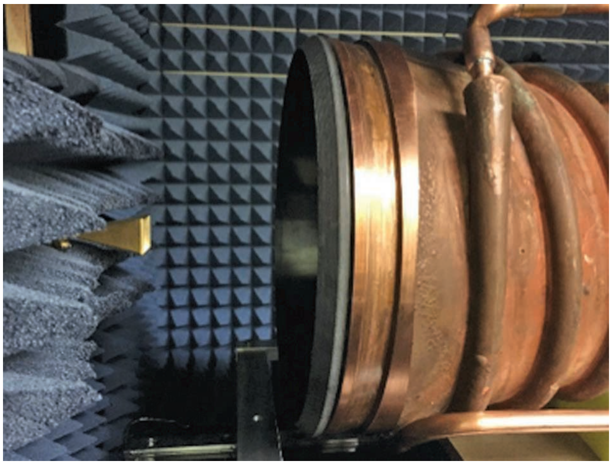

FIGURE 4. A microwave blackbody. (Photo courtesy of Derek Houtz.)

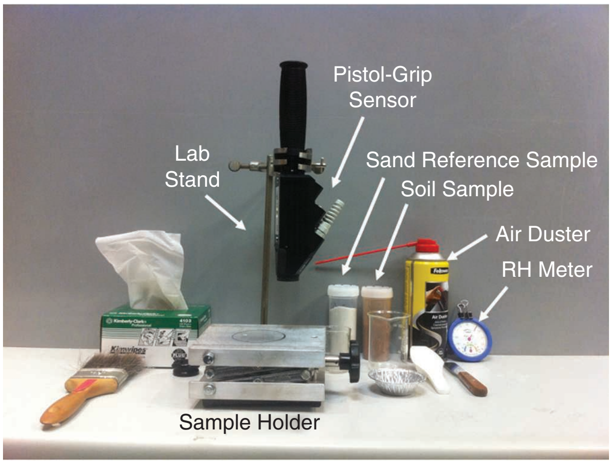

FIGURE 5. The lab setup for measuring spectra of soil samples. RH: relative humidity. (Photo courtesy of Eyal Ben-Dor.)

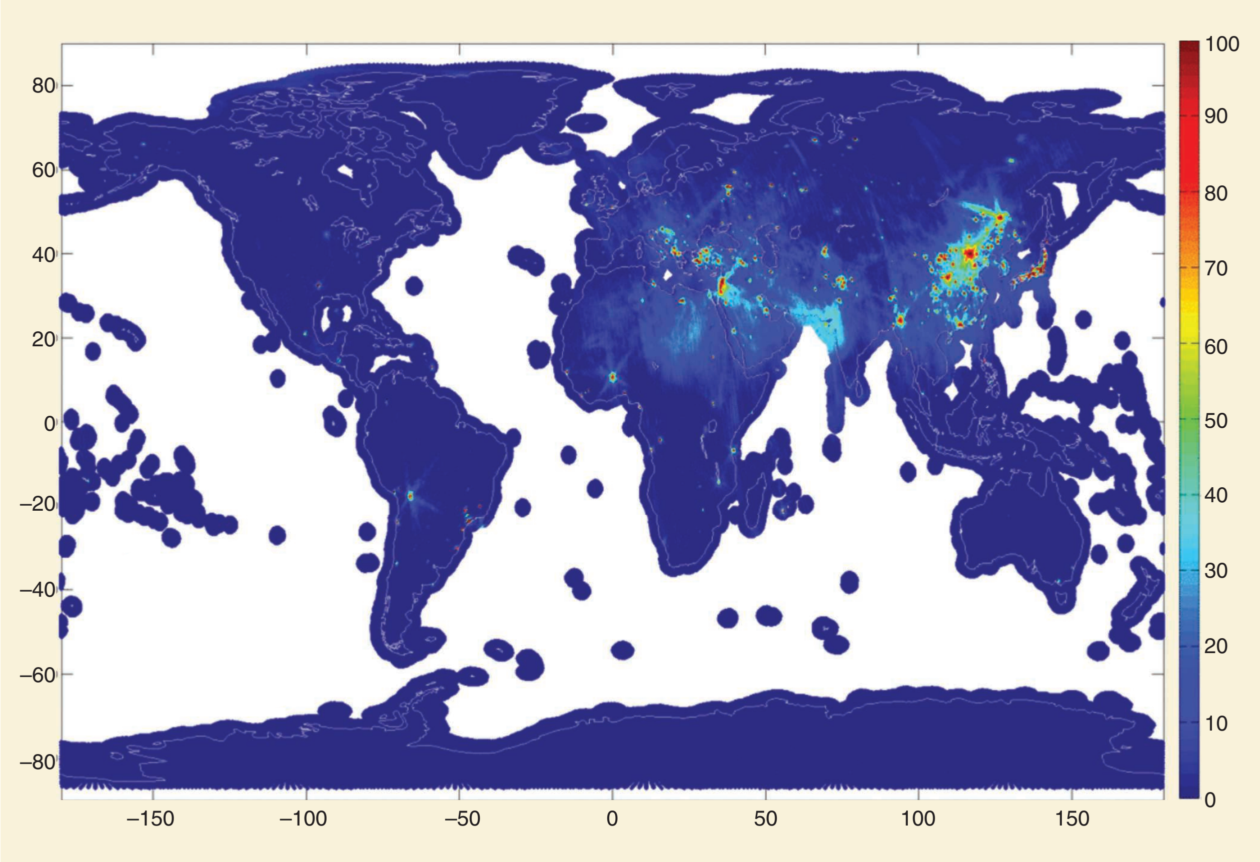

FIGURE 6. A probability map of sustained RFI occurrences for February 2014 from the European Space Agency's Soil Moisture and Ocean Salinity mission's descending passes. (Image courtesy of Roger Oliva.)

NEW PROJECT

CHAIR: ROGER OLIVA

The Frequency Allocation in Remote Sensing TC of the GRSS is consulting with stakeholders in the microwave remote sensing community to determine the best approach and optimal content for a standard that Earth-observing sat missions could follow in assessing, mitigating, and reporting radio-frequency interference (RFI) in bands dedicated to remote sensing (Figure 6). The TC received a seed grant from the Committee on Standards of the IEEE Technical Activities Board.

VOLUNTEER EFFORT

The standards development projects described previously are supported by experts from remote sensing companies, instrument manufacturers, research institutions, and national standards institutes and are developed through a transparent, consensus-based process that relies on volunteer efforts. Manufacturers have an interest in working on standards so as to have well-defined requirements to which they can claim conformance. Individuals are willing to dedicate their time and expertise to developing standards in a desire to shape the direction of an emerging technology, improve the quality and availability of remote sensing products, stay current on the state of the art, and network with others working on a particular problem. There is a common, overarching motivation that volunteers share, which is to advance the utilization of Earth-observation data for the betterment of humanity by helping to make those data more consistent, accessible, and applicable for all those who can benefit from their use.

To become engaged with any of these projects, contact the chairs. To learn more about what the GSEO TC does and how it operates, visit the committee webpage at https://www.grss-ieee.org/community/technical-committees/standards-for-earth-observations/ and/or sign up to the mailing list at https://www.grss-ieee.org/tc_lists/tclist_signup.html?tc=SEO.

AUTHOR INFORMATION

Siri Jodha S. Khalsa (sjsk@nsidc.org) is a research associate at the National Snow and Ice Data Center, University of Colorado, Boulder.

REFERENCE

[1] "Developing standards," IEEE, Piscataway, NJ. [Online]. Available: https://standards.ieee.org/develop/index.html

GRS

LINDA BAILEY HAYDEN

Prof. Sebastiano B. Serpico: Modeling the Important Impact of Research on Education

Selected by an independent major awards committee and approved by IEEE Geoscience and Remote Sensing Society (GRSS) President Prof. Paolo Gamba and the GRSS Administrative Committee, the GRSS Education Award was presented to IEEE Fellow Sebastiano Bruno Serpico (Figure 1). "Congratulations to Professor Serpico on this well-deserved award, which recognizes his outstanding contribution to the teaching of remote sensing," said Josée Lévesque, chair of the GRSS Education Committee.

Prof. Serpico epitomizes the important impact of research on education. His work has provided learning and publication opportunities for dozens of students (Figure 2). As the head of Image Processing and Pattern Recognition for the Polytechnic School of the University of Genoa Remote Sensing for Environment and Sustainability Lab, he has hosted several visiting professors in addition to working with masters, Ph.D., and postdoctoral students. He has supervised more than 70 M.Sc. degree students and many Ph.D. students, some of whom have continued their research activities in remote sensing and become well-known experts in the scientific community.

THE GRSS EDUCATION AWARD WAS ESTABLISHED TO RECOGNIZE AN INDIVIDUAL WHO HAS MADE SIGNIFICANT EDUCATIONAL CONTRIBUTIONS TO THE FIELD OF GEOSCIENCE AND REMOTE SENSING.

Prof. Serpico received his laurea (M.S.) degree in electronic engineering and his Ph.D. degree in telecommunications from the University of Genoa, Italy. He is a full professor of telecommunications at the Polytechnic School of the University of Genoa and a member of the university's Academic Senate. He teaches courses in

FIGURE 1. Prof. Sebastiano Serpico (right) receives the GRSS Education Award from GRSS President Prof. Paola Gamba.

FIGURE 2. Prof. Serpico instructs his students.

Digital Object Identifier 10.1109/MGRS.2020.2998332
Date of current version: 21 September 2020

FIGURE 3. Prof. Serpico delivers a lecture.

the areas of remote sensing, pattern recognition, and telecommunications (Figure 3). He has also taught courses at the University of Cagliari and the University of Trento. His current research interests focus mainly on pattern recognition for remote sensing image analysis.

Prof. Serpico provided strategic contributions for the foundation and management of two engineering programs: one in telecommunications engineering and the other in engineering for natural risk management. From May 2003 to April 2019, he was chair of the Institute of Advanced Studies in Information and Communication Technologies. Other important roles include project manager for numerous research projects and evaluator of project proposals for various European Union, Italian Space Agency, and Italian Ministry of Education and Research programs. He is the author (or coauthor) of more than 250 scientific articles published in journals and conference proceedings. He received the Best Paper Award at the 2010 IEEE Workshop on Hyperspectral Image and Signal Processing and the Interactive Symposium Paper Award at the 2016 IEEE Geoscience and Remote Sensing Symposium (IGARSS). He is an associate editor of *IEEE Transactions on Geoscience and Remote Sensing* (*TGRS*) and was a guest editor of two special issues of *TGRS* and one special issue of *Proceedings of the IEEE*. From 1998 to 2002, he was chair of the Society of Photo-Optical Instrumentation Engineers/EUROPTO conferences on signal and image processing for remote sensing, and he served as cochair of IGARSS 2015 in Milan, Italy.

GRSS EDUCATION AWARD

The GRSS Education Award was established to recognize an individual who has made significant educational contributions to the field of geoscience and remote sensing. In selecting an individual, factors considered are the significance and innovativeness of the educational contribution and the extent of its overall impact. The contribution can be made at any level, including K–12, undergraduate and graduate teaching, professional development, and public outreach. It can also be in any form (e.g., textbooks, curriculum development, or education program initiatives). GRSS membership or affiliation is required. The awardee receives a certificate and plaque.

The 2019 GRSS Education Award certificate presented to Prof. Serpico included the citation "in recognition of his outstanding educational contributions to geoscience and remote sensing." Educators agree that, through research, students develop critical thinking expertise as well as effective analytical and communication skills that are in demand worldwide.

AUTHOR INFORMATION

Linda Bailey Hayden (lbhayden@ecsu.edu) is with Elizabeth City State University, North Carolina.

GRS

YIQING GUO, JUNPENG ZHANG, ADNAN FAROOQ AWAN, XIAOLIN CHEN, AND XIUPING JIA

Activities of the IEEE GRSS University of New South Wales Canberra Student Chapter

The IEEE Geoscience and Remote Sensing Society (GRSS) University of New South Wales (UNSW) Canberra Student Chapter is young and vibrant. It was formally established in December 2018 and was the first IEEE GRSS Student Chapter in Australia. Dr. Yiqing Guo served as the inaugural chair and was succeeded by Adnan Farooq Awan. Currently, Junpeng Zhang and Xiaolin Chen serve as the chair and vice chair, respectively. Dr. Xiuping Jia has served as the advisor since the Student Chapter was established.

Based at UNSW Canberra, the Student Chapter brings together students from the university who share a common interest in geoscience and remote sensing. It provides a platform where members can exchange ideas and discuss potential opportunities. It also aims to promote geoscience and remote sensing activities by reaching out to nonmember students on campus.

ACTIVITIES DURING 2019

To better promote the GRSS UNSW Canberra Student Chapter, an official website has been created, and Chapter news and activities are regularly posted on the site. In addition, a social media webpage has been set up on Facebook. An official logo designed for the Student Chapter by Vice Chair Chen and approved by the GRSS combines elements of the UNSW Canberra logo with the GRSS logo (Figure 1). The logo has been posted on the Student Chapter's official website and social media pages, with the purpose of promoting public identification and recognition.

On 22 May 2019, a seminar was organized, with Chapter Chair Awan, a Ph.D. candidate at UNSW Canberra, presenting a talk on weed classification using deep learning and hyperspectral imagery (Figure 2). Based on his research, Awan showed the potential of advanced remote sensing and machine learning techniques in empowering the traditional task of weed management.

Throughout 2019, Student Chapter members collaborated on their Student Grand Challenge project, "A Drone-based Sensing System to Support Satellite Image Analysis for Rice Farm Mapping." With financial support from the GRSS, scientific equipment was purchased, and three field experiments were conducted collaboratively among Student Chapter members (Figure 3).

FIGURE 1. The official logo of the IEEE GRSS UNSW Student Chapter.

FIGURE 2. Adnan Farooq Awan gives a talk.

Digital Object Identifier 10.1109/MGRS.2020.2997823
Date of current version: 21 September 2020

From 28 July to 2 August 2019, four Student Chapter members, along with Student Chapter advisor Dr. Jia and UNSW Canberra professor and IEEE Fellow Scott Tyo, attended the 2019 IEEE International Geoscience and Remote Sensing Symposium (IGARSS) in Yokohama, Japan (Figure 4), and presented five research papers. During a special session, Dr. Guo reported the activities of the Student Chapter as of July 2019. Kien Nguyen gave an oral presentation at the Student Paper Contest session as one of the finalists selected, and he was also a winner of the IGARSS 2019 Three Minute Thesis contest.

On 1 and 8 November 2019, members attended two seminars organized by the IEEE Australian Capital Territory Section and the UNSW Student Chapter. The first seminar, presented by Prof. Alfredo Huete from the University of Technology Sydney, covered multi- and hypertemporal satellite applications for phenology and pollen forecasting. The second seminar, led by Prof. John P. Kerekes from the Rochester Institute of Technology, focused on remote sensing system engineering research.

PLANS FOR 2020

The following activities were planned for the coming year.

- The New Student Welcoming Morning/Afternoon Tea, which seeks to encourage more new students to join the GRSS and increase its membership. This will be an opportunity to introduce the GRSS and the UNSW Canberra Chapter and encourage involvement in GRSS activities.
- The GRSS in Science and Industry Seminar Series, which helps GRSS student members connect with people from industry and research institutions. Speakers from commercial companies and governmental bodies will be invited. Seminars given by the speakers help GRSS student members understand how geoscience and remote sensing technologies are being applied for practical use.
- The Student High-Impact Publication Seminar Series, which is part of the UNSW Canberra School of Engineering's research student activities. The series invites students who have published in top GRSS journals to present their research, with the hope of encouraging other student members to attend GRSS conferences and publish papers in GRSS journals.

The UNSW Canberra Student Chapter has been and will continue to be a community where geoscience and remote sensing students can learn and share. With enormous support from the IEEE and GRSS, we are confident that the Student Chapter will achieve more in the future.

FIGURE 3. Dr. Yiqing Guo operates a drone during a field experiment.

AUTHOR INFORMATION

Yiqing Guo (yiqing.guo@student.adfa.edu.au) is with the University of New South Wales, Canberra, Australia.

Junpeng Zhang (junpeng.zhang@student.adfa.edu.au) is with the University of New South Wales, Canberra, Australia.

Adnan Farooq Awan (a.awan@student.adfa.edu.au) is with the University of New South Wales, Canberra, Australia.

Xiaolin Chen (xiaolin.chen1@student.adfa.edu.au) is with the University of New South Wales, Canberra, Australia.

Xiuping Jia (x.jia@adfa.edu.au) is with the University of New South Wales, Canberra, Australia.

GRS

FIGURE 4. Student members and colleagues of UNSW Canberra gather at IGARSS 2019. From left to right: Kien Nguyen, Xiaolin Chen, Meng Xu, Xiuping Jia, Scott Tyo, Liz Ritchie-Tyo, Clair Stark, Dr. Yiqing Guo, and Junpeng Zhang.

KEELY ROTH AND SHAWN KEFAUVER

Adapting to COVID-19 Challenges and Moving Forward With GRSS Diversity and Inclusion at IGARSS 2020

The year 2020 has brought a different kind of diversity to us all: a diversity of challenges as we shift our work and lifestyles to cope with the continuing COVID-19 pandemic. More than ever, this global pandemic has brought issues of equality, diversity, equity, and inclusion to the forefront of public view. Large-scale social demonstrations and protests have unfolded across the United States and other countries in support of policy changes to ensure law enforcement's equitable treatment of all individuals. As learning has moved to a virtual online setting, working families have taken on new roles as educators, all while trying to balance this with their day jobs. Millions of people who work in essential jobs have braved the risk of infection to continue to earn a paycheck and to provide necessary services.

THIS GLOBAL PANDEMIC HAS BROUGHT ISSUES OF EQUALITY, DIVERSITY, EQUITY, AND INCLUSION TO THE FOREFRONT OF PUBLIC VIEW.

The IEEE Geoscience and Remote Sensing Society (GRSS) has also adapted to overcome the challenges of 2020 while ensuring that our mission and the community we provide for our members remain strong. For the first time, the IEEE International Geoscience and Remote Sensing Symposium (IGARSS) will be fully virtual, a shift made possible by many dedicated GRSS members. The Inspire, Develop, Empower, Advance (IDEA) Committee has also made the shift. Our conference events, part of the Technology, Industry, and Education track at IGARSS, will also be in a virtual format this year.

We are excited to share that our Women in GRSS forum this year, the "IDEA and WISE-E Inspire and Empower" panel, will be held Friday, 25 September, at 12–1:30 p.m. Eastern time. This event will be co-organized with the Women in Science, Engineering, and the Environment (WISE-E) group, and we will take you on a tour of women scientists and engineers working in the geosciences and remote sensing. We will also be holding a photo contest to encourage members to share their stories and experiences as a diverse group of technical researchers in our discipline, with the winner announced during the event. In lieu of our Women in GRSS luncheon, we will hold a GRSS Diversity and Inclusion Fireside Chat (Wednesday, 21 October, at 12–1:30 p.m. Eastern time). This event will include our annual IDEA Committee activities update and will subsequently kick off a moderated discussion around how our committee can 1) better assess diversity and inclusion within the GRSS and 2) design and launch initiatives that have a high impact on the Society. The panelists will focus on different types of diversity and inclusion initiatives, how to measure their success, and what barriers they address. We hope you are well, and we look forward to engaging with you during our 2020 IGARSS events!

GRS

Digital Object Identifier 10.1109/MGRS.2020.3014486
Date of current version: 21 September 2020

Remote Sensing Code Library (RSCL)

What is RSCL?

RSCL is a publication of IEEE GRSS, just like the GRSS Transactions and the GRSS Newsletter, but distributes computer codes associated with geoscience remote sensing.

What types of codes?

a) Instrument-Related: Processing, calibration, deconvolution, etc.
b) Application: Relating scene geophysical parameters to sensor output (direct problems) or vice versa (inverse problems)

The codes are organized by:

a) Wavelength range (microwave, visible, IR)
b) Sensor type (active, passive, GPS, etc.)
c) Application area (ocean salinity, topography, ocean winds, atmospheric temperature profile, etc.)

Where do the codes come from?

The RSCL codes are developed by members of the GRSS community. All codes undergo a thorough review process before they are accepted and published.

Who can use the codes?

Anyone interested in geoscience remote sensing.

Are the codes citable?

Absolutely. Published codes are assigned DOI numbers, just like journal articles. When journal article authors use a code in support of their article, they are expected to cite that code, thereby giving the code author credit for developing it and making it available for use by other members of the GRSS community.

What does it cost?

There are no publication fees.

How do I submit a code?

The instructions are available at: https://rscl-grss.org/index.php

What are examples of recently published RSCL codes?

[DOI: 10.21982/pzj2-fm81] Optimized Twin Dictionaries (OTD) for Hyperspectral and Multispectral Image Fusion Han, Xiaolin; Xue, Jing-Hao; Sun, Weidong

[DOI: 10.21982/4vaf-b861 _target:] QMOD4 QuikSCAT v4 geophysical model function Long, David

[DOI: 10.21982/2q1x-5x14] Pansharpening Toolbox Vivone, Gemine; Alparone, Luciano; Chanussot, Jocelyn; Dalla Mura, Mauro; Garzelli, Andrea; Restaino, Rocco

[DOI: 10.21982/dpp9-e397] SCoBi bistatic radar simulator Eroglu, Orhan; Boyd, Dylan; Kurum, Mehmet

[DOI: 10.21982/M8M05W] RelDielConst_Vegetation.m Ulaby, Fawwaz

For more information, contact the RSCL Editor in Chief,
Prof. David Long at long@byu.edu

Digital Object Identifier 10.1109/MGRS.2020.3018658


What + If = IEEE